Exactly solvable light-matter interaction models for studying filamentation dynamics

by
Jeffrey M. Brown

A Dissertation Submitted to the Faculty of the

College of Optical Sciences

In Partial Fulfillment of the Requirements
For the Degree of

Doctor of Philosophy

In the Graduate College

The University of Arizona

April 25, 2016

THE UNIVERSITY OF ARIZONA
GRADUATE COLLEGE

As members of the Dissertation Committee, we certify that we have read the dissertation prepared by Jeffrey M. Brown entitled:

Exactly solvable light-matter interaction models for studying filamentation dynamics

and recommend that it be accepted as fulfilling the dissertation requirement for the Degree of Doctor of Philosophy.

_____ Date: April 11, 2016
Miroslav Kolesik

_____ Date: April 11, 2016
Jerome V. Moloney

_____ Date: April 11, 2016
Ewan M. Wright

Final approval and acceptance of this dissertation is contingent upon the candidate's submission of the final copies of the dissertation to the Graduate College.

I hereby certify that I have read this dissertation prepared under my direction and recommend that it be accepted as fulfilling the dissertation requirement.

_____ Date: April 11, 2016
Miroslav Kolesik

Statement by Author

This dissertation has been submitted in partial fulfillment of requirements for an advanced degree at The University of Arizona and is deposited in the University Library to be made available to borrowers under rules of the Library.

Brief quotations from this dissertation are allowable without special permission, provided that accurate acknowledgment of source is made. Requests for permission for extended quotation from or reproduction of this manuscript in whole or in part may be granted by the head of the major department or the Dean of the Graduate College when in his or her judgment the proposed use of the material is in the interests of scholarship. In all other instances, however, permission must be obtained from the author.

Signed: _____ Jeffrey M. Brown _____

Approval by Dissertation Director

This dissertation has been approved on the date shown below:

Miroslav Kolesik Associate Professor of Optical Sciences	Date

Acknowledgements

I would like to extend my sincerest gratitude to the many people that aided me in my research efforts. I would like to thank my advisor Miroslav Kolesik for being a great mentor and teacher, Jerry Moloney for the opportunity to be a part of the ACMS research group that provided a great environment for research and learning, and allowed for travel to conferences and workshops, and Ewan Wright for helpful discussions and guidance. I also would like to thank Per Jakobsen and Farhad Faisal for their collaboration and fruitful visits to Arizona, and the other members of our research group for their support and friendship.

I also would like to thank the Optical Sciences Center for giving me the opportunity to learn through quality curriculum and to be surrounded by excellent faculty. Lastly, I would like to thank the United States Air Force Office of Scientific Research for the MURI grants FA9550-10-1-0561 and FA9550-13-1-0228 that provided funding and collaboration opportunities.

Dedication

To my beloved Tova

Table of Contents

Table of Contents—*Continued*

Table of Contents—*Continued*

List of Figures

List of Figures—*Continued*

List of Figures—*Continued*

List of Figures—*Continued*

List of Figures—*Continued*

List of Figures—*Continued*

List of Figures—*Continued*

Abstract

This dissertation demonstrates the usefulness of exactly solvable quantum models in the investigation of light-matter interaction phenomena associated with the propagation of ultrashort laser pulses through gaseous media. This work fits into the larger research effort towards remedying the weaker portions of the standard set of medium modeling equations commonly used in simulations. The ultimate goal is to provide a self-consistent quantum mechanical description that can integrate Maxwell and Schrödinger systems and provide a means to realistically simulate nonlinear optical experiments on relevant scales. The study of exactly solvable models begins with one of the simplest quantum systems available, one with a 1D Dirac-delta function potential plus interaction with the light field. This model contains, in the simplest form, the most important "ingredients" that control optical filamentation, i.e. discrete and continuum electronic states. The importance of both states is emphasized in the optical intensity regime in which filaments form, where both kinds of electronic states simultaneously play a role and may not even be distinguishable. For this model atom, an analytical solution for the time-dependent light-induced atomic response from an arbitrary excitation waveform is obtained. Although this system is well-known and has been studied for decades, this result is probably the most practically useful and general one obtained thus far. Numerical implementation details of the result are also given as the task is far from trivial. Given an efficient implementation, the model is used in light-matter interaction simulations and from these it is apparent that even this toy model can qualitatively reproduce many of the nonlinear phenomena seen in experiments. Not only does this model capture the basic physics of optical filamentation, but it is also well-suited for high harmonic generation simulations. Next, a theoretical framework for using Stark resonant states (or metastable states) to represent the medium's polarization response is presented. Researchers have recognized long ago the utility of Gamow resonant states as a description of various decay processes. Even though a bound electron experiences a similar decay-like process as it transitions into the continuum upon ionization, it was unclear whether field-induced Stark resonant states carry physically relevant information. It is found that they do, and in particular it is possible to use them to capture a medium's polarization response. To this end, two quantum systems with potentials represented by a 1D Dirac-delta function and a 1D square well are solved, and all the necessary quantities for their use as medium models are presented. From these results it is possible to conjecture some general properties that hold for all resonance systems, including systems that reside in higher than one dimensional space. Finally, as a practical application of this theory, the Metastable Electronic State Approach (MESA) is presented as a quantum-based replacement for the standard medium modeling equations.

Chapter 1

Introduction

1.1 Standard approach to light-matter interactions

Propagation of ultrashort, off-resonant optical pulses in atomic gases produces a broad range of extreme nonlinear optical effects including high-harmonic generation [1], synthesis of attosecond pulse forms [2], and optical filamentation [3, 4]. While it is generally accepted that the origin of these phenomena resides in the quantum mechanical nature of the light-matter interaction, the standard approach of modeling the nonlinearity underlying filamentation so far does not provide a unified quantum treatment. Instead a piecewise approach to modeling light-matter interactions is used where individual phenomena are treated separately, e.g. instantaneous third-order nonlinearity for bound electrons, a Drude model for free electrons, and a host of other "corrections". The piecewise construction of the current medium model is an artifact of both historical discovery where phenomenological terms were added to explain new observations in experiment, and also of conceptual description where the electron is seen as either bound to the atom or totally free.

The "standard" approach to modeling light-matter interactions for ultrashort laser pulses in gases is to combine separate equations describing each observable phenomena into a medium response function. An example propagation equation that is well suited for propagating short laser pulses over large distances is the Unidirectional Pulse Propagation Equation (UPPE [5]). For linearly polarized light, $E(z, k_\perp, \omega)$ is the spatio-temporal electric field spectrum of the pulsed waveform with frequency ω and wavevector k_z and its dynamics are governed by

$$\partial_z E(z, k_\perp, \omega) = ik_z E(z, k_\perp, \omega) + \frac{i\omega^2}{2\epsilon_0 c^2 k_z} P_{NL}(E(z, k_\perp, \omega)) - \frac{\omega}{2\epsilon_0 c^2 k_z} J_{NL}(E(z, k_\perp, \omega)). \tag{1.1}$$

The first term on the right hand side represents the linear propagation of light where the z-component of the optical wavevector is given by

$$k_z(k_\perp, \omega) = \sqrt{\omega^2(1 + \chi(\omega))/c^2 - k_\perp^2}. \tag{1.2}$$

In these equations c is the speed of light, ϵ_0 is the free space permittivity, χ is the linear susceptibility of the medium, and $k_\perp$ is the component of the wavevector that is perpendicular to the propagation direction. In addition to linear propagation there are two nonlinear source terms that represent coupling of the electric field to the medium: the nonlinear polarization P_{NL} and the nonlinear current J_{NL}. A large amount of

research has gone into finding accurate descriptions for these two terms, as they govern a majority of the interesting dynamics seen in ultrashort pulse propagation. Providing an accurate description of these two nonlinear terms is paramount, and this dissertation presents forward progress in this area and offers practical replacements for all or most of the equations that are be described below.

Commonly used equations for the two nonlinear source terms are detailed in review papers by Couairon [3] and Bergé [4]. For propagation in atomic gases, the two most important phenomena to capture are the instantaneous Kerr effect and ionization. The nonlinear polarization P_{NL} can be modeled as a Taylor series in E when the optical fields are not too large

$$P_{NL} = \epsilon_0 \left[\chi^{(2)}E^2 + \chi^{(3)}E^3 + \chi^{(4)}E^4 + \chi^{(5)}E^5 + \ldots\right]. \tag{1.3}$$

For isotropic media such as gases, even orders of χ do not appear. For many simulations it is enough to include only up to third-order nonlinearity (Kerr effect)

$$P_{NL} = 2\epsilon_0 n_0 n_2 |E|^2 E, \tag{1.4}$$

though there has been some recent debate over the inclusion of higher order terms [6, 7], which is discussed later in greater detail. In Eq. (1.4) n_0 is the background refractive index and n_2 is the nonlinear refractive coefficient. The value of n_2 is essentially the strength of the nonlinearity for the particular medium and is therefore an important simulation parameter. Also note that the Kerr effect is modeled as an instantaneous effect meaning that it has no memory of the past field values, but is only dependent on the current electric field value. This choice in modeling also ignores any spectral dependence or nonlinear dispersion. It has been shown that the value of n_2 for sapphire has a weak wavelength dependence [8], hinting at a slightly delayed nonlinearity. For atomic gases however, such memory effects were (so far) not measured directly, though one publication has appeared during this writing [9].

If laser pulse durations are long enough, then the stimulated Raman effect can be included in the nonlinear polarization as

$$P_{NL} = 2\epsilon_0 n_0 n_2 \left[(1-\alpha)E^2 + \alpha \int_0^\infty R(t-\tau)E^2(\tau)d\tau\right] E(t). \tag{1.5}$$

Using this P_{NL} instead of (1.4) can account for non-instantaneous effects, such as molecular vibrations and movement of the atomic nuclei during molecular rotation or reorientation induced by the incident field, through the memory function R that can contain oscillatory and phenomenological damping terms. The parameter α denotes the fraction of delayed response present in the Kerr effect.

The phenomenon of ionization is commonly modeled by a free electron density ρ contributing to the nonlinear current J_{NL} under the influence of the electric field E.

The nonlinear current is conceptually split into components representing a response from plasma and also absorption (abs), and obey the following equations of motion

$$\begin{aligned} J_{NL} &= J_{plasma} + J_{abs} \\ \frac{\partial J_{plasma}}{\partial t} &= \frac{e^2}{m_e}\rho E - \frac{1}{\tau_c} J_{plasma} \\ \frac{J_{abs}}{\epsilon_0 n_0 c} &= \frac{W(|E|^2)U}{|E|^2}(\rho_{nt} - \rho)E \\ \frac{\partial \rho}{\partial t} &= W(|E|^2)(\rho_{nt} - \rho) + \frac{\sigma}{U}\rho|E|^2 - a\rho^2. \end{aligned} \tag{1.6}$$

The last line shows that the change in free electron density is a sum of multiphoton ionization, avalanche ionization and a phenomenological damping term to account for electron recombination with its parent atom. The variables and constants in (1.6) are defined as follows: e and m_e are the electron charge and mass, τ_c is the electron collision time, $W(|E|^2)$ is the rate of ionization of an atom with potential U, ρ_{nt} is the density of neutral atoms, a is the electron recombination rate and the cross section σ for inverse Bremsstrahlung follows the Drude model [10]

$$\sigma = \frac{k_0}{n_0 \rho_c} \frac{\omega_0 \tau_c}{(1 + \omega_0^2 \tau_c^2)} \tag{1.7}$$

where ρ_c is the critical plasma density. Accurately representing the rate of ionization W in (1.6) is extremely important for simulations as slight changes in this rate can drastically alter the results of a propagation simulation. This rate is usually represented as a power-law $W = \sigma_K |E|^K$ [11] with parameters σ_K and K chosen to fit experimentally measured rates of ionization over a fixed range of laser intensities. There are more general ways to formulate an equation for W and they are based on Keldysh formulation [12, 13] or PPT theory [14, 15].

The theory laid out thus far was developed when lasers were less intense and had longer pulses than are available at this writing. To account for what is witnessed in experiment, a simulation could contain at an absolute minimum 3 adjustable parameters (n_2, σ_K, K), but more likely contains more than 9 (n_2, σ_K, K, α, $R(t)$, τ_c, σ, a, ρ_c) that may not be completely independent of each other or constant over a large range of laser intensities and wavelengths. With an increasing number of parameters, it becomes difficult to gain information from these parameters since (1) they may not be unique and multiple sets of parameters could fit a particular laser pulse and medium scenario, and (2) they may not be describing the medium properties alone, but actually the one specific scenario of a laser pulse interacting with a medium. Evidence for these assertions can be found by calculating the exact light induced nonlinear polarization P_{NL} of a simple quantum system (1D Dirac-delta potential model, detailed in Chapter 2) and comparing it to the minimal standard approach

which uses the 3 parameters n_2, σ_K, and K. Figure 1.1 shows that the parameters seem to include the laser pulse properties. The left plot shows that for a given laser pulse and medium scenario, it is possible to find a set of parameters where the standard approach gives a response that matches the exact response from the 1D Dirac-delta potential model. If the laser intensity slightly increases, the same parameters no longer match the response from the quantum simulation (right plot). This is especially true in the later part of the pulse which is dominated by effects from newly freed electrons. Since these parameters are intended to describe the medium properties, this raises some doubts about the standard approach's predictive abilities.

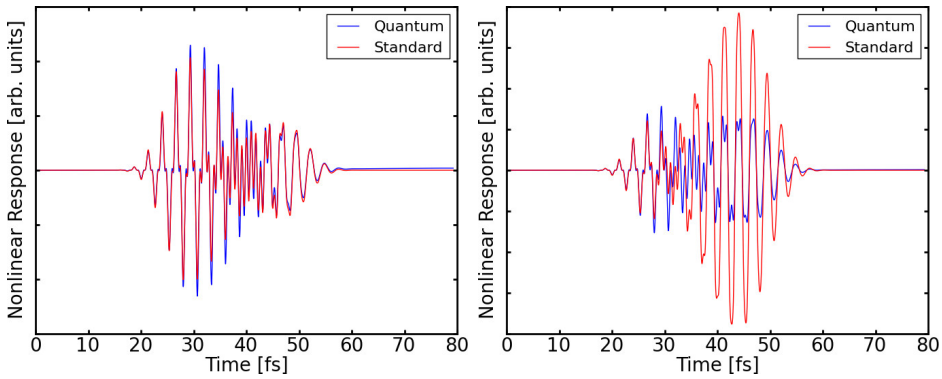

FIGURE 1.1. To illustrate that the standard approach's parameters (n_2, σ_K, K) include information about the laser pulse, the time dependent nonlinear response P_{NL} of a medium interacting with an 800nm laser pulse is calculated using two methods: the standard approach and the quantum calculation found by numerically solving the TDSE. (Left) For a pulse with peak pulse intensity of $7 \times 10^{17} W/m^2$, it is possible to find a set of parameters so that the standard approach produces a response that matches the quantum system's response. (Right) Using the same parameter values, the pulse intensity is increased to $9 \times 10^{17} W/m^2$, and the standard and quantum responses no longer match.

The large number of adjustable parameters is not the only problem with the standard approach. There are some conceptual problems also [16], namely

- the standard equations assume that electrons are strictly bound or free, and neglect weakly bound states,
- ionization is modeled as an instantaneous rate and therefore contains no memory of the field, restricting W to a single wavelength even though filaments contain a broad spectrum,
- and that Kerr and freed electron related phenomena are modeled completely independently when it is known that they arise from a common origin. Considering that the relative proportion of Kerr and plasma is probably the weakest

aspect of the standard equations, the possibility of independently fitting or parameterizing the two undermines the whole theory.

These conceptual problems and also the inconsistencies pointed out in Figure 1.1 show the need for better models to describe light-matter interactions for short, intense laser pulses. The weakest part of the standard equations is concerned with ionization dynamics and weakly bound states. Describing this properly requires a quantum description of the atom. This problem is known and has been an active area of research for the last decade. Some examples of this research are given below in order to give context to what is presented in this dissertation.

1.2 Research landscape

The inconsistencies within the standard approach are known and many research groups are pursuing remedies. There have been many different approaches to extending or refining the current theoretical approach in order to better capture the time dependent response of an atom in a strong light field. An important investigation technique used is based on time-dependent Schrödinger equation (TDSE) simulations of simple yet realistic atoms, such as hydrogen, where the response of a single atom is probed by an intense short pulse of light and the resulting polarization or susceptibility is analyzed. The results of these single atom simulations have been extremely useful in demonstrating the standard approach's inconsistencies and have produced results that are in direct contrast to the phenomenological way the standard approach represents the instantaneous Kerr effect and rate equations for ionization. For example, Nurhuda et al. [17] found theoretically using atomic hydrogen that the behavior of nonlinear susceptibility is strongly dependent on the intensity, increasing linearly until it saturates at high intensities, and that simply extracting a useful set of parameters to capture this effect that were valid over a large range of pulse intensities was difficult. They came to the same conclusion as was displayed in Figure 1.1, that extracted parameters were tied to the excitation pulse properties. Later the same group found [18] that this saturation effect is closely linked to depletion of the ground state and therefore results from coupling to the continuum, a conceptual picture that does not exist in the standard approach. The important role of weakly bound states is also supported by the work of Richter et al. [19] that uses the Kramers-Henneberger atomic model to investigate the role of highly energetic Rydberg-like states that still interact with the atomic potential. They found that their interaction with the light field produced a marked response and cannot be ignored. It has become apparent that for off-resonant pulse excitation the quantum coherent nature of the light-matter interaction becomes key, and the distinction between bound and freed electrons employed in the standard approach has become problematic. Another example comes from Béjot et al. [20] who used strong-field quantum calculations of hydrogen to reveal a time-dependent negative Kerr response and showed that the current perturbative

model of polarizability (third-order + Drude) is missing a substantial additional negative contribution associated with ionization channel closures, where the minimum number of photons required to ionize an atom increases by several units as the field intensity increases [21]. Another example shown by Volkova et al. [22, 23] is that electron dynamics display a significant nonperturbative character and therefore quantum mechanical perturbation theory cannot capture the full dynamics. They also showed [24] using direct TDSE simulations that the polarization response from free electrons changes the sign of susceptibility.

While these simulations have been instructive, it is unfortunate however that it is difficult to extract useful parameters (such as susceptibility) to be used in the standard modeling equations framework for a wide range of laser pulse scenarios. This difficulty stems from the fact that even if a total quantum mechanical polarization response for an atom can be calculated, how this response maps onto separate phenomenological parameters is unclear. The single atom TDSE examples mentioned above demonstrate that the current light-matter modeling equations are flawed and cannot capture the more richer picture of the field induced electron dynamics.

Dramatic changes to the standard modeling equations have been attempted in recent years. Around 2009-2010 experiments were performed [6, 7] that hinted at a Higher-Order Kerr Effect (HOKE). This effect added more terms to the instantaneous Kerr effect (1.4) by including higher order susceptibilities in the polarization power series (1.3). These additional higher order terms were suggested in order to produce a saturation of the instantaneous nonlinear response at intensities that were still below where significant plasma is generated. After this many papers were published, both for and against the addition of higher order instantaneous coefficients. M. Petrarca et al. [25] showed that higher-order Kerr improve quantitative modeling of laser filamentation. They simulated the propagation of pulses using two models for the refractive index: the current model which contains only the nonlinear refractive index n_2 and a newer model that includes additional HOKE terms n_4, n_6, n_8 that were measured from experiment. UPPE was used for propagation and both models include PPT calculated ionization rate. They saw for short pulses ($< 100fs$), the HOKE model produced peak plasma densities for a range of peak laser intensities that are closer to experiment than the current model. They conclude that instantaneous saturation of the refractive index n improves qualitative modeling and that this can be done with only experimentally measured values for index with no adjustable parameters. There were more papers supporting the inclusion of HOKE terms [26, 27, 28] stating that the role of recently freed electrons was not as important as once thought. However, there were also numerous papers against HOKE. Time-dependent saturation of susceptibility was witnessed by Köhler [29] using 1D and 3D TDSE for hydrogen interacting with short pulses at 800nm. They found that the instantaneous equation for HOKE could not reproduce the time dependent saturation of the nonlinear response. Instead they saw that the observed saturation was due to the accumulation of free

or nearly free electrons. Similar conclusions were found by others both in simulation and experiment [30, 31, 32, 33]. Regardless of the outcome of the debate, it should be emphasize that the standard modeling equations are on a fairly weak foundation, and that a radically new approach to modeling light-matter interactions is needed.

Unfortunately, simply replacing the current medium model with a realistic quantum system is problematic. Numerically solving the TDSE coupled to field propagation equations over the space and time scales relevant to filamentation in gases poses a formidable computational task that will not be realistic in the foreseeable future. Forefront simulations (termed MASP) have appeared [34, 35], where Maxwell's equations are coupled to a TDSE simulation with a plasma model to capture freed electrons that exit the computational boundary. Unfortunately MASP simulations are limited to very small spatial domains $\approx 1mm^3$. It may be necessary to even include many-body effects as simplified models have shown [36] that the many-body interactions strongly enhance the ionization. There is even evidence that the semi-classical light-matter interaction picture may not fully capture electron dynamics when the ground state population is depleted and therefore QED should be used [37]. Although these theories aim to completely capture light-matter interactions, they are also very computationally expensive and their inclusion in future pulse propagation simulations is far off.

This dissertation presents progress towards remedying the inconsistencies in the standard approach and towards the development of a new self-consistent first principles based medium model that is computationally efficient. The approach presented here takes the middle road between adding new correction terms to the standard approach, such as in the HOKE, and implementing a TDSE simulation of realistic atoms coupled to a propagation simulation like MASP. Instead, a small collection of exactly solvable quantum systems is studied and although these systems are not representative of true atoms, their self-consistent treatment of light-induced electron dynamics will be a helpful guide in the development of better medium models.

1.3 Dissertation organization

This dissertation is based on the collective results of the published papers below. The material is presented in roughly the same order as the publication timeline, except that theoretical developments are separated from applications.

- J. M. Brown, A. Lotti, A. Teleki, and M. Kolesik, "Exactly solvable model for nonlinear light-matter interaction in an arbitrary time-dependent field", *Phys. Rev. A*, Vol. 84, No. 063424 (2011)

- M. Kolesik, E. M. Wright, J. Andreasen, J. M. Brown, D. R. Carlson, and R. J. Jones, "Space-time resolved simulation of femtosecond nonlinear light-matter interactions using a holistic quantum atomic model: Applications to

near-threshold harmonics", *Opt. Express*, Vol. 20, Issue 14, pp. 16113-16128 (2012)

- J. M. Brown, E. M. Wright, J. V. Moloney, and M. Kolesik, "On the relative roles of higher-order nonlinearity and ionization in ultrafast light-matter interactions", *Opt. Lett.*, Vol. 37, Iss. 10, pp. 1604-1606 (2012)

- M. Kolesik, J. M. Brown, J. V. Moloney, and D. Faccio, "History-dependent effects in subcycle-waveform strong-field ionization", *Phys. Rev. A*, Vol. 90, No. 3, 033414 (2014)

- J. M. Brown and M. Kolesik, "Properties of Stark resonant states in exactly solvable systems", *Advances in Mathematical Physics* Vol. 2015, Article ID 125832 (2015)

- M. Kolesik, J. M. Brown, A. Teleki, P. Jakobsen, J. V. Moloney, and E. M. Wright, "Metastable electronic states and nonlinear response for high-intensity optical pulses", *Optica*, 1, 323 (2015)

- A. Bahl, J. M. Brown, E. M. Wright, and M. Kolesik, "Assessment of the metastable electronic state approach as a microscopically self-consistent description for the nonlinear response of atoms", *Opt. Lett.* 40, 4987-4990 (2015)

- J. M. Brown, C. Shannor, E. M. Wright, and M. Kolesik, "Carrier-wave shape effects in optical filamentation", *Optics Letters* Vol. 40, Issue 5, pp. 859-862 (2016)

- J. M. Brown, P. Jakobsen, A. Bahl, J. V. Moloney, and M. Kolesik, "On the convergence of quantum resonant-state expansion", *J. of Math. Phys.* 57, 032105 (2016)

The rest of the dissertation is organized as follows. Chapter 2 begins the investigation into exactly solvable systems by studying the 1D Dirac-delta potential model. For this system, the time dependent nonlinear polarization $P_{NL}(t)$ and nonlinear current $J_{NL}(t)$ when interacting with an arbitrary laser field $F(t)$ is analytically solved (a more detailed derivation is presented in Appendix B). Even though this model atom has been studied for decades, this result is one of the most general and practically useful advancements, as it allows the 1D Dirac-delta model to be included in pulse propagation simulations. The derived equations for $P_{NL}(t)$ and $J_{NL}(t)$ are non-trivial to implement in software, therefore space is given to describe how a fast numerical library can be developed. Having an exact nonlinear response for a quantum model is extremely useful in the exploration of nonlinear phenomena and for the validation of other response models.

Chapter 3 begins by describing how to integrate the response of the 1D Dirac-delta model into a pulse propagation simulation. At the time of this writing this was the first successful pairing of a UPPE propagator and a fully quantum description of the medium. The first application of the new model is a simulation of the high harmonic generation spectrum of a laser pulse focused into a Xenon gas jet. The results show that the model successfully reproduces a qualitatively correct harmonic spectrum and therefore is well-suited for high harmonic generation simulations. Next, the single atom nonlinear response is used to investigate the existence of the higher order Kerr effect (HOKE) nonlinearity, an effect that if true would require large changes to the understanding and modeling of medium response equations. Given that the 1D delta model provides a self-consistent nonlinear response with no adjustable parameters, it is used to show that the proposed HOKE terms are not necessary and that a quantum medium representation adequately describes what was witnessed in the experiment that spawned the idea of HOKE. Both of these application reinforce the belief that even toy models, such as the 1D Dirac-delta potential, are useful in investigating nonlinear phenomena.

Given that the 1D Dirac-delta model contains only a single bound state and that it can successfully reproduce qualitative features in HHG, emphasizes that the transition from bound to continuum states are the dominant origin of nonlinear effects seen during pulse propagation. In order to better capture this transition, Stark resonant states are considered in Chapter 4 as a way to describe the ionization process and weakly bound states, since they represent an electron decaying into the continuum. Many things are still unknown about resonant states and non-Hermitian quantum systems, therefore a thorough description of the properties of resonant states and how to use them as basis functions in time dependent problems is given. Next, two exactly solvable quantum systems with potentials represented by a 1D Dirac-delta function and a 1D square well are presented, and all of the quantities necessary to use them as a medium model are explicitly derived (more detailed derivations are presented in Appendix C and Appendix D). From these calculations a new Airy function integration technique is discovered (presented in Appendix A). Comparing the derived quantities for the 1D Dirac-delta and 1D square well systems, some general properties that are valid for all resonant state systems are conjectured. These conjectures not only add to the knowledge of resonant states, but are also useful in extending the theoretical framework to more realistic atomic potentials in higher dimensions. The end of this chapter presents an investigation into whether the 1D Dirac-delta resonant state basis functions form a complete basis.

Chapter 5 presents applications of using resonances as a medium model. The Metastable Electronic State Approach (MESA) serves as a practical replacement for the standard modeling equations, in that it captures the light-induce quantum response of an atom, but still retains the same computational complexity. This opens up the opportunity to use a fully quantum description of the medium in pulse propa-

gation simulations. The next two applications investigate how the quantum medium models react to the carrier field of a laser pulse and to what extent does the atomic medium remember the past ionization dynamics. The results show that indeed quantum systems react to the spectrum of the interacting pulse and that for some experiments, such as ionization enhancment through weak seeding, a fully quantum description of the medium is required. Finally, in Chapter 6, open questions are discussed.

Chapter 2

1D Dirac-Delta Potential Model

2.1 Introduction

In extreme nonlinear optics, systems are "automatically attracted" into a regime where both bound and free electronic states play equally important roles. The model that we study represents the minimal system that can capture the interplay between Kerr-like (caused by bound states) and plasma-like (caused by free electronic states) responses of the medium to the excitation by high intensity optical pulses. Many properties of this exactly solvable system have been known for quite some time, such as its eigenstates and resolvent, and the survival probability in the strong field approximation. Given that the necessary fundamental quantities are known, it is surprising however that the time dependent current or dipole moment has not been solved. There are two sides to the results that we present. First, we calculate exact formulas for the evolution of the current and/or dipole moment in an arbitrary time-dependent field. Despite the fact that the system has been studied for a long time in many different context, ours are new results which will greatly extend the utility of the model as a test-bed system. Second, we have developed efficient implementation for the induced current formulas. To help an interested reader in their practical application, we devote significant room to the numerical algorithm.

We envision two main areas in which our results will find practical application. In simulation of femtosecond filaments, they will allow qualitative-level studies in which the weakest links in the standard model will be replaced by a self-consistent quantum model. For high-harmonic generation (HHG) modeling, we present an exactly solvable alternative to the strong-field approximation. Both, the strong-field approximation and the model described here have only a single bound state plus a continuum of free states, therefore the range of physics that they capture is similar. The advantage of the present approach is that it is an exact solution valid throughout the full frequency bandwidth, including the fundamental as well as the highest harmonic frequencies.

2.2 Properties

The quantum model we study describes a single particle subjected to a homogeneous external field and a short-range contact potential. The time-dependent Schrödinger equation for this "one-dimensional atom" can be written as

$$i\partial_t\psi(x,t) = \left[-\tfrac{1}{2}\partial_x^2 - B\delta(x) - xF(t)\right]\psi(x,t). \tag{2.1}$$

Here, B is the strength of the Dirac-delta interaction, and $F(t)$ stands for the intensity of a time-dependent electric field. Atomic units have been chosen to simplify the notation. The above equation is merely symbolic unless a proper meaning is given to the delta potential. The precise Hamiltonian definition (see e.g. [38, 39]) of this system specifies the contact interaction as a condition which all functions that belong to the Hamiltonian domain must fulfill, namely

$$\frac{d\psi(0^+)}{dx} - \frac{d\psi(0^-)}{dx} = -2B\psi(0), \tag{2.2}$$

which means that the wavefunctions are continuous, but exhibit a discontinuity in their derivative. For positive B, this gives rise to a single bound (ground) state

$$\psi_G(x) = \sqrt{B}e^{-B|x|} \tag{2.3}$$

with energy $E_g = -B^2/2$. Explicit expressions are known for all continuum (positive energy) states, as well as for the Hamiltonian resolvent in a static field (see e.g. [40, 41]).

This toy model has often been utilized as a test-bed in the area of strong light-matter interaction. As one would expect for an exactly solvable system, it has been studied for its mathematical properties and physical applications alike. For the mathematical aspects, we refer the reader to books on Schrödinger operators [42] and singular perturbations in differential operators [43]. For its physical implications, Geltman [44] investigated time-dependent ionization in strong electrostatic fields. Explicit results for the time dependence of the survival probability of the decaying ground state were given by Arrighini and Gavarini in [45], and also by Elberfeld and Kleber [46], who used this system to model tunneling from a quantum well and derived useful analytic results for an arbitrary time-dependent external field. Cavalcanti et. al [41] described generalizations to higher dimensions and made a connection between deviations from the exponential decay and long-lived resonances. Two short-range attractive potentials were used to describe molecular ionization in a static field [47], and a double delta potential was also studied by Álvarez and Sundaram [48]. Generalization to an arbitrary finite number of delta-potential interactions was given by Uncu et al. [49] as a model for impurities in GaAs/GaAlAs junctions. Villalba and González-Díaz introduced a delta potential into the Dirac equation [50]. Teleki took advantage of the exact solvability of this system to gain insight into possible manifestation of higher-order nonlinearity in strong optical fields [51].

There are numerous works in previously published literature which either investigate one dimensional atom models themselves, or use them as tools to test and study numerical techniques and theories. Much of this work was done in the context of stabilization in strong fields [52]. Numerical and eigenstate expansions have been applied [53], and the Floquet method was also used [54] with the system discussed here. Approximate ionization rates were calculated in [55], and numerical simulations

of photoionization were performed in [56]. More recently, there have been a number of papers in which various approximate and numerical methods are applied to one-dimensional systems, such as state-specific expansion [57], Kramers-Henneberger frame transformation [58] and least-squares fitting of time evolution [59]. This model also served as a test-bed for numerical simulation techniques [60] and analytic theories [61, 62].

Collectively, the works referenced above illustrate an interesting point, which perhaps remains valid in a wider context. Although the model including a short-range delta potential is formally exactly solvable, it is still far from trivial to extract useful information from it. Therefore approximate approaches are often utilized, which unfortunately goes against the spirit of studying a model system in an exact setting. It is this fact that provides the motivation for investigating nonlinear phenomena with an exactly solvable quantum system. Although this concrete system has been studied for a long time, exact solutions for arbitrary time-dependent external fields were not published. We present such solutions together with a method to implement them in software.

The next section is devoted to the derivation of the probability current evolution for an arbitrary time dependent field. The main result is stated for the current observable, while analogous expressions for the time-dependent dipole moment are summarized in the section thereafter. In our final results, we exactly eliminate the component that is linear in the driving field $F(t)$. The rationale for doing so is that this model will be used to describe the nonlinear response, while linear medium properties can be efficiently incorporated using standard approaches. After that we discuss how to efficiently implement the nonlinear current formulas. Since this work mainly aims to present new results concerning the delta-function atom model, we devote a relatively small room to illustrations. These verify that the results based on the analytic solution coincide with the direct numerical solution of the time-dependent Schrödinger equation (which requires orders of magnitude more numerical effort), and that the implementation is robust, stable, and works accurately even in extreme regimes, such as for high-harmonic generation with long-wavelength driving pulses. Finally, we briefly discuss various options that our results open for applications in computer simulation of light-matter interactions.

2.3 Probability current

One of the main difficulties when integrating the time-dependent Schrödinger equation and Maxwell equations is that the history of a quantum system must be calculated at each spatial point resolved by the Maxwell solver. This is necessary to extract time-dependent observables, and it requires resolution of the wave function in space. Our goal is to eliminate the spatial dimension from the quantum system, and derive expressions directly for the dipole moment and current observables. Elberfeld

et al. [46] achieved this for the probability that the system remains in the ground state. We follow the same strategy and extend it for the nonlinear current and dipole calculations. In this chapter, only the main quantities and steps necessary to solve for the nonlinear current are presented. A more detailed derivation that includes all intermediate steps is available in Appendix B.

There are three main insights for solving this problem. The first, is the important realization that "everything" can be known, at least in principle, if $\psi(x = 0, t)$ is determined for all times t. The second is that the wavefunction away from the delta potential is free and moves as a classical particle plus quantum diffusion. The third is that there are useful cancellations and identities throughout the derivation. These cancellations are typical of many exactly solvable models and help us to more easily compute the final result by avoiding calculating quantities that will sum to zero.

The solution for the wave function $\psi(x, t)$ can be cast in the form [46] $\psi(x, t) = \psi_F(x, t) + \psi_S(x, t)$. The first wavefunction $\psi_F(x, t)$ describes the electron beginning in the ground state $\psi_G(x)$ and propagating under the influence of the external field only with no interaction with the delta potential

$$\psi_F(x, t) = \int_{-\infty}^{\infty} dx' K_F(x, t|x', 0)\psi_G(x'). \tag{2.4}$$

The Volkov K_F propagator can be conveniently expressed through quantities related to the motion of a classical electron driven by $F(t)$, namely classical position $x_{cl}(t)$, momentum $p_{cl}(t)$, and action $S_{cl}(t)$. Explicitly,

$$\begin{aligned} K_F(x, t|x', t') &= e^{i\phi(x,t,x',t')} K_0(x - x_{cl}(t), t|x' - x_{cl}(t'), t') \\ K_0(x, t|x', t') &= \frac{1}{\sqrt{2\pi i(t - t')}} e^{-\frac{(x-x')^2}{2i(t-t')}} \\ \phi(x, t, x', t') &= x p_{cl}(t) - x' p_{cl}(t') - \left[S_{cl}(t) - S_{cl}(t')\right]. \end{aligned} \tag{2.5}$$

Each of these classical quantities can be calculated directly from the field $F(t)$

$$\begin{aligned} p_{cl}(t) &= -\int_0^t F(\tau) d\tau \\ x_{cl}(t) &= \int_0^t p_{cl}(\tau) d\tau \\ S_{cl}(t) &= \frac{1}{2}\int_0^t p_{cl}^2(\tau) d\tau. \end{aligned} \tag{2.6}$$

The second wavefunction $\psi_S(x, t)$ describes scattering of the electron with the delta

potential and then propagation in the field $F(t)$

$$\psi_S(x,t) = -i\int_0^t dt' \int_{-\infty}^{\infty} dx' K_F(x,t|x',t')\left[-B\delta(x')\right]\psi(x',t') \tag{2.7}$$
$$= iB\int_0^t dt' K_F(x,t|0,t')\psi(0,t').$$

Before beginning the derivation, we would like to point out an important issue regarding practical implementation. For an initial condition given by the ground state, ψ_F and ψ_S do not have characteristics representative of the full solution. This means that significant cancellations occur between the two, which is dangerous numerically. It is therefore imperative to identify these cancellations and eliminate them before numerical evaluation.

The observable of interest, which gives rise to current density in Maxwell's equations, is the total current contribution from one "atom:"

$$J(t) = \int_{-\infty}^{+\infty} J(x,t)dx \tag{2.8}$$

where the probability current density

$$J(x,t) = \Im\left\{\psi^*(x,t)\nabla\psi(x,t)\right\}. \tag{2.9}$$

and can be written as a sum of contributions originating from the two components of the wave function:

$$J(x,t) = \Im\left\{\psi_F^*\nabla\psi_F + \psi_F^*\nabla\psi_S + \psi_S^*\nabla\psi_F + \psi_S^*\nabla\psi_S\right\}. \tag{2.10}$$

Before evaluating each of these terms, we will first calculate $\psi(0,t)$.

2.3.1 Integral equation for $\psi(0,t)$

We see from the equation of the scattered wavefunction ψ_s in (2.7), that in order to calculate the total wavefunction $\psi(x,t)$, we must know the full time history of the value of wavefunction at the location of the delta function $\psi(0,t)$. The value of $\psi(0,t)$ satisfies the following integral equation

$$\psi(0,t) = \int_{-\infty}^{+\infty} dy K_F(0,t|y,0)\psi_G(y,0) + iB\int_0^t dt' K_F(0,t|0,t')\psi(0,t'). \tag{2.11}$$

To proceed, we will use the following ansatz

$$\psi(0,t) = \sqrt{B}A(t)e^{-iS_{cl}(t)+i\frac{B^2}{2}t}, \tag{2.12}$$

which is chosen to reduce rapid phase oscillations from the classical action and ground state energy. Using the ansatz we find the envelope function $A(t)$ to be

$$A(t) = \psi_R(-x_{cl}(t), t) + \frac{iB}{\sqrt{2\pi i}} \int_0^t dt' W(t,t') \exp\left[\frac{i(x_{cl}(t) - x_{cl}(t'))^2}{2(t-t')}\right] A(t') \quad (2.13)$$

where W represents a singular integration weight

$$W(t,t') = \frac{e^{+i\frac{B^2}{2}(t'-t)}}{\sqrt{t-t'}}, \quad (2.14)$$

and the wavefunction ψ_R is represented as a sum of complementary error functions

$$\psi_R(x,t) \equiv \frac{e^{+Bx}}{2}\mathrm{erfc}\left(\frac{iBt+x}{\sqrt{2it}}\right) + \frac{e^{-Bx}}{2}\mathrm{erfc}\left(\frac{iBt-x}{\sqrt{2it}}\right). \quad (2.15)$$

Equations (2.12) - (2.15) constitute the first step towards evaluation of physical observables for an arbitrary time dependent field. This integral equation has a singular kernel, and is in fact closely related to the Abel integral equation [63]. A numerical solution of such equations requires care, but it can be done efficiently. We defer the implementation details to a later section, in which we address numerical issues.

2.3.2 Elimination of classical current contributions

Since the transformation of (2.10) to an explicit form is rather lengthy, it is desirable to simplify this procedure. Importantly, the following reduction also eliminates, to a large degree, the mutual cancellation between different contributions in the final result. Let us consider the derivative terms in (2.10), and see that they receive contribution from two sources. The first is the argument of the free particle propagator K_0 and the second is the phase ϕ of the Volkov propagator K_F. The latter results in multiplication by the classical momentum $p_{cl}(t)$. After factoring these equations, we obtain

$$\nabla K_F(x,t|x',t) = \left[\frac{i\left(x - x_{cl}(t) - x' + x_{cl}(t')\right)}{t-t'} + ip_{cl}(t)\right] K_F(x,t|x',t') \quad (2.16)$$

$$\nabla \psi_F(x,t) = \left[\frac{i(x - x_{cl}(t))}{t} + ip_{cl}(t)\right] \psi_F(x,t) \quad (2.17)$$

and note that both K_F and ψ_F are eigenfunction of the derivative operator with eigenvalues involving classical position and momentum. Using the derivative expressions and grouping terms multiplied by momentum, we see that $J(t)$ contains

$$p_{cl}(t) \int_{-\infty}^{\infty} dx \left\{\psi_F^* \psi_F + \psi_F^* \psi_S + \psi_S^* \psi_F + \psi_S^* \psi_S\right\}, \quad (2.18)$$

where the integral gives unity since it is the conserved norm of the full wave-function. Thus, all contributions that originate from $\partial_x e^{i\phi(x,t,x',t')}$ will collectively yield $p_{cl}(t)$ and do not need to be evaluated explicitly. Moreover, they are linear in F and therefore not interesting for our purposes. An alternative view of this reduction is to realize that norm conservation implies an identity that $A(t)$ must satisfy. Because ψ_F alone is a product of unitary evolution, its norm is equal to one at all times. Consequently, other contributions to the wavefunction norm must mutually cancel giving us a remarkable identity:

$$\langle\psi_F|\psi_S\rangle + \langle\psi_S|\psi_F\rangle + \langle\psi_S|\psi_S\rangle = 0 \tag{2.19}$$

which will be used to greatly simplify the calculation of current. Explicitly this identity is

$$\begin{aligned}\Re\Big\{ -iB^{-1}\int_0^t dt_1 A^*(t_1) \times \Big[e^{-Bx_{cl}(t_1)}\mathrm{erfc}\left(\frac{(1+i)(Bt_1+ix_{cl}(t_1))}{2\sqrt{t_1}}\right) \\ + e^{+Bx_{cl}(t_1)}\mathrm{erfc}\left(\frac{(1+i)(Bt_1-ix_{cl}(t_1))}{2\sqrt{t_1}}\right)\Big]\Big\} \\ = \frac{(-1)^{\frac{3}{4}}}{\sqrt{2\pi}}\int\int_0^t dt_1 dt_2 W(t_1,t_2) e^{\frac{i[x_{cl}(t_1)-x_{cl}(t_2)]^2}{2(t_1-t_2)}} A(t_2)A^*(t_1)\end{aligned} \tag{2.20}$$

and is used to reduce the number of expressions that are proportional to the momentum p_{cl}. In what follows, we assume that either of the two reduction methods was used in the calculation, allowing us to omit all corresponding contributions. This amounts to ignoring $\partial_x\phi(x,t,x',t')$ whenever ∂_x acts on K_F.

Next, we split the calculation of the induced current into terms corresponding to (2.10). We are only interested in extracting the part of the current which is nonlinear in the driving field $F(t)$, and we will show how this can be done exactly.

2.3.3 Current contribution J_{FF}

The first term to evaluate the current due to ψ_F:

$$J_{FF} = \Im\int dx\ \psi_F^*\nabla\psi_F\ . \tag{2.21}$$

We know that this term is the electron under the influence of the external field and that it started in the ground state with zero momentum. Inspecting the propagator K_F we see that the wavefunction will under go free wave-packet spreading, but be shifted in position and momentum space by their respective classical quantities due to the field. We therefore assume that the current contribution from this term is simply the classical momentum value $J_{FF}(t) = p_{cl}(t)$.

This can be shown by explicit calculation also. We begin evaluating the spatial integral within ψ_F, which amounts to two Gaussian integrals, and find its result to be

$$\psi_F(x,t) = \frac{1}{2}\sqrt{B}e^{ixp_{cl}(t)-iS_{cl}(t)}e^{\frac{1}{2}iB^2t} \times \left[e^{B(+x-x_{cl}(t))}\mathrm{erfc}\left(\frac{+x-x_{cl}(t)+iBt}{\sqrt{2it}}\right)\right. \\ \left. + e^{B(-x+x_{cl}(t))}\mathrm{erfc}\left(\frac{-x+x_{cl}(t)+iBt}{\sqrt{2it}}\right)\right] \tag{2.22}$$

(see equations 2.11-2.14 in Elberfeld et al. [46]). With the help of ψ_R (2.15) we rewrite

$$\psi_F(x,t) = \sqrt{B}e^{ixp_{cl}(t)-iS_{cl}(t)}e^{\frac{1}{2}iB^2t}\psi_R(x-x_{cl}(t),t) \tag{2.23}$$

and insert it and its conjugate back into J_{FF} and substitute $y = x - x_{cl}(t)$, then the current contribution is

$$J_{FF} = \int_{-\infty}^{+\infty} dy\, \psi_R^*(y,t)\frac{d}{dy}\psi_R(y,t) + p_{cl}(t)\int_{-\infty}^{+\infty} dy\, \psi_F^*(y,t)\psi_F(y,t). \tag{2.24}$$

The symmetry in (2.22) with respect to x makes ψ_R an even function. The first integrand is then an odd function and results in zero upon integration. The second integral will be unity due to ψ_F being a normalized wavefunction. We see again that $J_{FF}(t) = p_{cl}(t)$ and that it is linear in the field. Since we ultimately aim to use the nonlinear current in simulations, this term will be neglected since its contribution can be included with classical equations.

2.3.4 Current contribution J_{SS}

Let us now calculate the current contribution due to the scattered wavefunction ψ_S

$$J_{SS} = \Im \int dx\ \psi_S^* \nabla \psi_S\ , \tag{2.25}$$

and extract its nonlinear part $J_{SS}^{(nl)}$. Inserting the explicit expression we can rewrite this term, disregarding terms multiplied by $p_{cl}(t)$, as

$$J_{SS} = \Im\left[B^3\int_0^t\int_0^t dt_1 dt_2 A(t_2)A^*(t_1)I(t_1,t_2)\right] \tag{2.26}$$

where $I(t_1,t_2)$ is the result of the spatial integral

$$I(t_1,t_2) = \int_{-\infty}^{\infty} dx \frac{[x-x_{cl}(t)+x_{cl}(t_2)]}{2\pi i(t-t_1)^{\frac{1}{2}}(t-t_2)^{\frac{3}{2}}} e^{i\frac{B^2}{2}(t_2-t_1)} e^{\frac{i[x-x_{cl}(t)+x_{cl}(t_2)]^2}{2(t-t_2)} - \frac{i[x-x_{cl}(t)+x_{cl}(t_1)]^2}{2(t-t_1)}}. \tag{2.27}$$

Note that the classical action phase from the propagator has been absorbed by the ansatz for $\psi(0,t)$. The integration order was exchanged between (2.25) and (2.26), which is justified when a small imaginary part is added to the time variable to make the integral over x convergent for fixed $t_{1,2}$. The integral is Gaussian, and can be evaluated directly. We find that

$$I(t_1,t_2) = \frac{(-i)^{\frac{3}{2}}}{\sqrt{2\pi}} W(t_1,t_2) \frac{x_{cl}(t_1) - x_{cl}(t_2)}{t_1 - t_2} e^{\frac{i[x_{cl}(t_1)-x_{cl}(t_2)]^2}{2(t_1-t_2)}}. \tag{2.28}$$

It becomes evident that I is a function of $t_{1,2}$ but does not depend on t.

To further simplify numerical evaluation, the double integral over the rectangle $(0,t)\times(0,t)$ is split into integration over triangles, $\int_0^t dt_1 \int_0^t dt_2 = \int_0^t dt_1 \int_0^{t_1} dt_2 + \int_0^t dt_2 \int_0^{t_2} dt_1$. In the latter term, we rename $t_1 \leftrightarrow t_2$ and verify that the two integrals have complex conjugate integrands. This essentially reduces the complexity of calculation, but implementing the integrals still proved to be difficult. It was easy to numerically overflow the exponential terms seen in many of the integrals. Therefore we found that it was very important to sum as many of the arguments of exponentials before exponentiating them.

At this point, we can eliminate the linear part of this current contribution. The classical position $x_{cl}(t)$ is linear in F, therefore we must remove the zero-order part from the rest of the integrand in (2.26). The first field-dependent contribution from the exponential in $I(t_1,t_2)$ is of second order, and $A(t)$ reduces to one for zero field. In order to remove the linear part of their product, we subtract unity from this expression which appears when (2.28) is inserted in (2.26)):

$$e^{\frac{i[x_{cl}(t_1)-x_{cl}(t_2)]^2}{2(t_1-t_2)}} A^*(t_1)A(t_2) \to e^{\frac{i[x_{cl}(t_1)-x_{cl}(t_2)]^2}{2(t_1-t_2)}} A^*(t_1)A(t_2) - 1. \tag{2.29}$$

The nonlinear current contribution from the scattering wavefunction is

$$\begin{aligned} J_{SS}^{(nl)} = 2\Im \Bigg\{ \int_0^t dt_1 \int_0^{t_1} dt_2 \frac{(-i)^{\frac{3}{2}} B^3 W(t_1,t_2)}{\sqrt{2\pi}} \frac{x_{cl}(t_1) - x_{cl}(t_2)}{t_1 - t_2} \\ \times \left[e^{\frac{i[x_{cl}(t_1)-x_{cl}(t_2)]^2}{2(t_1-t_2)}} A^*(t_1)A(t_2) - 1 \right] \Bigg\}. \end{aligned} \tag{2.30}$$

Similar to the integral equation for $\psi(0,t)$, the integrand is singular when $t_2 \to t_1$. Fortunately, the singularity is not stronger, since the classical position difference vanishes and the corresponding fraction converges to the classical momentum. Discussion of the numerical aspects that are important in evaluating this expression is postponed to a dedicated section.

2.3.5 Current contribution J_{FS}

To find the current due to the mixed terms, we evaluate the spatial integral

$$J_{FS} = \Im \int_{-\infty}^{\infty} dx \left(\psi_F^* \nabla \psi_S + \psi_S^* \nabla \psi_F\right). \tag{2.31}$$

It is more difficult to calculate, but it simplifies to a rather compact final expression. Just as with J_{SS}, we will also systematically drop all contribution arising from $\partial_x \phi$, since we have established that their contribution is irrelevant for our purposes.

In this derivation, there are two spatial variables of integration. One is x and the other is the auxiliary variable originating in the initial state $\psi_G(z)$. Integration over z should be executed first, however, integrating first over x gives the same result with less work. When we insert explicit expressions for the wavefunction components $\psi_{F,S}$, the integration order is changed such that $\int dx$ is done first. Again, the change of integration order is permissible if we assume a small imaginary part in the time variable, which makes the integrals convergent. At this stage we obtain

$$J_{FS} = \Im \int_{-\infty}^{\infty} dz \int_0^t dt_1 \sqrt{\frac{2}{\pi}} \frac{(-1)^{\frac{3}{4}} B^2}{t_1^{\frac{3}{2}}} e^{-i\frac{B^2}{2}t_1} e^{-B|z|} e^{\frac{i[z+x_{cl}(t)]^2}{2t_1}} A^*(t_1)[z + x_{cl}(t_1)], \tag{2.32}$$

where we have added two expressions coming from $\psi_F^* \nabla \psi_S$ and $\psi_S^* \nabla \psi_F$, respectively, each contributing the same imaginary part.

Next, we perform integration over the variable z. This is done separately for $z < 0$ and $z > 0$, with each integration resulting in a number of terms containing error functions of complex arguments. Fortunately, considerable simplification occurs when the two parts are joined. Since multiple equivalent ways exist to represent the result, the most appropriate should be chosen with future calculations in mind. In particular, subtracting order-of-one quantities at large negative and positive times should be avoided. A compact form suitable for numerical evaluation can be given using complementary error functions:

$$\begin{aligned} J_{FS} = \Im \Bigg\{ iB^3 \int_0^t dt_1 A^*(t_1) \Bigg[& e^{+Bx_{cl}(t_1)} \mathrm{erfc}\left(\frac{(1+i)(Bt_1 - ix_{cl}(t_1))}{2\sqrt{t_1}}\right) \\ & - e^{-Bx_{cl}(t_1)} \mathrm{erfc}\left(\frac{(1+i)(Bt_1 + ix_{cl}(t_1))}{2\sqrt{t_1}}\right) \Bigg] \Bigg\}. \end{aligned} \tag{2.33}$$

This is not our final result, since J_{FS} still contains contributions linear in $F(t)$. Note that the expression in square brackets is an odd function of $x_{cl}(t)$ and by the same token an odd function of F. Thus, the first-order term of the Taylor expansion in x_{cl} will be subtracted, in order to cancel the unwanted linear response:

$$J_{FS}^{(nl)} = J_{FS} - \Im \left\{ 2B^3 \int_0^t dt_1 x_{cl}(t_1) \left(iB \ \mathrm{erfc}\left(\frac{(1+i)B\sqrt{t_1}}{2}\right) - \frac{1+i}{\sqrt{\pi t_1}} e^{-i\frac{B^2}{2}t_1} \right) \right\} \tag{2.34}$$

where we have again used that as $F \to 0$, $A(t) \to 1$. Expressions (2.33), (2.34) together with (2.30) constitute our final result. They allow us to calculate the exact nonlinear current induced by an arbitrary time-dependent field $F(t)$. The total nonlinear current can written explicitly in terms of time integrals as

$$J^{(nl)} = J^{(nl)}_{SS} + J^{(nl)}_{FS} \tag{2.35}$$

where

$$\begin{aligned} J^{(nl)}_{SS} = 2\Im \Bigg\{ \int_0^t dt_1 \int_0^{t_1} dt_2 \frac{(-i)^{\frac{3}{2}} B^3 W(t_1,t_2)}{\sqrt{2\pi}} \frac{x_{cl}(t_1) - x_{cl}(t_2)}{t_1 - t_2} \\ \times \left[e^{\frac{i[x_{cl}(t_1) - x_{cl}(t_2)]^2}{2(t_1 - t_2)}} A^*(t_1) A(t_2) - 1 \right] \Bigg\} \end{aligned} \tag{2.36}$$

and

$$\begin{aligned} J^{(nl)}_{FS} &= \Im \left\{ iB^3 \int_0^t dt_1 A^*(t_1) e^{+Bx_{cl}(t_1)} \mathrm{erfc} \left(\frac{(1+i)(Bt_1 - ix_{cl}(t_1))}{2\sqrt{t_1}} \right) \right\} \\ &- \Im \left\{ iB^3 \int_0^t dt_1 A^*(t_1) e^{-Bx_{cl}(t_1)} \mathrm{erfc} \left(\frac{(1+i)(Bt_1 + ix_{cl}(t_1))}{2\sqrt{t_1}} \right) \right\} \\ &- \Im \left\{ 2B^3 \int_0^t dt_1 x_{cl}(t_1) \left(iB \ \mathrm{erfc} \left(\frac{(1+i)B\sqrt{t_1}}{2} \right) - \frac{1+i}{\sqrt{\pi t_1}} e^{-i\frac{B^2}{2}t_1} \right) \right\} . \end{aligned} \tag{2.37}$$

2.4 Dipole moment

Evolution of the dipole moment induced by an external field can be calculated in the same manner as the current. The calculation is somewhat more involved, and the structure of the final result is also less suitable for numerical evaluation. Since the current and dipole observables can be converted from one to the other by integration with respect to time, in practical applications users will likely choose the former. However, we do want to complete the picture with listing their explicit expressions.

The full dipole moment is decomposed into components analogous to those we used for the current

$$P = P_{FF} + P_{FS} + P_{SS} \ . \tag{2.38}$$

In order to make the relationship between dipole and current derivations more apparent, we will not eliminate the linear part. The first contribution is obtained utilizing a symmetry argument:

$$P_{FF} = x_{cl}(t) \ , \tag{2.39}$$

and the P_{SS} component can be written in the following form, which makes it easy to verify that its time derivative corresponds to J_{SS} as expected:

$$P_{SS} = 2\Re\left\{\int_0^t dt_1 \int_0^{t_1} dt_2 \frac{(-1)^{\frac{3}{4}} B^3 W(t_1,t_2)}{\sqrt{2\pi}} e^{\frac{i[x_{cl}(t_1)-x_{cl}(t_2)]^2}{2(t_1-t_2)}} A^*(t_1)A(t_2) \right. \\ \left. \frac{x_{cl}(t)(t_1-t_2)+x_{cl}(t_1)(t_2-t)+x_{cl}(t_2)(t-t_1)}{t_1-t_2}\right\}. \tag{2.40}$$

The derivative with respect to the upper integration bound vanishes due to symmetry of the integrand. If one takes the derivative of the integrand with respect to t, it gives the expression we have found for J_{SS}. Similarly, P_{FS} can be put in a form which makes it evident that $\partial_t P_{FS} = J_{FS}$. This term evaluates to

$$P_{FS} = \Re\Bigg\{ iB^2 \int_0^t dt_1 A^*(t_1) \\ \Bigg[e^{-Bx_{cl}(t_1)} \mathrm{erfc}\left(\frac{(1+i)(Bt_1+ix_{cl}(t_1))}{2\sqrt{t_1}}\right) \\ [x_{cl}(t1)-x_{cl}(t)+iB(t-t_1)] \\ + e^{+Bx_{cl}(t_1)} \mathrm{erfc}\left(\frac{(1+i)(Bt_1-ix_{cl}(t_1))}{2\sqrt{t_1}}\right) \\ [x_{cl}(t1)-x_{cl}(t)-iB(t-t_1)]\Bigg]\Bigg\}. \tag{2.41}$$

Note that both P_{SS} and P_{FS} contain terms proportional to $x_{cl}(t)$. If these are collected, the identity (2.19) is obtained, which means that their sum is zero and they can be ignored.

Even with this cancellation, the dipole representation is more difficult to evaluate when compared to the current. This is mainly due to the fact that time t appears inside both integrands. If coded as written, this method's complexity would scale as N_t^3. This unfavorable behavior can be reduced to N_t^2 with clever programming, but the resulting algorithm is still more complex than that of the current. This is why in applications it will be more effective to calculate time-dependent current. If the dipole moment is required, it can be obtained by integrating along the time axis. To convert the dipole moment from atomic units to medium polarization, we simply multiply by ea_0N, the product of electron charge, atomic unit of length, and the number density of atoms per unit of volume. Regardless of the calculation method, either the current or dipole moment can be used in a pulse propagation simulator, since they produce equivalent driving terms in the optical evolution equations.

2.5 Implementation and verification

In summary, the procedure used to calculate the current induced by an optical-frequency pulse characterized by the field strength $F(t)$ consists of

- calculating the quantities related to the classical electron trajectory: $p_{cl}(t)$, $x_{cl}(t)$ and $S_{cl}(t)$,
- solving the integral equation for $A(t)$ as specified in (2.12) - (2.15),
- and evaluating the nonlinear current contributions from (2.30), (2.33), (2.34).

If the time-dependent quantities are represented on a grid with N_t sampling points, the computational complexity of this procedure scales as N_t^2. Therefore, it is important to design an algorithm which can be accurate even with a long temporal step.

Integrals with the singular integration weight (2.14) must be calculated in both the integral equation for $A(t)$ and in J_{SS}. To achieve an acceptable accuracy for time steps as long as one tenth of the atomic unit of time, the singularity must be treated analytically. To do this, we calculate an integral of the form

$$\int_0^t W(t,\tau) f(\tau)$$

with a representation of f sampled on a discrete set $\{\tau_i\}$. This allows the approximation

$$\int_{\tau_i}^{\tau_{i+1}} W(t,\tau) f(\tau) = \int_{\tau_i}^{\tau_{i+1}} W(t,\tau) P(\tau)$$

where $P(\tau)$ is an interpolating polynomial of $\{f(\tau_i)\}$ spanning a vicinity of the interval (τ_i, τ_{i+1}). We have tested linear and second-order methods, and have concluded that the first-order method is accurate enough to not warrant restricting the time step. With the locally linear approximation to f, the integral over a sub-interval is then given by pre-calculated weights

$$\int_{\tau_i}^{\tau_{i+1}} W(t,\tau) f(\tau) = w(t,i) f(\tau_i) + w(t,i+1) f(\tau_{i+1}).$$

Note that for a regular temporal grid, only a single weight-vector $w(i-j)$ needs to be stored. The same is true for an order-n method which requires n integration weight vectors $w^{(n)}(k)$. Explicit expressions for these integration weights depend on the ground-state energy $B^2/2$, and can be readily calculated in terms of error functions with complex arguments. The resulting integration algorithm is fast, as it only requires several multiplications per grid point.

When solving the integral equation for $A(t)$, we evolve the solution along the temporal axis as the formula suggests. At each point t_c, integration over its past, $\int_0^{t_c-\Delta t}$, is performed using the above scheme. This is why the method scales as N_t^2. The same scheme is also applied to the last sub-interval, $\int_{t_c-\Delta t}^{t_c}$, with the current endpoint carrying the unknown $A(t_c)$. The endpoint value then appears on both sides and can be expressed. The singular integration scheme is also applied to the inner integral

in $J_{SS}^{(nl)}$. For the outer integral, we have used integration rules of various orders, and found that a simple first-order scheme is satisfactory. Numerical evaluation of $J_{FS}^{(nl)}$ requires calculation of complex complementary error functions. Because they are dependent on the classical position x_{cl}, these quantities can not be pre-calculated. Consequently, an implementation for $\mathrm{erf}(z)$ which works in the entire complex plane is required. For this we have used the Faddeeva package by Steven G. Johnson[1].

To verify that our implementation of the nonlinear current produces correct results, we performed comparisons with solutions obtained from direct numerical simulations of the time-dependent Schrödinger equation (2.1). The delta-function potential was implemented as a condition specifying the value at the cusp of the derivative located at the origin as stated by (2.2). The time-stepping scheme was taken from Visscher [64], and reflecting boundary conditions were used at the edges of the computational domain.

We choose to show an illustration for the time-dependent dipole moment instead of the current, because dipole moment plots are more intuitive as their low-frequency components are more prominent and resemble the temporal shape of the driving pulse. In order to facilitate comparison with the nonlinear component of the induced dipole moment, the latter was extracted from two simulations that used the same temporal shape of the driving pulse:

$$P^{(nl)}(t) = \lim_{\epsilon \to 0} \left[P(\{F(t)\}) - \frac{1}{\epsilon} P(\{\epsilon F(t)\}) \right].$$

Here, the second simulation occurs at a very low intensity, and represents the linear (in F) contribution to the total polarization P. The scaling factor ϵ reduces the driving field amplitude to where observed nonlinear effects become negligible. Subtracting the linear part leaves us with the nonlinear response which can be compared to our calculations using analytic formulas.

A rather fine grid resolution and short integration step was required for the the time-domain Schrödinger equation (TDSE) simulation which generated the comparison data sets shown here. We used a numerical grid with the spacing of 0.025 (in atomic units) and 50000 points, and the time-step was only 0.00025 (in atomic units). Figure 2.1 shows our analytic calculation compared to the TDSE simulations performed with two different domain sizes. Perfect agreement is achieved for a sufficiently large TDSE domain, verifying that our implementation of the analytic expressions for the nonlinear current is indeed correct. Deviations only occur when the TDSE numerical grid is too small to accommodate the spreading wavefunction in the later stages of evolution. Analytic solutions do not suffer from such finite-size artifacts thanks to the fact that the spatial variable has been integrated out.

Having verified correctness of the implementation, the question of stability of our method must be addressed. Because the algorithm mimics evolution of the current

[1] http://ab-initio.mit.edu/wiki/index.php/Faddeeva_Package

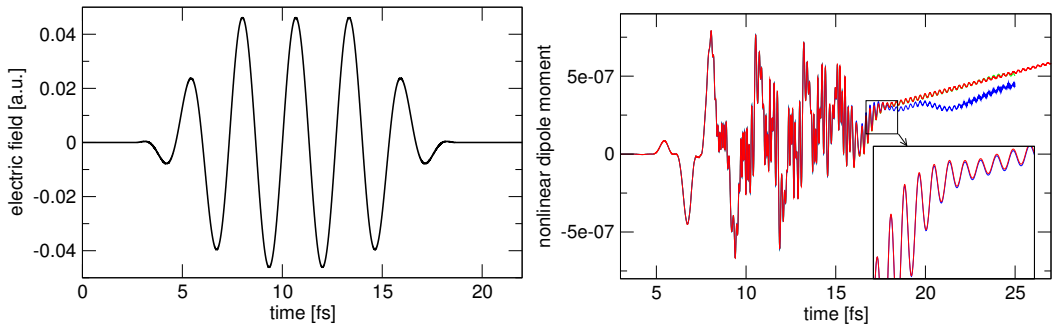

FIGURE 2.1. (Left) This is the input field that we use for comparing our exact calculations to a TDSE simulation. The wavelength is $1.3\mu m$ and the peak intensity is $10^{18}W/m^2$. (Right) We compare the nonlinear dipole moment using a direction integration of the TDSE using Visscher's method (blue and green) to the exact equations (red). Two domain resolutions are used for the TDSE simulation, where the green curve was calculated using a higher resolution than the blue curve. From the inset we see that we have good agreement between methods, given a high enough domain resolution for Visscher's method, which verifies that our derivation and implementation regarding the exact equations are correct.

components along the time axis, instability could prevent its practical application. While we have no formal proof that the method is stable, we have observed no indications of the opposite, even when using extremely long temporal grids containing a few hundred thousand points. We take this as a strong indication that the numerical implementation as described in this section is indeed stable.

To complete this section, we want to illustrate the utility of our results for the field of High-Harmonic Generation (HHG) driven by ultra-intense, femtosecond-duration optical pulses. Figure 2.2 shows an example of the spectrum of high harmonics in the nonlinear current driven by an infrared optical pulse. This nonlinear response can be integrated into a carrier-resolving pulse propagation solver such as UPPE [5] to model generation, build-up, and subsequent propagation of harmonic radiation.

Importantly, the present quantum model provides a self-consistent alternative to the several model "functions" that are normally implemented as independent components in such simulations. Namely, it provides a mechanism for ionization, it describes the current due to free electrons, and it also contributes to Kerr-type nonlinearity originating from the ground-to-continuum transition. Moreover, it generates lower harmonics, including the fundamental, and thus significantly contributes to reshaping of the pump pulse. Because our model is an exact solution, there is no question about all these effects being mutually consistent, which can hardly be said about the standard modeling equations used in simulations of optical filamentation and harmonic generation.

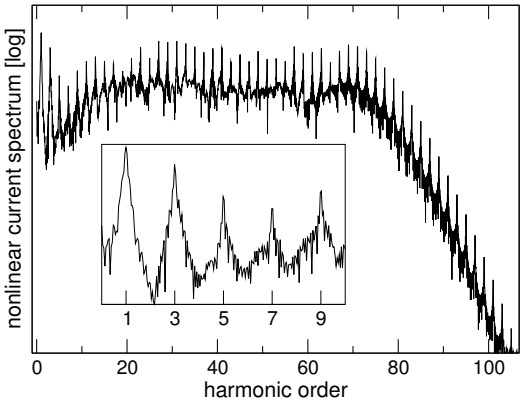

FIGURE 2.2. High-harmonic spectrum of the nonlinear current induced by a $\lambda = 1.3\mu$m pulse. The intensity of the driving field was $10^{18}W/m^2$; constant during 13 optical cycles, and with leading and trailing ramps of 4-cycle duration. The inset shows the detail of the spectrum for low harmonics. Unlike in the strong-field approximation, low-frequency current and dipole moment components are exact, and can be included in the Maxwell equation solver as a source which affects the propagation of the pump pulse.

We want to emphasize that while the model requires significant computation, the numerical effort to evaluate the current formulas is acceptable even for fully spatially resolved Maxwell-Schrödinger systems. To give at least a rough idea, at the time of this writing a simple filament simulation may currently take fifty hours. This may be ten times longer than one using the standard model, but qualitative studies are indeed feasible.

2.6 Summary

We extend the range of exact results for the quantum model of a one dimensional particle with a short-range contact potential, moving under the influence of an arbitrary time-dependent external field. Specifically, we derive expressions for both the current and dipole moment, and extract their components that are nonlinear with respect to the driving field. With applications in mind, we also describe an algorithm for numerical evaluation, and demonstrate its robust implementation. Typically, a temporal grid will contain up to ten thousand of points, and a single solution will take a few seconds. This is indeed a significant effort, but an acceptable price for an exact solution of a quantum system

Our results are useful in the general area of high-intensity light-matter interactions, where they can be used as a test-bed system for theories and simulation methods, which describe strongly nonlinear evolution on extremely short time scale. In particular, in the field of optical filamentation, they serve as a tool to study pos-

sible improvements to current models, especially the parts concerning ionization and free electrons. Because the present model, having only one bound state, does not contribute Kerr nonlinearity originating in the bound-to-bound transitions, one can combine the standard instantaneous Kerr effect, with frequency-dependent linear susceptibility, and this one-dimensional quantum system into a self-consistent, qualitative model for femtosecond filamentation. For the area of high-harmonic generation, the derived current and dipole formulas represent an exactly solvable alternative to the widely used strong-field approximation. Moreover, they unify treatment of the pump and harmonic radiation.

Chapter 3

Applications of 1D Dirac-Delta Potential Model

3.1 Introduction

We have seen from the end of Chapter 2 in Figure 2.1 that the 1D Dirac-delta model's nonlinear response to an intense short pulse contains the Kerr effect and effects due to freed electrons. It is encouraging that even though this is a simple toy model, the time dependent atomic response contains the features that one would expect given a short and intense laser pulse. Furthermore, since we derived the exact response this means that we have access to a very wide range of harmonics, demonstrated in Figure 2.2, and that these harmonics are generated in the correct relative ratios to each other. Despite the familiarity of the responses features and the assurances of an exactly solvable model, we did not know whether there was something pathological about the system itself. Given that it has only a single bound state, lives in one dimensions, and that the shape of the delta potential is far from a real atomic potential, does that limit the nonlinear phenomena that it can capture? The goal of this chapter is to detail how we attempted to answer this question by presenting two applications where we used the 1D Dirac-delta model to success. These applications boosted our confidence that the model could be taken seriously as an investigative tool with the hope that it could replace current medium models or, at a minimum, point us to the parts of the standard modeling equations that are in need of replacement. Since the inclusion of a fully quantum atomic model into UPPE had not been done before, we devote a section to explain exactly how we connected the two before we discuss the two applications.

The first application was to model propagation of a short pulse though a Xenon gas jet to produce very high harmonics. It was the first time that we used the UPPE simulator with a quantum media model, and therefore we will describe in detail how we married the two. We modeled two aspects of an experimental setup in [65]. The first was the angularly dependent HHG by focusing the beam into the gas jet. The second, was an XUV frequency comb generator where a short pulse was propagated multiple round trips in a passive cavity. We found that UPPE using the 1D Dirac-delta model was able to qualitatively reproduce both the HHG gas jet spectrum and the frequency comb spectrum.

The second application was to address the open question (around 2011) of the existence of the higher order Kerr effect (HOKE). We used only the response from a single atom in a pump-probe scheme to calculate an effective susceptibility. We

witnessed that unlike in HOKE where higher order nonlinear index terms depend on instantaneous intensity only, the susceptibility calculated from the 1D Dirac-delta model remembers the field's history. This is evident since the susceptibility decreases when the field is present until it eventually becomes negative due to a large quantity of freed electrons. We concluded that it is not possible that negative higher order indexes could account for this time dependent behavior.

3.2 Connecting to UPPE

Before we get to the applications, we must discuss how one would use the nonlinear response of the 1D delta model in a propagation scenario where the medium is a gas. In the standard model, there are a number of independent contributions both in the polarization and in the current density. They include the optical Kerr effect, ionization in strong fields and a freed-electron density evolution equation, separately modeled losses due to ionization, avalanche ionization, defocusing effects of freed electrons, and losses due to freed electrons described in terms of an effective Drude-plasma model [3].

Our computational approach for simulating femtosecond nonlinear light-matter interactions reflects the fact that the above mentioned effects are all manifestation of the single electronic system response to the strong optical field. The goal is to achieve a unified description, and reduce multiple independent model parameters. In general, our model involves three components for describing an atomic gas:

- A description of the linear dispersive properties of the gas via a complex-valued frequency dependent susceptibility $\chi(\omega)$.
- The 1D δ-potential quantum model for modeling the nonlinear current J due to ground state to continuum transitions. This will incorporate the effects of ionization, HHG, and ionization induced absorption and refraction in a holistic fashion.
- A Kerr-like nonlinearity and associated nonlinear polarization P to capture the nonlinear optical response due to the ground state to excited bound state transitions. This will contribute processes such as four-wave mixing, self-phase modulation, and self-focusing. (For a molecular gas we may also add a time-delayed nonlinear response to capture Raman effects)

The three medium components χ, J, P are coupled into the field-propagation equation which encompasses all frequency components from the fundamental to high harmonics. While we use the Unidirectional Pulse Propagation Equation, we emphasize that this approach may be implemented with any pulse-propagation simulator that resolves the carrier wave of the optical field.

3.2.1 Linear dispersive properties

Inclusion of the linear dispersive properties of the medium over the full span of harmonics is important to properly incorporate the phase-matching and re-absorption that affect the spatial evolution of the generated harmonics. In our spectral solver this does not present a problem as long as suitable data is available for the index of refraction and absorption properties in a sufficiently wide spectral range. The medium is characterized in terms of the linear complex susceptibility $\chi(\omega)$, and the pulse propagation method utilizes this information in the propagation constant $k_z(\omega, k_\perp) = \sqrt{\omega^2(1+\chi(\omega))/c^2 - k_\perp^2}$ at each frequency or wavelength resolved by the numerical simulation.

3.2.2 Quantum atomic model for the nonlinear response

The integration with the pulse propagation solver is in principle the same as for any other nonlinear medium response. Having calculated the evolution of the optical field up to a given propagation distance, the history of the electric field at a given point in space is converted to the external field $F(t)$ in atomic units. This drives the quantum system, and the induced current is computed from the equation (2.37). The nonlinear current is next converted from the atomic units, and multiplied by the number density atoms at the point in space. The resulting macroscopic current density is included in the right-hand-side of the UPPE equation. We remark that since we only incorporate the *nonlinear* current from the quantum model into the UPPE, we do not double-count by erroneously including linear properties from the 1D atomic model. Also note that it is not an option to retain the linear part of the model's response instead of $\chi(\omega)$ introduced in the previous subsection. This is because in a real medium $\chi(\omega)$ originates in virtual transitions among a large number of states, and it would be difficult to model this from first principles. The linear susceptibility arising from our 1D atomic model is far too simplistic to capture the chromatic properties of a gas to any realistic degree.

We would like to illustrate that our 1D δ-potential atomic model displays features for HHG that are qualitatively similar to those obtained using the strong field approximation applied to the more exact 3D Hydrogen-like atomic model. To this end Figure 3.1 shows an example of a harmonic spectrum of the nonlinear current induced in the 1D model atom for an ionization potential of 12 eV, characteristic of Xenon, and a ten-cycle pulse of center wavelength $\lambda = 800$nm and peak intensity$1.5 \times 10^{18}\mathrm{W/m^2}$. This harmonic spectrum exhibits the characteristic high-harmonic generation plateau with a high frequency cut-off. The cut-off predicted by the formula from the standard HHG model [66, 67, 68] is indicated by the arrow in Fig. 3.1 for our parameters. Furthermore, the harmonic spectrum includes the 9^{th} harmonic which occurs near the ionization potential up to around the 40^{th} harmonic, and thus constitutes an example of near-threshold HHG where the generated harmonics straddle the ionization

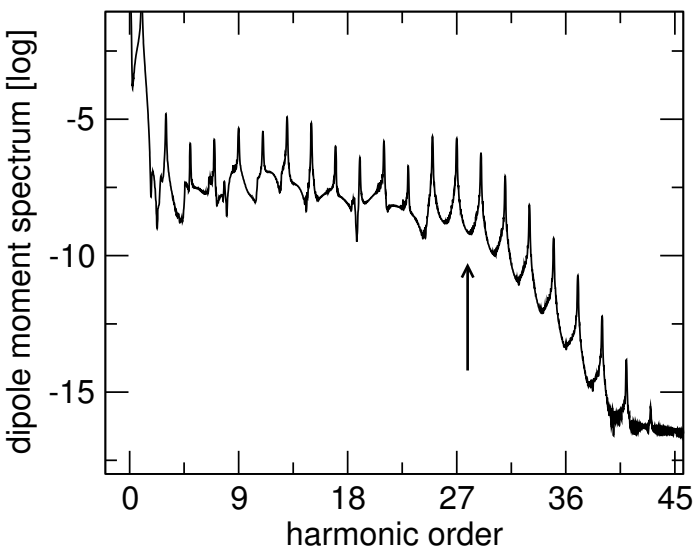

FIGURE 3.1. High-harmonics in the spectrum of the dipole moment induced by a pulse at $\lambda = 800$nm. The intensity was 1.5×10^{18}W/m^2, kept constant over duration of ten optical cycles. The arrow marks the location of cut-off energy calculated for these conditions.

energy. What is shown in Fig. 3.1 is the spectrum of the nonlinear polarization P that appears in the Maxwell equations and not the spectrum of the radiation actually generated. Importantly the harmonic spectrum shown is exact, within the context of our 1D model, over the whole frequency range and in particular at low frequencies.

Finally we point out some pros and cons of our 1D model versus the strong-field approximation. The strong field approximation is often utilized in numerical atomic simulations of HHG, and describes the 3D atomic system in terms of a single bound state, the ground state, and a continuum of free electron continuum states [67]. In this sense it addresses a similar spectrum of electronic states as our 1D model, albeit in 3D. A distinct advantage of the strong field approximation is that it can in principle be used for an elliptically polarized driving field, whereas our 1D model is restricted to linear polarization. On the other hand, ours is an exact solution of a well-defined system, and as such it is valid throughout the whole frequency spectrum. Unlike the strong field approximation, it accounts for "all electron trajectories" not only those that give rise to the harmonic radiation. In particular, the low-frequency components of the nonlinear current response affect the propagation of the driver pulse through ionization, defocusing by freed electrons, ionization losses, and the nonlinear focusing.

3.2.3 Nonlinear Kerr effect

The δ-potential atomic model only incorporates the nonlinear contribution of ground state to continuum transitions. To capture the nonlinear contribution of virtual

ground state to bound state electronic transitions we include a term representing the nonlinear Kerr effect of the form

$$P(t) = 2\epsilon_0 n_0 n_2 E^2(t) E(t), \tag{3.1}$$

where n_2 is the nonlinear index and n_0 is the linear refractive index. This effect enters the propagation equation via the nonlinear polarization term, and gives rise to self-focusing and a cascade of lower-harmonic radiation.

3.3 High harmonic generation

Given that we now know how to include the three medium components χ, J, P, we now investigate high harmonic generation from a Xenon gas jet. As mentioned before,

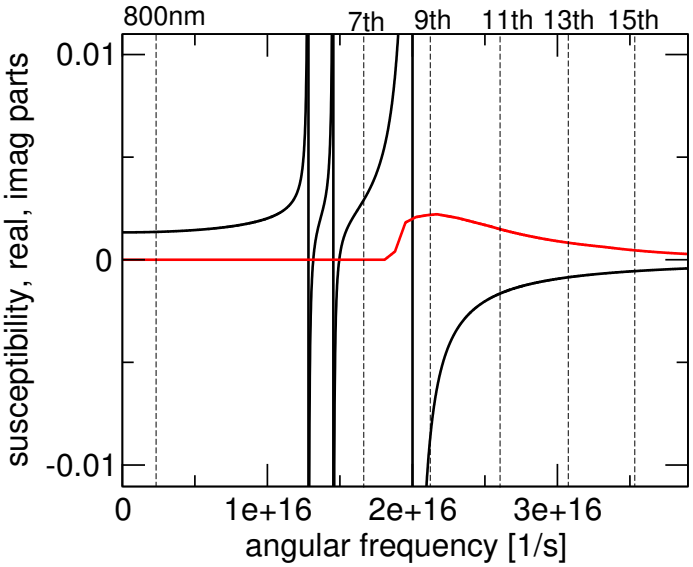

FIGURE 3.2. Real (dark lines) and imaginary (red line) parts of the linear susceptibility of Xenon as employed in the numerical simulations. The vertical dashed lines mark the fundamental wavelength of the fundamental field at 800 nm, and several of its harmonic are also indicated.

in order to use Xenon as part of our medium model, we need its linear optical properties. Figure 3.2 shows the real (solid dark line) and imaginary (red line) parts of the susceptibility as functions of the angular frequency of the electromagnetic field. To create the data set displayed in Figure 3.2 we have combined Xenon data downloaded from *http://henke.lbl.gov/optical_constants/* with the refractive-index parameterization obtained from [69] to create a tabulated representation of the linear susceptibility over a range of frequencies that spans the fundamental at 800 nm wavelength up to its 35^{th} harmonic. Note that with the real and imaginary parts of the susceptibility

function coming from separate sources, and with no absorption data available for photon energies below 10 eV, our parameterization does not satisfy the Kramers-Kronig relations. At the time of this writing, better data was not available. Nevertheless, while not a perfect model of the Xenon gas for all frequencies this data set employed serves as an illustration example in which all electromagnetic frequencies are treated on the same footing by the propagation solver, which operates on the full electric field. Generally the accuracy of the linear propagation will be limited by the quality of the available data for the linear susceptibility.

3.3.1 HHG in a xenon gas jet

The incident pulse in each case is Gaussian in space and time with pulse duration $t_p = 85$ fs and center wavelength of 800 nm, and focused spot size w_0. We model the Xenon gas jet as a vertical column which is tapered along the propagation or z-axis according to the jet pressure profile indicated by the dotted line in Figure 3.3. This pressure or density profile has a constant region of length $L = 200$ μm between $z = 100 - 300$ μm and tapers off on each side of this region. For the examples, we used 20 Torr for the maximal pressure in the gas jet. The input beam is focused at $z = 100$ μm close to the entrance (case A) and close to the exit (case B) of the gas jet. The variation of the on-axis intensity along the z-axis is illustrated in Figure 3.3.

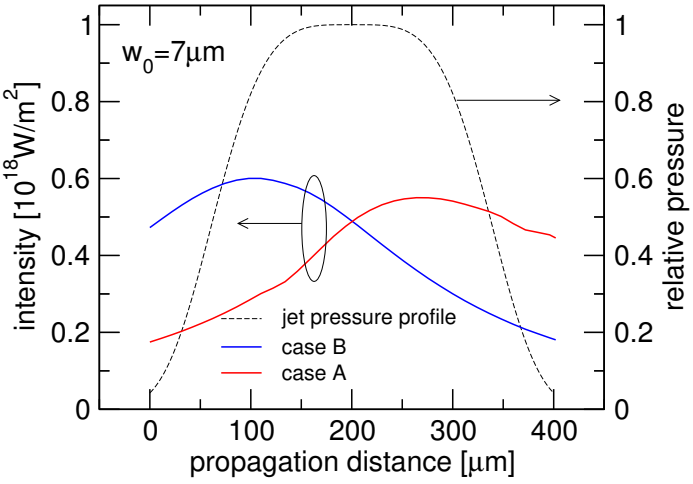

FIGURE 3.3. Gas jet profile and on-axis intensity for a beam focused at the entrance (case A) and at the exit (case B).

We now present fully resolved simulations of pulse propagation and harmonic generation. As a means to present our results we have chosen to plot the angularly resolved spectra for selected harmonics as they propagate through the gas jet. Such spectra have previously been utilized in both numerical simulations and were measured experimentally [70, 71]. For example, with reference to Figure 3.4, each panel

shows a color encoded plot of the spectral intensity (red being maximum and blue minimum) as a function of the transverse wavenumber representing angular spread along the horizontal axis, the center corresponding to zero propagation angle, and frequency along the vertical axis for the harmonic indicated. In particular, the frequency axis in each panel is centered on the harmonic order and has a spread of one half of the harmonic spacing. The results are arranged into a (3×3) array of panels, the panels are arranged vertically according to the propagation distance into the gas jet, the top panel being the entrance and the bottom panel the exit of the gas jet, and the panels are arranged horizontally from left to right for harmonic orders 9, 11 and 13.

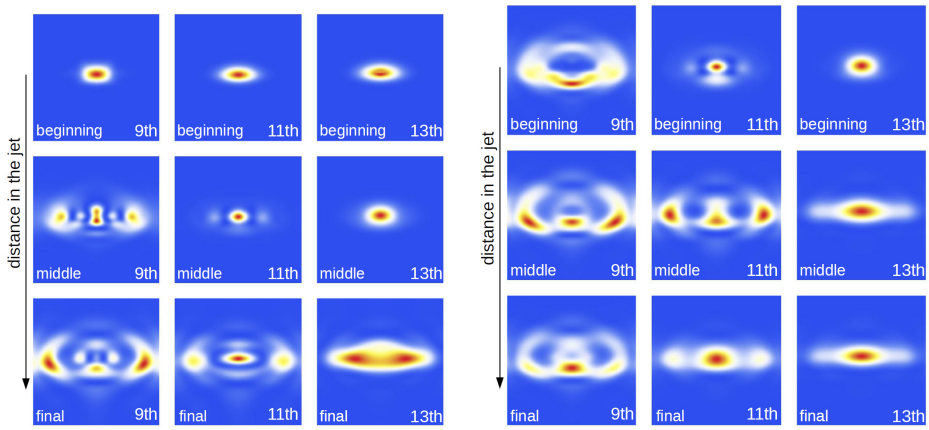

FIGURE 3.4. (Left) Focus at gas jet exit. (Right) Focus at gas jet entrance. Angularly resolved spectra of the 9th, 11th, and 13th harmonics at three different propagation distances through the gas jet. Each panel shows a frequency region (vertical axis) corresponding to one half of the harmonic order, centered at the given harmonic frequency. The horizontal extent of each panel corresponds to the transverse wavenumber and thus represents the angle of propagation.

The calculated angularly resolved spectra are shown in Figure 3.4 for (left) focusing at the exit, and (right) focusing at the entrance of the gas jet, and we note that there is a marked difference between the angularly resolved spectra for the two cases. This is consistent with general expectations based on phase-matching [72, 73, 74]. For example, on-axis phase-matching requires cancellation between the accumulated Gouy phase-shift and the accumulated atomic phase-shift due to the quantum path taken by the electron. The Gouy phase-shift is a positive quantity whereas the quantum phase is proportional to the z-derivative of the incident beam intensity due to the dependence of the quantum phase on the electron quiver energy, which is positive for case (a) with the beam focused at the exit, and negative for the case (b) with the beam focused at the entrance to the gas jet. Thus on-axis phase matching is not a possibility for the case (a) with the input beam focused at the exit, whereas phase-

matching is a possibility in case (b) with focusing at the entrance to the gas jet. The difference in the angularly resolved spectra evident for cases (a) and (b) in Figure 3.4 may thus be traced to expected differences in phase-matching conditions [73].

If we further examine the angularly resolved spectra at the exit of the gas jet, shown as the lower set of panels in Figure 3.4 for cases (a) and (b) we observe further consequences of the different phase-matching conditions: For case (a) for which strict on-axis phase-matching is not possible we see that the off-axis HHG emission is more significant with respect to the on-axis emissions for each harmonic order than for case (b) where on-axis phase-matching is possible. This is particularly pronounced for the 13^{th} harmonic where case (a) is dominated by off-axis emission whereas case (b) is dominantly on-axis emission. So the results of our simulations are compatible with expectations based on on-axis phase-matching [72, 73].

3.3.2 HHG in a femtosecond enhancement cavity

As a final illustration, we show results for harmonic generation in a xenon gas jet placed inside a passive femtosecond enhancement cavity (fsEC). This experimental configuration has been demonstrated as a means to generate XUV frequency combs with the harmonic light being generated at each cavity round trip [75, 76]. In this geometry the ionized gas jet behaves as a nonlinear medium at the focus of a 6m ring cavity. A pair of 15cm radius of curvature focusing mirrors lead to an intracavity spot size of $w_0 = 15\mu$m within the jet. The fsEC has a 1% input coupler that allows pulse energy enhancement over 200 times relative to the incident pulse train leading to peak intensities in excess of 1×10^{14} W/cm^2 when the gas jet is off. The harmonics are coupled out of the cavity using a thin sapphire plate, aligned at Brewster's angle for the fundamental pulse, and resolved spatially by reflection from an XUV grating.

For initial conditions in these simulations, we have utilized a previously calculated temporal profile of the pulse just before it enters the gas jet. This pulse profile was obtained from a 1D steady-state calculation of the fundamental pulse building up inside the fsEC in the presence of the xenon gas and includes the effects of cavity dispersion. The high nonlinearity of ionization leads to chirped pulses circulating in the cavity and limits the achievable intensities in this geometry. Details of this model and its implications for HHG in a fsEC can be found in Ref. [77].

Yet another modification of the current model consists in including the surviving plasma in the jet based on the estimated levels calculated in [77] . Because the 20 ns cavity round-trip time is too short for the plasma to decay entirely, the pulse propagating through the jet experiences defocusing due to electrons freed during the previous passes. These electrons have been liberated from their parent atom for a sufficiently long time, and have equilibrated into a true plasma (note that the free-electron states included in the quantum model that drives the pulse propagator are of different nature: they did not have enough time to thermalize, and their interactions is mainly with the nearby parent ion). Therefore, the influence of the plasma remnant

can be included within the linear chromatic properties of the gas. Here we also assume that the diffusion resulted in a nearly homogeneous spatial distribution of free electrons, and the corresponding modification of the refractive index is constant over the cross-section of the beam. Of course, the spectral nature of our pulse propagation solver allows us to endow this susceptibility contribution with the correct frequency dependence: $\chi(\omega) \sim -\omega_{plasma}^2/\omega^2$.

Figure 3.5 shows simulated and experimental spectra of harmonics from 7th to 15th. While details of relative strength of harmonics 9th to 15th depend on the exact placement of the beam focus with respect to the center of the jet (compare the two panels on the left), and on the absorption included in our simulation (compare full and dashed lines), we see that harmonics 11 and 13 are the most pronounced, and that harmonic power starts to decrease at harmonics 15th (there are many more harmonics generated, but are not discernible on the linear scale of this figure). This is compatible with the spectrum recorded in the experiment. On the other hand, the simulated 7th harmonic seems to be too strong. We think that this is mainly due to the fact that the model susceptibility of the gas has no absorption at this wavelength (this is due to limited frequency extent of the available data, see the red line in Figure 3.2). The effect of medium absorption is indeed clearly visible in the 9th harmonic where our model absorption data exhibit a maximum. These results make it thus evident that it is important to obtain as realistic as possible a data set for both the index of refraction and absorption of the gas.

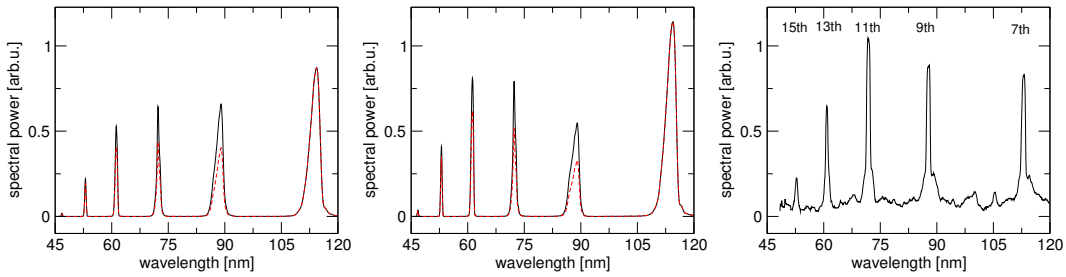

FIGURE 3.5. Harmonic spectrum calculated (left panels) for conditions reflecting those in the femtosecond enhancement cavity. Dashed and full line compare results for simulation with and without inclusion of losses. Left most panel: beam focus at the "entrance" into the gas jet. Middle panel: beam focus at the "exit" from the gas jet. Experimental spectrum shown in the right panel, with an account for the grating efficiency.

We certainly did not expect that the simplistic one-dimensional quantum model put forward here could qualitatively reproduce many of these experimental results. However, we saw the above comparison as very encouraging — it showed that the model, especially when coupled with good-quality dispersion and absorption data for the gas, can serve as a practical tool to study the qualitative trends that govern the

nonlinear interactions that span the frequency range from infrared to high harmonics. The results boosted our confidence in the use of simple, exactly solvable models to model high harmonic generation experiments.

3.4 Higher-order Kerr effect

Around 2010 and for a number of years after, the higher-order Kerr effect (HOKE) for molecular gases [6, 7] was a topic of particular contention in the nonlinear optics community. The claims of HOKE were that the ultrafast nonlinear changes in refractive index are higher than linear in intensity, that it changes sign (becoming negative) for high enough intensity, and that it can occur before significant densities of freed electrons (or plasma) appear. Observations of HOKE proposed a revision to the accepted paradigm for femtosecond filamentation [78], suggesting that the role of plasma in filaments is not as important as previously thought. A number of papers followed, both supporting (e.g. [26, 27, 28]) and rejecting (e.g. [30, 31, 32, 33]) this view.

Since we had recently derived the exact time-dependent current for the 1D delta potential model, we saw this as an opportunity to use the model as an investigative tool. Perhaps such a simple, yet self-consistent model could illuminate whether the claims of HOKE were valid. Up until then there had been relatively little theoretical elucidation of its microscopic origins. Teleki *et al.* [51] studied nonlinear refraction in gases using a 1D atomic model and found nonlinear refraction akin to HOKE in the quasi-static limit, but conjectured that plasma defocusing would effectively mask HOKE. In contrast, Brée *et. al* [28] found that HOKE can precede significant ionization based on the nonlinear Kramers-Kronig relations applied to multiphoton ionization of the atoms. Volkova *et al.* [22] performed 3D quantum simulations of a silver atom and concluded that they found no reason to modify the existing paradigm of filamentation.

It was suggested that HOKE arises precisely from ground-continuum atomic transitions, where ground-bound state transitions yield at most a saturable self-focusing nonlinearity. Since the 1D delta model contains only a single bound state, it provided a means to assess whether ground-continuum atomic transitions could produce the features of HOKE, and we found that it could not. However, we did find evidence that signatures of a higher-order nonlinearity could be found in the low-order harmonics of the pump center frequency. Another reason to use the 1D delta model is that we have an exact equation for the nonlinear current, making it immune to numerical issues. To compare, the 3D atomic quantum simulations, e.g. Ref. [18, 22], involved separating the nonlinear response from the much larger linear response in the full optical response. Such a procedure could be prone to numerical issues and careful attention to simulation parameters must be taken and convergence studies must be made.

Our diagnostic approach involves a pump-probe scheme with the electric field profile shown in Figure 3.6. Specifically, the 1D atomic system is driven with a strong pump pulse that has a region of constant intensity, and linear leading and trailing edges. At the same time, the system is exposed to a much weaker probe, the duration of which exceeds that of the pump. In this way we may sample the system response at times before, during, and after the pump pulse. Physically, our goal is to extract the *effective* susceptibility experienced by the probe due to the modification of the medium by the strong pump.

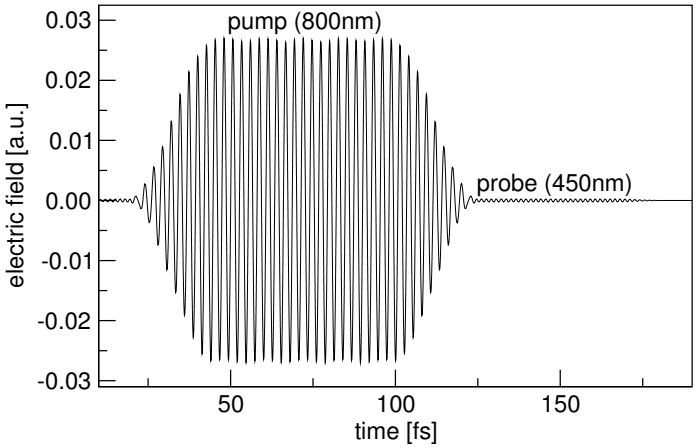

FIGURE 3.6. Electric field of the pump−probe waveform. The probe ($\lambda = 450$nm) appears as a weak background with the duration extending before and after the much stronger pump pulse ($\lambda = 800$nm).

The time-dependent susceptibility is defined operationally through the following procedure: For a given temporal profile of the electric field $E(t) = E_{pump}(t) + E_{pr}(t)$ we calculate the nonlinear current J induced in the 1D atomic system using the exact solutions [79], then a second calculation is done with the pump alone. The difference of the two is therefore the response of the pump-affected system to the probe:

$$J_{pr}(t) \equiv J(E_{pump}, E_{pr}) - J(E_{pump}, 0) \approx \frac{\delta J}{\delta E_{pr}} E_{pr} \ . \tag{3.2}$$

For high intensities $J(t)$ exhibits rich spectra including high-harmonics (see Figure 3.7), but here we concentrate on the response around the frequency of the probe itself.

From the current probe response $J_{pr}(t)$ we extract the component $J_{filt}(t)$ corresponding to frequencies in the vicinity of the probe center frequency by applying a filter in the spectral domain with a bandwidth of one quarter of the center frequency. Having isolated $J_{filt}(t)$ from its background, the polarization response $P_{filt}(t)$ is obtained by integration in time. This then serves to define the effective

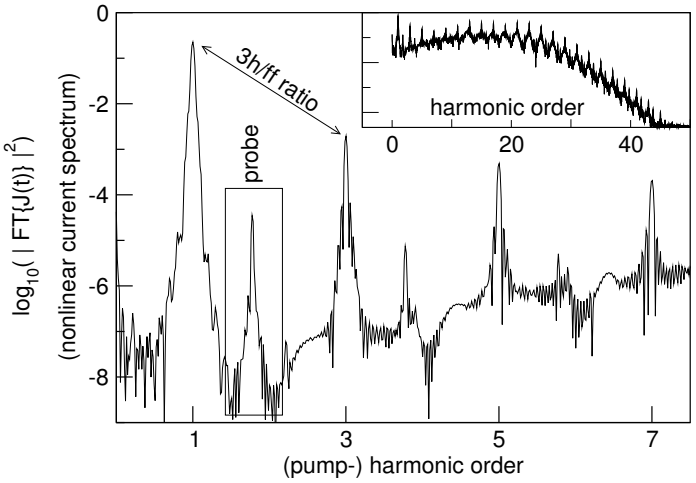

FIGURE 3.7. Log-scale spectrum of the nonlinear current, $\log_{10}(|\mathrm{FT}\{J(t)\}|^2)$, with the inset showing its high-harmonic extent. The effective susceptibility is extracted from the vicinity of the fundamental probe frequency marked by a rectangle. Another interesting quantity is the ratio between the third- and fundamental-frequency powers indicated by the arrow.

nonlinear optical susceptibility by dividing the complex-valued analytic signals of the nonlinear polarization and probe (i.e. quantities for which $P_{filt}(t) = \mathrm{Re}\{\mathcal{P}_{filt}(t)\}$, $E_{pr}(t) = \mathrm{Re}\{\mathcal{E}_{pr}(t)\}$):

$$\Delta\chi(t) \equiv \mathcal{P}_{filt}(t)/\mathcal{E}_{pr}(t) \ . \tag{3.3}$$

The real part of this susceptibility reflects the time evolution of the nonlinear refractive index experienced by the probe. Note that this is a way to characterize a single atom response, and that propagation effects (i.e. phase matching) also affect the actually generated radiation.

If we denote by I_{sat} the intensity at which HOKE starts to manifest itself, then for peak pulse intensities $I < I_{sat}$ we expect that the effective susceptibility will be proportional to the local pulse intensity. This case is illustrated qualitatively by the dashed line in Figure 3.8 for HOKE behavior shown on the left and for the pump probe pulse in Figure 3.6. In the first scenario in which HOKE can indeed manifest itself before ionization occurs, then for $I > I_{sat}$ the qualitative variation of the effective susceptibility with time should take the form shown as the thin solid line in Figure 3.8: The characteristic dip in the time variation of the time-dependent susceptibility appears since for $I > I_{sat}$ HOKE should depress the nonlinear susceptibility for the highest intensities in the pulse. For even higher intensities $I > I_c$, I_c being the intensity at which the HOKE reverses sign, the time variation of the susceptibility takes on the generic form shown as the thick solid line in Figure 3.8.

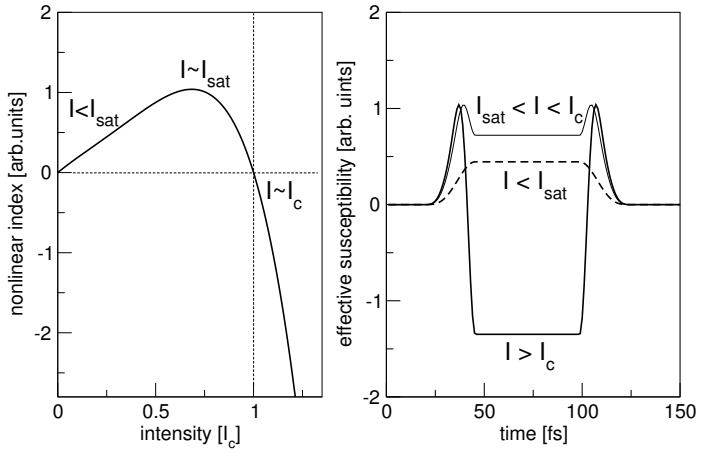

FIGURE 3.8. Qualitative schematics of the effective time-dependent susceptibility (right) in a system with an instantaneous HOKE-like nonlinearity (left). Bat-ear features appear at both leading and trailing edge of the pump pulse for a sufficiently high intensity.

In contrast, for the second scenario in which a combination of the standard Kerr effect plus defocusing due to ionized electrons provides a qualitative model, we would expect to see that the nonlinear susceptibility would increase monotonically in time until ionization occurs after which the nonlinear susceptibility would decrease monotonically until the pump pulse terminates. After the pump pulse, a negative susceptibility persists as long as the freed electrons remain. For low intensities such that ionization does not occur the time variation should be the same as the dashed line in Figure 3.8.

Next we turn to which of the above two scenarios best reflects the results of our exact simulations based on the 1D atomic model for the nonlinear current and polarization. Figure 3.9 shows that we observe the second or standard scenario. While at lower intensities the susceptibility follows the intensity envelope of the pump as expected for the Kerr effect, the almost linear decrease with time for higher intensities is clearly due to increasing number of "freed electrons" which produces defocusing or negative nonlinear refraction. Importantly, this behavior is qualitatively independent of the ionization energy of the system. That is, for higher E_g the system exhibits weaker nonlinearity, and the ionization onset occurs at higher intensities. Our pump-probe diagnostic based on the 1D atomic model does not exhibit significant manifestations of HOKE in the frequency band of the probe field, in agreement with the conclusions arrived at based on the 3D atomic simulations of Ref.[22].

From the above observations it seems that the effective susceptibility could be well approximated by the model currently used in filamentation modeling. At the

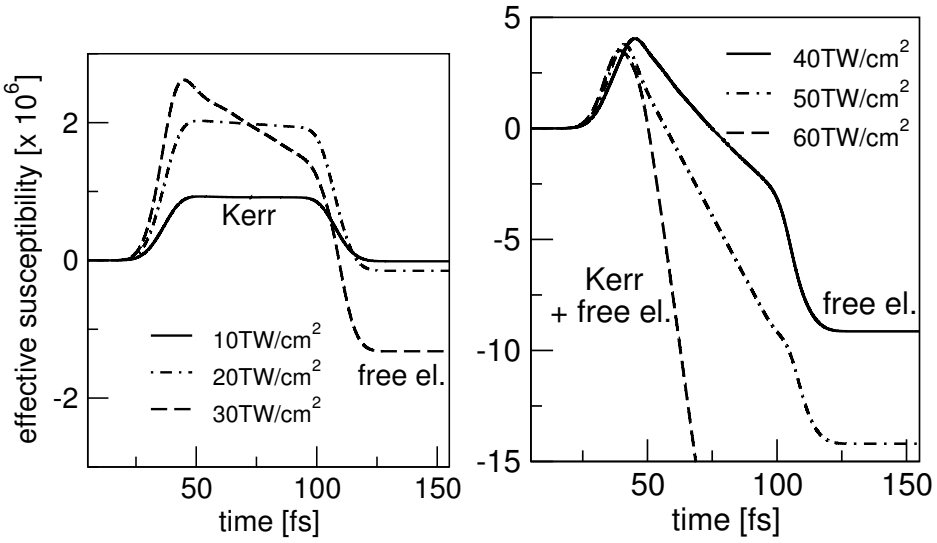

FIGURE 3.9. The effective time-dependent susceptibility experienced by the probe at lower (left) and higher (right) pump intensities. Data shown for the ground-state energy of $E_g = 10$eV. The same qualitative behavior is observed for other E_g values. Labels (Kerr, free electrons) indicate main contributing effects.

same time, it has been shown that the nonlinear behavior of this model in the quasi-static regime deviates from the Kerr effect [51], raising the question of whether any signatures of higher-order nonlinearity can survive?

The answer is in the affirmative, and can be readily deduced from the example in Figure 3.7 which shows that the peaks corresponding to the fundamental and third harmonic frequency have different heights. This is incompatible with the standard instantaneous Kerr effect plus the Drude plasma-like response from free electrons, and thus signals the influence of higher-order nonlinearities. Indeed, the Drude plasma does not contribute to the third harmonic at all, and the ratio between the spectral power of the fundamental and the third harmonic due to Kerr effect must be one. To see this, consider a local field $E_0 \cos(\omega t)$, for which the instantaneous Kerr polarization would be $P = \epsilon_0 \bar{n}_2 N_a E_0^3 \cos(\omega t)^3$, and the corresponding nonlinear current density is obtained as $J = \partial_t P = 3/4\epsilon_0 \omega \bar{n}_2 N_a E_0^3 [\cos(\omega t) + \cos(3\omega t)]$, showing that the ratio between the strength of the third and the fundamental harmonics of the *nonlinear current* is one (while it is 1/9 in the nonlinear polarization). Note that the effective susceptibility only describes the *source* that appears in the Maxwell's equations, and not directly the generated radiation.

3.5 Summary

The 1D Dirac-delta model has proven useful for investigating and qualitatively reproducing nonlinear optical phenomena, such as HHG. Due to its self-consistent treatment of these phenomena, the model is also useful for pointing out inconsistencies in newly proposed theories, such as HOKE. The key advantages of the model are that we have an exact solution and that it is possible to incorporate it as part of a medium model into a carrier resolved propagator, such as UPPE. It is really a strong advantage to be able to use a quantum model during propagation, since we can test which phenomena arise from the atom itself or come from propagation effects alone. Since the model is conceptually simple in that there exist only a single bound state, we can confidently say that witnessed nonlinear phenomena are only due to bound to continuum transitions and the density of freed electrons. The ability for us to investigate the origin of these effects was crucial in building our intuition of how microscopic mechanisms manifest themselves at the laboratory scale.

We saw that the 1D Dirac-delta model reproduced the HHG spectrum generated in a Xenon gas jet experiment. The ability of the model to produce a wide range of harmonics, while still accurately reproducing the low frequency portions gives it an advantage over the traditional strong field approaches. We were encouraged to see that when coupled with a good linear model that the 1D Dirac-delta could be a useful tool for guiding HHG investigations.

We found that the 1D Dirac-delta model suggest that higher order nonlinearities exist, but together with the effects from plasma. Consequently, the HOKE cannot have the consequences that made it such a hotly debated topic. We demonstrated that the effective susceptibility calculated from an instantaneous HOKE equation did not match the one from the 1D delta model. Furthermore, the instantaneous HOKE susceptibility lacked any signs of the accumulation of freed electrons, which was visible in the extracted susceptibility from the 1D Dirac-delta model. This comes from the fact that a quantum model retains memory of the past ionization dynamics. We will explore this idea of "memory" in Chapter 5 and attempt to gauge how large of an effect it has on the nonlinear response.

Chapter 4

Resonant States

4.1 Introduction

We saw in Chapter 3 that even though the 1D Dirac-delta model's response can come only from bound to continuum transitions, it faithfully reproduced the qualitative features seen in HHG experiments. This means that this transition dominates the nonlinear response, and we should therefore attempt to better capture the process of ionization when designing a medium model. We also wondered how important is the quantum system's memory of past field values in the generation of the nonlinear response? We saw when comparing the HOKE susceptibility to the delta model's that there was a large qualitative difference in the time dependent shape. This hints that there are electron states that remember the past ionization dynamics.

Resonant states encapsulate the quantum coherence between the bound and free states since they directly describe the flow of electron probability to and from the continuum. We know that electrons are neither fully bound or free in the presence of an external field, but are instead weakly-bound. We thought it was worth pursuing the question of whether resonant states would provide a natural theoretical framework to describe the ionization process.

Resonant states have been used to solve a wide range of problems in the fields of nuclear physics [80, 81], quantum chemistry [82], nonlinear optics [51, 83, 84] and semiconductor physics [46, 85]. They can also be used to model leaky optical waveguide modes [86]. Despite their widely recognized utility, relatively little is known about their general properties since they do not live in the familiar Hilbert space associated with Hermitian quantum mechanics [87]. The properties and issues that are less well-understood than in Hermitian quantum mechanics include inner products, normalization and completeness [88, 89, 90, 91, 92, 93, 94, 95], complex expectation values [96, 97] and their physical interpretation [98]. Despite the mathematical difficulties related to their applications, resonant states do contain valuable physical information and it is important to investigate systems that could provide some guidance.

Beyond developing a deeper understanding of exactly solvable systems, the additional motivation for this investigations is in the use of resonant states as a basis for time dependent Schrödinger evolution, with applications in modeling electron ionization and nonlinear polarization due to a time varying optical pulse field [83]. Detailed study of exactly solvable systems with Stark resonant states brings multiple benefits. First, having explicit expressions for complex-valued observables and the ability to study their field- and time-dependence gives intuition of how one maps

these complex values and open-system dynamics back to the real expectation values and the norm-preserving evolution found in Hermitian quantum mechanics of a closed system. Such a connection is crucial for applications in nonlinear optics (e.g. [83, 99, 100]). Secondly, the ability to compare different resonance systems may indicate which properties or relations are universally valid or common to all resonance systems. This topic is discussed in Section 4.5, where for example, we have witnessed in numerical simulations a field-dependent relation connecting the expectation values of the gradient of the atomic potential to the resonant state pseudo-norm for one- and three-dimensional systems. Such universal properties not only expand the knowledge of what is known about resonant states, but are also quite useful in numerical simulations.

In this chapter we begin by presenting some general properties that are true for all resonant states. We define a generalized inner product that is based on a specific contour. This generalized inner product is used extensively to regularize divergent integrals found throughout the theory. Using this theoretical framework, we apply it to two exactly solvable systems: the 1D Dirac-delta function potential and the 1D square well potential and derive all the necessary expressions to use their resonant states as a way to calculate the time dependent dipole moment from an arbitrary field. Based on what we learned from calculating the quantities for the two concrete cases, we can conjecture some general properties that are true for all resonant systems with piecewise constant potentials, and possibly true in general of all resonant state systems, even in higher dimensions. We end with a discussion of the completeness of the 1D Dirac-delta potential system.

4.2 General properties

In this section, we give some background of the class of Hamiltonians that we want to investigate. We begin with a 1D Hamiltonian that is parameterized by the strength of the external field F

$$H(F) = -\frac{1}{2}\nabla^2 + V(x) - xF, \tag{4.1}$$

where the function $V(x)$ represents the atomic potential. To study the Stark resonances, one usually assumes outgoing wave boundary conditions at $x \to \infty$ and seeks solutions of $H\psi_k = E_k\psi_k$ where E_k is the eigenvalue. With outgoing boundary conditions, the system is open as the particle can escape toward $x \to \infty$ and the operator H is non-Hermitian. Therefore the energy E_k, along with many other observables, are complex-valued. Without Hermiticity, we lose many of the guarantees of Hermitian quantum mechanics, such as conservation of the number of particles, real-valued observables, square integrable wavefunctions, etc. There is not yet a full consensus on how to handle and interpret many of these quantities, including normalization and inner products.

Due to the non-square-integrable character of wavefunctions ψ_k, the standard inner product and normalization prescriptions do not apply, since the integrals normally used to calculate them are divergent. Some regularization method must be used, and a number of approaches can be found in the literature [88, 91, 101]. However, it is important to appreciate that there may not be as much choice as it may seem in how the Stark resonant states should be normalized. For example, if a resonant-state expansion of a Green's operator exists, the eigenstates appear in it with a definite "norm" [102]. In what follows we utilize bi-orthogonality of the Stark resonant system, and obtain the eigenstates with such preferred normalization factors.

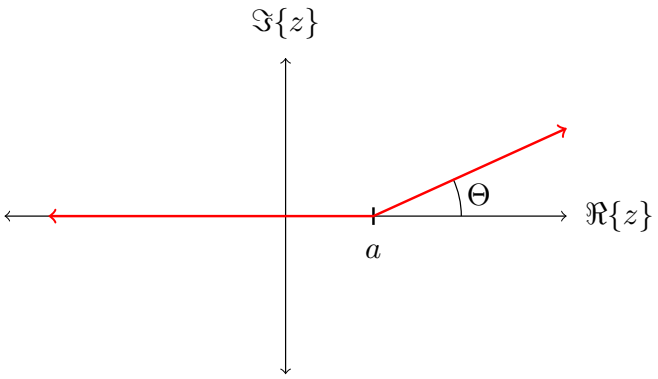

FIGURE 4.1. The contour $\mathcal{C}$ (red) in the complex plane that serves as a "complexified" spatial axis in a model of an open quantum system in which a non-Hermitian Hamiltonian (4.1) acts in the space of functions defined along the contour. Both smooth and piece-wise linear contours are admissible for our purposes. In this example, the domain of the Hamiltonian would be specified by requiring that $f(a^-) = f(a^+)$, and that an analogue of the Cauchy-Riemann condition, $f'(a^-) = e^{-i\Theta} f'(a^+)$, is satisfied for derivatives along the contour for all $f \in D(H)$. We also assume that the potential $V(x)$ has a compact support with a "radius" smaller than a, so that non-analytic potentials can be considered.

We consider the Hamiltonian H to act on functions living on a complex contour $\mathcal{C}$, where the contour follows the real axis in the vicinity of the atom, and then deviates from the real axis far from the origin. To select the space of outgoing wavefunctions, the contour departs into the upper complex plane as $x \to \infty$. The shape of this contour is inconsequential, except its property that it approaches infinity in the sector of the complex plain in which all outgoing waves, and in particular the resonant states, decay exponentially. One possible example utilizing a piece-wise linear path is shown in Fig. 4.1. At the far end of the contour, outgoing wavefunctions that behave as $\sim e^{ikx} \to e^{-kIm\{z\}}$ (with positive k) decay exponentially. Thus, the introduction of the contour is in the spirit of the external complex scaling.

The differential expression H acting in the space of functions defined along the contour results in a non-Hermitian operator that represents an open system. A c-product defined as a contour integral

$$\langle\phi|\psi\rangle \stackrel{\text{def}}{=} \int_{\mathcal{C}} \phi(z)\psi(z)\mathrm{d}z \tag{4.2}$$

is the tool that replaces the standard scalar product in working with non-self-adjoint operators. A formal argument can be made that if two resonant states belong to two different eigenvalues, then they are orthogonal w.r.t. the above c-product [103], and the latter can serve as a definition for a pseudo-norm in resonant states. We aim to avoid any reliance on formal operator properties. Instead, we show by explicit calculation of the underlying contour integrals that the following orthogonality relation holds for outgoing Stark resonances

$$\langle\psi_n|\psi_k\rangle \stackrel{\text{def}}{=} \int_{\mathcal{C}} \psi_n(z,F)\psi_k(z,F)\mathrm{d}z = N_n^2(F)\delta_{nk}. \tag{4.3}$$

In particular, we verify the orthogonality of different functions ($n \neq k$), and we evaluate the normalization factor $N_n(F)$ explicitly for two exactly solvable models.

We assume that the potential $V(x)$ has a compact support contained in $(-d,+d)$. Thus, the asymptotic form of both the conventional and resonant wavefunctions can be obtained as a combination of Airy functions, $c_1 Ai + c_2 Bi$. The requirement that the solutions are regular for $x \to -\infty$ dictates $c_2 = 0$. For $x > 0$ one can use combinations $Ci^{\pm}(x) = Bi(x) \pm iAi(x)$ which behave as outgoing $(+)$ and incoming $(-)$ waves at $x \to \infty$. Representation of the eigenstates of the original H (i.e. the one that acts on the real axis) which is particularly suitable for our purposes can be written as

$$\psi_E(x) = \begin{cases} \frac{-2Ai[\alpha(x+E/F)]}{U\sqrt{D^+(E)D^-(E)}} & x < -d \\ \frac{i}{U}\sqrt{\frac{D^-(E)}{D^+(E)}}Ci^+[\alpha(x+E/F)] - \frac{i}{U}\sqrt{\frac{D^+(E)}{D^-(E)}}Ci^-[\alpha(x+E/F)] & x > +d \end{cases} \tag{4.4}$$

where $\alpha = -(2F)^{1/3}$, U is the normalization factor, and $D^{\pm}(E)$ are sought expressions representing the eigenvalue equations for outgoing $(+)$ and incoming $(-)$ wavefunctions. The fact that the original operator (i.e. the one acting on the real axis) is self-adjoint guarantees that the above states can be normalized to a delta-function in energy,

$$\int_{-\infty}^{\infty} \psi_E^*(x)\psi_{E'}(x)dx = \delta(E-E'). \tag{4.5}$$

It is sufficient to examine the asymptotic behavior of these states (4.4) to verify that this normalization is obtained with $U = 2^{2/3}F^{1/6}$. While a particular normalization is not crucial for us, the above form of eigenstates allows us to infer the form of the

resonant wavefunctions sought below in the two exactly solvable systems (Section 4.4.1 and 4.4.2). To obtain the remaining portion(s) of energy eigenstates, one has to "fill in" the wavefunction in the central region of $-d$ to d, and in doing so satisfy whatever conditions a given potential imposes on them. In both cases treated here, this means to find functions that are continuous and to require continuity of derivatives in the square-well case, and a "cusp condition" in the Dirac-delta case. This procedure reveals the concrete form of expressions $D^{\pm}(E)$ for a given $V(x)$. The asymptotic form of the energy eigenstates as shown in (4.4) indicates the form of the resonant wavefunctions. For example if we find a complex-energy root of $D^{+}(E) = 0$ the incoming part of the wavefunction Ci^{-} will be eliminated. At the same time a pole will appear in the projection onto the outgoing wavefunction. This tells us that the resonance behaves as Ai and Ci^{+} for large negative and positive x, respectively. Given that we know the general form of the eigenstates will be sums of airy functions, we are able to establish formulas for normalization, and to verify the orthogonality relation (4.3) by making use of the formula (VS 3.50) in Vallée & Soares [104] which gives a primitive (antiderivative) function for a square of arbitrary combination of Airy functions. Likewise, to verify the mutual orthogonality w.r.t. (4.3) for different resonant states, we use the formula (VS 3.53), together with the fact that the complex energies satisfy the eigenvalue equation(s) allowing us to use D to simplify expressions.

4.3 Time evolution

Let us now use these resonant states as a basis and evolve them using Schrödinger's equation. If we represent a particular quantum state Ψ as a sum over resonant states, plus a "background,"

$$\Psi(x,t) = \sum_n c_n(t)\psi_n(x, F(t)) + \psi_B(x,t) \tag{4.6}$$

and ask what is its evolution due to the time-dependent field $F(t)$, then we can find a system of equations describing the evolution of coefficients c_n with the help of orthogonality relation (4.3)

$$c_n'(t) = -ic_n(t)E_n(F(t)) + \sum_k c_k(t)F'(t)\left\langle \partial_F \psi_n | \psi_k \right\rangle, \tag{4.7}$$

where $F'(t)$ is the time derivative of the electric field. Here we have assumed that the expansion states ψ_n are slaved to the time-dependent field, and are normalized to unity, $\langle \psi_m(F(t)) | \psi_n(F(t)) \rangle = \delta_{mn}$, at all times. Here we neglect the coupling to the "background" ψ_B which originates from the continuum contribution contained in various resonant-state expansions. We have found that for systems initially in the ground state, the temporal decay of resonant states represents ionization and that the

flow of probability out of the space spanned by $\{\psi_k\}$ manifests itself as the increase of the norm $||\psi_B||$. With this approach, we have seen that even using a single state, such as the resonance originating from the ground state, is very good approximation to the 1D Dirac-delta model's exact solution.

Equation (4.7) identifies the quantities that we aim to calculate. First, we need the complex-valued energies E_n. Second, we require normalization and a orthogonality relation (4.3) to be satisfied by all resonant states. To evaluate the induced polarization, we also need the generalized dipole moments

$$d_{nk} = \langle\psi_n|x|\psi_k\rangle = \int_{\mathcal{C}} \psi_n(z,F) z \psi_k(z,F) \mathrm{d}z, \tag{4.8}$$

and lastly we must calculate the coupling terms $\langle\partial_F\psi_n|\psi_k\rangle$, which describe the change of the resonant-state basis as it evolves slaved to the external field. The coupling terms can be related to the dipole moment matrix elements with the help of the following argument utilizing the parametric dependence of the Hamiltonian on F [105, 106]:

$$\partial_F \langle\psi_n| H(F) |\psi_k\rangle = (\partial_F E)\delta_{nk} = -(E_n - E_k)\langle\partial_F\psi_n|\psi_k\rangle - \langle\psi_n| x |\psi_k\rangle . \tag{4.9}$$

Moreover, for the normalized resonances the coupling terms are anti-symmetric in indices n, k, since $\partial_F\delta_{nk} = \partial_F \langle\psi_n|\psi_k\rangle = \langle\partial_F\psi_n|\psi_k\rangle + \langle\psi_n|\partial_F\psi_k\rangle = 0$. This means that we have $\langle\partial_F\psi_n|\psi_k\rangle = -\langle\psi_n|\partial_F\psi_k\rangle$ and for $n = k$ the self-coupling vanishes $\langle\partial_F\psi_k|\psi_k\rangle = 0$ as a consequence of the c-product symmetry. Thus, the evolution system (4.7) can be alternatively written with the substitution

$$\langle\partial_F\psi_n|\psi_k\rangle = \begin{cases} 0 & n = k \\ -\langle\psi_n| x |\psi_k\rangle / (E_n - E_k) & n \neq k \end{cases} \tag{4.10}$$

We should be careful to verify the relations in this section and not just rely on the formal derivation. For example we do not have a precise definition of the adjoint here. Instead we have used a c-product, which may not be strictly the same as its Hermitian counterpart. Therefore it is not a priori clear that these derivations are justified. That is why we do not want to rely on the relations until we work out some of them directly, by solving these quantities for two exactly solvable systems. Next we present explicit calculations of the quantities necessary for time evolution of resonant state systems for two instances of the potential V. The first is for the 1D Dirac-delta function potential and the second is for the 1D square well potential. Many of the integrals that we encounter are not found in published literature. We therefore developed a new integration technique (detailed in Appendix A) that will allow us to rewrite the unknown integrals in terms of known ones. This technique was the key in our ability to rigorously show that the formal relations in this section were indeed correct.

4.4 Exact results

4.4.1 1D Dirac-delta potential

In this section we present the explicit equations needed to perform time evolution of a resonance system with the 1D Dirac-delta potential. Many of the intermediate steps of the calculations have been omitted, therefore a more detailed derivation is presented in Appendix C.

We begin by assuming the unnormalized wavefunction ansatz for an outgoing resonance in the form

$$g(x,F) = \begin{cases} Ci(\alpha\beta)Ai[\alpha(x+\beta)] & x<0 \\ Ai(\alpha\beta)Ci[\alpha(x+\beta)] & x>0 \end{cases} \tag{4.11}$$

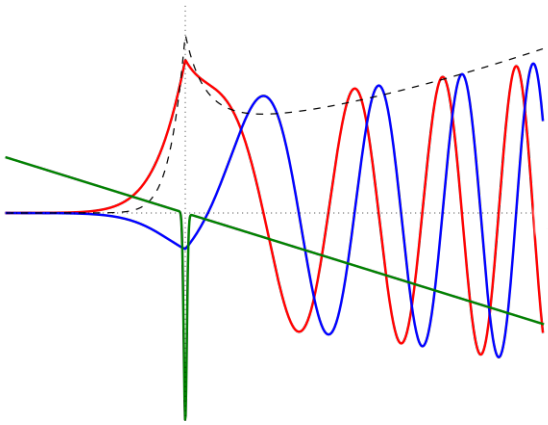

FIGURE 4.2. Spatial representation of an outgoing resonance wavefunction (red is real part, blue is imaginary part, dashed is norm) for the 1D Dirac-delta potential in the presence of an external field (green). Note that the cusp boundary conditions are satisfied at $x = 0$ and also the outgoing wave-like feature for $x > 0$.

The Dirac-delta potential is defined as $V(x) = -B\delta(x)$, where B is the depth of the potential, and the eigenstate representations (4.4) are valid with $d = 0$. The delta function potential imposes a boundary condition on the wavefunction's value and derivative

$$\frac{d\psi(0^+)}{dx} - \frac{d\psi'(0^-)}{dx} = -2B\psi(0). \tag{4.12}$$

This "cusp condition," when applied to the above eigenstate parameterization leads directly to the well-known [51] expression for the eigenvalue equation for resonant

energies:

$$D^{\pm}(E) \equiv 1 - \frac{2\pi B}{(2F)^{1/3}} Ai\left(\frac{-2E}{(2F)^{2/3}}\right) Ci^{\pm}\left(\frac{-2E}{(2F)^{2/3}}\right). \tag{4.13}$$

Complex-valued solutions to $D^{+}(E) = 0$ determine the resonant energies of the outgoing Stark functions that we plot in Figure 4.3.

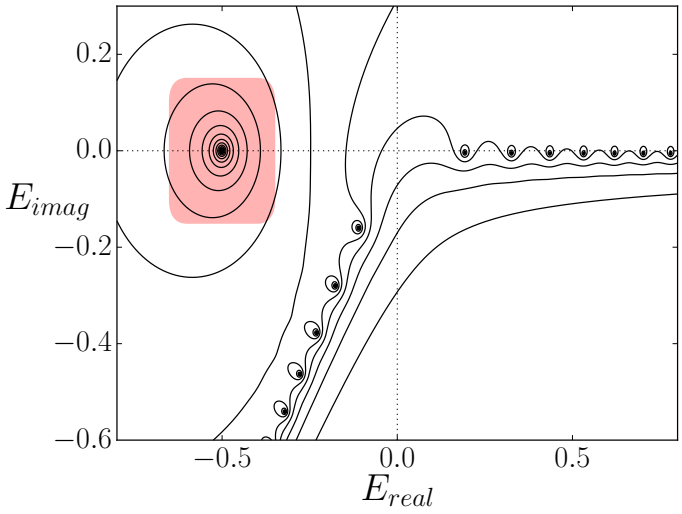

FIGURE 4.3. Outgoing resonance eigenvalue equation landscapes, based on Equation (4.13), for 1D Dirac-delta potential with $B = 1$ in the external field $F = 0.03$. We have highlighted the resonance that arises from the field-free ground state in red. There exists two other families of resonances: a fast decaying set along the angle $-2\pi/3$, and a longer living family originating from continuum states close to the positive real axis. To visualize the locations of the energy eigenvalues, we evaluate (4.13) over a range of E in the complex plane, and convert $|D|$ to a height map via the formula $(1 - (1 + |D|^{0.3})^{-1} + \epsilon)^{-1}$, so that its roots are represented by poles that are easy to locate ($\epsilon \approx 0.1$).

To calculate the contour integral(s), the corresponding primitive functions are evaluated at points of discontinuities of the potential, as well as at both ends of the contour, and this is where the choice of the contour is important. The resonant wavefunctions decay exponentially for $x \to -\infty$, and the corresponding boundary terms vanish. On the other side of the contour, the asymptotic behavior of the primitive function is dominated by

$$Ci^{+}[\alpha(z+\beta)] \approx \frac{e^{-i\pi/4} \exp\left[+i\frac{2}{3}[-\alpha(z+\beta)]^{3/2}\right]}{\sqrt{\pi}[-\alpha(z+\beta)]^{1/4}} \tag{4.14}$$

where $\alpha = -(2F)^{1/3}$, $\beta = E_n/F$, and E_n is a root of the eigenvalue equation. It is straightforward to verify that asymptotically along the contour, where $z \sim \rho e^{i\Theta}$,

this function decays for arbitrary fixed β as $\rho \to \infty$. Thus, the boundary terms brought by this end of the contour also vanish. Moreover, since the integrands are in all cases entire functions (containing no singular points), the precise shape of the integration path does not affect the outcome. As a result, in any piece-wise constant atomic potential $V(x)$ it is only the special points of $V(x)$ that give rise to non-zero contribution(s).

Thus, direct integration along the contour, followed by simplifications making use of the eigenvalue equation and the Wronskian for Airy functions yields the following normalization factor for the Stark resonance in the Dirac-delta model

$$N^2 = \frac{Ai(\alpha\beta)Ci'(\alpha\beta) + Ai'(\alpha\beta)Ci(\alpha\beta)}{\alpha\pi} = \frac{1}{\alpha\pi}\left[\psi'(x=0^+) + \psi'(x=0^-)\right]. \quad (4.15)$$

Next we calculate the generalized dipole matrix elements, both diagonal and off-diagonal. Expressed with the help of unnormalized resonance eigenfunctions $g[\alpha(x+\beta_{m,n})]$, the contour integrals that we need to evaluate is

$$\langle\psi_m|\, x\, |\psi_n\rangle = \frac{1}{N_n^2}\int_{\mathcal{C}} g[\alpha(x+\beta_m)]\, z\, g[\alpha(x+\beta_n)]\; dz. \quad (4.16)$$

Note that these quantities differ from their Hermitian counterparts as there is no complex conjugation in the integrand, and the result is complex-valued [97]. Here we assume that the contour $\mathcal{C}$ is chosen such that it only starts to deviate from the real axis for $x > d$, i.e. outside of the potential support. For both the delta-potential model and for the square-well potential system, we integrate over each distinct interval of constant potential V making use of the formula (VS 3.51). As the shape of the contour ensures vanishing contributions from its ends, one only needs to evaluate the primitive functions at $x = 0$ for Dirac-delta and $x = \pm d$ for the square well system.

For the diagonal matrix element in the Dirac-delta potential model, we obtain the following expression in terms of Airy functions

$$\begin{aligned}\langle\psi_n|\, x\, |\psi_n\rangle_D = \frac{1}{N_n^2}\frac{Ai(\alpha\beta_n)Ci(\alpha\beta_n)}{3\alpha^2} \times [Ai'(\alpha\beta_n)Ci(\alpha\beta_n) - Ai(\alpha\beta_n)Ci'(\alpha\beta_n)] \\ + \frac{2E}{3FN_n^2}\underbrace{\frac{1}{\alpha}\left[(Ai'(\alpha\beta_n)Ci(\alpha\beta_n))^2 (Ai(\alpha\beta_n)Ci'(\alpha\beta_n))^2\right]}_{-N_n^2}. \quad (4.17)\end{aligned}$$

This result can be further simplified using the formula for the normalization factor N^2 together with the eigenvalue equation (4.13), and is found to be related to the change in the eigenvalue w.r.t. the field F:

$$\langle\psi_n|\, x\, |\psi_n\rangle_D = \frac{1}{6\pi^2\alpha B N_n^2} - \frac{2E}{3F} = -\partial_F E_n, \quad (4.18)$$

where the second equality can be verified by differentiating the eigenvalue equation (4.13) with respect to F.

For the off diagonal dipole matrix elements, we use (VS 3.54). Utilizing $C_{n,k} = Ci(\alpha\beta_{n,k})$ and $A_{n,k} = Ai(\alpha\beta_{n,k})$ to shorten the notation, we find that

$$\begin{aligned}\langle\psi_n|\, x\,|\psi_k\rangle_D = \frac{1}{N_n N_k}\frac{2}{\alpha^5(\beta_n-\beta_k)^3}\big[&C_nC_kA_n'A_k - C_nC_kA_nA_k' \\ &- A_nA_kC_n'C_k + A_nA_kC_nC_k'\big] \\ +\frac{1}{N_nN_k}\frac{2}{\alpha^4(\beta_n-\beta_k)^2}\big[&C_nC_kA_n'A_k' - A_nA_kC_n'C_k'\big].\end{aligned} \tag{4.19}$$

Grouping terms in order to identify Wronskians allows us to simplify the expression down to

$$\langle\psi_n|\, x\,|\psi_k\rangle_D = \frac{F}{2(E_n-E_k)^2}\left[\frac{N_n}{N_k}+\frac{N_k}{N_n}\right], \tag{4.20}$$

which in turn can be written solely in terms of the wavefunction properties at $x=0$

$$\langle\psi_n|\, x\,|\psi_k\rangle_D = \frac{-F}{\alpha(E_n-E_k)^2}\left[\psi_n'(0^-)\psi_k'(0^-) - \psi_n'(0^+)\psi_k'(0^+)\right] \tag{4.21}$$

with ψ' standing for the derivative of the *normalized* Stark wavefunction.

We now turn our attention to the terms $\langle\partial_F\psi_n|\psi_k\rangle$ identified in (4.7). These quantities mediate the connections between Stark resonances of a given system at different values of the field F, and we call them accordingly coupling terms. They are needed to describe the evolution of the system in a time-dependent $F(t)$. Instead of trusting the formally derived relation (4.10), we compute these quantities through direct integration. Thus, our result can be also interpreted as a direct verification of (4.10) for two model systems. Moreover, the procedure and the particular representation of the results lead us to a generalization for arbitrary one-dimensional systems with short-range potentials.

To calculate the coupling terms, we first differentiate the wavefunction w.r.t. the field F and then integrate

$$\int_{-\infty}^{\infty}(\partial_F\psi_n)\psi_k dx = \frac{1}{N_nN_k}\int_{-\infty}^{\infty}(\partial_F g_n)g_k dx - \frac{(\partial_F N_n)}{N_n}\underbrace{\int_{-\infty}^{\infty}\psi_n\psi_k dx}_{\delta_{nk}}. \tag{4.22}$$

It is clear that the diagonal ($n=k$) coupling terms between normalized states vanish, and we only need to calculate off diagonal elements and therefore can disregard the second term, leaving only the integral $\langle\partial_F g_n|g_k\rangle$. For the model with the Dirac-delta

potential, the integral is

$$\begin{aligned}
\langle \partial_F g_n | g_k \rangle_D = \Delta C_n' C_k \int_{-\infty}^{0} Ai[\alpha(x+\beta_n)] Ai[\alpha(x+\beta_k)] dx \\
+\Delta A_n' A_k \int_{0}^{\infty} Ci[\alpha(x+\beta_n)] Ci[\alpha(x+\beta_k)] dx \\
+\Delta C_n C_k \int_{-\infty}^{0} Ai'[\alpha(x+\beta_n)] Ai[\alpha(x+\beta_k)] dx \\
+\Delta A_n A_k \int_{0}^{\infty} Ci'[\alpha(x+\beta_n)] Ci[\alpha(x+\beta_k)] dx \\
-\frac{2}{3\alpha^2} C_n C_k \int_{-\infty}^{0} x Ai'[\alpha(x+\beta_n)] Ai[\alpha(x+\beta_k)] dx \\
-\frac{2}{3\alpha^2} A_n A_k \int_{0}^{\infty} x Ci'[\alpha(x+\beta_n)] Ci[\alpha(x+\beta_k)] dx
\end{aligned} \tag{4.23}$$

where $\Delta = 1/(3\pi^2\alpha^3 B N^2)$, and A_k, B_k, C_k stand for the corresponding Airy functions or their combinations evaluated at $\alpha\beta_k$ (i.e. at $x = 0$).

The above integrals contain terms of two kinds. The first group can be evaluated making use of known, previously published Airy integrals. These have the form $\int_a^b ABdx$, where A, B are a linear combination of Airy functions with arguments $\alpha(x+\beta)$, where β is different in A and B. Thus, the first two lines in (4.23) can be dealt with, although it requires lengthy computations. Then there are integrals of the type $\int_a^b A'Bdx$ and $\int_a^b xA'Bdx$. No known formulas are available for these, and we have developed a new integration technique that we outline in Appendix A. As a result, an analytic solution for $\langle \partial_F g_n | g_k \rangle_D$ can be obtained.

We proceed by simplifying the individual integrals on the RHS of (4.23) pairwise. The first pair is calculated using (VS 3.53), while the last two pairs will use the identities found in Appendix A. The intermediate expression reads

$$\begin{aligned}
\langle \partial_F g_n | g_k \rangle_D = \frac{\Delta}{\alpha^2(\beta_n - \beta_k)} \Big[A_n' A_k C_n C_k' - A_n A_k' C_n' C_k \Big] \\
- \frac{\Delta}{\alpha^2(\beta_n - \beta_k)} \Big[A_n' A_k' C_n C_k - A_n A_k C_n' C_k' \Big] \\
- \frac{2}{3\pi\alpha^5} \frac{1}{(\beta_n - \beta_k)^2} \Big[\beta_n C_n A_n - \beta_k C_k A_k \Big] \\
- \frac{4}{\alpha^7} \frac{1}{(\beta_n - \beta_k)^3} \Big[A_n' C_n A_k' C_k - A_n C_n' A_k C_k' \Big]
\end{aligned} \tag{4.24}$$

The first two lines can be simplified using the Wronskian and normalization factors, while the third can be rewritten with the help of the eigenvalue equation. Combining

these shows that the first three lines sum up to zero, leaving only the last term which we write in terms of derivatives of the wavefunctions at the origin

$$\langle \partial_F \psi_n | \psi_k \rangle_D = \frac{F}{\alpha \left(E_n - E_k\right)^3} \left[\psi_n'(0^-)\psi_k'(0^-) - \psi_n'(0^+)\psi_k'(0^+) \right]. \tag{4.25}$$

Comparing this expression to (4.21), it is clear that the relation between coupling term and off diagonal dipole matrix elements (4.10) is valid.

4.4.2 1D square well potential

We now turn out attention to a system that is similar to the 1D Dirac-delta function model, but due to its finite width potential allows for the inclusion of multiple bound states. The hope is that this system will be useful for investigating what role addition bound states play in the ionization dynamics. As in the previous section, many intermediate steps have been omitted. A more detailed derivation is presented in Appendix D. For a system with a square-well potential of width $2d$, and depth V_0, the unnormalized wavefunctions are

$$g(x,F) = \begin{cases} \kappa_0 Ai[\alpha(x+\beta)] & x < -d \\ \kappa_1 Ai[\alpha(x+\beta')] + \kappa_2 Bi[\alpha(x+\beta')] & -d < x < d \\ \kappa_3 Ci[\alpha(x+\beta)] & x > +d \end{cases} \tag{4.26}$$

with coefficients κ_i to be fixed to ensure continuity of wavefunction value and derivative across well boundaries. For these function to become resonant states the energies in $\beta = E/F$ and $\beta' = (E - V_0)/F$ must be solutions to the eigenvalue equation(s) we present next.

It is a much longer calculations to obtain the eigenvalue equation equation [107, 108] for the square-well potential compared to the delta function potential, but it is essentially the same procedure. One needs to connect the outer regions with a linear combination of Airy functions (4.26), and eliminate the unknown coefficients. The result reads

$$D^{\pm}(E) \equiv (A_0 A_1' - A_0' A_1)(B_2 C_3' - B_2' C_3) - (A_0 B_1' - A_0' B_1)(A_2 C_3' - A_2' C_3) \tag{4.27}$$

where we utilized shorthand notations to compress the otherwise long expression. A, B, and C stand for the corresponding Airy functions, and primes denote derivatives. For a well with depth V_0 and half-width d, the subscripts indicate on which sides of the well walls the arguments of the functions are evaluated, with $0, 1, 2, 3$ representing $\alpha(x+\beta)$ at $x = -d-\epsilon, -d+\epsilon, +d-\epsilon$ and $x = +d+\epsilon$, respectively, and $\beta = E/F$ for outside, and $\beta = (E - V_0)/F$ inside the well. Thus, the subscripts 0 and 1 represent Airy functions evaluated just outside and inside the left boundary of the well, while subscripts 2 and 3 represent arguments at the right boundary of the well.

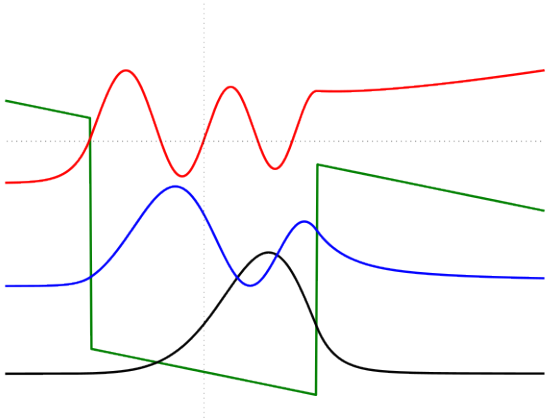

FIGURE 4.4. Here we plot the spatial representation of the norms of outgoing resonant wavefunctions (black, blue and red) for a square well potential (green) with a constant external field F. Note that there are multiple bound states, unlike the delta potential which supports only a single bound state.

The main differing feature is the possibility of multiple bound states (in Figure 4.5, highlighted in red) in the square-well potential, while the Dirac-delta system only supports a single bound state. However, there exist two other infinite families of resonances, just as was the case for the delta potential. The "right" family has eigenvalues located along the real axis and corresponds to longer living states, while the "left" family, with energies along the ray $\arg(z) = -2\pi/3$, are fast decaying, short-lived states. This resonance structure is most likely a generic feature at least in case of short-ranged attractive potentials.

To calculate the normalization factor for the square-well system, a similar but more complicated procedure to evaluate (4.3) using formula (VS 3.50) results in a surprisingly simple expression:

$$\begin{aligned} N^2 &= \frac{V_0}{F}\left[(A_2C_3' - A_2'C_3)^2A_0^2 - (A_0'A_1 - A_0A_1')^2C_3^2\right] \\ &= \frac{V_0}{F}\left[\psi(x=-d)^2 - \psi(x=d)^2\right]. \end{aligned} \tag{4.28}$$

Let us proceed with the dipole matrix calculations for the square well potential. The matrix elements can be found by again making use of (VS 3.51) and (VS 3.54). Thanks to the continuity properties of the wavefunction, many terms that arise in

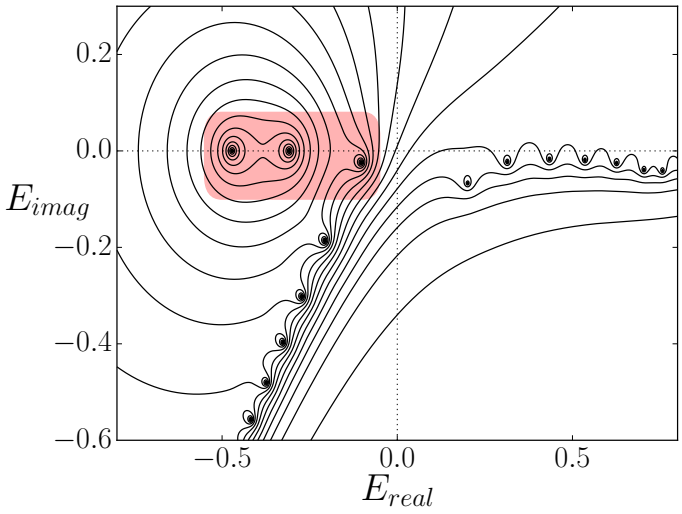

FIGURE 4.5. Outgoing resonance eigenvalue equation landscapes for square-well potential with $d = 4$ and $V_0 = -0.5$ in the external field $F = 0.03$. Note the existence of multiple bound states highlighted in red.

the course of this calculation cancel, and the resulting diagonal terms are

$$\begin{aligned}\langle\psi_n|\, x\, |\psi_n\rangle_S = &\frac{V_0}{3F}\left[(d-4\beta)\psi(-d)^2 + (d+4\beta)\psi(d)^2\right] \\ &+ \frac{2V_0^2}{3F^2}\left[\psi(-d)^2 - \psi(d)^2\right] \\ &+ \frac{2V_0}{3F\alpha}\left[\psi'(-d)^2 - \psi'(d)^2\right]\end{aligned} \tag{4.29}$$

which is simplified further using the normalization factor (as was done in the delta model calculations) to

$$\langle\psi_n|\, x\, |\psi_n\rangle_S = \frac{2V_0 - 4E_n}{3F} + \frac{V_0 d}{3F}\left[\psi(-d)^2 + \psi(d)^2\right] + \frac{2V_0}{3\alpha F}\left[\psi'(-d)^2 - \psi'(d)^2\right]. \tag{4.30}$$

It can be checked numerically that the these diagonal elements are also equal to $-\partial_F E_n$, just as in the delta potential model. Unfortunately up to this point we have not derived this expression directly by taking the derivative of the square well's eigenvalue equation w.r.t. the field F and simplifying. The equations are simply too large.

Now we calculate the off-diagonal elements. When using (VS 3.54), taking into account continuity of the wavefunction allows us to ignore terms that do not involve an x and the sum $\beta_n + \beta_k$. Since every other term cancels, the resulting equation is

surprisingly simple:

$$\langle\psi_n|\, x\, |\psi_k\rangle_S = \frac{V_0}{(E_n - E_k)^2}\left[\psi_n(-d)\psi_k(-d) - \psi_n(d)\psi_k(d)\right]. \tag{4.31}$$

One should note the similarity with its counterpart formula for the Dirac-delta model (4.21). We thus arrive at the conclusion that all dipole matrix elements can be expressed in simple formulas which only depend on the values of the wavefunctions (and their derivatives) at the special points given that characterize the potential. It will be interesting to see if these results can be generalized for arbitrary systems with piecewise constant potentials.

For the coupling term, we have a combination of integrals involving Airy functions and their derivatives, similar to what was seen in the delta model, namely

$$\begin{aligned}
\langle\partial_F g_n|g_k\rangle_S = &\int_{-\infty}^{-d} \kappa_0'\gamma_0 Ai[\alpha(x+\beta_n)]Ai[\alpha(x+\beta_k)]dx \\
&+ \int_{-d}^{d} (\kappa_1' Ai[\alpha(x+\beta_n)] + \kappa_2' Bi[\alpha(x+\beta_n)]) \\
&\qquad \times (\gamma_1 Ai[\alpha(x+\beta_k)] + \gamma_2 Bi[\alpha(x+\beta_k)])dx \\
&+ \int_{d}^{\infty} \kappa_3'\gamma_3 Ci[\alpha(x+\beta_n)]Ci[\alpha(x+\beta_k)]dx \\
&+ \frac{\alpha}{3F}\int_{-\infty}^{\infty} (3E_n' + x - 2\beta_n) g'[\alpha(x+\beta_n)]g[\alpha(x+\beta_k)]dx \\
&+ \frac{2\alpha V_0}{3F^2}\int_{-d}^{d} g'[\alpha(x+\beta_n)]g[\alpha(x+\beta_k)]dx
\end{aligned} \tag{4.32}$$

where γ and κ are the coefficients that guarantee continuity of g_n and g_k, respectively, at the well boundaries. These factors are expressed in terms of Airy functions, and depend on F through α, β_n and β_k. Their primed notations represent derivatives w.r.t. to F. Using the shorthand notation, it is easier to see the structure of the integrals:

$$\begin{aligned}
\langle\partial_F g_n|g_k\rangle_S = &\int_{-\infty}^{-d} (\partial_F\kappa_0)\gamma_0 A_n A_k dx \\
&+ \int_{-d}^{d} [(\partial_F\kappa_1)A_n + (\partial_F\kappa_2)B_n][\gamma_1 A_k + \gamma_2 B_k]dx \\
&+ \int_{d}^{\infty} (\partial_F\kappa_3)\gamma_3 C_n C_k dx \\
&+ \frac{\alpha}{3F}\int_{-\infty}^{\infty} (3E_n' + x - 2\beta_n) g_n' g_k dx \\
&+ \frac{2\alpha V_0}{3F^2}\int_{-d}^{d} g_n' g_k dx.
\end{aligned} \tag{4.33}$$

Coupling terms (4.33) for the square-well system can also be calculated in analytic form, but due to excessive number of terms comprising the result they are not listed here. In principle, a similar procedure to simplify the square-well coupling term (4.33) should work. However, the resulting expression is extremely large and we could not find a practical way to compress it to a manageable length. The main difficulty in simplifying the square well result is that the eigenvalue equation is much more complicated than the delta system (compare (4.13) to (4.27)). Nevertheless, having explicit formulas in terms of Airy functions, we verified numerically that the integrated result does relate to the dipole matrix element as suggested by (4.10):

$$\langle \partial_F \psi_n | \psi_k \rangle_S = \frac{-V_0}{(E_n - E_k)^3} \left[\psi_n(-d)\psi_k(-d) - \psi_n(d)\psi_k(d) \right]. \tag{4.34}$$

Explicit equations for all quantities necessary to perform a TDSE simulation using the delta and square well resonant states as a basis have been shown.

4.5 Generalizations

Comparing equations for the square well norm (4.28) and off diagonal dipole elements (4.31) we see that they have a similar form, with wavefunction values evaluated at discontinuities of the potential V. While the same result can be easily written explicitly with Airy functions, this particular form indicates that the expressions are in fact sums over atomic potential discontinuities, with weights corresponding to the potential-value jumps. This suggests the following generalization of the normalization and dipole matrix element formulas for a system with an arbitrary piecewise constant potential:

$$N^2 = \sum_i \frac{\Delta V_i}{F} \psi(x_i)^2 \tag{4.35}$$

and

$$\langle \psi_n | \, x \, | \psi_k \rangle_S = \frac{1}{(E_n - E_k)^2} \sum_i \Delta V_i \psi_n(x_i) \psi_k(x_i) \tag{4.36}$$

where the sums contain all potential discontinuities. It is in fact not too difficult to realize that the procedures utilized above can be modified for a more general case of potential shape as shown in Figure 4.6. From there, one can take a continuum limit, approximating an arbitrary potential as a limit of piecewise constant functions, and arrive at

$$N^2 = \frac{1}{F} \int \frac{dV}{dx} \psi(x_i)^2 dx \tag{4.37}$$

and

$$\langle \psi_n | \, x \, | \psi_k \rangle = \frac{1}{(E_n - E_k)^2} \int \frac{dV}{dx} \psi_n(x) \psi_k(x) dx. \tag{4.38}$$

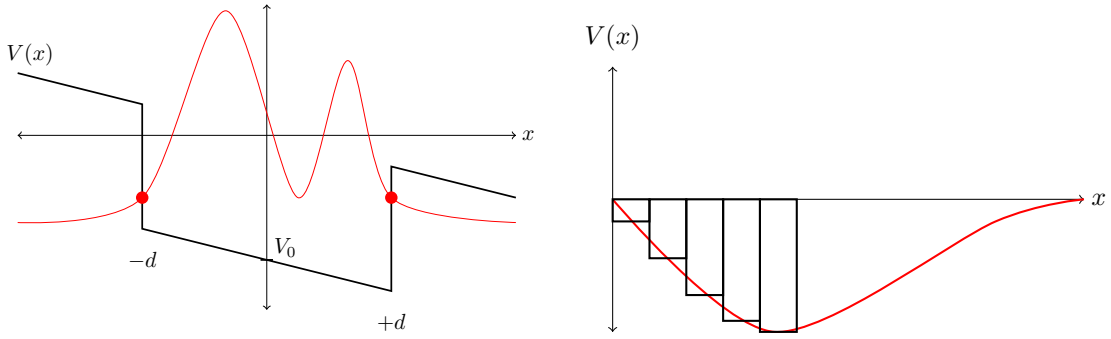

FIGURE 4.6. (Left) We see for the square well that quantities such as norm and dipole matrix elements can be represented in terms of wavefunctions evaluated at discontinuities in the potential. (Right) We can picture that it is possible to extend these relations to more general potential shapes, by viewing them as a sum of square wells.

We have assumed that the potential is short-range and the integration in these formulas is along the real axis (i.e. the contour $\mathcal{C}$ is not necessary for convergence).

This is an intriguing result, because an identical formula can be derived for the discrete energy eigenstates of a self-adjoint Hamiltonian by evaluating its double commutator with the position operator. However, here we have Stark resonances represented by complex-valued functions living on the contour $\mathcal{C}$. So it seems that as long as the normalization and "scalar product" are defined with the help of pairing (4.3), the Stark resonant states satisfy relations analogous to those obeyed by their self-adjoint counterparts.

We have seen in simulation that the relation between the Stark resonance pseudonorm and the generalized expectation value of the "atomic" potential gradient could be valid for three-dimensional systems also. It is tempting to speculate that the off-diagonal dipole element relation (4.38) could be generally valid for Stark resonant states in three dimensions.

4.6 Completeness

In this section we want to tackle the problem of completeness of the 1D delta potential model's resonant states. If the resonant states can serve as a complete set of basis functions, then we can represent any arbitrary wavefunction as a sum of resonant states. We ask if it is possible to represent a physical wavefunction, or perhaps only a portion of it, as a series in resonant states, such as in the formal theory laid out in Section 4.3 where we showed a sum of resonant states under Schrödinger evolution.

We are motivated to ask this question since it has been shown in several cases that resonant states can in fact provide an extremely efficient "vehicle" to describe

the dynamics in a physical system. For example, Tolstikhin et al. have shown that in the adiabatic regime, the whole dynamic of a strongly driven quantum system can be represented by a single resonant state [109, 110]. Perhaps the most complete example of resonant state expansion in an initial value quantum problem has been given for decay in systems with short-range potentials [92, 111]. We also have proposed how Stark resonances can be used to describe nonlinear light-matter interactions [83] and will give more detail in the following chapters.

The problem of determining completeness has several facets, with the first being how the coefficients of the expansion can be calculated. The second, having obtained the expansion coefficients, is the resulting series actually convergent? Finally, what is the space of functions that admit such resonant state expansions? In addition one can ask if such representations, where and when they exist, could be used as tools to describe the time-dependent quantum-mechanical evolution. Unlike in the case of Hermitian Hamiltonians, these are difficult questions to answer. In fact, very little is known in general, and there are only isolated examples of such expansions. Here we show that while an expansion into resonant states for the 1D delta potential works only for functions define on the negative axis ($x < 0$), the overlap with the potential is still fully captured with the resonance series. We believe that this property can be generalized to piecewise constant potentials and show that resonant series convergence including the support of the potential.

Despite these difficulties, we see it worthy to tackle such a problem since it is now possible due only to our development of formal theory and 1D delta example laid out earlier in this chapter.

4.6.1 Numerically evaluating coefficients

Here again is how we expand an arbitrary wavefunction Ψ in terms of resonant states ψ_n along with a background wavefunction ψ_B

$$\Psi(x,t) = \sum_n c_n(t)\psi_n(x, F(t)) + \psi_B(x,t).$$

The background wavefunction ψ_B is necessary if the resonant states are not complete in the usually quantum mechanical sense, and helps "fill in" the space of functions that cannot be represented by resonant states alone. Also keep in mind that we want the background wavefunction to not interact with the potential so that it can represent the free electron plasma in our medium model.

We begin by attempting to calculate the coefficients c_n in the resonant state expansion. This illustration will help clarify what we try and do before we jump into the more difficult math to prove convergence of the states. As a rule, numerical simulations of the time-dependent Schrödinger equation implement some kind of transparent boundary conditions, especially when the modeled system is exposed to an external field which causes ionization. Here we simulate the system on the contour $\mathcal{C}$ that

will play the role of the spatial axis (see Figure 4.1). Such an approach does two things. First, replacing the real axis by $\mathcal{C}$ gives a particularly effective realization of transparent boundary conditions (we refer the reader to [112] for details of numerical implementation). Second, this "complexification" of the equation restricts the simulation to the function space with outgoing-wave behavior at the edge of the computational domain. The resulting open system constitutes a natural test-bed for the hypothesis that the Stark resonant states can form a basis.

In principle, any function could be used as "test target." However, it is most likely easier to obtain resonant-state expansion for a function that is a product of temporal evolution in the system. This is why we have performed a number of different simulations to create test wavefunctions that were subsequently expanded into resonant states. This section is to illustrate the general behavior of such approximations.

We initialize the system with a localized, Gaussian packet solution in the region $x < 0$, switch on the external field to a constant value, and let the system evolve for a short period of time. The result of the evolution is in general a wavefunction with a support that extends into $x > 0$, and nicely illustrates how the accuracy of the expansion depends on the position w.r.t. the Dirac-delta potential. Figure 4.7 depicts an example of the result for $F = 1/20$, and $a = 80$. We have chosen the latter value relatively large in this example in order to contain whole of the wavefunction within the part of the computational domain unchanged by the boundary layer. The figure shows a wavefunction that developed a wave-packet that propagated across the delta-potential into $x > 0$ region, as well as a portion of the wavefunction that partially "reflected" from the potential well. The presence of the Dirac-delta potential shows in the cusp at $x = 0$.

Figure 4.7 shows that the resonant state expansion can approximate the simulated expansion very well. However, while the agreement is near perfect for $x < 0$, the gap between the expansion and its target is clearly visible for $x > 0$. This behavior is quantified in the right hand panel which shows the error, defined as the absolute value of the difference, versus the position. Including more terms in the expansion clearly improves the result for negative x, but the error does not seem to improve for positive x even if hundreds of terms are used. Moreover, this illustration only utilizes the ground-state resonance plus up to three hundred resonances of family-A. If even a few family-C resonances are used, the agreement for $x > 0$ deteriorates exponentially. In certain cases the family-C resonance terms do improve the expansion *at small negative* x, but they always cause exponential blow up for $x > 0$.

In summary, this numerical test strongly suggests that the resonant state expansion converges on the negative axis, while it is likely that it diverges exponentially at $x > 0$. Even in the convergent region, where a few terms result in a very good approximation, the quality of the fit improves exceedingly slowly with the increasing number of terms included. In what follows, we verify that these indications are in fact correct. Before we move on, we should make the point that the split into outgoing

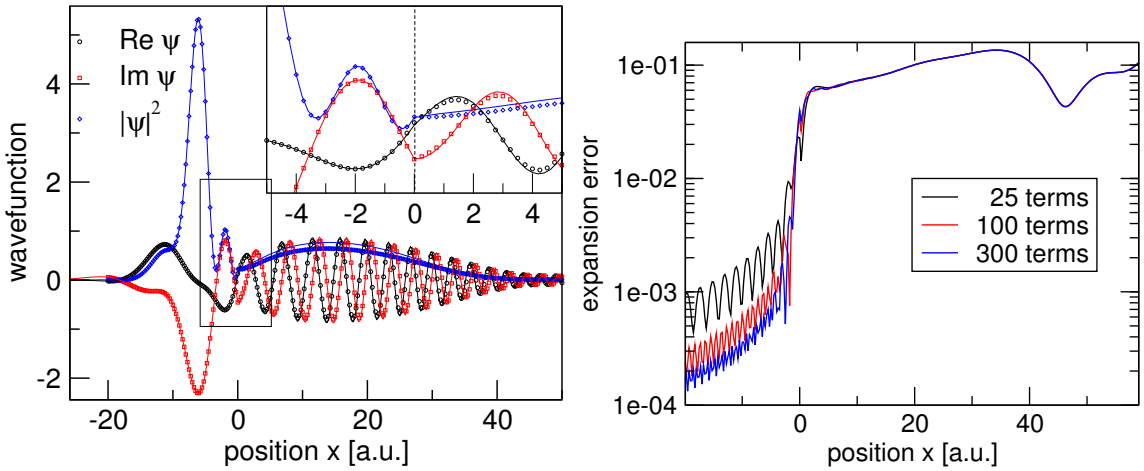

FIGURE 4.7. Numerically simulated "target wavefunction" (full lines) vs. the series expansion using Stark resonances (symbols, left). The inset zooms into the central portion of the domain (rectangle), with the dashed line indicating the location of the Dirac-delta potential. The right panel shows how the error depends on the number of family-A terms included.

and incoming parts of the wavefunction is not unique, and that there are different ways to create the expansion. Next we will show two of them and illustrate that one can manipulate the divergent properties of the example we just saw. However, in the end they have the same properties as we show in the next two examples.

4.6.2 Resonant state expansion, version I

The point of departure is the completeness relation for the self-adjoint Hamiltonian, written as applied to an arbitrary wavefunction $\phi(x)$:

$$\phi(x) = \int \delta(x-y)\phi(y)dy = \iint \psi_W(x)\psi_W(y)\phi(y)dW\,dy, \tag{4.39}$$

where the integration is over the whole real axis, and W stands for a variable that will later be continued into complex plane. We will use E for an energy integration variable that will remain confined to the real axis. Figure 4.8 shows the integration path used in this section and the following section to relate the continuum representation of the wavefunction to a sum over resonance pole residues.

Motivated by the fact that we have two sets of resonances, each forming an orthogonal system, we split the wavefunction into outgoing and incoming parts,

$$\psi_E = \psi_E^+ + \psi_E^-, \phi(y) = \phi^+ + \phi^- = \int A(E)[\psi_E^+(y) + \psi_E^-(y)]dE. \tag{4.40}$$

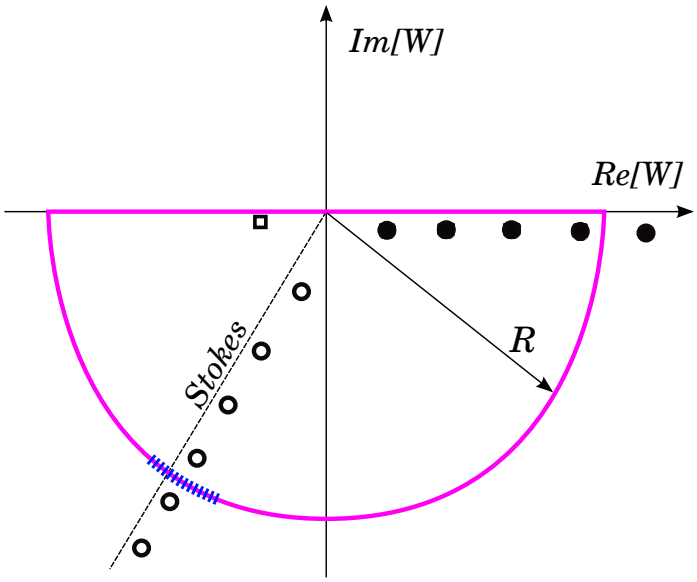

FIGURE 4.8. Three families of Stark resonances in the 1D Dirac-delta model. The ground-state resonance pole is shown as an open square symbol, family-A resonances are full circles, and family-C poles are open circles. Spacing in family A and C depends on the field strength, poles travel towards $W = 0$ for $F \to 0$, and become increasingly "crowded." The contour indicates the integration path used to convert continuum representation of a wavefunction into a sum over resonance pole residues in Subsections 4.6.2 and 4.6.3. The blue-dashed portion of the contour passes through a saddle point between two resonance poles.

Here we choose to identify the two components with the structure of the energy eigenstates and in particular take into $\psi_E^+(y)$, the part proportional to Ci^+. This is very natural for $x > 0$ as these functions behave as outgoing waves. For $x < 0$, one has to make a choice which is not unique. We use the second representation of $\psi_E(x)$, $x < 0$ written in terms of $Ci^\pm$, Eqn. (4.4). Then we treat each part of the wavefunction separately

$$\phi^\pm(x) = \int A(E) \int \psi_W(x) I^\pm(W, E) dW dE, \tag{4.41}$$

where

$$I^\pm(W, E) = \int \psi_W(y) \psi_E^\pm(y) dy = \lim_{\epsilon \to 0} \int \psi_W(y) \psi_{E \pm i\epsilon}^\pm(y) dy \tag{4.42}$$

is the overlap between the complete energy eigenstate and what we have chosen to be its outgoing part. The regularized integral above can be evaluated exactly using formulas from Vallée [104], plus the fact that ψ_W satisfies the cusp and continuity conditions, while $\psi_E^\pm$ is merely continuous.

To calculate the integral representing an "overlap" between the energy eigenstate $\psi_W(y)$ and the outgoing part of the same, $\psi^+_E(y)$,

$$I^+(W,E) = \int_{-\infty}^{+\infty} \psi_W(y)\psi^+_E(y)dy = \lim_{\epsilon\to 0}\int_{-\infty}^{+\infty} \psi_W(y)\psi^+_{E+i\epsilon}(y)dy, \tag{4.43}$$

we split the integration into $x < 0$ and $x > 0$ regions, and use the appropriate definitions for the wavefunctions involved. In both regions one deals with linear combinations of Airy functions, and the formula (3.53) of Ref. [104] applies for an indefinite integral

$$\int \psi_W(y)\psi^+_{E+i\epsilon}(y)dy = \frac{F}{\alpha^2(W-E+i\epsilon)}\left[\psi'_W(y)\psi^+_{E+i\epsilon}(y) - \psi_W(y)(\psi^+)'_{E+i\epsilon}(y)\right]. \tag{4.44}$$

To obtain the definite integral, note that the right hand side vanishes for $|y| \to \infty$, and only the singular point $y = 0$ contributes, giving

$$I^+(W,E) = \frac{F}{\alpha^2(W-E+i\epsilon)}\left[\psi'_W(y)\psi^+_{E+i\epsilon}(y) - \psi_W(y)(\psi^+)'_{E+i\epsilon}(y)\right]^{y=0^-}_{y=0^+}. \tag{4.45}$$

This can be simplified using the fact that both functions involved are continuous at $y = 0$, so we have

$$I^+(W,E) = \frac{F}{\alpha^2(W-E+i\epsilon)}\left[\psi'_W(y)|^{0^-}_{0^+}\psi^+_{E+i\epsilon}(0) - \psi_W(0)(\psi^+)'_{E+i\epsilon}(y)|^{0^-}_{0^+}\right]. \tag{4.46}$$

Because ψ_W also satisfies the cusp condition, we eliminate its derivative to simplify the above further

$$I^+(W,E) = \frac{F\psi_W(0)}{\alpha^2(W-E+i\epsilon)}\left[\frac{2}{\alpha}\psi^+_{E+i\epsilon}(0) - (\psi^+)'_{E+i\epsilon}(y)|^{y=0^-}_{y=0^+}\right]. \tag{4.47}$$

Now it is time to insert concrete expressions for the wavefunctions, namely

$$\psi_W(0) = \frac{-2Ai[\alpha W/F]}{N\sqrt{D^+(W)D^-(W)}},\ \psi^+_{E+i\epsilon}(0) = \frac{i}{N}\sqrt{\frac{D^-(E)}{D^+(E)}}Ci^+[\alpha E/F], \tag{4.48}$$

and

$$(\psi^+)'_{E+i\epsilon}(y)|^{y=0^-}_{y=0^+} = \frac{i}{N}\sqrt{\frac{D^-(E)}{D^+(E)}}\left\{\frac{Ai'[\alpha E/F]}{Ai[\alpha E/F]}Ci^+[\alpha E/F] - (Ci^+)'[\alpha E/F]\right\}. \tag{4.49}$$

Derivatives above can be eliminated by using the expression for the Wronskian, and a straightforward algebra leads to the result

$$I^+(W,E) = \frac{1}{2\pi i}\frac{1}{W-E\mp i\epsilon}\frac{Ai[\alpha W/F]}{Ai[\alpha(E\pm i\epsilon)/F]}\frac{\sqrt{D^+(E)D^-(E)}}{\sqrt{D^+(W)D^-(W)}}. \tag{4.50}$$

A similar procedure is used to solve $I^-(W,E)$ for incoming resonances and we find that we can represent both as

$$I^{\pm}(W,E) = \frac{\pm 1}{2\pi i}\frac{1}{W-E\mp i\epsilon}\frac{Ai[\alpha W/F]}{Ai[\alpha(E\pm i\epsilon)/F]}\frac{\sqrt{D^+(E)D^-(E)}}{\sqrt{D^+(W)D^-(W)}}. \tag{4.51}$$

As a sanity check, note that $I^+(W,E)+I^-(W,E)=\delta(W-E)$ and we recover the self-adjoint Hamiltonian completeness relation.

Next, we aim to convert (4.41) into a discrete sum over resonant states. We start with the case $x>0$ for which we expect, based on the previous numerical study, that the expansion will not converge. To keep notation concise, let us concentrate on the integral over W in (4.41),

$$\int \frac{1}{W-E-i\epsilon}\frac{i}{N}\left(\frac{Ai[\alpha W/F]Ci^+[\alpha(x+W/F)]}{D^+(W)} - \frac{Ai[\alpha W/F]Ci^-[\alpha(x+W/F)]}{D^-(W)}\right). \tag{4.52}$$

We wish to close the integration contour by a big semi-circle of finite large radius R connecting points $W=\pm R$ in the lower half-plane (see Figure 4.8) thus avoiding the pole of the first integrand term. For a finite R the integral is equal to the sum over simple pole residues of $1/D^+(W)$. Using asymptotics of Airy functions (e.g. [113]), it is not difficult to realize that the first and the second term in the brackets diverges exponentially for large $|W|$ in the sector $-2\pi/3<\arg(W)<0$ and $0<\arg(W)<2\pi/3$, respectively. As a consequence, the integral contribution from the semi-circle diverges, and so must the series as we take $R\to\infty$. This corroborates the expectation that for $x>0$ the resonant expansion does not converge.

Let us turn our attention to $x<0$, where we expect to obtain a convergent series. Using $\psi_W(x)$ in (4.41), we have

$$\begin{aligned}\int &\frac{1}{W-E-i\epsilon}\frac{i}{N}\\ &\times\left(\frac{Ai[\alpha(x+W/F)]Ci^+[\alpha W/F]}{D^+(W)} - \frac{Ai[\alpha(x+W/F)]Ci^-[\alpha W/F]}{D^-(W)}\right)dW.\end{aligned} \tag{4.53}$$

This time, both terms in the brackets decay as $|W|\to\infty$, irrespective of the direction. One can therefore close the integration contour either through the upper or lower complex half-plane, and then express the integral as a sum over residues, obtaining

$$\phi^{(+)}(x) = \frac{i}{\alpha N}\sum_n \frac{g_n^+(x)}{R'^+(\alpha\beta_n)}\int A(E)\frac{\sqrt{D^+(E)D^-(E)}}{Ai[\alpha(E+i\epsilon)/F](\beta_n-E/F)}dE \tag{4.54}$$

and, naturally, a similar expression for $\phi^{(-)}(x)$. This is indeed the sought discrete state expansion, but we are not done yet as we want to show that the expansion coefficients

are in fact the same as when obtained by a direct projection onto resonant states ψ_n. For this purpose, we will take the outgoing part of the given wavefunction

$$|\phi^+\rangle = \sum_n |\psi_n^+\rangle\langle\psi_n^+|\phi^+\rangle, \tag{4.55}$$

where the projection is understood in terms of the contour integral along $\mathcal{C}$. The right-hand-side can be written as

$$\sum_n \int_{\mathcal{C}} dy \psi_n^+(x)\psi_n^+(y) \int dE A(E)\psi_E^+(y) \equiv \sum_n \int dE A(E) u_n(E,x) \tag{4.56}$$

where the "coefficient" is

$$u_n(E,x) = \psi_n^+(x) \int_{\mathcal{C}} dy \psi_n^+(y)\psi_E^+(y) = \frac{1}{P_n^2} g_n^+(x) \int_{\mathcal{C}} dy g_n^+(y)\psi_E^+(y). \tag{4.57}$$

This integral can be evaluated exactly, taking into account that the resonance wavefunction is continuous and it satisfies the cusp condition, while ψ_E^+ is only continuous. Performing a similar integration procedure use in (4.42)-(4.51), we find that

$$u_n(E,x) = \frac{1}{P_n^2} g_n^+(x) \frac{1}{\alpha^2(\beta_n - E/F)} g_n^+(0) \left[\frac{2}{\alpha}\psi_E^+(0) - (\psi_E^+)'(x)|_{0+}^{0-} \right]. \tag{4.58}$$

Using expressions for $g_n(0)$ and ψ_E one obtains a more explicit

$$u_n(E,x) = \frac{g_n^+(x)}{P_n^2} \frac{Ai[\alpha\beta_n] Ci^+[\alpha\beta_n]}{\alpha^2(\beta_n - E/F)} \frac{i}{\pi N Ai[\alpha E/F]} \sqrt{D^+(E)D^-(E)} \tag{4.59}$$

and realize that the numerator in the second fraction can be simplified to a constant, $-\alpha/(2\pi)$. Inserting the result into (4.56), one obtains series representation which is the same as (4.54). This confirms that the coefficients can be evaluated as the contour integrals along the complexified axis $\mathcal{C}$.

On one hand, the derivations of this section corroborate indications about the resonant series behavior we gleaned through the numerical test. On the other hand, the above treatment invites questions. In particular, one should wonder if it is not possible to choose a different split $\phi = \phi^+ + \phi^-$ for which the contour integral and consequently the series would converge. Clearly, one could choose a different ϕ^+ for negative x, or one could decide to start splitting only beyond a large positive a, e.g. keeping $\phi^+ = \phi^- = \phi/2$ for $x < a$. In the next section we show that one can indeed obtain a different resonant series, but the basic fact that it only converges for $x < 0$ will remain intact.

4.6.3 Resonant state expansion, version II

Let us return to the completeness relation of the original Hamiltonian, formally rewritten as follows

$$\delta(x-y)=\int\psi_E(y)\psi_E(x)dE=\iint\psi_E(y)\psi_W(x)\delta(E-W)dEdW. \tag{4.60}$$

Without changing the result, we can multiply the integrand by a function that reduces to unity for $W=E$, and we also represent the delta function as in

$$\begin{aligned}\delta(x-y)=\iint\psi_E(y)\psi_W(x)&\frac{\sqrt{D^+(E)D^-(E)}}{\sqrt{D^+(W)D^-(W)}}\\&\times\frac{1}{2\pi i}\left[\frac{1}{W-E-i\epsilon}-\frac{1}{W-E+i\epsilon}\right]dEdW.\end{aligned} \tag{4.61}$$

Applying this unity decomposition to a given wavefunction $\phi(x)$ we get

$$\phi(x)=\frac{1}{2\pi i}\sum_{s=\pm1}\int A(E)\sqrt{D^+(E)D^-(E)}\int\frac{\psi_W(x)}{\sqrt{D^+(W)D^-(W)}}\frac{s}{W-E-is\epsilon}dWdE \tag{4.62}$$

where $A(E)=\int\phi(y)\psi_E(y)dy$ is the wavefunction in the energy representation. To convert the integral over W into a sum over resonant states cases $x<0$ and $x>0$ need to be investigated separately. We start with the former, for which one has to evaluate

$$\phi^{\pm}(x)=\frac{\pm1}{2\pi i}\int A(E)\sqrt{D^+(E)D^-(E)}\int\frac{-2Ai[\alpha(x+W/F)]}{ND^+(W)D^-(W)}\frac{1}{W-E\mp i\epsilon}dWdE. \tag{4.63}$$

Analysis of the asymptotics of the second integrand's first term for large $|W|$ leads to (written for $F=1$ to compress the notation):

$$\frac{-2Ai[\alpha(x+W)]}{D^+(W)D^-(W)}\sim-\frac{e^{\sqrt{-2W}x}}{2^{1/12}\sqrt{\pi}(-W)^{1/4}}e^{-2/3\sqrt{2}(-W)^{3/2}}\qquad|\arg(W)-\pi|<\pi/3 \tag{4.64}$$

$$\sim\frac{(1+i)e^{-i\sqrt{2W}x}W^{1/4}}{2^{1/12}\sqrt{\pi}}e^{+2/3i\sqrt{2}W^{3/2}}\qquad0<\arg(W)<2\pi/3 \tag{4.65}$$

$$\sim\frac{(1-i)e^{+i\sqrt{2W}x}W^{1/4}}{2^{1/12}\sqrt{\pi}}e^{-2/3i\sqrt{2}W^{3/2}}\qquad-2\pi/3<\arg(W)<0 \tag{4.66}$$

Thanks to terms containing $W^{3/2}$, the above expressions are exponentially small for large $|W|$. We can therefore close the integration contour and apply the residue theorem. We do this through the lower (Figure 4.8) and upper half plane for ϕ^+ and ϕ^-, respectively. After converting integral over W into a discrete sum over residues for

ϕ^+, we multiply by $Ci^+[\alpha\beta_n]/Ci^+[\alpha\beta_n]$, and use that $R^-(\alpha\beta_n)Ci^+[\alpha\beta_n] = 2iAi[\alpha\beta_n]$ (a consequence of the eigenvalue equation) in the denominator to obtain

$$\phi^+(x) = \sum_n g_n^+(x) \int \frac{A(E)\sqrt{D^+(E)D^-(E)}}{\beta_n - E/F} dE \frac{i}{\alpha N} \frac{1}{R'^+(\alpha\beta_n)Ai[\alpha\beta_n]}. \tag{4.67}$$

Similar manipulations result in an analogous resonant state expansion of $\phi^-(x)$, with $g_n^+(x) \to g_n^-(x)$, $\beta_n \to \beta_n^*$, and $R'^+ \to R'^-$. In summary, we have shown that $\phi(x)$ that has a compact-support energy-representation, $A(E)$,

$$\phi(x) = \int A(E)\psi_E(x)dE, A(E) = \int \phi(x)\psi_E(x)dx \tag{4.68}$$

can be written as a discrete resonant-state series (for $x < 0$):

$$\phi(x) = \phi^+(x) + \phi^-(x) \equiv \sum_n \frac{ic_n^+ g_n^+(x)}{\alpha N R'^+(\alpha\beta_n)} - \sum_n \frac{ic_n^- g_n^-(x)}{\alpha N R'^-(\alpha\beta_n^*)} \tag{4.69}$$

where the expansion coefficients are evaluated in the energy representation

$$c_n^+ = \int \frac{A(E)\sqrt{D^+(E)D^-(E)}}{Ai[\alpha\beta_n](\beta_n - E/F)} dE,\ c_n^- = \int \frac{A(E)\sqrt{D^+(E)D^-(E)}}{Ai[\alpha\beta_n^*](\beta_n^* - E/F)} dE. \tag{4.70}$$

This result means that the system of Stark resonances is complete in the sense that an arbitrary wavefunction can be expressed as their superposition, and the resulting series converges point wise for $x < 0$. The question addressed next is if the same applies on the positive real axis. Although the answer is negative, it provides a useful insight as to why exactly the family-C causes divergence of the resonant expansion. In contrast to the first version of the resonant-state series, the divergent behavior is reduced to a "minimum" caused by the fact that an integration contour must pass through the vicinity of some resonance poles. We therefore proceed to outline the main points of the argument.

Using the expression for the energy eigenstate for positive x in (4.62), the counterpart of (4.63) becomes

$$\begin{aligned}\phi^\pm(x) = &\int A(E)\sqrt{D^+(E)D^-(E)}dE \\ &\times \int \frac{\pm 1}{W - E \mp i\epsilon} \left[\frac{Ci^+[\alpha(x + W/F)]}{D^+(W)} - \frac{Ci^-[\alpha(x + W/F)]}{D^-(W)}\right] \frac{dW}{2\pi N}.\end{aligned} \tag{4.71}$$

In order to convert $\int dW$ into a closed-loop integral, we need to investigate the asymptotic behavior of the last term in the above expression. It turns out that also

in this case the integrand decays exponentially for large $|W|$ (once again, written for $F = 1$):

$$\frac{Ci^+[\alpha(x+W)]}{D^+(W)} - \frac{Ci^-[\alpha(x+W)]}{D^-(W)} \sim$$

$$\sim \frac{ie^{\sqrt{-2W}x}}{2^{1/12}\sqrt{\pi}(-W)^{1/4}} e^{-2/3\sqrt{2}(-W)^{3/2}} \qquad |\arg(W) - \pi| < \pi/3 \qquad (4.72)$$

$$\sim -\frac{(1-i)e^{-i\sqrt{2W}x}W^{1/4}}{2^{1/12}\sqrt{\pi}} e^{+2/3i\sqrt{2}W^{3/2}} \qquad 0 < \arg(W) < 2\pi/3 \qquad (4.73)$$

$$\sim -\frac{(1+i)e^{+i\sqrt{2W}x}W^{1/4}}{2^{1/12}\sqrt{\pi}} e^{-2/3i\sqrt{2}W^{3/2}} \qquad -2\pi/3 < \arg(W) < 0 \qquad (4.74)$$

It thus appears that we can close the contour and express the integral as a sum over residues. In doing so, only one of the first and second terms contributes to ϕ^+ and ϕ^- as we close the contour in the lower and upper half-plane, respectively. Similarly to the case of negative x, we multiply by $Ai[\alpha\beta_n]/Ai[\alpha\beta_n]$ and rewrite in terms of the resonant wavefunctions. The result is the identical expansion as for $x < 0$ listed in (4.69)-(4.70). At this point one could think that the Stark resonance system is complete in the usual sense i.e. on the whole real axis, but such a conclusion would be erroneous. In fact, the above argument that the "big semi-circle" part of the integration contour has a vanishing contribution contains a subtle flaw.

The problem is that for any finite radius R of the big semi-circle, the integration contour passes between the poles of family-C resonances as shown in Figure 4.8. While the highest point in the saddle decreased for $R \to \infty$ in the case of negative x, it turns out to increase exponentially for all positive x. This behavior can be readily verified by inspection of the integrand in the vicinity of the family-C resonant poles, and comparing the saddle properties for increasing radius R. The result is that there is a finite contribution to the contour integral from the section indicated by red dashed line in Figure 4.8, and this contribution diverges as R increases. So, while along each ray the above asymptotics (4.74) is valid (with the exception of the Stokes line) the formula can not be applied to the short section of the contour that passes between the poles as for any finite R this portion of the contour is not yet in the asymptotic region. This gives a divergent contribution to the contour integral which in turn implies that the resonant expansion also diverges for all positive x.

To finish this section, it may be interesting to note that the resonant-state series can be analytically continued into complex plane. Doing this separately for the outgoing component ϕ^+ in (4.69), and continuing x to z on the contour $\mathcal{C}$, one obtains a convergent series provided $a = 0$ and $\theta \geq \pi/3$ (Figure 4.8). This is a consequence of the fast exponential decay of outgoing family-C resonant functions along the contour $\mathcal{C}$. Naturally, the incoming part ϕ^- converges in a similar way for $\arg(z) \leq -\pi/3$. We have verified this observation numerically (data not shown).

4.6.4 Numerical illustration of convergence

Formulas (4.69) and (4.70) summarize the main result of this work. Here we subject them to a numerical test. Besides a sanity check, it is meant to illustrate that while the two versions of the resonant expansions differ, they share the same qualitative behavior, which is point-wise convergence on negative, and exponential divergence on the positive real axis. Unlike in version I, version II does not utilize integration contour $\mathcal{C}$, since the expansion coefficients are calculated from the energy-representation of the given wavefunction, $A(E)$.

Of course one should ask first for what kind of wavefunctions do the expansion coefficients exist in the first place. Without going into details, it can be shown that they are defined for any compact-support $A(E)$. Alternatively, one can view

$$\tilde{A}^{\pm}(W) = \int \frac{A(E)\sqrt{D^+(E)D^-(E)}}{W - E \pm i\epsilon} dE \tag{4.75}$$

that appears in (4.63), as a projection of the energy-representation wavefunction. Indeed, written for $U(E) = A(E)\sqrt{D^+(E)D^-(E)}$ the above can be understood as

$$U^+ = \frac{1}{2}U + \frac{1}{2i}\mathcal{H}\{U\} \tag{4.76}$$

where the second term is the Hilbert transform, which can act on $U \in L^p(\mathbf{R})$, $p > 0$. Moreover, it is easy to see that the above operation is in fact a projection because $U^+ + U^- = U$ and $(U^+)^+ = U^+$. In other words, the transformation is just another way to define the outgoing and incoming part of the given wavefunction. In this sense, the second version of the resonant expansion is not qualitatively different from version I, and this is indeed reflected in how similar the expansion coefficients are (compare (4.70) and (4.54)). However, version II is free of the artifacts in the split-off wavefunction at $x = 0$. Unfortunately, the expansion coefficients are more difficult to evaluate, because it must be done in the energy representation.

In order to avoid compounding of numerical error in subsequent integral calculations, we test our expansion formulas directly in the energy representation: An exact energy eigenstate is chosen, so that $A(W) = \delta(W - E)$ and all coefficients of the resonant expansion can be easily evaluated provided β_n are available with sufficient accuracy. Of course if any energy eigenstate could be approximated, so could any physical wavefunction. Figure 4.9 illustrates the expansion test for two select energies, namely $E = -1/2$ and $E = 1$. The former is an eigenstate that is "close" to the ground-state resonance which dominates its expansion. As a result, the agreement is very good over a wide range of x as is seen in the left panel of the figure. For $E = 1$, one can see the same situation as in our first numerical test. The expansion error is small for $x < 0$, but deviations increase very quickly for positive x. In summary, this numerical investigation verifies the properties of the resonant-state expansion derived in the previous section.

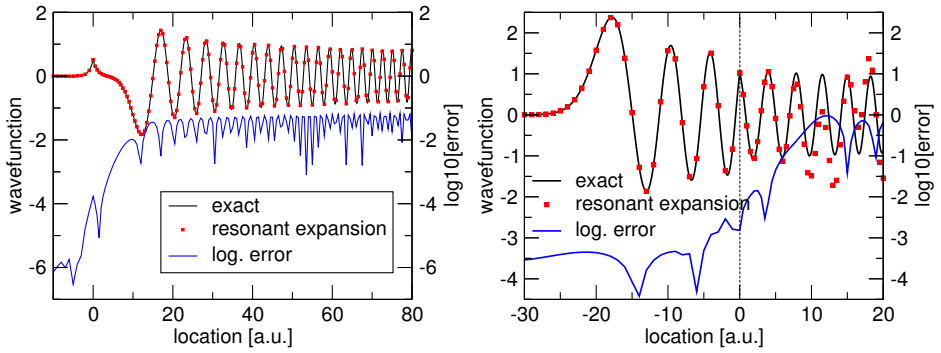

FIGURE 4.9. Resonant expansion test. The exact energy eigenstate ($E = -1/2$ left, $E = 1$ right panel) is shown in full black line. Series expansion is represented by symbols, and the lower blue line depicts the logarithm of the error (vertical axes on right).

We have found that the reason for the divergent behavior of the second type of the resonant expansion can be identified with the integration contour passing through a saddle between two resonant poles of family-C. We believe that this property may be shared by other expansions, including those of Green's operators, and that the divergent behavior of the series on the positive axis is a common phenomenon. We speculate that the divergent part of the contour integral can be estimated, e.g. using steepest descent method, and the divergent part of the expansion could be identified and perhaps even removed.

4.7 Summary

We have derived analytic expressions for a number of quantities that characterize the Stark resonant states in two exactly solvable systems. The first model studied in this work is the one-dimensional particle in a Dirac-delta potential with additional homogeneous field, and the second has the square-well potential. We have studied these systems as open, non-Hermitian models, and identified a natural choice for the pairing connecting the states in the domain of the Hamiltonian with the states in the domain of its adjoint operator. With respect to this pairing, Stark resonances form a orthogonal system, and many of their properties can be evaluated analytically. Despite the fact that both models have been studied for years, explicit expressions for their (pseudo-) norms, dipole moment expectation values and their relations connecting the resonant state wavefunctions at different field values are new. Our results thus further the understanding of the mathematical properties that underline the Stark effect. Moreover, we have shown that certain results naturally extend to a wide class of one-dimensional models, and we have also identified relations that appear to be candidates for properties generally applicable to three-dimensional Stark systems. In

particular, we have found that the generalized dipole moment matrix elements between the non-physical resonant states can be related to the expectation values of the atomic potential gradient in a way that is completely analogous to relations that hold for real-valued discrete-energy eigenfunctions in Hermitian systems. We speculate that these relation apply generally in three dimensions, and could be used in numerical calculations to assess the fidelity of the resonant eigenfunctions. An important by-product of this study is a new integration technique applicable to combinations of Airy functions that represent Stark resonances in one dimensional models with piecewise constant potentials.

We have also shown analytically, and illustrated numerically, the convergence properties of the Stark resonant state expansion for the wavefunctions representing a one-dimensional quantum particle in a Dirac-delta potential, exposed to a homogeneous electric field. Our main result is that while the resonant expansion diverges for all positive x, it is convergent on the negative portion of the real axis. It has to be emphasized it is not required that for the series to converge at $x < 0$ the support of the wavefunction be within the region of $x < 0$; All coefficients of the expansion are well-defined in terms of the energy representation even if the x-representation of the wavefunction extends to $x > 0$. However, convergence only occurs on the negative axis, and it is rather slow. While very few first terms usually provide an excellent approximation to a given wavefunction, the error decreases slowly upon inclusion of more terms. As for the practical implications of our findings, we believe that the result for this simple, exactly solvable system reveals the general property of the resonance expansion particularly with Stark resonances, namely that the convergence can only be point-wise over a limited spatial domain. Nevertheless, despite the lack of global convergence, it is possible to obtain quite accurate approximations of functions with a rather small number of resonant states. This suggests that there may exist a portion of the wavefunction which can be accurately approximated in terms of resonant expansion and will help to identify exactly what aspect of the physical wavefunction can be represented with Stark resonances.

Finally, results presented in this chapter have an immediate practical impact on modeling of light-matter interactions in strong time-dependent optical fields in the framework of the Metastable Electronic State Approach [83], which we discuss in more detail later in Section 5.2.

Chapter 5

Applications of Resonant States

5.1 Introduction

In this chapter we show three applications where resonant states are used as a medium model. The first application is the Metastable Electronic State Approach (MESA), which is a practical example of using resonant states to model the light-matter interactions associate with strong light pulses. MESA has a huge computational advantage over solving Schrödinger's equation directly. This is done by performing a one-time computationally expensive simulation where we generate a quantum response function, such as nonlinear dipole moment, over a wide range of field values. Once these values are tabulated, then values can be simply "looked-up" during a propagation simulation. This results in a fast medium model that is on the same computational effort as the standard medium model equations. This results in a practical implementation of UPPE connected to a first-principles based medium model with no free parameters.

More specifically, we calculate the off resonant nonlinear optical response of a system that is described by resonant states. As described in the previous chapter, we split the wavefunction into metastable part and background part. MESA assumes that the ground state resonance dominates and that its response adiabatically follows the field. To improve this approximation we later add a "post-adiabatic" correction that takes into account a small time history of the field. We find that for shorter wavelengths (800nm) this correction closes the gap between MESA and the exact solution of the delta model nonlinear response, but for longer wavelengths ($2\mu m$) the correction is unnecessary. We compare MESA's response to a 3D coulomb-like system and find that the shape is the same. The time dependent response to a given field is also qualitatively similar.

The second application uses the 1D delta model and its associated resonant states to show that ionization dynamics are not instantaneous, but that there exists some memory of the carrier's shape. We do this by engineering two pulses that contain the same energy but different carrier shape and find that the quantum model can distinguish them, whereas the standard approach's rate equation treatment cannot. How does a single bound state quantum system remember past field values? We reason that the memory comes from the longer living family of resonances whose energies are near the positive axis, since they exists long enough to remember the history of excitation. This memory effect is only seen for near-IR wavelengths and becomes negligible in the mid-IR region.

The third application is inspired by experiments where the ionization yield and

spectrum due to a strong pump pulse is greatly modified by adding a small harmonic seed pulse. We ask whether a fully quantum treatment is necessary to reproduce these effects. We find that propagation plays a negligible role and that a resonant state medium model can reproduce what is seen in experiment. This is evidence that medium models need to take into account pulse spectrum.

These three applications showcase the valuable contributions that exactly solvable systems and resonant states provide.

5.2 Metastable electronic state approach (MESA)

In this section we propose and demonstrate that the ultrafast, off-resonant nonlinear optical response of atoms may be accurately calculated in terms of metastable or resonant states as opposed to the more common bound and continuum states of the free atom. In particular, we consider solutions of the atomic time-independent Schrödinger equation including the quasi-static applied electric field. These states have complex energies where the imaginary parts are related to the metastable state lifetime. Metastability refers to the fact that while these states ionize and thus "decay" over relatively long times, when observed on shorter time-scales in the vicinity of the atom, they are difficult to distinguish from the normal (i.e. field-free) electronic states. The atomic wavefunction may be split into two components $\psi = \psi_M + \psi_F$, in which ψ_M is expressed as a superposition of metastable states that is used to calculate the nonlinear optical response arising from the quantum coherent light-matter interaction. In contrast, ψ_F accounts for electrons that are to all intents and purposes freed from their parent ion and contribute to a classical current density. This portion of the wavefunction is populated by the losses from the metastable states, and is subsequently driven by the applied electric field according to the Ehrenfest's theorem. The metastable portion of the wavefunction, ψ_M , gives rise to a complex, non-perturbative nonlinear response which only reduces to the usual optical Kerr effect in the limit of a weak field. Using examples we demonstrate that our approach, that we term "the Metastable Electronic State Approach" or simply MESA, provides an extremely economical computational method to calculating the nonlinear optical response: Already retaining only the ground metastable state in adiabatic approximation can provide a quantitative model for the nonlinear optical response and strong-field ionization, and further improvement is shown to result from retaining post-adiabatic corrections.

The medium model that we develop is based on the 1D Dirac-delta model. The theory shown in 4.4.1 allows us to calculate every quantity needed. The most important quantity in this approach is the complex-valued expectation value of the dipole moment $X(F)$. This value can be calculated in two ways. If one can use the eigenvalue equation (4.13) to accurately calculate a finely sampled set of energies $E(F)$, then (4.18) is convenient since $X(F) = \partial_F E(F)$. The alternative is to directly in-

tegrate the dipole moment equation $X(F) = \int_C \psi(z) z \psi(z) dz$ along a contour that decays the expontentially growing part of the wavefunction, such as in Figure 4.1. We mention both ways since there seems to be a lack of good quality libraries for calculating Airy functions in the entire complex plane. The best library available at the time of this writing is a Python module called mpmath [114]. In Figure 5.1 we plot the ground state dipole moment $X_0(F)$ over a range of field strengths.

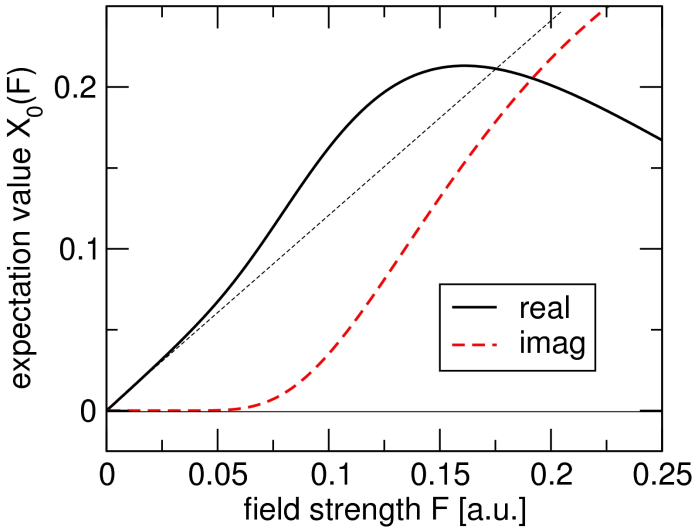

FIGURE 5.1. Complex-valued expectation value of the dipole moment in the metastable ground state as a function of the external field strength. The fine dashed line indicates the linear susceptibility. The gap between the thin dashed and the thick black line represents the nonlinear response, Equation (5.3).

Its real part is super-linear for weak fields (Kerr effect), and it saturates and decays in very strong fields, whereas the imaginary part is intimately related to the ionization losses. As noted in Section 3.4 the saturation and decay of the real part is accompanied by rapid growth of the freed electron population which produces a defocusing nonlinear response. This generic behavior turns out to be the same for more realistic 3D quantum systems. It is this curve that serves as the backbone for the MESA. If you can calculate $X_0(F)$ for quantum systems with different potentials, then you can use the MESA to connect it to a propagation simulation.

5.2.1 General scheme

The central idea of the method we put forward (MESA) is to abandon the traditional description of the quantum evolution in terms of Hamiltonian eigenstates. Instead, we argue that for a system exposed to a strong external field, such as due to a high-intensity optical pulse, it is more natural to utilize metastable states. They are superpositions of the (field-free) bound and free electronic states, reflecting the current

strength of the field and the probability density "leakage" due to ionization [115]. We assume that it is possible to represent the wavefunction split into "metastable" and "free" components, $\psi = \psi_M + \psi_F$.

Our method is motivated by Berggren's completeness relations [91] employed in nuclear scattering theory

$$1 = \sum_n |\psi_n\rangle\langle\psi_n| + \int_L d\lambda |\phi_\lambda\rangle\langle\phi_\lambda|, \tag{5.1}$$

where the sum projections onto several resonant states, and the integral involving scattering states ϕ proceeds along a contour L that deviates from the real axis in order to include the poles corresponding to the complex energies of the resonances included in the first term. In our method one or more resonant states represent ψ_M which we assume to be the part of the wavefunction interacting strongly with the atomic potential. The "remainder" of the wavefunction, ψ_F is projected from the full state via the continuum component of the above completeness relation. Note that our approximation does not rely on completeness of the resonant states. Rather the key assumption is that the continuum part of the wavefunction, ψ_F, is so spread out in space that its interaction with the atom may be neglected. If it is, we do not need to know any specific properties of ψ_F, because the quantity of interest, namely the current, can be obtained from the Ehrenfest's theorem. Validity of this approximation obviously depends on the initial state, and it is not a priori obvious that a small number of resonant states can capture the "interacting part" of the wave function sufficiently accurately. However, our numerical examples below demonstrate that even a single ground state resonance provides an extremely good approximation.

We are specifically interested in the case of off-resonant excitation, meaning that the instantaneous frequency $\omega_{eff}(t) = \frac{\partial \Phi}{\partial t}$ of the applied field $F(t) = A(t)\cos(\Phi(t))$ should remain well below the ionization frequency $I/\hbar$ for all times, I being the ionization energy. Our method should therefore be more accurate for longer wavelengths and we find this to be the case. Moreover, for the case of the exactly solvable 1D Dirac-delta model there is an analytic result which states that the lowest metastable state exactly captures the quantum atomic dynamics in the adiabatic or quasi-static approximation for which $\hbar\omega_{eff}(t)/I << 1$ [109].

We will first concentrate on the adiabatic approximation. For the initial condition in the ground state the adiabatic wavefunction [109] becomes dominated by the ground state resonance and the solution is

$$c_0^{(a)}(t) = \exp\left\{-iE_G t - i\int_{-\infty}^{t} \left[E_0(F(\tau)) - E_G\right] d\tau\right\}\ , \tag{5.2}$$

where E_G is the field-free ground state energy. If the field is not too strong, the ground state resonance dominates at all times, and then the generalized dipole-moment expectation is the main contribution to the induced polarization $P(F(t)) = |c_0(t)|^2 X_0(F(t))$

[97]. In pulse propagation simulations the linear medium properties are captured exactly by a spectral solver. To avoid double-counting, only the nonlinear part of the atom polarization is used and coupled to the Maxwell equations. This we obtain as

$$P^{(nl)}(F(t)) = P(F(t)) - \lim_{\epsilon \to 0} \frac{1}{\epsilon} P(\epsilon F(t)) \ , \tag{5.3}$$

where the second term tends to the linear part of the response as the auxiliary parameter ϵ gets small. The polarization (5.3) is our first contribution to the nonlinear medium response. The second comes from ψ_F, in the form of a classical current, because we assume that this is the "distant part" of the wavefunction that is not interacting with the atom anymore. The population of ψ_F grows at a rate equal to the metastable decay, so that the total probability is conserved as it should be in a closed system. Thus, the ionization rate is given by the imaginary part of the ground state resonance complex energy, and the ionized fraction of atoms obey

$$\partial_t \rho(t) = [1 - \rho(t)] \Im\{2E_0(F(t))\} \ . \tag{5.4}$$

The current induced by freed electrons is obtained from Ehrenfest's theorem, and is evaluated by integrating

$$\partial_t J(t) = \rho(t) F(t) \ . \tag{5.5}$$

Note that this induced current only arises after ionization which is a highly nonlinear process, and it therefore does not contain a component linear in the field-strength. Thus, the two functions $X_0(F)$ and $E_0(F)$ are needed to characterize the nonlinear optical response of the system. The proposed model has structure similar to the one used in filamentation simulations, with $P^{(nl)}(t)$ and $J(t)$ coupled into pulse propagation equations. However, the meaning of its components is new: Kerr response is now contained within the nonlinear polarization of the metastable state, which now also includes contribution from the continuum states. Moreover, what used to be the Drude current is now solely due to electrons NOT in the resonant state(s) included in our treatment. Thus, the wavefunction split, and therefore the relative contributions of polarization and current density, will depend on how many metastable states we can explicitly account for. As of now we only include the ground state resonance. Next we look at how the higher-order states can be accounted for in an approximate fashion.

5.2.2 Post-adiabatic corrections

The purpose of this section is to describe three kinds of corrections that take MESA beyond the adiabatic approximation outlined above. In doing so, we will strive to formulate our theory in such a way that it will only require the knowledge of a *single* metastable state, namely the one related to the ground state. This will greatly simplify practical applications, because it is relatively simple to characterize

the ground state resonance while it may be more difficult to calculate properties of higher metastable states. The assumption underlying the following consideration is one of a weak field $F(t)$, which is changing slowly. This is the case for many regimes in extreme nonlinear optics, where typical intensities attained in hot spots are still two orders of magnitude weaker than atomic fields. Moreover, the propagation dynamics dynamically adjusts the evolving pulse such that the peak intensity is clamped. As a result the quantum state is strongly dominated by the contribution from the metastable ground state, and we construct the post-adiabatic corrections under this assumption.

The first correction of the adiabatic solution is obtained by solving (4.7) for the expansion coefficients c_n driven by the dominant c_0. Using the adiabatic ground state coefficient $c_0^{(a)}(t)$ we can approximate solutions for higher-order resonances as

$$c_n'(t) = -ic_n E_n(F(t)) + c_0^{(a)}(t)F'(t)\left\langle \partial_F \psi_n | \psi_0 \right\rangle \quad n > 0. \tag{5.6}$$

We asymptotically expand the coefficients allowing us to write the first term in the expansion using the adiabatic coefficient (5.2)

$$\begin{aligned} c_n^{(1)}(t) = \int_{-\infty}^{t} du \exp\left\{ -iE_G(t-u) - i\int_u^t \left[E_n(F(\tau)) - E_G\right] d\tau \right\} \\ \times c_0^{(a)}(u)F'(u)\left\langle \partial_F \psi_n(F(u)) | \psi_0(F(u)) \right\rangle . \end{aligned} \tag{5.7}$$

We can bring constant terms such as E_G and those not including integration variables u, τ out of the integral, and recover the equation for $c_0^{(a)}(t)$

$$\begin{aligned} c_n^{(1)}(t) = c_0^{(a)}(t) \int_{-\infty}^{t} du \exp\left\{ -i\int_u^t \left[E_n(F(\tau)) - E_0(F(\tau))\right] d\tau \right\} \\ \times F'(u)\left\langle \partial_F \psi_n(F(u)) | \psi_0(F(u)) \right\rangle . \end{aligned} \tag{5.8}$$

We approximate this integral by arguing that the energy difference in the exponent is highly oscillatory compared to the rest of the integrand. This gives us the first order correction term in terms of the adiabatic coefficient

$$c_n^{(1)}(t) \approx -ic_0^{(a)}(t) \frac{F'(t)\left\langle \partial_F \psi_n(F(t)) | \psi_0(F(t)) \right\rangle}{E_n(F(t)) - E_0(F(t))}. \tag{5.9}$$

Feeding this intermediate result back into the equation for the ground state resonance, $c_0^{(1)}(t)$ is obtained in the same form as $c_0^{(a)}(t)$, only with the resonant energy E_0 replaced by the corrected one:

$$E_0^{(R)}(F(t)) = E_0(F(t)) - \sum_{n\neq 0} \frac{(F'(t))^2 \left(\left\langle \psi_0 | \partial_F \psi_n(F(t)) \right\rangle\right)^2}{\left[E_n(F(t)) - E_0(F(t))\right]} . \tag{5.10}$$

Evaluation of this quantity requires the knowledge of higher-order resonant states. Fortunately, an approximation in terms solely of ψ_0 can be obtained as follows. First, since the energies $E_n(F)$ accumulate close to zero, at least in relatively weak fields, they are dominated by E_0, which can approximate the denominator in (5.10). Next, because normalization to unity for all F ensures that $\langle\psi_0|\partial_F\psi_n\rangle = -\langle\partial_F\psi_0|\psi_n\rangle$, the numerator in (5.10) can be rewritten, moving the action of ∂_F onto ψ_0 and thus giving rise to $\sum_{n\neq 0}\ldots|\psi_n\rangle\langle\psi_n|\ldots$. Our second assumption is that at least within the space of the solutions that evolve from the ground state, system of $\{\psi_n\}$ is complete, and this projection can be approximated by $1-|\psi_0\rangle\langle\psi_0|$. Then we can simplify the above correction to

$$E_0^{(R)}(F(t)) = E_0(F(t)) + \frac{(F'(t))^2}{E_0(F(t))}\langle\partial_F\psi_0(F(t))|\partial_F\psi_0(F(t))\rangle \ . \tag{5.11}$$

This modifies both the real and imaginary part of the complex metastable energy. It is the imaginary part that is more important for our purposes because it increases the ionization yield. Figure 5.2 illustrates this effect, and shows ionization yields caused by a driving pulse in the adiabatic and post-adiabatic (i.e. with correction (5.11)) approximations, compared to the exact solution. It is evident that the correction becomes negligible for longer wavelengths. At shorter wavelengths, it significantly decreases the gap between the adiabatic and exact solutions, thus justifying the approximations adopted in the derivation. Perhaps the most important observation to be made here is that even the uncorrected adiabatic solution provides rather accurate ionization rates. For practical purposes in the field of optical filamentation, especially in near and mid infrared, the adiabatic treatment should therefore be sufficient.

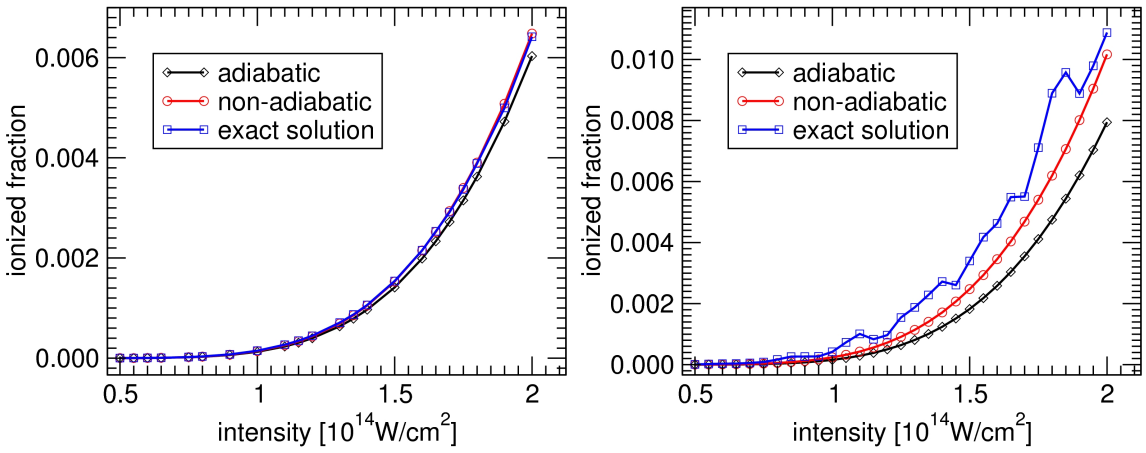

FIGURE 5.2. Ionization yield as a function of the intensity of the driving pulse. Exact, adiabatic and corrected solutions are compared. Left and right panel correspond to wavelengths of $\lambda = 2400$nm and $\lambda = 800$nm, respectively.

However, there is one post-adiabatic correction that should be included in such simulations, because it captures the losses the optical field must suffer due to ionization. Interestingly, this correction is connected to the *imaginary part* of the metastable expectation value of the dipole moment. To derive the corresponding nonlinear polarization term one has to include the first corrections $c_n^{(1)}$ of the wavefunctions when evaluating the expectation value of the dipole moment. Then, under the same approximation as in the derivation of the corrected resonant energy (5.11), one obtains the following estimate

$$P_{NL}^{(corr)}(t) \sim \frac{1}{E_G} \Im \left\{ \frac{\partial}{\partial t} \langle \psi_0(F(t)) | X | \psi_0(F(t)) \rangle \right\} \ . \tag{5.12}$$

This component of the nonlinear polarization turns out to be responsible for a major part of nonlinear losses. It is a microscopically motivated replacement for the purely phenomenological current which is routinely introduced into the standard filamentation model [3] in order to salvage energy conservation. Our comparative simulations show that the amount of losses caused by $P_{NL}^{(corr)}$ is actually quite similar to that obtained in the phenomenological treatment. It is fair to say that (5.12) is an approximation, yet it is a first step beyond the current method. Naturally, it could be improved provided one can calculate higher resonant states.

Finally, the third correction originates in the split between ψ_M and ψ_F, and the fact that the response of the latter is approximated by a Drude-like classical current as if this portion of the wavefunction was completely free. A generalized version of (5.5) should contain an additional term,

$$\partial_t J(t) = \rho(t) F(t) + v_i \partial_t \rho(t) \ , \tag{5.13}$$

where v_i stands for the initial velocity of freed electrons, which "disappear" from ψ_M and are "injected" into ψ_F. This correction can give rise to an important contribution to THz generation, and will be discussed in detail elsewhere. However, because it only generates a DC-like, low-frequency current, it has a negligible influence on the propagation of the driving pulse and can be safely ignored for that purpose.

5.2.3 Comparison with exact solutions

The exactly solvable 1D Dirac-delta system is an ideal test-bed to assess accuracy of the proposed light-matter interaction description. We utilize the time-dependent exact solution for the non-linear response given in Ref. [79]. This is then compared with the nonlinear response calculated as described in the previous sections.

The sole adjustment we make before comparing these results concerns the low-frequency part of the response described above. It shows up as a constant current after the driving pulse vanishes, reflecting the net average velocity imparted on the ionized electrons. While it is possible to capture this effect in the resonance-response

model, at present an estimate of v_i requires one adjustable parameter. We therefore filter out the very low-frequency part of the exact response and add this to the MESA result in order to compare the nonlinear response.

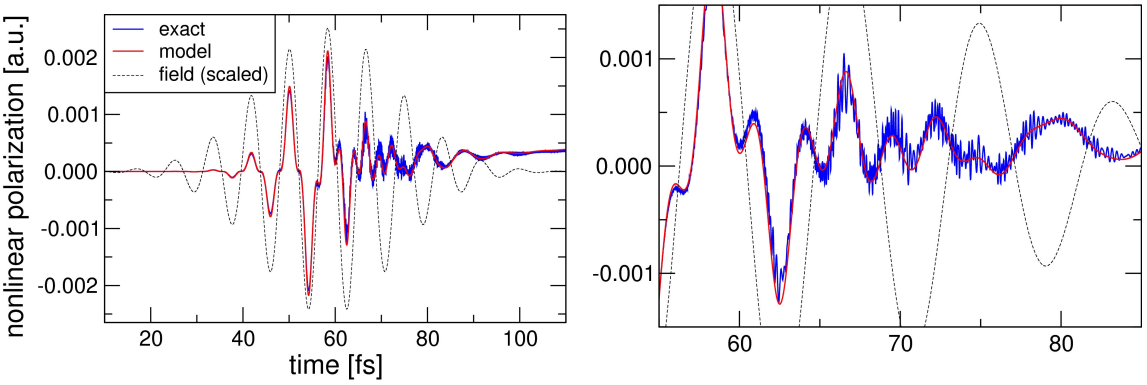

FIGURE 5.3. Nonlinear response of the 1D Dirac-delta system to a $\lambda = 2.5\mu$m driving pulse indicated by thin dashed line. The exact response is shown as blue solid line, and the resonant-response model result is shown in thick red. The left panel demonstrates accurate overall agreement between approximate and exact solutions. The right panel zooms in in order to highlight that our response model "filters out" very high-frequency components.

Figure 5.3 illustrates that very good agreement can be achieved between the exact and approximated nonlinear response for a 2.5 micron wavelength driving pulse. One can see that the approximate solution follows the exact one while it filters out the very high-frequency components. These are due to higher-order resonances and are therefore absent in our post-adiabatic approximation. The panels show that these response oscillations are too fast to affect the optical-frequency components of the driving pulse. For simulation of pulse propagation, it is therefore quite convenient that the model response does not follow them.

We thus can conclude that the proposed method captures precisely that frequency part of the total nonlinear response which is responsible for the back-reaction of the medium on the driving pulse. At the same time even small-scale details in the nonlinear response shape are reproduced quite well.

5.2.4 3D Hydrogen-like model atom

Having seen that the nonlinear response of the exactly solvable 1D Dirac-delta model can be reproduced by the metastable-state response model quite accurately, the important question is if it still works for more realistic systems. The crucial difference being that one has to resort to approximate methods to find, and "measure" properties of the ground state resonance. In the following we describe the procedure that

allows one to obtain parameterized nonlinear response from a series of TDSE simulations of a given system. The Hamiltonian represents a single-electron, hydrogen-like system,

$$H = -\frac{1}{2}\Delta - \frac{1}{\sqrt{a^2 + x^2 + y^2 + z^2}} - xF(t) \tag{5.14}$$

with a "soft" Coulomb potential and a time-dependent external field $F(t)$ representing the optical pulse.

To obtain the ground state resonance as a function of the static-field strength F, we start a TDSE simulation in the numerical ground state, and add transparent boundary conditions realized as a perfectly matched layer (PML) to the computational domain. Because the ground state resonance is the longest-living state, the initial wavefunction is driven toward it during the simulated real-time evolution while the "unwanted" states decay as they leak through the PML layers. Once the solution stabilizes, we characterize this ground state resonance by calculating the metastable expectation value for its dipole moment. We also extract its complex-valued resonance energy. This process is repeated for a range of field strengths, and the relevant data are tabulated. We envision that this kind of procedure will be applied when working with realistic (single-active-electron) models of atoms and perhaps even molecules.

Figure 5.4 shows the real and imaginary parts of metastable dipole moment $X_0(F)$. We have determined this quantity as a function of the field strength on different-size grids, and with three different implementations of the PML boundary. Two data sets, obtained for grid sizes of $L = 100$ a.u and $L = 150$ a.u., are shown in the figure to match closely, thus indicating that convergence is achieved already on relatively small computational domains. It should be noted that if one attempts to determine the standard quantum-mechanical expectation value of the dipole moment, no convergence can be reached because metastable wavefunctions diverge at infinity. It is thus crucial that our method works with the metastable generalization of the dipole moment.

Importantly, comparing Fig. 5.4 to Fig. 5.1, one can see that the behavior of the field-induced dipole is qualitatively the same in the 3D system as in the exactly solvable 1D model. This makes us believe that features of $X_0(F)$ are quite generic.

Together with the field-dependent metastable ground state energy $E_0(F)$, tabulation of the nonlinear of the dipole moment $X_0(F)$ shown in Fig. 5.4 constitutes the core data that characterizes the quantum system, and makes it possible to calculate its response to arbitrary pulsed excitation. Note that the TDSE simulations to obtain these data sets require a significant, but only one-time numerical effort.

5.2.5 Comparison with TDSE solutions

To demonstrate that the nonlinear response can be calculated the same way also for a more realistic system, we have generated time-dependent solutions of the Schrödinger equation for our hydrogen-like system, exposed to a near-infrared frequency pulse.

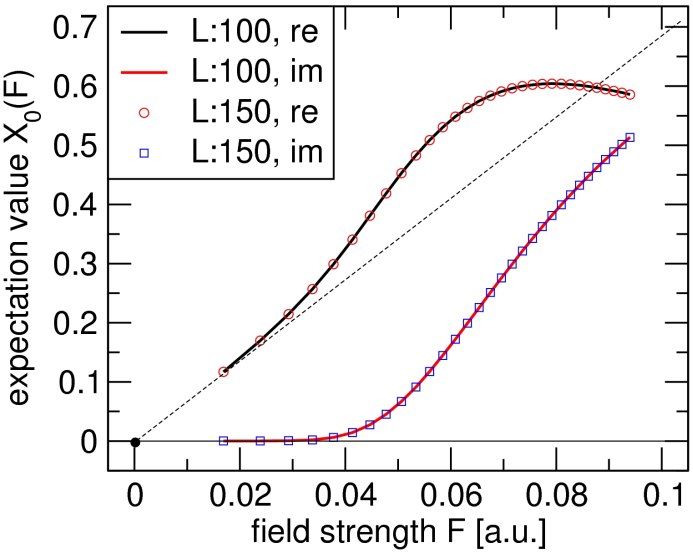

FIGURE 5.4. Complex-valued dipole moment of a 3D Hydrogen-like model atom, measured in the metastable state born from the ground state as a function of the external field strength. Data obtained for two computational domain size L are shown, indicating fast convergence.

For comparison purposes, we remove the linear polarization from our numerical solutions. We also remove a low-frequency background which only contributes to the THz generation that would not not affect dynamics of the driving infra-red pulse.

Figure 5.5 shows an example in which both Kerr-like and plasma-like responses show up in the leading and trailing edge of the pulse, respectively. Regimes like this one, when counter-acting components of the nonlinear response manifest themselves on similar scales are of utmost importance for extreme nonlinear optics, since the filamentation physics is naturally influenced by this kind of dynamic balance.

We have chosen the shape of the excitation pulse to have a flat middle portion in order to better visualize different processes that would control the dynamics of the propagating pulse. In the leading edge of the pulse, the polarization is in phase with the optical field. During this time, the self-focusing response dominates. In the trailing edge, in contrast, we see the response being out of phase, which is a sign that it acts mainly as a defocusing mechanism. In the temporal middle of the pulse one can see that the two compete. Importantly, the agreement between the numerically exact and the response calculated with the proposed model is rather good.

5.2.6 Application example: Femtosecond filamentation

As an illustrative example of the utility of MESA we consider a femtosecond filament created by a 30 fs optical pulse propagating in a model gaseous medium. The medium

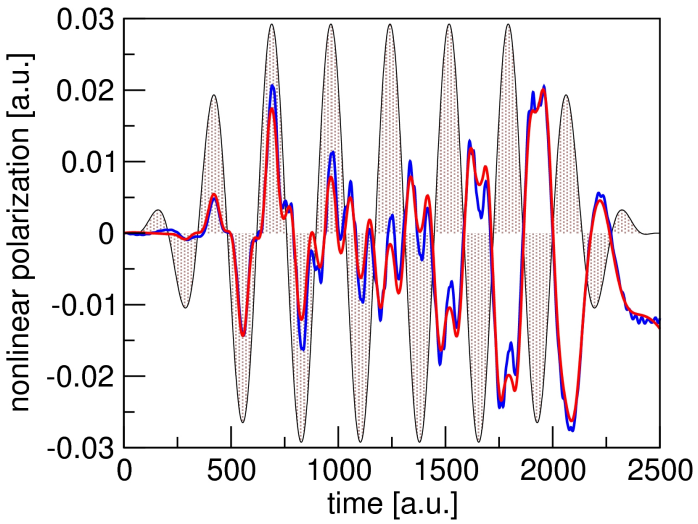

FIGURE 5.5. Nonlinear response of a hydrogen-like system to a $\lambda = 2\mu$m driving pulse indicated by the shaded area(s). The exact TDSE response is shown in blue dashed line, and the resonant-response model result is shown in red.

consists of atoms at atmospheric pressure, each responding to the optical field as described above. Besides the nonlinear atomic response, the medium has a linear susceptibility which we choose the same as that of air. This is implemented as a part of the linear optical propagator [11]. To execute the simulation, we utilize the generalized unidirectional pulse propagation equations framework (gUPPEcore) [116] with a medium-module that implements the MESA response.

The parameters of our illustration are chosen to create a situation in which several processes affecting the dynamics act simultaneously. In particular, we choose the wavelength $\lambda = 2$ μm, for which the generation of new harmonics, along with their subsequent "temporal walk-off," are more relevant than for 800 nm pulses. Furthermore, we assume relatively tight focusing geometry, with $f = 50$ cm. This is to verify that the defocusing properties of the model are sufficient to arrest the self-focusing collapse which is made more severe by the external focusing.

Figure 5.6, showing the on-axis energy fluence versus propagation distance for two different initial pulse intensities, demonstrates that it is indeed the case. The defocusing effects are mainly due to free electrons. Figure 5.7 shows the linear density of freed electrons generated versus propagation distance. The model accounts for the corresponding energy losses via the imaginary part of the induced dipole moment.

Figure 5.8 shows the spectrum for propagation distances just before and after the filament. Well-defined harmonic orders are obvious before the collapse: They give rise to an additional collapse regularization that is much stronger than for $\lambda \sim 800$nm. Eventually, extremely broad supercontinuum is generated in the filament (full line).

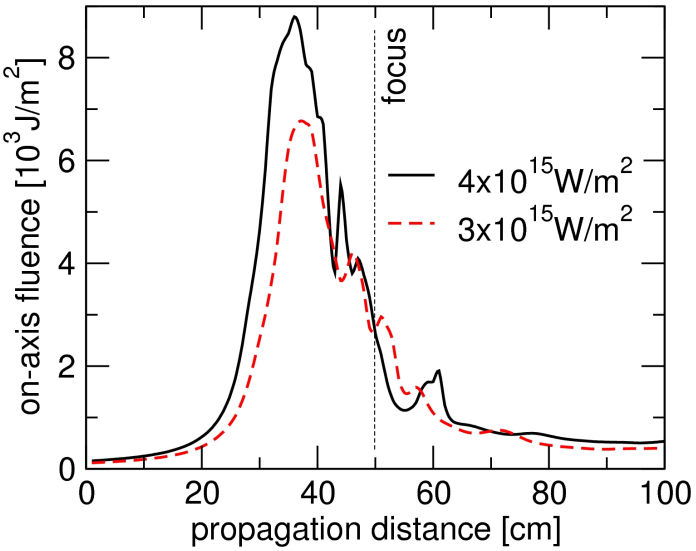

FIGURE 5.6. On-axis energy fluence in a filament created by 30 fs, $\lambda = 2.0\mu$m pulse. The two curves represent simulations with the indicated initial intensity.

In contrast to the more studied near-IR regime, at this and still longer wavelengths the spectral dynamics coupled with the dispersion properties of the medium become the most important physical mechanism controlling filamentation. It thus becomes crucial that properties of third- and fifth-harmonic generation, together with the free-electron generation, and accompanying energy losses, are all modeled in a unified manner, so that as the wavelength is varied all processes are included in correct proportion.

Importantly for our demonstration, all relevant effects are captured in a self-consistent way, without the necessity and even possibility of parameter tuning. To our knowledge this is the first demonstration of a filament simulation *on an experimentally relevant scale* in which the light-matter interaction description relies on first principles.

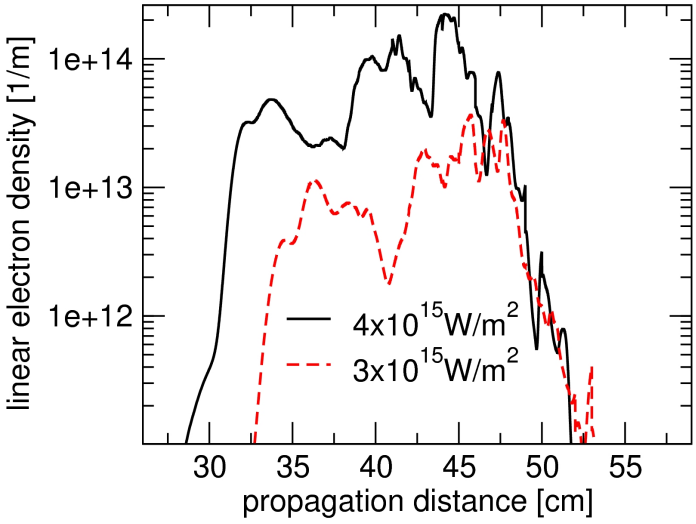

FIGURE 5.7. Free electrons generated per unit of propagation length.

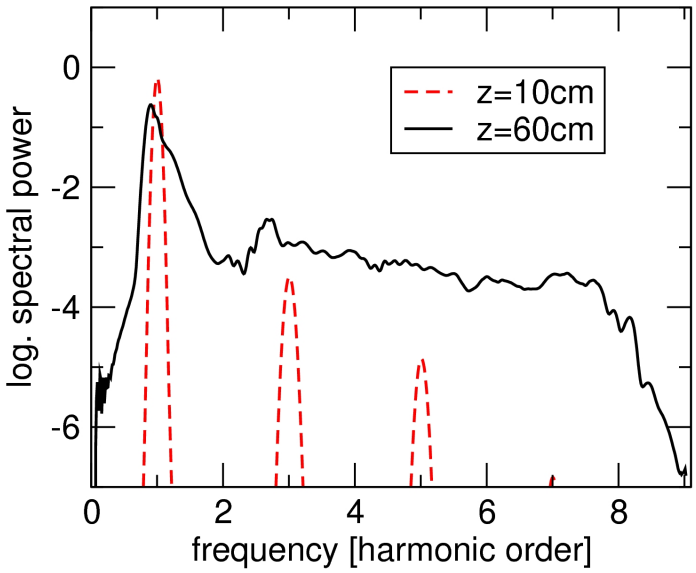

FIGURE 5.8. Supercontinuum generation in a femtosecond filament. Spectrum before the collapse exhibits well-separated harmonic orders.

5.3 Subcycle pulse engineering

For the second application of resonances, we unveil the sub-femtosecond dynamics of light-matter interactions and show that ionization is not an instantaneous process and, on the contrary, exhibits a marked memory effect. This conclusion is supported by numerically solving the time-dependent Schrödinger equation (TDSE). Moreover, we also employ an exactly solvable 1D Dirac-delta atom model [79] that allows one to capture the light interaction with the atom, and reveals the same memory effects observed with the full TDSE. The memory effects described here imply that the plasma densities will differ and depend on the specific sub-cycle shape of the laser pulse waveforms as a result of the attosecond scale ionization dynamics that are not captured by standard models. In order to highlight this, we compare two specific waveforms that deliver identical plasma densities in the standard model but differ significantly when simulated using both the TDSE and the exactly solvable 1D Dirac-delta potential model.

Of course, the fact alone that ionization depends on the temporal structure of the driving field is not new. For example, Refs. [117] and [118] study the effects induced by chirp. In particular, [118] utilized very high frequencies and rather extreme chirps. Here we reveal history-dependence for long-duration wave-trains of optical-frequency fields. Moreover, we work in a regime characterized by significantly lower intensities when per-cycle ionization yield remains very low, yet the effect continues to accumulate over long time-scales. In [117], the role of the precise wave-shape was demonstrated in the photo-electron energy spectra. It was explained by the standard dynamics of free electrons in the time-dependent external field in which the ion potential plays no role. The mechanism revealed in this section is different in that it requires presence of both the optical field and the interaction with the atom or ion. Moreover, the ionization yield differences we obtain in different driving waveforms are orders of magnitude larger than in [117]. In fact, they scale with the duration of the pulse. We will show that these novel features are intimately connected to the dynamics of the "to-be-ionized" electron wave-packet still weakly interacting with the atomic potential.

5.3.1 Model descriptions

We compare three models for describing the ionization process. The first is the standard approach that we described in Section 1.1 and is an ionization model commonly used in numerical simulations of light-matter interactions in ultra-short optical pulses and is based on the notion of the ionization rate, $W(E(t))$, which specifies the number of atoms ionized per unit of time in the field of strength E. In this approach, the history of the system exposed to the time-dependent electric field of the optical pulse is irrelevant. The rate of free electron production only depends on the instantaneous value of the electric field $E(t)$ or, alternatively, on the cycle-averaged intensity $I(t)$.

An estimate of the rate W is usually obtained from, e.g., PPT theory, and is often parameterized in the form of an effective power-law. Alternatively, a tabulation of W can be used. Irrespective of the actual implementation, the important feature present in virtually all current simulations is that the ionization rate does not depend on the history of the system. In the regime of weak ionization, the survival probability for an atom to remain not ionized can be calculated as $p(t) = 1 - \int_{-\infty}^{t} W(E(\tau))d\tau$.

The second model used to detect the quantum memory effects is the time-domain 3D Schrödinger equation solved numerically for a single active electron atom model,

$$i\partial_t\psi(\rho, z, t) = -\frac{1}{2}\Delta\psi + V(\rho, z)\psi + F(t)z\psi \tag{5.15}$$

with a Coulomb potential V and a time-dependent field strength $F(t)$, which represents the electric field of an optical pulse. The computational domain is endowed with perfectly matched layer (PML) transparent boundary conditions to absorb the outgoing component of the field-driven wavefunction. The observable of interest is the norm of the wavefunction $|\langle\psi(t)|\psi(t)\rangle|^2$, with its decay interpreted as a measure of ionization [35].

For the third model, we employ the exactly solvable 1D Dirac-delta quantum system. For our purposes here, it is important to recall that the spectrum of this system consists of a single bound (ground-) state plus a continuum of positive energies corresponding to "free" states [51]. As soon as an arbitrarily weak field F is switched on, the continuum spectrum extends over the whole real axis, and the ground-state is transformed into a decaying resonant state, highlighted in red in Fig. 4.3. There is also an infinite set of short-lived resonances (metastable states) which correspond to the quasi-localized wave-packets temporarily trapped between the classically forbidden territory (due to the external field potential) and the binding Dirac-delta potential. These resemble Fabry-Perot resonances in that their complex energies are approximately equidistant with positive real parts. These states located near the real axis in Fig. 4.3, correspond to positive energies which would not be bound in the absence of the external field. However, their wavepackets spend enough time in the vicinity of the atom potential that they can "remember" the history of excitation. Note that the quantum-particle current due to the external field is completely classical in the absence of the atomic potential. Consequently, electronic states must be able to survive close to the ion in order to exhibit any dependence on the history of the excitation.

There exists yet another family of resonances (along the angle $-2\pi/3$ in Fig. 4.3) corresponding, roughly speaking, to the negative continuum energies (in the field). These states are coupled to the ground-state resonance because of the time-dependence of the external field, but have exceedingly short lifetimes. As such they act as to renormalize the decay rate of the resonant ground state.

Here we take advantage of the fact that we have the exact solution for the induced dipole moment (2.38)-(2.41) and current (2.35)-(2.37), and the survival probability

of the ground-state can be calculated exactly after the laser pulse has passed. The observable most suited for the present purposes is the value of the wavefunction at $\psi(z = 0, t)$, i.e. at the point where it "overlaps" with the contact potential. The reason we utilize this particular quantity is twofold. First, its value for times after the driving pulse has passed represents the population of the ground state. Second, its temporal evolution during the pulse reveals high-frequency oscillations due to the resonant states which mediate the memory effects we aim to study.

Besides the certainty that comes with an exact solution, the rationale behind using this Dirac-delta atom model is that it allows us to demonstrate that the existence of bound states is not a necessary condition for occurrence of quantum memory effects. Indeed, this system has no other bound states other than the ground, yet the short-lived resonances turn out to be sufficiently stable to cause the dependence of the effective ionization rate on the history of the system.

5.3.2 Excitation with synthesized waveforms

To construct pulsed waveforms with attosecond scale temporal features, we superimpose multiple harmonics as in Ref. [119] resulting in a delta-like train of peaks that are achieved by adding all harmonics in phase and with equal amplitudes. A similar pulse train, but with opposite sign of the electric field is then generated and delayed with respect to the first. Fig. 5.9 shows waveform A (left panel and red-dashed line in right panel) obtained by choosing the delay $\tau_d = 0.5T$ (with T being the fundamental cycle period), such that the high-intensity pulses of opposite polarity are equidistantly spaced in time and waveform B (black-solid line in right panel), with $\tau_d = 0.3T$, which results in a pattern of strong-intensity pulses of opposite sign that hit as a fast double-pulse, after which a longer period of relatively low-intensity follows. Any ionization model that neglects the history of the system will predict that these two waveforms yield essentially identical ionization rates. This is demonstrated in Fig. 5.10 (left) which shows the survival probability of an atom described by the standard ionization model. The small deviation is to be attributed to the differences of the relatively weak "backgrounds" in the two driving waveforms.

Next we examine how this behavior changes when the full quantum dynamics is accounted for in the TDSE simulated model atom. We have examined a range of intensities and wavelengths, and found that memory effects exhibit strong influence on the effective ionization rate, as summarized in the following.

The right panel of Fig. 5.10 shows the comparison of the survival probability of the atom when it is exposed to the waveforms A or B derived from the fundamental wavelength $\lambda = 800$ nm. We find that the total ionization displays a remarkable difference, with waveform A roughly three times stronger than waveform B. This is a clear evidence that when shaping waveforms at the sub-femtosecond scale, non trivial light-matter interaction dynamics will occur that are not captured by the "stationary" ionization rates.

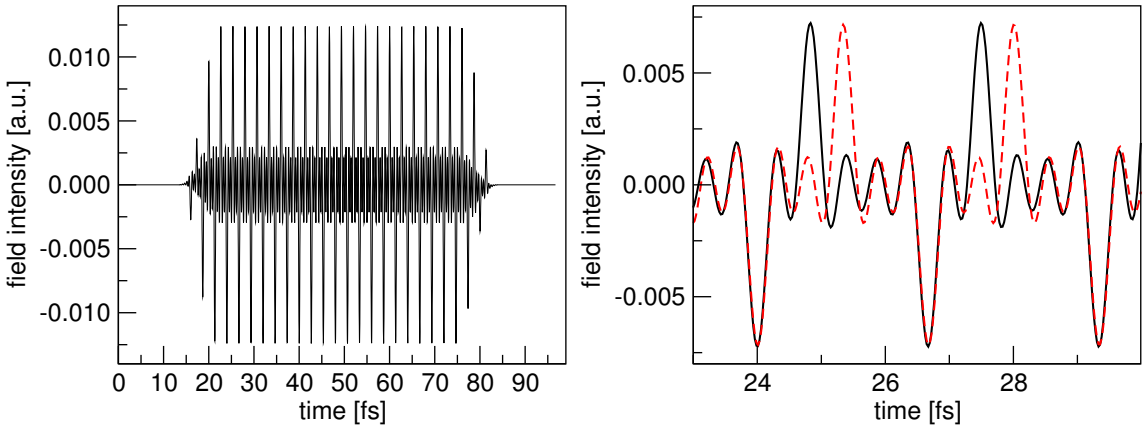

FIGURE 5.9. Synthesized sub-cycle pulse trains. The left panel shows the intensity versus time (in femtoseconds). Only pulse train A is shown because at this scale waveform B looks the same. The right panel shows two fundamental periods in both pulse streams. Note that the strong unipolar impulses are the same in amplitude, and only differ in their relative timing.

We may expect that the history-dependent effects must disappear at sufficiently slow driving, as one should then enter a fully adiabatic regime. The onset of this behavior can indeed be observed in Fig. 5.11. The left panel is obtained for $\lambda = 1200$ nm. Here, the difference in the ionization rates becomes smaller, though its is still very pronounced. Interestingly, it is now waveform B that is causing stronger ionization. This behavior is likely be due to a resonance, possibly in conjunction with the Stark-effect induced shifts in the spectrum of the system. Which waveform is more ionizing is not only system-specific, but also may depend on the intensity of the driving field.

Finally at even longer wavelength $\lambda = 2400$ nm, the right panel of Fig. 5.11 shows that memory effects become negligible, and the ionization is essentially the same in both waveforms. As expected for this long wavelength we have entered the adiabatic regime, in which the system follows the instantaneous value of the driving field and the relative timing between unipolar impulses is therefore unimportant. The transition into the adiabatic regime occurs similarly for the exactly solvable Dirac-delta system. In that case it is also possible to show analytically that non-adiabatic corrections scale with $1/\lambda^2$.

We have thus seen that the ionization efficiency *differences* depend on the fundamental wavelength and thus on the spectral content of the electric field waveform. The fact that the two types of excitation can result in larger or smaller ionization rates at different wavelengths suggests that resonances mediated by the bound states of the atom affect the outcome. One could thus assume that the existence of multiple bound states is a necessary condition to observe memory effects in the ionization.

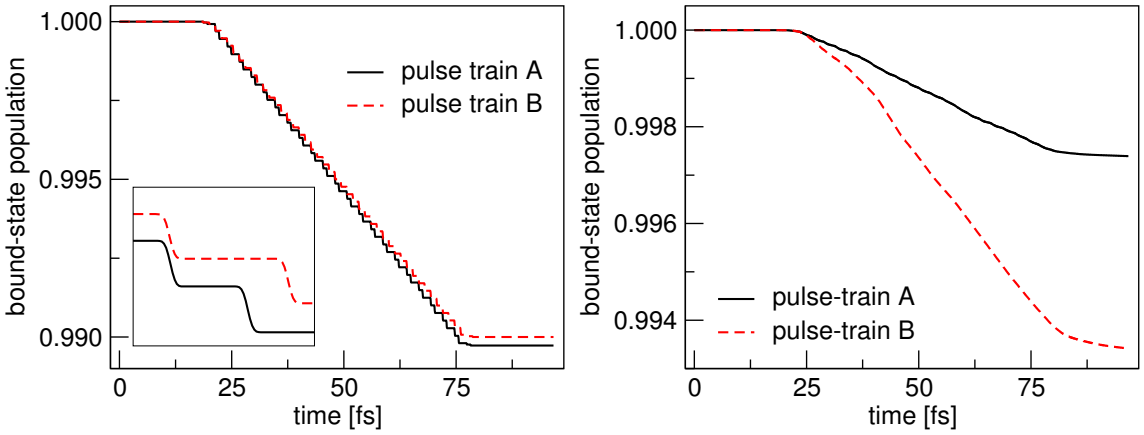

FIGURE 5.10. Survival probability (non-ionization) of a model atom as calculated by the rate-ionization model (left panel) and according to the TDSE (right panel). The effective multiphoton order for the rate model is $K = 6.5$ and the ionization cross-section is chosen such that the final ionization probability in pulse train A is 1 percent. The fundamental excitation wavelength is $\lambda = 800$ nm. The inset in the left panel shows a detail of the bound-state population vs time, and illustrates that the most of the ionization occurs during the strong electric-field impulses. These "steps" are smoothed out in the TDSE measurement due to the size of the computational domain.

However, as we demonstrate in the following, it turns out that the mere existence of a single bound state (e.g. the ground state) in conjunction with the energetic continuum is sufficient for the coherent memory effects to set in as soon as the driving waveform is sufficiently "fast."

In order to show this, we employ the exactly solvable 1D Dirac-delta potential model to investigate waveform timing effects in the ionization and dynamics of the driven quantum system. Figure 5.12 shows the behavior of the wavefunction amplitude $\psi(x = 0, t)$ when the system is exposed to the same pulse trains we used above for the more realistic atom model. Its final value after excitation ceases is a direct measure of the non-ionization survival probability. Comparison of the two panels reveals that the ionization yield is drastically dependent on the timing of the electric field pulses. In other words, the system exhibits memory, as it makes a difference whether an equivalent electric field impulse follows quickly after a previous one. This effect is further illustrated in Fig. 5.13 which shows a zoom into Fig. 5.12. A feature to note is the different amplitude of the wavefunction oscillation immediately following the second field impulse. Ref. [109] showed that in the adiabatic approximation, it is exactly the amplitude of the metastable state born from the ground state that describes the wavefunction of the system and in particular $\psi(x = 0, t)$. The latter, when calculated in such approximation shows a smooth curve slaved to the optical

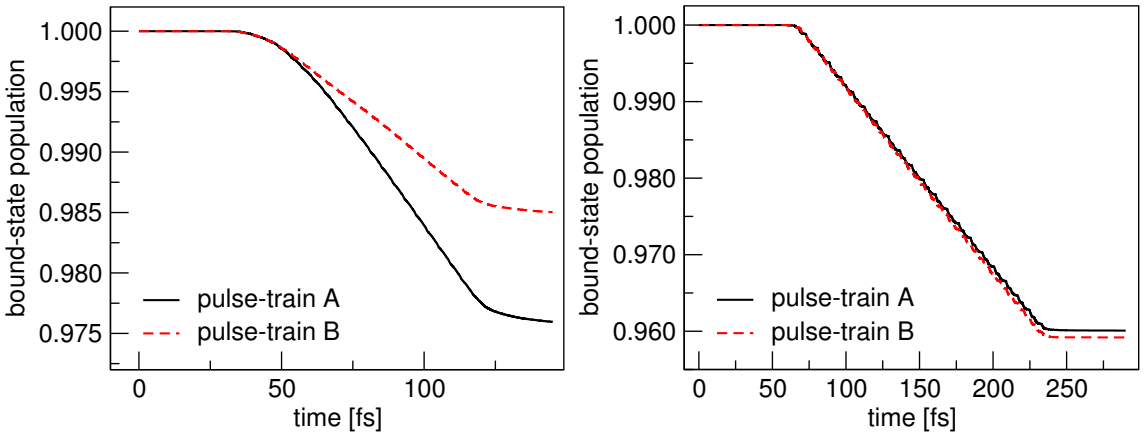

FIGURE 5.11. Ionization in synthesized pulse trains for fundamental harmonic wavelengths $\lambda = 1200$ nm (left panel) and $\lambda = 2400$ nm (right panel).

field and has no dependence on the history. This tells us that what we see is the interference between the ground-state amplitude and the resonant states near the real axis shown in Fig. 4.3. The stronger "ringing" caused by the waveform A suggests that the increase in the ionization yield is mediated by these resonant states. It is clear from these simulations that the quantum systems remember past ionization dynamics and that their response is not only due to the instantaneous field value. If we are to improve the current medium models, then we must take into account the effects of memory.

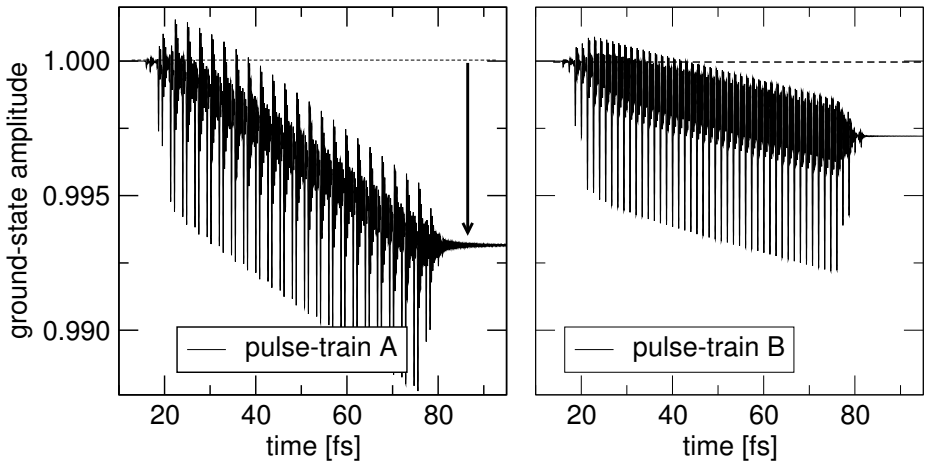

FIGURE 5.12. Exactly solvable 1D Dirac-delta potential model exposed to a multicolor time-dependent driving field. Ground-state amplitude $\psi(x = 0, t)$ is shown as a function of time. It exhibits adiabatic following of the driving field (large-scale variations) together with high-frequency oscillations due to interference between the ground and continuum states (causing, in particular, excursion exceeding unity). The final value after excitation reflects ionization (indicated by arrow) and shows that different pulse timings result in different effective ionization rates.

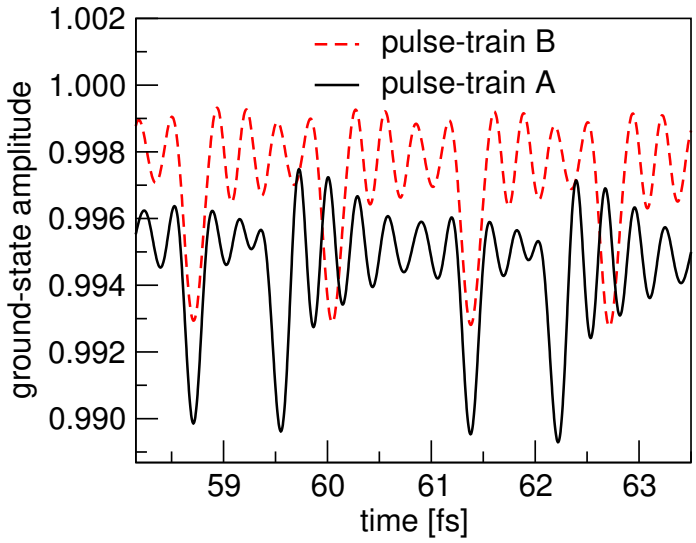

FIGURE 5.13. Zoomed-in view of resonance excitation on the same data as shown in the previous Figure 5.12. Plots illustrate "shaking" of the electronic wavefunction in the external field. Note the increased amplitude of oscillation after the second impulse in pulse train A. These oscillations are due to excitation of the resonant states found near the real axis in Fig. 4.3.

5.4 Carrier wave effects

For the third application, we investigate how carrier-wave shaping via multicolor optical fields plays an important role in nonlinear optical regimes in which the atoms and/or molecules become partially ionized and freed electrons are driven by the strong optical field. A prominent example of this is the use of two-color fields to control High-Harmonic Generation (HHG) and emission of attosecond pulses. In contrast there has been relatively little work on the effect of such pulse shaping on the refractive part of the nonlinear response, nominally due to bound electrons, which affects propagation via self-phase modulation in space or time. In particular, while the role of the carrier-envelope phase on optical filamentation has been investigated, multicolor optical fields present a more formidable theoretical challenge due to the large spectral bandwidth that must be captured.

Several recent experimental and theoretical works have appeared that unveil surprisingly pronounced effects related to the subcycle shape of the pulse temporal waveform, and the present work has been inspired by such experiments. More specifically, the idea of subcycle engineering of optical filamentation formation by means of a weak third-harmonic (TH) seed pulse was proposed by Béjot et al. [120, 121], and the same group also showed that secondary radiation created by optical filaments can affect their subsequent propagation [122]. In this way the precise shaping of the carrier-wave on the sub-cycle scale, with concomitant modification of the filament, was demonstrated to control both the density and spatial distribution of the generated plasma.

An even earlier series of experiments performed at the University of Central Florida stands out and highlights the surprising influence seed pulses can have on optical filamentation [123, 124]. They showed that a strong supercontinuum enhancement can be achieved by means of a seed pulse with energy significantly smaller than the filament. To the best of our knowledge the interpretation of this finding is still incomplete, and the standard simulation and modeling approach fails to explain how such a *weak seed pulse* can give rise to such pronounced effects.

The fact that weak seed fields can control the propagation, spectral content, and plasma generation for optical filaments that are orders of magnitude stronger is very intriguing, and underpins the questions we address in this work. Specifically, in Ref. [121] the mechanism through which a weak TH pulse affects the dynamics of two-color ionization was identified using time-domain Schrödinger equation (TDSE) simulations, and a phenomenological model utilizing a large number of parameters was proposed. Here we address whether a full TDSE treatment is indispensable, or it is possible to capture these effects using a simpler, though still microscopically founded, scheme that can be readily integrated into pulse propagation simulations.

Another question concerns the underlying physics: Is there an alternative and perhaps more intuitive view than the mechanism put forward in [121], namely quantum interference between ionization channels involving different color photons? In this

work we identify local temporal peaks in the composite electric field as the unifying, most important effect that underlies both the supercontinuum and plasma generation control with weak seed pulses. Utilizing and comparing an exact quantum treatment to a quasi-static approximation based on the single-state Metastable Electronic State Approach (ssMESA) [83], we show that an adiabatic description, in which the response of the system does not depend on the previous evolution but only on the instantaneous value of the electric field, is sufficient to capture all qualitative features of the above mentioned experiments.

We employ numerical simulations of optical filamentation in a two-color pulse comprising both pump and seed with full spatial and temporal resolution. In order to address the question of what is the necessary level of treatment of the light-matter interaction, we employ two atomic models coupled to the gUPPEcore pulse propagation solver. The first model involves a one-dimensional hydrogen-like atom with a Dirac-delta [51] potential driven by the external time-dependent field due to the optical pulse. The conceptual simplicity of this idealized approach serves two purposes in this work: First, the fact that a model with a single bound state can capture the essential dynamics implies that the underlying mechanisms do not depend on the details of the discrete atomic spectrum. In particular, we can show that the ionization enhancement in a carrier-shaped field does not depend on the increasing density of states below the ionization threshold or on transient Freeman resonances [125] and/or Stark shifts in strong fields. This sheds additional light on the TDSE-based interpretation given in [121].

The second rationale for utilizing this particular system is that we can take advantage of the existence of an exact solution for the nonlinear polarization and current density induced by an arbitrary time-dependent field [51, 79, 126]. It makes it feasible to integrate the spatially resolved pulse propagation modeling with the numerically exact solution for the nonlinear response of the quantum system, were the latter is evaluated at every point of the spatial computational grid encompassing the whole focal volume. Such a task would be prohibitively expensive should one use a 3D quantum model.

The second light-matter interaction model uses the ssMESA for noble gas atoms [127]. We start from the Single Active Electron (SAE) models of noble gas atoms, utilizing the SAE potentials given in [128]. For a specific model of an atom, numerical simulations of the corresponding Schrödinger equations are used to collect the necessary input data. Figure 5.14 illustrates the properties that are extracted from such a simulation for the case of Argon, i.e. the nonlinear dipole and imaginary energy versus field strength F, both given in atomic units [a.u.]. While ssMESA does not use the nonlinear index n_2 per se, the n_2 values extracted from the full nonlinear response compare favorably with the measurements shown in Ref. [127, 129]. This approach is microscopically self-consistent in the sense that nonlinear polarization and the ionization rate are automatically in correct proportion, and as such it is an

ideal test bed.

In order to identify the minimal quantum-based description required to capture the effects under discussion, we do not apply any of post-adiabatic corrections to ssMESA described in [83]. This results in a model in which both the nonlinear polarization and the ionization rate depend only on the instantaneous value of the electric field. By demonstrating that this description successfully captures all features of the dynamics seen in the experiment of [120, 121], we are able to deduce that the enhancement effect is essentially adiabatic and that retardation effects in the quantum light-matter interaction do not play a dominant role.

Finally, to perform spatially resolved pulse propagation simulations, the nonlinear interaction models described above are supplemented with the linear frequency-dependent susceptibility for the medium. In particular, we use the refractive index versus wavelength taken from [69, 130] as inputs for our spectral gUPPEcore simulator.

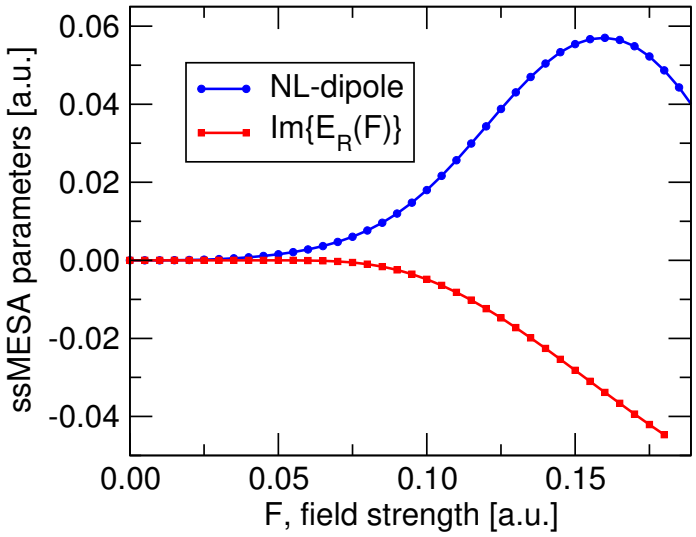

FIGURE 5.14. Argon atom model and the representation of its response in the single-state MESA. In the adiabatic approximation the atomic response is described in terms of the nonlinear dipole moment (w.r.t. field strength) of the Stark resonance connected to the ground-state, and the imaginary part of the resonance's energy (all quantities in atomic units).

We characterize the input field by the nominal pulse and beam parameters that would be attained at the point of the geometrical focus were they propagated linearly. Our first numerical experiment uses a tightly focused pulsed beam: This geometry reduces propagation effects, and emphasizes the role of the nonlinear response. The gUPPEcore solver was used to numerically propagate two 12 fs (FWHM) pulses, the pump pulse of wavelength 796 nm with an intensity of 1×10^{18} W/m^2, and

the seed pulse of wavelength 266 nm with an intensity of 1×10^{16} W/m^2. The relative phase delay of the seed pulse was varied between 0 and 2π with respect to the pump. Both pulses were given a focused spot size radius of 10 μm. Two numerical experiments were simulated using identical pulse properties. The first utilized the exactly solvable Dirac-delta model with the ionization potential adjusted to that of Hydrogen or Argon, and the second simulation was done with an ssMESA-based model of Argon.

First we used the exactly solvable Dirac-delta model in a simulation of ionization yield in a pump-seed configuration in which the phase of the third-harmonic seed pulse controls the ionization yield. In particular, the results in Fig. 5.15 reproduce the behavior observed in the experiment [120] in that the ionization yield is a periodic function of the TH phase. Here the ionization yield is characterized using the linear electron density in inverse meters, obtained as the transverse integrated electron plasma density. Furthermore, the ionization yield enhancement is significant despite the small TH energy compared to the pump, thereby validating that the one-dimensional atomic model can capture the enhancement. We note, however, that the phase of the curve depicted in Fig. 5.15 is slightly shifted, with the minimum located somewhat beyond $\phi_{\mathrm{TH}} = \pi/2$ where one would expect destructive interference between the pump and the third-harmonic seed pulse. We can intuit this by noting that our definition of the relative phase between the pump and control pulses is with respect to linear propagation. It is therefore not unexpected to observe a shift caused by accumulation of nonlinear phase during the pulse propagation, despite the tight focus geometry.

The next question we address is whether it is necessary to retain the full time-dependent quantum dynamics implicit in the exact model to capture the oscillations in Fig. 5.15. In a comparative simulation we use ssMESA which is based on a single-electron approximation within the adiabatic approximation. We use Argon for our simulated medium in a fully resolved propagation simulation of a tightly focused pulse. The simulation results for the corresponding linear electron density are shown in Fig. 5.16(a) at the point of linear focus. In accordance with the experiment, and in qualitative agreement with the simple exact model results shown in Fig. 5.15, the ionization yield is seen to be a periodic function of the relative carrier phase between the pump and the weak third-harmonic pulse. Inspection of the electric field carrier wave, shown in the insets in Fig. 5.16(a) and in Fig. 5.16(b), reveals that the occurrence of enhanced peaks in the temporal profile closely correlates with the higher ionization yield. Thus even though the third harmonic seed has a relatively small power, the concomitant local field enhancement and a crossover from flattened to sharp carrier-wave peaks is evident and indeed underpins the enhanced nonlinear absorption.

Overall, the shape of the ionization yield plot is similar to that obtained with the exact quantum treatment, and this allows us to deduce that the ionization enhance-

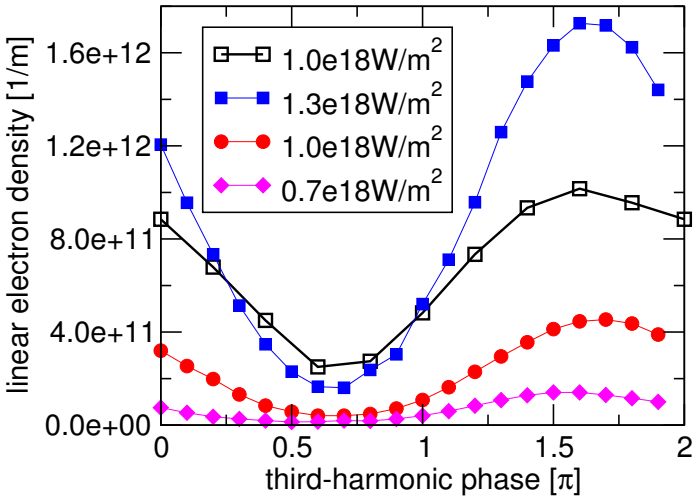

FIGURE 5.15. Ionization yield in a pump pulse seeded with a weak third-harmonic pulse. The curves show the number of electrons generated over the the whole cross-section of the beam at the propagation distance corresponding to the linear focus. This simulation result was obtained with the Dirac-delta quantum system (open symbols: $E_g = 13.6$eV, filled symbols: $E_g = 15.6$eV with density scaled $5\times$). The method utilizes an exact solution capturing all potential quantum coherence effects and possible dependence on the history of the system.

ment is adiabatic in nature. In other words, it can be described with a model in which the ionization rate depends solely on the instantaneous value of the driving field but not on the previous history of the driven atom. This is a welcome observation from the simulation and modeling standpoint, as it means that instead of a full solution of the Schrödinger equation coupled to the nonlinear pulse propagation, one can utilize computationally less expensive approximations, such as ssMESA.

Next we show that the qualitative picture does not change when propagation effects start to play a role. The following simulations correspond to the experiment of Béjot et al. using a 1mJ, 100fs, 796nm pump pulse with a 30μJ TH seed. To explore both short and longer filamentation regimes, the pulses are focused to a beam waist of 25μm (Fig. 5.17) or 150μm (Figs. 5.18 and 5.19).

As shown in Fig. 5.17 for the short filament, the ssMESA model captures both the ionization yield enhancement, and the significant spectral power increase in the $600-700$ nm region (c.f. Figs. 3h, 3i in [120] (arxiv v.) — here we prefer to show the complete spectrum on the log scale), as well as the shortening of the plasma channel. Once again the qualitative experimental features are well captured on the basis of the adiabatic ssMESA without the need for TDSE simulations.

For a longer filament, it was shown experimentally that one can control the spatial modulation of the free electron density by adjusting the relative phase of the third

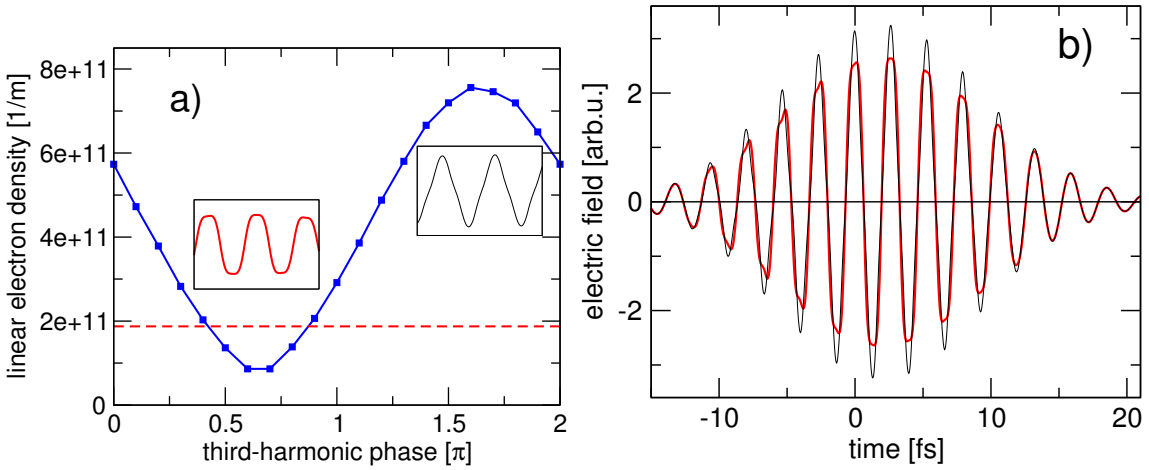

FIGURE 5.16. a) Ionization yield in a pump pulse seeded with a weak third-harmonic pulse. This simulation utilized a model of Argon based on the single-state MESA. The dashed line represents the ionization yield without the harmonic seeding. The insets show the shape of the carrier wave corresponding to minimal and maximal plasma production, and the overall pulse profiles for the two cases are compared in b). This result indicates that the ionization enhancement is driven by the local peaks in the electric field profile.

harmonic seed pulse [120], and ssMESA can faithfully reproduce this effect also. Figure 5.18, which should be compared with Fig. 4 in Ref. [120], shows that in a longer filament the electron density exhibits oscillations as a function of the propagation distance. This longitudinal modulation can be controlled by the TH pulse timing, which shifts the "phase" of the plasma density modulation curve according to "movement" of locations over which the seed pulse interferes with the pump constructively. Fig. 5.19 illustrates how this behavior depends on the gas pressure: The plasma modulation depth and the modulation "wavelength" both decrease with the gas density, reflecting the gas density dependence of the phase-velocity difference between the pump and third-harmonic wavelengths. This behavior, which reproduces the pressure dependence seen in the experiment, further indicates that propagation effects play a minimal role in the given setting, and that the essential physics is controlled by the single-atom response to the carrier-shaped optical field.

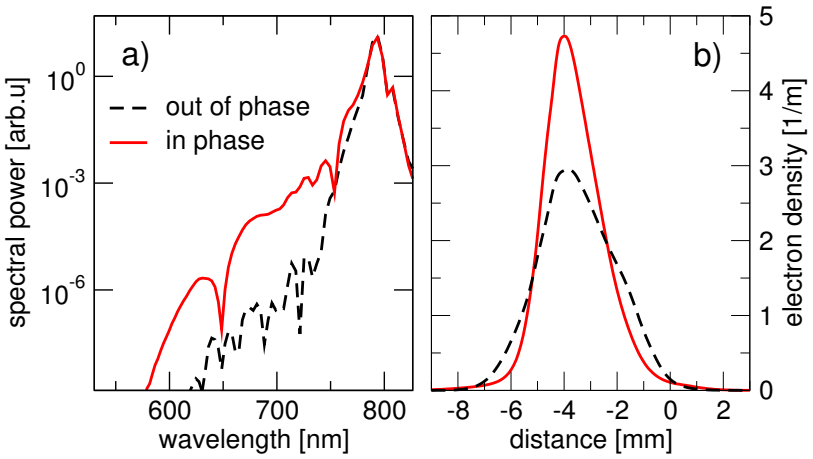

FIGURE 5.17. Carrier-shape effect in a short filament. When the third-harmonic and fundamental fields align in phase in the focal region, the supercontinuum spectrum (a) and plasma generation (b) is significantly enhanced, while the FWHM length of the filament shortens.

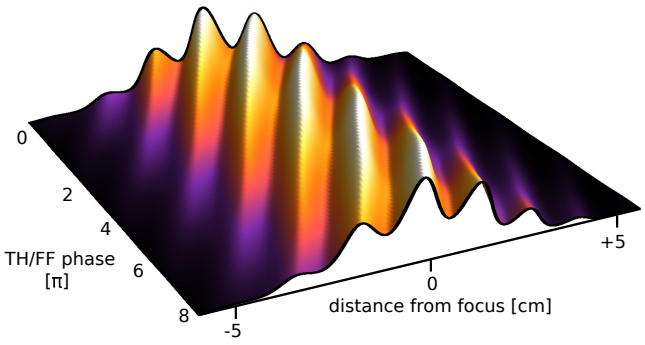

FIGURE 5.18. Ionization yield in a loosely focused filament, using an ssMESA Argon model. The plasma density exhibits a modulation which can be shifted forward or backward by adjusting the pump-seed carrier phase.

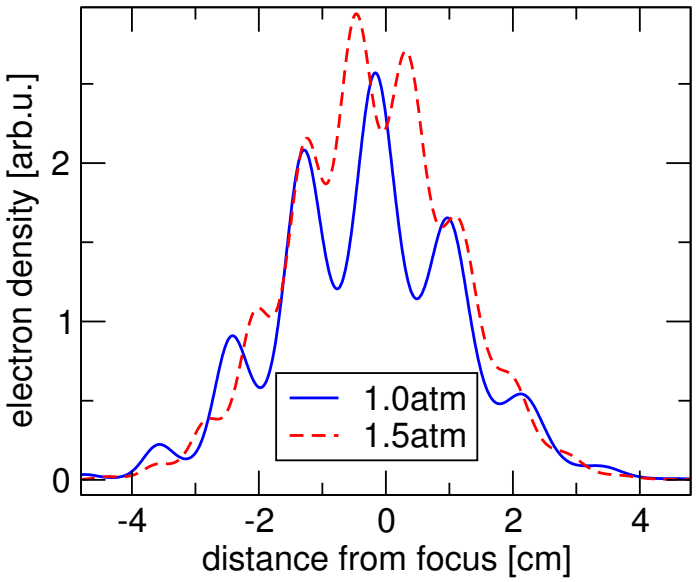

FIGURE 5.19. The modulation of the spatial plasma density distribution depends on the pressure, and reflects the walk-off distance between the phases of the pump and the seed waves. Density profiles shown were scaled in order to show that the density-modulation length is inversely proportional to the gas pressure.

5.5 Summary

We have shown in this chapter that metastable states can be useful in investigating nonlinear phenomena. We have introduced the metastable state approach for calculating the ultrafast, off-resonant nonlinear optical response of gases, and demonstrated its accuracy and computational economy. As a test bed we employed a 1D atomic model that allows for comparison of MESA against exact solutions, and excellent agreement between the exact and approximate results were obtained for the nonlinear optical response even using only a single metastable state in adiabatic approximation. We have also identified post-adiabatic corrections which are responsible for the slight increase of ionization rate, and for losses that the optical field suffers as a consequence of ionization. The approach was also applied to a 3D hydrogen-like model with similarly good agreement between MESA and TDSE simulations. As a demonstration of the computational economy of MESA an example of optical filamentation was presented. We note that MESA yields a model for the ultrafast nonlinear optical response with no free parameters for a given gas. Importantly, from a practical simulation point of view, the approach has a computational complexity comparable to that of the standard light-matter interaction model used in optical filamentation. In this sense the method provides a microscopically founded replacement.

We then moved on to show that in the non-adiabatic regime the atom dynamics, and in particular ionization yields are strongly influenced by "field-dressed, weakly bound states", i.e. electronic states that survive in the vicinity of the atom or molecule for some time, even if only for a fraction of the optical cycle and are thus exposed to both the atomic potential and to the driving field. These dynamically driven superpositions are able to "record" the history of the system and exhibit a strong response even to weak fields. History dependent effects may therefore occur even at low, readily achievable intensities and in driving waveforms with all frequencies much lower than the ionization potential with potential applications in molecular fragmentation dynamics [131] and in the general field of extreme nonlinear optics, e.g. high harmonic generation.

Lastly, we have shown that the variety of enhancements that can appear in seeded filament propagation, namely ionization yield, supercontinuum spectrum, and plasma extension, can be captured in simulations using a MESA based light-matter interaction model in its simplest form, namely without any post-adiabatic corrections, utilizing a single meta-stable state. This means that the mechanism is approximately adiabatic in the sense that the atom reacts mainly to the instantaneous value of the electric field in a two-color pulse, and that this process does not invoke quantum retardation effects and the outcomes exhibit little dependence on the history of the atom.

It may seem surprising that an effect which can be understood as interference between different channels of multi-photon ionization [120] can be qualitatively captured already at the quasi-static level. However, our interpretation of the two-color

effects neither reduces to a simple tunneling model nor is it in contradiction with the multiphoton picture. Indeed, the same way a TDSE simulation can seamlessly capture both the tunneling and the multiphoton regimes, and it does this without explicit invocation of multiphoton channels, the ssMESA, which builds on the same SAE potential as the TDSE, can straddle these different regimes. Of course, this is not to say that *quantitative* agreement with experiment, should absolute-scale measurements become available, would not require post-adiabatic corrections.

The important conclusion is that while quantum effects are clearly at play in optical filaments driven by broad spectrum pulses, it is not necessary to use a full time-domain Schrödinger equation to capture them. We have demonstrated that one also does not need to resort to painstaking adjustment of many degrees of freedom in a parameterized model [121] to fit the nonlinear absorption, refraction and ionization to achieve the displayed qualitative agreement with the experiment. We emphasize that in these simulations we used no adjustable model parameters, and the totality of the model atom response derives solely from the quantum model we utilized to describe the atom. Our findings thus make the prospect of practical modeling of filamentation driven by multi-color fields, including field propagation much more tangible.

Chapter 6
Open Questions

The theoretical framework presented in this dissertation opens up exciting new research opportunities as it is now possible to use a quantum description of the medium in ultrashort pulse propagation simulations. With any newly developed theory there are still unresolved questions to be answered.

The first open question is related to the completeness of the Stark resonant states. The 1D Dirac-delta potential and the 1D square well potential support at least one bound state and also two other families of resonances, one near the positive real energy axis (called "Right family" resonances) and another along the ray $\theta = -2\pi/3$ in the complex energy plane (called "Left family" resonances). Currently, it is unclear which resonant states contribute most to a model's polarization response, and if it is possible to approximate the model's exactly calculated response using only a finite number of resonances. In Section 4.6 it was shown that an expansion in terms of the resonant states of the 1D Dirac-delta potential model is partially complete. The Right family resonances can be used as a basis to represent an arbitrary function on the negative spatial axis, but not on the positive axis, and that including any of the Left family resonances exponentially deteriorates the agreement between expansion and original function on the positive axis. This limited convergence property may be a general property of Stark resonance expansions and therefore greatly affects their use as a medium model. In Section 5.2, the addition of a post-adiabatic correction energy (5.11) improved the correspondence of MESA's response to the exactly calculated time dependent solution of the 1D Dirac-delta model (see Figure 5.2). One key assumption of this correction is that for states evolving from the ground state, the system of resonant states $\{\psi_n\}$ is complete, and that the projection $1 - |\psi_0\rangle \langle\psi_0|$ accounting for resonances other than the ground state can be used. From the practical success of MESA, it appears that including some information about the resonance families qualitatively improves the model. The ability of the 1D Dirac-delta model to respond to the carrier's shape, as demonstrated in Section 5.3, supports this assumption as well. It was assumed that even though the model contains only a single bound state, the field induced excitations of the Right family resonances produce the dramatic change in ionization yield seen in Figures 5.12 and 5.13. Therefore the Right family does play some role in the medium's dynamics.

It is possible to test if including an additional finite number of resonances with the ground state improves the accuracy of the medium model, similar to MESA's post-adiabatic correction. This is done by calculating the depletion of the ground state for three resonance-based medium models, each containing a different num-

ber of resonances that belong to the 1D Dirac-delta potential. These are compared to the exactly calculated ground state depletion, which implicitly includes all resonances. Figure 6.1 compares the four models, each with ground state energy equal to $-15.76eV$, interacting with a $800nm$ laser pulse with duration $25fs$ and peak intensity $10^{18}W/m^2$. The population curve labeled G is calculated using only the ground state resonance and is essentially the adiabatic approximation. The curve labeled GR is from a model containing the ground state plus one of the Right family resonances, and the curve labeled GRL contains the ground state, one Right family resonance and one Left family resonance. The last model labeled Exact is the quantity $|\psi(0,t)|^2$ calculated from the exact time dependent solution for the 1D Dirac-delta model. This value corresponds to the ground state population after the pulse has passed and is the correct ground state depletion to which the other three models are compared. For this particular laser pulse scenario, the model including only the ground state resonance underestimates the depletion of the ground state, while the model which includes an additional resonance from the Right family overestimates the depletion. The model which includes a Left family resonance results in a final ground state population of greater than unity, which is unphysical. It is a surprising result since it was thought that the Left family resonances, with a large imaginary component of their energy, would decay very rapidly in time compared to the Right family resonances and would therefore play almost no role in the time dynamics. One possible explanation for this behavior may be found by inspecting the eigenvalue spectrum in Figure 6.2. As the resonance energies increase, the energetic spacing between resonances decreases. Given the coupling matrix element equation

$$\langle \partial_F \psi_n | \psi_k \rangle_D = \frac{F}{\alpha \left(E_n - E_k\right)^3} \left[\psi_n'(0^-)\psi_k'(0^-) - \psi_n'(0^+)\psi_k'(0^+) \right]$$

it becomes clear that higher energy states are more tightly coupled. Numerically calculating the real and imaginary parts of a system's coupling matrix elements also supports this claim, as illustrated in Figure 6.3, where the magnitude of the coupling elements for a resonance system containing the ground state plus the first five Right family resonances are illustrated. It may simply not be possible to include a finite number of Left or Right family resonances, given that the preferential coupling to higher resonant states will essentially drain ground state resonance of population (at least that is apparent for the Right family of resonances). It is perhaps necessary that any resonance-based model must account for all resonant states. To this end, one potential research avenue is to investigate whether a closed form solution exists for the summation of coupling terms in the time evolution equations

$$c_n'(t) = -ic_n(t)E_n(F(t)) + \sum_k c_k(t)F'(t) \langle \partial_F \psi_n | \psi_k \rangle .$$

Since what appears is essential a weighted sum over the off-diagonal dipole matrix elements $\langle \partial_F \psi_n | \psi_k \rangle = - \langle \psi_n | x | \psi_k \rangle / (E_n - E_k)$, perhaps some generalization of the

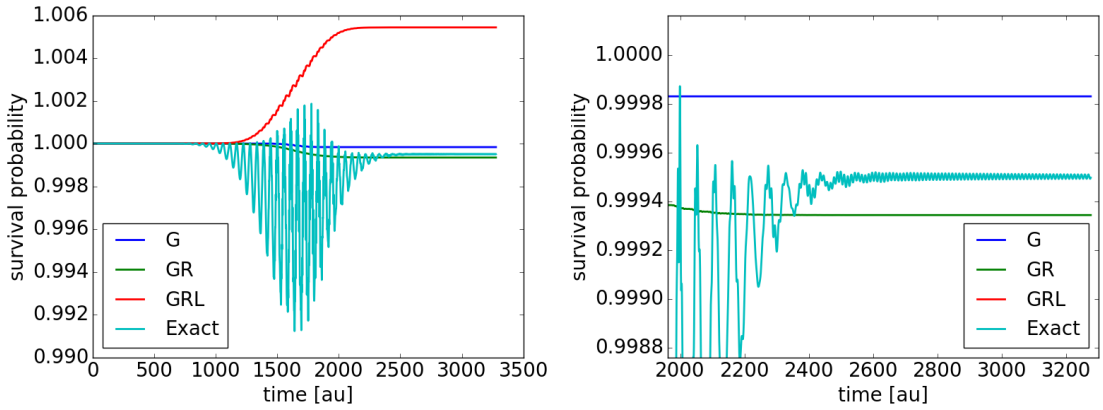

FIGURE 6.1. (Left) The time dependent survival probability (decrease in ground state population) for three resonance-based medium models (G, GR, GRL) containing the 1D Dirac-delta potential is compared to the exactly calculated ground state depletion. The labels signify which resonances are included in each model: G is the ground state, R is the first resonance in the Right family, L is the first resonance in the Left family, and Exact is the exact solution $|\psi(0,t)|^2$ whose value after the pulse has passed is equal to the ground state population. Including the R resonances can dramatically change the ionization dynamics and including the L resonances produces unphysical results. (Right) Zoomed in picture near the end of the simulation.

Thomas-Reiche-Kuhn sum rule [132, 133, 134, 135] (for an introductory text, see Wikipedia[1]) is possible, though it remains to be seen if it can be applied to non-Hermitian Hamiltonians and operators. This would be a marvelous discovery to add to the knowledge of resonant states and would immediately benefit practical implementations of MESA.

Another open question is how to map complex-valued observables from non-Hermitian quantum mechanics back to their real-valued counterparts in Hermitian quantum mechanics. Brody [89] gives an equation for the expectation value for bi-orthogonal states $\langle \hat{F} \rangle = \sum_{n,m} \bar{c}_n c_m f_{nm} / \sum_n \bar{c}_n c_n$ where $c_{n,m}$ are the coefficients of an expansion in terms of resonant states. This expectation value has the same form as the Hermitian expectation value, except that the values $f_{nm} = \int_{\mathcal{C}} \psi_n(z) f \psi_m(z) dz$ are calculated using the contour integral defined in Section 4.2. Simply taking the real part of the complex-valued observable is incorrect, since both real and imaginary parts appear to contain useful information, as has been shown in the post-adiabatic correction term for the nonlinear polarization, Eq. (5.12). So far, no consensus of a correct transformation between Hermitian and non-Hermitian observables has been published. Another useful quantity to determine would be a non-Hermitian coun-

[1] https://en.wikipedia.org/wiki/Oscillator_strength

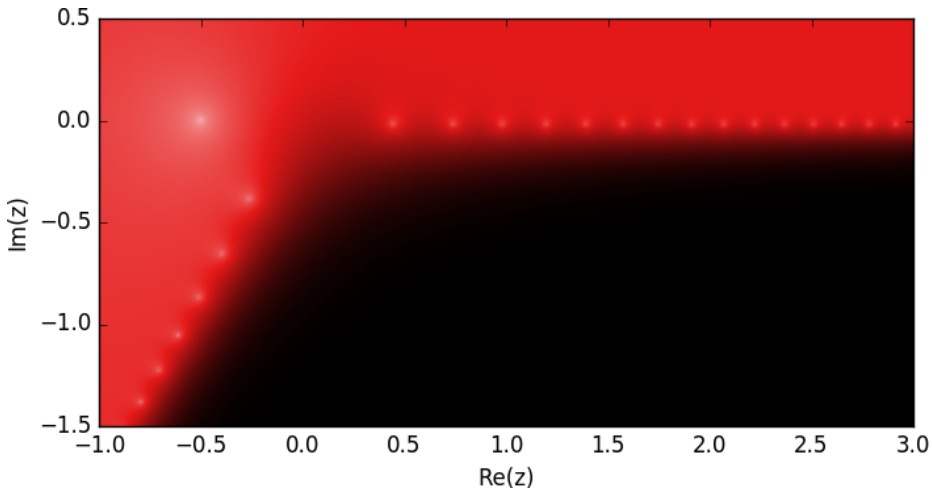

FIGURE 6.2. Resonance energy landscape for the delta potential with energy z. Note that the resonance energy spacing decreases for higher energy states (further from the origin).

terpart to Ehrenfest's theorem. This would probably require a formal definition of a commutator-like operator for bi-orthogonal states and so far this has not been realized.

The next open question concerns the bound state energy spectrum of a resonance-based medium model and to what extent it must match the spectrum of a realistic atom in order to reproduce its response. The success of the 1D Dirac-delta potential model in qualitatively reproducing common nonlinear effects is surprising, given that it contains only a single bound state. In Section 4.4.2, a complete theory for the 1D square well potential was developed. This model has a distinct advantage over the delta potential in that it allows for the inclusion of multiple bound states and therefore provides a means to investigate how additional bound states contribute to a medium's response. In Figure 6.4 the bound state energies for two different well dimensions are displayed. Unlike in realistic atoms, where the highest density of states are found near the continuum, the square well potential has the densest region of bound states near the bottom of the well. It is unclear whether the unusual bound state configuration will adversely affect its ability to approximate the response of a realistic atomic gas, such as Argon. Simply ignoring transitions to particular states in order to produce a more realistic spectrum may be a possible solution. It is now possible to numerically solve for the resonances of a 3D coulomb-like potentials [136]. Such resonance systems may provide another tool for investigating whether the spectrum of the medium model must match the realistic spectrum of a gas. Although, the shape of the field-induced nonlinear polarization response may prove to be more important than the arrangement of bound states that produced it.

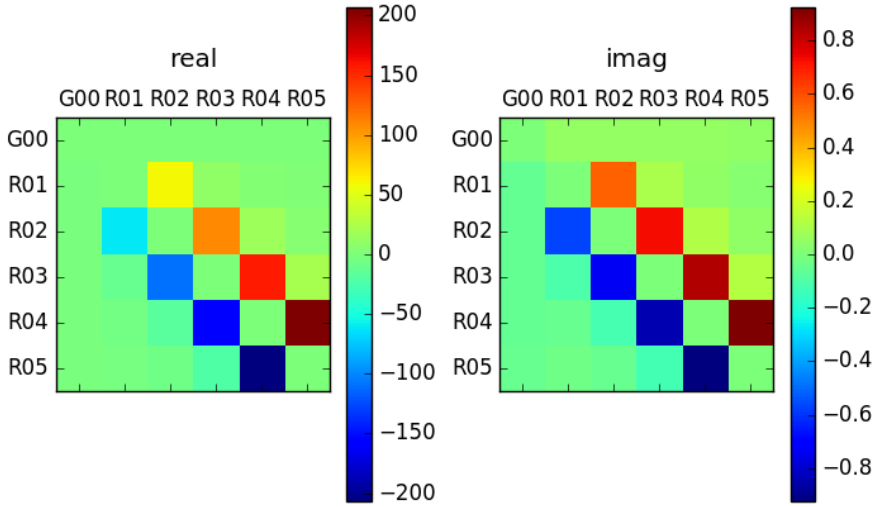

FIGURE 6.3. Coupling matrix elements $\langle \partial_F \psi_n | \psi_k \rangle$ for the ground state G00 and the first five Right family resonances R01 − R05 for a field $F = 0.001$ and ground state energy $E_g = -15.76eV$. Note that the strongest coupling is between neighboring states and that due to the closer spacing of higher energy states, the strength of coupling is larger also.

A related avenue of research is to further develop MESA for more realistic potentials for atomic gases commonly used in experiments, such as argon. Recent progress in direct experimental characterization of optical nonlinearities at ultrafast time scales brought quantitative results concerning the self-focusing nonlinearity [137] as well as free-electron generation [138] in various gases. Importantly, spatio-temporal profiles of the nonlinear responses can now be obtained essentially free of propagation effects. Given that the nonlinear polarization of many noble gases have similar shapes, as illustrated in Figure 6.5, it may be possible to capture this shape as a parametric function with fitting parameters found directly from experiment.

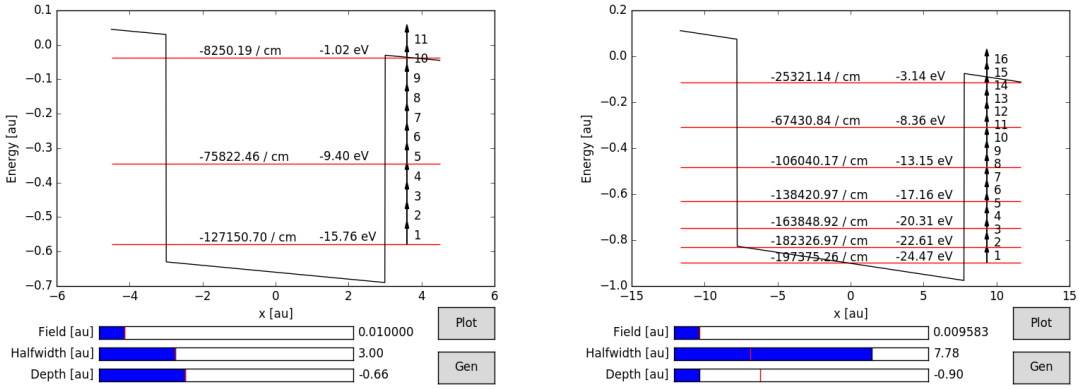

FIGURE 6.4. The dimensions of the square well potential determine the number of bound states. Note that the bound state energy spacing is most dense at the bottom of the well, which differs from a realistic atom. The vertical arrows on the right side represent photon energies at 800nm and illustrates whether states are on- or off-resonance to the driving field.

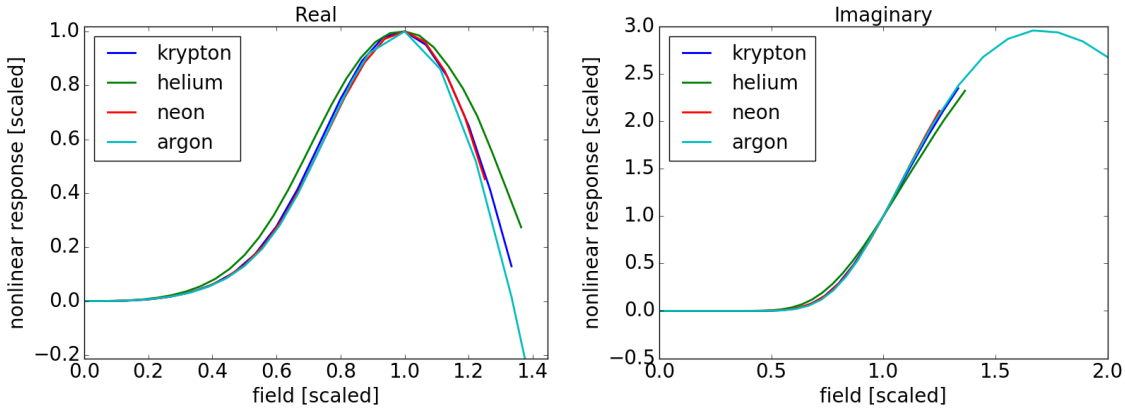

FIGURE 6.5. Scaling the nonlinear polarization responses of noble gases shows that they have the same characteristic response to the field.

Appendix A

Airy Integration Technique

The Airy integration technique outlined in this Appendix is used to evaluate integrals that contain linear combinations of Airy functions A, B and their derivatives A', B', where the two sets of functions have shifted arguments. A shorthand notation of $A = A[\alpha(x + \beta_n)]$ and $B = B[\alpha(x + \beta_k)]$ is used throughout. The two unknown integrals of interest are

$$\int_{-\infty}^{\infty} A'Bdx \quad \text{and} \quad \int_{-\infty}^{\infty} xA'Bdx, \tag{A.1}$$

where the integration over x is understood to be along the contour $\mathcal{C}$ (Figure 4.1). Simply applying integration by parts leads nowhere since the solutions always involve integrals that are also not known. The technique described here circumvents that problem. For an integral whose integrand has the form $x^n A'B$, the following steps are performed:

1. Multiply the integrand $x^n A'B$ by x
2. Differentiate w.r.t. x and integrate
3. Repeat 1 & 2 with the "symmetric" integrand $x^n AB'$
4. Subtract the two equations

Using this procedure it is found that the unknown integrals can be written in terms of known integrals, which do not contain derivatives of A or B, and are therefore found in published literature [104]. The procedure relies on the fact that wavefunctions and their derivatives are continuous at jumps of $V(x)$. Moreover, A and B must be resonant eigenstates that belong to the orthonormal system w.r.t. the pairing defined by the the contour integral along $\mathcal{C}$ (4.3). As such, the formulas derived below do not apply to arbitrary combinations of Airy functions. On the other hand, the method does apply to a general case of Stark resonances in piecewise constant potential and in this sense the results shown below are general. In the next sections this integration technique is applied to the integrands $A'B$ and $xA'B$ to demonstrate its usefulness.

A.1 Integrating $A'B$

To solve the integral of $A'B$, the first step is to multiply by x and differentiate

$$\partial_x(xA'B) = A'B + \alpha xA''B + \alpha xA'B' = A'B + \alpha^2 x(x + \beta_n)AB + \alpha xA'B'. \tag{A.2}$$

Next, both sides are integrated and the results contain both known and unknown Airy integrals

$$\underbrace{xA'B\Big|_{-\infty}^{+\infty}}_{=0} = \underbrace{\int_{-\infty}^{\infty} A'Bdx}_{want} + \underbrace{\alpha^2 \int_{-\infty}^{+\infty} x^2 ABdx + \alpha^2\beta_n \int_{-\infty}^{\infty} xABdx}_{known} + \alpha \underbrace{\int_{-\infty}^{\infty} xA'B'dx}_{unknown}. \tag{A.3}$$

To remove the unknown integrals that contain both derivative functions A' and B', the "symmetric" integrand is differentiated,

$$\partial_x(xAB') = AB' + \alpha xA'B' + \alpha xAB'' = AB' + \alpha xA'B' + \alpha^2 x(x+\beta_k)AB, \tag{A.4}$$

and then integrated, in order to find the complementary equation to (A.3)

$$\underbrace{xAB'\Big|_{-\infty}^{+\infty}}_{=0} = \underbrace{\int_{-\infty}^{\infty} AB'dx}_{unknown} + \underbrace{\alpha^2 \int_{-\infty}^{\infty} x^2 ABdx + \alpha^2\beta_k \int_{-\infty}^{\infty} xABdx}_{known} + \alpha \underbrace{\int_{-\infty}^{\infty} xA'B'dx}_{unknown}. \tag{A.5}$$

Next, (A.3) and (A.5) are subtracted

$$\int_{-\infty}^{\infty} A'Bdx - \int_{-\infty}^{\infty} AB'dx = -\alpha^2(\beta_n - \beta_k)\int_{-\infty}^{\infty} xABdx. \tag{A.6}$$

It is possible to relate the two terms on the LHS using the fact that AB vanishes at the ends of the integration contour: $\int A'Bdx + \int AB'dx = 0$. Given this, the unknown integral is now written in terms of a known one (VS 3.54 [104])

$$\int_{-\infty}^{\infty} A'Bdx = -\frac{\alpha^2}{2}(\beta_n - \beta_k)\underbrace{\int_{-\infty}^{\infty} xABdx}_{3.54}. \tag{A.7}$$

Here the integration technique was used for an integral along the entire contour, but it is possible to apply the same technique to integrals over a finite range (a, b). The only change would be the inclusion of the LHS terms of (A.3) and (A.5) evaluated at the points a and b. A finite-range integral over $(-d, d)$ appears during the calculation of the coupling term for the square well potential in Equation (4.33).

A.2 Integrating $xA'B$

To solve this integral, the same procedure is used: Multiply the integrand by x, differentiate and then subtract "symmetric" integrand.

$$\partial_x(x^2A'B) = 2xA'B + \alpha x^2A''B + \alpha x^2A'B' = 2xA'B + \alpha^2x^2(x+\beta_n)AB + \alpha x^2A'B' \tag{A.8}$$

$$\partial_x(x^2AB') = 2xAB' + \alpha x^2AB'' + \alpha x^2A'B' = 2xAB' + \alpha^2x^2(x+\beta_k)AB + \alpha x^2A'B' \tag{A.9}$$

Subtract (A.8) and (A.9) and then integrate

$$0 = 2\left[\underbrace{\int_{-\infty}^{\infty} xA'Bdx}_{want} - \underbrace{\int_{-\infty}^{\infty} xAB'dx}_{unknown}\right] + \alpha^2(\beta_n - \beta_k)\underbrace{\int_{-\infty}^{\infty} x^2ABdx}_{known}. \tag{A.10}$$

Just as was done for the integrand $A'B$, the two terms within the square braces can be related using integration by parts plus an orthogonality argument. As a result, the sought integral can be written in terms of a known integral (VS 3.55)

$$\int_{-\infty}^{\infty} xA'Bdx = -\frac{\alpha^2(\beta_n - \beta_k)}{4}\underbrace{\int_{-\infty}^{\infty} x^2ABdx}_{3.55}. \tag{A.11}$$

Appendix B

Derivation of Nonlinear Current

B.1 Initial equations

In this Appendix a detailed derivation of the probability current for the 1D Dirac-delta model is presented. The initial equations that govern probability current and the quantum system's wavefunction are

$$J(x,t) = \Re\left\{\psi^*(x,t)\left[\frac{1}{i}\nabla\psi(x,t)\right]\right\} \tag{B.1}$$

$$\psi(x,t) = \psi_F(x,t) + \psi_S(x,t) \tag{B.2}$$

$$\psi_F(x,t) = \int \mathrm{d}x'\, K_F(x,t|x',0)\psi_B(x') \tag{B.3}$$

$$\psi_S(x,t) = iB\int_0^t \mathrm{d}t'\, K_F(x,t|0,t')\psi(0,t') \tag{B.4}$$

where

$$\psi_B(x) = B^{1/2}e^{-B|x|} \tag{B.5}$$

$$K_F(x,t|x',t') = e^{i\phi(x,t,x',t')}K_0(x-x_{cl}(t),t|x'-x_{cl}(t'),t') \tag{B.6}$$

$$K_0(x,t|x',t') = \frac{1}{\sqrt{2\pi i(t-t')}}e^{-\frac{(x-x')^2}{2i(t-t')}} \tag{B.7}$$

$$\phi(x,t,x',t') = xp_{cl}(t) - x'p_{cl}(t') - \left[S_{cl}(t) - S_{cl}(t')\right]. \tag{B.8}$$

With these equations the current $J(t)$ can be calculated from the current density by integrating over all space

$$J(t) = \int_{-\infty}^{\infty} J(x,t)dx. \tag{B.9}$$

An ansatz for $\psi(0,t)$ is made

$$\psi(0,t) = A(t)B^{1/2}e^{i\frac{B^2t}{2}}e^{-iS_{cl}(t)} \tag{B.10}$$

which helps reduce rapidly oscillating phase terms that appear in some of the integrals. This choice is used throughout the derivation. Next, the derivatives of each of the

components that make up $\psi(x,t)$ are computed

$$\nabla K_F(x,t|x',t) = \left[\frac{i\left(x - x_{cl}(t) - x' + x_{cl}(t')\right)}{t-t'} + ip_{cl}(t)\right] K_F(x,t|x',t') \tag{B.11}$$

$$\nabla\psi_B(x) = -B\mathrm{sgn}(x)\psi_B(x) \tag{B.12}$$

$$\nabla\psi_F(x,t) = \left[\frac{i(x - x_{cl}(t))}{t} + ip_{cl}(t)\right]\psi_F(x,t). \tag{B.13}$$

Given these derivatives, it is possible to evaluate $\nabla\psi(x,t)$

$$\nabla\psi(x,t) = \nabla\psi_F(x,t) + iB\int_0^t \mathrm{d}t'\,\nabla K_F(x,t|0,t')\psi(0,t') \tag{B.14}$$

$$\begin{aligned}\nabla\psi(x,t) = &\left[\frac{i(x - x_{cl}(t))}{t} + ip_{cl}(t)\right]\psi_F(x,t) \\ &+ iB\int_0^t \mathrm{d}t'\,\psi(0,t')\left[\frac{i\left(x - x_{cl}(t) + x_{cl}(t')\right)}{t-t'} + ip_{cl}(t)\right] K_F(x,t|0,t').\end{aligned} \tag{B.15}$$

Multiplying by $\frac{1}{i}$ gives one component of the probability current density that is written explicitly as

$$\begin{aligned}\frac{1}{i}\nabla\psi(x,t) = &\left[\frac{x - x_{cl}(t)}{t} + p_{cl}(t)\right]\psi_F(x,t) \\ &+ iB\int_0^t \mathrm{d}t'\,\psi(0,t')\left[\frac{x - x_{cl}(t) + x_{cl}(t')}{t-t'}\right] K_F(x,t|0,t') \\ &+ ip_{cl}(t)B\int_0^t \mathrm{d}t'\,\psi(0,t')K_F(x,t|0,t').\end{aligned} \tag{B.16}$$

The other necessary component is the complex conjugate wavefunction $\psi^*(x,t)$

$$\psi^*(x,t) = \psi_F^*(x,t) - iB\int_0^t \mathrm{d}t'\,\psi^*(0,t')K_F^*(x,t|0,t') \tag{B.17}$$

$$\psi_F^*(x,t) = \int \mathrm{d}x'\,K_F^*(x,t|x',0)\psi_B(x'). \tag{B.18}$$

Together, $\psi^*(x,t)$ and $\frac{1}{i}\nabla\psi(x,t)$ produce 6 terms that will be integrated over all space to find the probability current $J(t)$.

$$
\begin{aligned}
&\psi^*(x,t)\frac{1}{i}\nabla\psi(x,t) \\
&\quad= \underbrace{\left[\frac{x-x_{cl}(t)}{t}+p_{cl}(t)\right]\psi_F^*(x,t)\psi_F(x,t)}_{\text{I}} \\
&\quad+ \underbrace{\psi_F^*(x,t)iB\int_0^t \mathrm{d}t'\,\psi(0,t')\left[\frac{x-x_{cl}(t)+x_{cl}(t')}{t-t'}\right]K_F(x,t|0,t')}_{\text{II}} \\
&\quad+ \underbrace{\psi_F^*(x,t)p_{cl}(t)iB\int_0^t \mathrm{d}t'\,\psi(0,t')K_F(x,t|0,t')}_{\text{III}} \\
&\quad- \underbrace{\left[\frac{x-x_{cl}(t)}{t}+p_{cl}(t)\right]\psi_F(x,t)iB\int_0^t \mathrm{d}t'\,\psi^*(0,t')K_F^*(x,t|0,t')}_{\text{IV}} \\
&\quad+ \underbrace{B^2\left(\int_0^{t_1}\mathrm{d}t'\,\psi(0,t')\left[\frac{x-x_{cl}(t)+x_{cl}(t')}{t-t'}\right]K_F(x,t|0,t')\right)\left(\int_0^{t_2}\mathrm{d}t''\,\psi^*(0,t'')K_F^*(x,t|0,t'')\right)}_{\text{V}} \\
&\quad+ \underbrace{p_{cl}(t)B^2\left(\int_0^{t_1}\mathrm{d}t'\,\psi^*(0,t')K_F^*(x,t|0,t')\right)\left(\int_0^{t_2}\mathrm{d}t''\,\psi(0,t'')K_F(x,t|0,t'')\right)}_{\text{VI}}.
\end{aligned}
\tag{B.19}
$$

B.2 Useful identity

There is an important identity that can be used to simplify the calculation of the current $J(t)$. This identity is based on two properties of this system. The first is that the full wavefunction $\psi(x,t)$ and its constituent parts, ψ_F and ψ_S, are independently normalized and remain normalized during Schrödinger evolution. The second is that the propagator K_F (B.11) and free wavefunction ψ_F (B.13) are eigenfunctions of the derivative operator with eigenvalues involving two terms: one containing x and x_{cl} and another containing p_{cl}. This can be more easily seen by simplifying the notation and using Dirac notation. The short-hand notation K_F represents $iB\int_0^t \mathrm{d}t'\,\psi^*(0,t')K_F^*(x,t|0,t')$ and the phrases *xterms* and *pterms* represent position terms and momentum terms, respectively, within the eigenvalues.

With this new notation, the derivative equations (B.11) and (B.13) and full wave-

function ψ are written as

$$\nabla K_F = [xterms + pterms]\, K_F \tag{B.20}$$
$$\nabla \psi_F = [xterms + pterms]\, \psi_F \tag{B.21}$$
$$\psi = \psi_F + K_F. \tag{B.22}$$

The probability current J can be expanded into

$$J = \psi^* \nabla \psi \tag{B.23}$$
$$J = \psi_F^* \nabla \psi_F + \psi_F^* \nabla K_F + K_F^* \nabla \psi_F + K_F^* \nabla K_F. \tag{B.24}$$

Grouping the terms of J into those multiplied by $xterms$ and $pterms$ gives

$$\begin{aligned} J = {} & pterms\, [\psi_F^* \psi_F + \psi_F^* K_F + K_F^* \psi_F + K_F^* K_F] \\ & + xterms\, [\psi_F^* \psi_F + \psi_F^* K_F + K_F^* \psi_F + K_F^* K_F]\,. \end{aligned} \tag{B.25}$$

The quantity $\psi_F^* \psi_F + \psi_F^* K_F + K_F^* \psi_F + K_F^* K_F$ is simply $\psi^* \psi$. Given that the quantum states ψ and ψ_F are normalized such that $\langle \psi | \psi \rangle = 1$ and $\langle \psi_F | \psi_F \rangle = 1$ forces the terms $\psi_F^* K_F + K_F^* \psi_F + K_F^* K_F$ to sum to zero. To summarize:

$$\langle \psi | \psi \rangle = \langle \psi_F | \psi_F \rangle + \langle \psi_F | K_F \rangle + \langle K_F | \psi_F \rangle + \langle K_F | K_F \rangle = 1 \tag{B.26}$$

and

$$\langle \psi_F | \psi_F \rangle = 1 \tag{B.27}$$

gives the identity

$$\langle \psi_F | K_F \rangle + \langle K_F | \psi_F \rangle + \langle K_F | K_F \rangle = 0. \tag{B.28}$$

The terms of (B.19) that are reduced by this identity are Term III, the part of Term IV multiplied by $p_{cl}(t)$, and Term VI.

B.3 Term I

Solving Term I begins by evaluating the spatial integral of $\psi_F(x,t)$ and its complex conjugate

$$\left[\frac{x - x_{cl}(t)}{t} + p_{cl}(t)\right] \psi_F^*(x,t) \psi_F(x,t) \tag{B.29}$$
$$\left[\frac{x - x_{cl}(t)}{t} + p_{cl}(t)\right] \underbrace{\int \mathrm{d}x'\, K_F^*(x,t|x',0) \psi_B^*(x')}_{\text{i}} \underbrace{\int \mathrm{d}x'\, K_F(x,t|x',0) \psi_B(x')}_{\text{ii}} \tag{B.30}$$

Part i is evaluated in the following steps

$$\int \mathrm{d}x'\, K_F^*(x,t|x',0)\psi_B^*(x') \tag{B.31}$$

$$\int \mathrm{d}x'\, e^{-i\phi(x,t,x',0)} K_0^*(x-x_{cl}(t),t|x'-x_{cl}(0),0)\psi_B^*(x') \tag{B.32}$$

$$\int \mathrm{d}x'\, e^{-ixp_{cl}(t)+ix'p_{cl}(0)+iS_{cl}(t)-iS_{cl}(0)} \frac{1}{\sqrt{-2\pi it}} e^{\frac{(x-x_{cl}(t)-x')^2}{2it}} B^{1/2} e^{-B|x'|} \tag{B.33}$$

$$\sqrt{\frac{iB}{2\pi t}} e^{-ixp_{cl}(t)+iS_{cl}(t)} \int \mathrm{d}x'\, e^{\frac{(x-x_{cl}(t)-x')^2}{2it}-B|x'|} \tag{B.34}$$

Because of the absolute value, the integral's domain must be split

$$\sqrt{\frac{iB}{2\pi t}} e^{-ixp_{cl}(t)+iS_{cl}(t)} \left(\int_{-\infty}^{0} \mathrm{d}x'\, e^{\frac{(x-x_{cl}(t)-x')^2}{2it}+Bx'} + \int_{0}^{\infty} \mathrm{d}x'\, e^{\frac{(x-x_{cl}(t)-x')^2}{2it}-Bx'} \right). \tag{B.35}$$

Both integrals have the same form and are simply Gaussian integrals:

$$\int_{-\infty}^{0} \mathrm{d}x'\, e^{-ax'^2+b_1x'-c} + \int_{0}^{\infty} \mathrm{d}x'\, e^{-ax'^2+b_2x'-c}, \tag{B.36}$$

where the coefficients are defined as

$$\begin{aligned} a &= \frac{i}{2t} \\ b_1 &= B + \frac{ix}{t} - \frac{ix_{cl}(t)}{t} \\ b_2 &= -B + \frac{ix}{t} - \frac{ix_{cl}(t)}{t} \\ c &= \frac{ix^2}{2t} - \frac{ixx_{cl}(t)}{t} + \frac{ix_{cl}^2(t)}{2t}. \end{aligned}$$

These integrals evaluate to exponentials and error functions

$$\frac{\sqrt{\pi} e^{\left(\frac{b_1^2}{4a}-c\right)}}{2\sqrt{a}} - \frac{\sqrt{\pi} e^{\left(\frac{b_1^2}{4a}-c\right)} \mathrm{erf}\left(\frac{b_1}{2\sqrt{a}}\right)}{2\sqrt{a}} + \frac{\sqrt{\pi} e^{\left(\frac{b_2^2}{4a}-c\right)} \mathrm{erf}\left(\frac{b_2}{2\sqrt{a}}\right)}{2\sqrt{a}} + \frac{\sqrt{\pi} e^{\left(\frac{b_2^2}{4a}-c\right)}}{2\sqrt{a}} \tag{B.37}$$

and are further simplified to

$$\frac{1}{2}\sqrt{\frac{\pi}{a}}\left(e^{\left(\frac{b_1^2}{4a}-c\right)}\left[1-\operatorname{erf}\left(\frac{b_1}{2\sqrt{a}}\right)\right]+e^{\left(\frac{b_2^2}{4a}-c\right)}\left[\operatorname{erf}\left(\frac{b_2}{2\sqrt{a}}\right)+1\right]\right) \tag{B.38}$$

$$\frac{1}{2}\sqrt{\frac{\pi}{a}}\left(e^{\left(\frac{b_1^2}{4a}-c\right)}\left[\operatorname{erfc}\left(\frac{b_1}{2\sqrt{a}}\right)\right]+e^{\left(\frac{b_2^2}{4a}-c\right)}\left[\operatorname{erf}\left(\frac{b_2}{2\sqrt{a}}\right)+1\right]\right) \tag{B.39}$$

$$\begin{aligned}\frac{1}{2}\sqrt{\frac{2\pi t}{i}}\Bigg(&e^{-\frac{1}{2}iB^2t+Bx-Bx_{cl}(t)}\left[\operatorname{erfc}\left(\sqrt{\frac{i}{2t}}\left(x-x_{cl}(t)-iBt\right)\right)\right]\\&+e^{-\frac{1}{2}iB^2t-Bx+Bx_{cl}(t)}\left[\operatorname{erf}\left(\sqrt{\frac{i}{2t}}\left(x-x_{cl}(t)+iBt\right)\right)+1\right]\Bigg).\end{aligned} \tag{B.40}$$

The free wavefunction $\psi_F^*(x,t)$ can now be represented in a reduced form

$$\begin{aligned}\frac{1}{2}\sqrt{B}e^{-ixp_{cl}(t)+iS_{cl}(t)}e^{-\frac{1}{2}iB^2t}\Bigg(&e^{B(x-x_{cl}(t))}\left[\operatorname{erfc}\left(\sqrt{\frac{i}{2t}}\left(x-x_{cl}(t)-iBt\right)\right)\right]\\&+e^{-B(x-x_{cl}(t))}\left[\operatorname{erf}\left(\sqrt{\frac{i}{2t}}\left(x-x_{cl}(t)+iBt\right)\right)+1\right]\Bigg).\end{aligned} \tag{B.41}$$

Since Part i and ii are complex conjugates, $\psi_F(x,t)$ is simply

$$\begin{aligned}\frac{1}{2}\sqrt{B}e^{ixp_{cl}(t)-iS_{cl}(t)}e^{\frac{1}{2}iB^2t}\Bigg(&e^{B(x-x_{cl}(t))}\left[\operatorname{erfc}\left(\sqrt{\frac{1}{2it}}\left(x-x_{cl}(t)+iBt\right)\right)\right]\\&+e^{-B(x-x_{cl}(t))}\left[\operatorname{erf}\left(\sqrt{\frac{1}{2it}}\left(x-x_{cl}(t)-iBt\right)\right)+1\right]\Bigg).\end{aligned} \tag{B.42}$$

To proceed with the spatial integration of Term I, the substitution $y = x - x_{cl}(t)$ is used, resulting in $\left[\frac{y}{t}+p_{cl}(t)\right]\psi_F^*(x,t)\psi_F(x,t)$ being equal to

$$\begin{aligned}&\left[\frac{y}{t}+p_{cl}(t)\right]\\&\cdot\frac{1}{2}\sqrt{B}e^{-ixp_{cl}(t)+iS_{cl}(t)}e^{-\frac{1}{2}iB^2t}\left(e^{By}\left[\operatorname{erfc}\left(\sqrt{\frac{i}{2t}}\left(y-iBt\right)\right)\right]+e^{-By}\left[\operatorname{erf}\left(\sqrt{\frac{i}{2t}}\left(y+iBt\right)\right)+1\right]\right)\\&\cdot\frac{1}{2}\sqrt{B}e^{ixp_{cl}(t)-iS_{cl}(t)}e^{\frac{1}{2}iB^2t}\left(e^{By}\left[\operatorname{erfc}\left(\sqrt{\frac{1}{2it}}\left(y+iBt\right)\right)\right]+e^{-By}\left[\operatorname{erf}\left(\sqrt{\frac{1}{2it}}\left(y-iBt\right)\right)+1\right]\right)\end{aligned} \tag{B.43}$$

and simplifying further it becomes

$$\left[\frac{y}{t}+p_{cl}(t)\right]\frac{B}{4}\left(e^{By}\left[\operatorname{erfc}\left(\sqrt{\frac{i}{2t}}\,(y-iBt)\right)\right]+e^{-By}\left[\operatorname{erf}\left(\sqrt{\frac{i}{2t}}\,(y+iBt)\right)+1\right]\right)$$
$$\cdot\left(e^{By}\left[\operatorname{erfc}\left(\sqrt{\frac{1}{2it}}\,(y+iBt)\right)\right]+e^{-By}\left[\operatorname{erf}\left(\sqrt{\frac{1}{2it}}\,(y-iBt)\right)+1\right]\right). \tag{B.44}$$

In order to calculate the total current $J(t)$ from Term I, the above expression is placed into an integral over all space. The two quantities representing $\psi_F(y,t)$ and $\psi_F^*(y,t)$ are found to be even functions. Therefore, the integral of the term multiplied by $\frac{y}{t}$ is odd and equal to zero. Given that $\psi_F(y,t)$ is normalized, the integral multiplied by $p_{cl}(t)$ is equal to one:

$$\underbrace{\int \mathrm{d}y\,\frac{y}{t}\psi_F^*(y,t)\psi_F(y,t)}_{0}+p_{cl}(t)\underbrace{\int \mathrm{d}y\,\psi_F^*(y,t)\psi_F(y,t)}_{1}. \tag{B.45}$$

Therefore, the total contribution from Term I is

$$\boxed{p_{cl}(t)}. \tag{B.46}$$

B.4 Term II

The next term to simplify is Term II which is written as

$$\psi_F^*(x,t)iB\int_0^t \mathrm{d}t'\,\psi(0,t')\left[\frac{x-x_{cl}(t)+x_{cl}(t')}{t-t'}\right]K_F(x,t|0,t'). \tag{B.47}$$

The first step is to expand the quantity under the time integral

$$\int_0^{t_1}\mathrm{d}t'\,\psi(0,t')\left[\frac{x-x_{cl}(t)+x_{cl}(t')}{t-t'}\right]K_F(x,t|0,t') \tag{B.48}$$

$$\int_0^{t_1}\mathrm{d}t'\,A(t')B^{1/2}e^{i\frac{B^2t'}{2}}e^{-iS_{cl}(t')}\left[\frac{x-x_{cl}(t)+x_{cl}(t')}{t-t'}\right]$$
$$\cdot\,e^{ixp_{cl}(t)-iS_{cl}(t)+iS_{cl}(t')}K_0(x-x_{cl}(t),t|-x_{cl}(t'),t') \tag{B.49}$$

$$B^{1/2}e^{ixp_{cl}(t)}e^{-iS_{cl}(t)}\int_0^{t_1}\mathrm{d}t'\,A(t')\left[x-x_{cl}(t)+x_{cl}(t')\right]\frac{e^{\frac{i}{2}B^2t'}}{t-t'}\frac{e^{-\frac{(x-x_{cl}(t)+x_{cl}(t'))^2}{2i(t-t')}}}{\sqrt{2\pi i}\sqrt{t-t'}} \tag{B.50}$$

arriving at the expression

$$\frac{B^{1/2}}{\sqrt{2\pi i}}e^{ixp_{cl}(t)}e^{-iS_{cl}(t)}\int_0^{t_1}\mathrm{d}t'\,A(t')\left[x-x_{cl}(t)+x_{cl}(t')\right]\frac{e^{\frac{i}{2}\left[B^2t'+\frac{(x-x_{cl}(t)+x_{cl}(t'))^2}{t-t'}\right]}}{(t-t')^{3/2}}. \tag{B.51}$$

Given the expanded expression for the time integral, Term II can now be written as

$$\psi_F^*(x,t)iB\left(\frac{B^{1/2}}{\sqrt{2\pi i}}e^{ixp_{cl}(t)}e^{-iS_{cl}(t)}\int_0^{t_1}\mathrm{d}t'\,A(t')\left[x-x_{cl}(t)+x_{cl}(t')\right]\frac{e^{\frac{i}{2}\left[B^2t'+\frac{(x-x_{cl}(t)+x_{cl}(t'))^2}{t-t'}\right]}}{(t-t')^{3/2}}\right) \tag{B.52}$$

and then as

$$B^{3/2}\sqrt{\frac{i}{2\pi}}e^{ixp_{cl}(t)}e^{-iS_{cl}(t)}\psi_F^*(x,t)\left(\int_0^{t_1}\mathrm{d}t'\,A(t')\left[x-x_{cl}(t)+x_{cl}(t')\right]\frac{e^{\frac{i}{2}\left[B^2t'+\frac{(x-x_{cl}(t)+x_{cl}(t'))^2}{t-t'}\right]}}{(t-t')^{3/2}}\right). \tag{B.53}$$

Substitute in the explicit expression for $\psi_F^*(x,t)$ that was evaluated in Term I and simplify, and Term II becomes

$$\begin{aligned}
&B^{3/2}\sqrt{\frac{i}{2\pi}}e^{ixp_{cl}(t)}e^{-iS_{cl}(t)}\cdot\frac{1}{2}\sqrt{B}e^{-ixp_{cl}(t)+iS_{cl}(t)}e^{-\frac{1}{2}iB^2t}\\
&\quad\cdot\left(e^{B(x-x_{cl}(t))}\left[\operatorname{erfc}\left(\sqrt{\frac{i}{2t}}\left(x-x_{cl}(t)-iBt\right)\right)\right]\right.\\
&\qquad\left.+e^{-B(x-x_{cl}(t))}\left[\operatorname{erf}\left(\sqrt{\frac{i}{2t}}\left(x-x_{cl}(t)+iBt\right)\right)+1\right]\right)\\
&\quad\cdot\left(\int_0^{t_1}\mathrm{d}t'\,A(t')\left[x-x_{cl}(t)+x_{cl}(t')\right]\frac{e^{\frac{i}{2}\left[B^2t'+\frac{(x-x_{cl}(t)+x_{cl}(t'))^2}{t-t'}\right]}}{(t-t')^{3/2}}\right).
\end{aligned} \tag{B.54}$$

Rearranging the expression results in

$$\begin{aligned}
&\frac{B^2}{2}\sqrt{\frac{i}{2\pi}}\int_0^{t_1}\mathrm{d}t'\,A(t')\frac{e^{-\frac{1}{2}iB^2(t-t')}}{(t-t')^{3/2}}\left[x-x_{cl}(t)+x_{cl}(t')\right]e^{\frac{i}{2}\frac{(x-x_{cl}(t)+x_{cl}(t'))^2}{t-t'}}\\
&\quad\cdot\left(e^{B(x-x_{cl}(t))}\left[\operatorname{erfc}\left(\sqrt{\frac{i}{2t}}\left(x-x_{cl}(t)-iBt\right)\right)\right]\right.\\
&\quad\left.+e^{-B(x-x_{cl}(t))}\left[\operatorname{erf}\left(\sqrt{\frac{i}{2t}}\left(x-x_{cl}(t)+iBt\right)\right)+1\right]\right).
\end{aligned} \tag{B.55}$$

Just as was done in Term I, the substitution $y = x - x_{cl}(t)$ is used to simplify the spatial integral

$$\frac{B^2}{2}\sqrt{\frac{i}{2\pi}}\int_0^{t_1} \mathrm{d}t'\, A(t')\frac{e^{-\frac{1}{2}iB^2(t-t')}}{(t-t')^{3/2}}\left[y + x_{cl}(t')\right] e^{\frac{i}{2}\frac{(y+x_{cl}(t'))^2}{t-t'}} \cdot \left(e^{By}\left[\mathrm{erfc}\left(\sqrt{\frac{i}{2t}}\,(y - iBt)\right)\right] + e^{-By}\left[\mathrm{erf}\left(\sqrt{\frac{i}{2t}}\,(y + iBt)\right) + 1\right]\right). \tag{B.56}$$

Grouping all the terms involving y and simplifying, the resulting expression to be integrated is

$$\frac{B^2}{2}\sqrt{\frac{i}{2\pi}}\int_0^{t_1} \mathrm{d}t'\, A(t')\frac{e^{-\frac{1}{2}iB^2(t-t')}}{(t-t')^{3/2}}\left[y + x_{cl}(t')\right] \cdot \left(e^{\frac{iy^2}{2(t-t')}+\left(B+\frac{ix_{cl}(t')}{t-t'}\right)y+\frac{ix_{cl}(t')^2}{2(t-t')}}\left[\mathrm{erfc}\left(\sqrt{\frac{i}{2t}}\,(y - iBt)\right)\right] + e^{\frac{iy^2}{2(t-t')}+\left(-B+\frac{ix_{cl}(t')}{t-t'}\right)y+\frac{ix_{cl}(t')^2}{2(t-t')}}\left[\mathrm{erf}\left(\sqrt{\frac{i}{2t}}\,(y + iBt)\right) + 1\right]\right). \tag{B.57}$$

Introducing the following coefficients

$$\begin{aligned} a &= \frac{i}{2(t-t')} \\ b_1 &= B + \frac{ix_{cl}(t')}{t-t'} \\ b_2 &= -B + \frac{ix_{cl}(t')}{t-t'} \\ c &= \frac{ix_{cl}(t')^2}{2(t-t')} \end{aligned}$$

greatly simplifies (visually also) the expression under the integral

$$\int \mathrm{d}y\, \left[y + x_{cl}(t')\right]\left(e^{ay^2+b_1y+c}\left[\mathrm{erfc}\left(\sqrt{\frac{i}{2t}}\,(y - iBt)\right)\right] + e^{ay^2+b_2y+c}\left[\mathrm{erf}\left(\sqrt{\frac{i}{2t}}\,(y + iBt)\right) + 1\right]\right). \tag{B.58}$$

To perform the integral, the first step is to complete the square in the exponential

$$\begin{aligned}\int \mathrm{d}y\ [y + x_{cl}(t')] \Bigg(& e^{a(y+\frac{b_1}{2a})^2 + c - \frac{b_1^2}{4a}} \left[\mathrm{erfc}\left(\sqrt{\frac{i}{2t}} (y - iBt) \right) \right] \\ & + e^{a(y+\frac{b_2}{2a})^2 + c - \frac{b_2^2}{4a}} \left[\mathrm{erf}\left(\sqrt{\frac{i}{2t}} (y + iBt) \right) + 1 \right] \Bigg)\end{aligned} \tag{B.59}$$

$$\begin{aligned}\int \mathrm{d}y\ [y + x_{cl}(t')] \Bigg(& e^{c - \frac{b_1^2}{4a}} e^{a(y+\frac{b_1}{2a})^2} \left[\mathrm{erfc}\left(\sqrt{\frac{i}{2t}} (y - iBt) \right) \right] \\ & + e^{c - \frac{b_2^2}{4a}} e^{a(y+\frac{b_2}{2a})^2} \left[\mathrm{erf}\left(\sqrt{\frac{i}{2t}} (y + iBt) \right) + 1 \right] \Bigg)\end{aligned} \tag{B.60}$$

The integral whose integrand contains y is equal to 0, since the sum of the Error Functions is actually the free wavefunction ψ_F, and therefore an even function. The only contribution from this term comes from the part multiplied by $x_{cl}(t')$.

$$\begin{aligned}& x_{cl}(t') e^{c - \frac{b_1^2}{4a}} \int \mathrm{d}y\, e^{a(y+\frac{b_1}{2a})^2} \left[\mathrm{erfc}\left(\sqrt{\frac{i}{2t}} (y - iBt) \right) \right] \\ & + x_{cl}(t') e^{c - \frac{b_2^2}{4a}} \int \mathrm{d}y\, e^{a(y+\frac{b_2}{2a})^2} \left[\mathrm{erf}\left(\sqrt{\frac{i}{2t}} (y + iBt) \right) + 1 \right]\end{aligned} \tag{B.61}$$

To proceed, another change of variables is necessary for the two integrals, where $z_1 = y + \frac{b_1}{2a}$ and $z_2 = y + \frac{b_2}{2a}$,

$$\begin{aligned}& x_{cl}(t') e^{c - \frac{b_1^2}{4a}} \int \mathrm{d}z_1\, e^{a z_1^2} \left[\mathrm{erfc}\left(\sqrt{\frac{i}{2t}} \left(z_1 - \frac{b_1}{2a} - iBt \right) \right) \right] \\ & + x_{cl}(t') e^{c - \frac{b_2^2}{4a}} \int \mathrm{d}z_2\, e^{a z_2^2} \left[\mathrm{erf}\left(\sqrt{\frac{i}{2t}} \left(z_2 - \frac{b_2}{2a} + iBt \right) \right) + 1 \right]\end{aligned} \tag{B.62}$$

$$\begin{aligned}& x_{cl}(t') e^{c - \frac{b_1^2}{4a}} \int \mathrm{d}z_1\, e^{a z_1^2} \left[\mathrm{erfc}\left(\sqrt{\frac{i}{2t}} z_1 + \sqrt{\frac{i}{2t}} \left(-\frac{b_1}{2a} - iBt \right) \right) \right] \\ & + x_{cl}(t') e^{c - \frac{b_2^2}{4a}} \int \mathrm{d}z_2\, e^{a z_2^2} \left[\mathrm{erf}\left(\sqrt{\frac{i}{2t}} z_2 + \sqrt{\frac{i}{2t}} \left(-\frac{b_2}{2a} + iBt \right) \right) + 1 \right].\end{aligned} \tag{B.63}$$

With the two substitutions, z_1 and z_2, the following identity[1] can be used

$$\int \mathrm{d}z\, e^{-\rho z^2} \mathrm{erf}(\alpha + \beta z) = \sqrt{\frac{\pi}{\rho}} \mathrm{erf}\left(\frac{\alpha \sqrt{\rho}}{\sqrt{\beta^2 + \rho}} \right).$$

[1] Gradshteyn & Ryzhik. "Table of Integrals, Series, and Products." Seventh Edition. §8.259

Using the identity, Term II is now written as

$$\frac{B^2}{2}\sqrt{\frac{i}{2\pi}}\int_0^{t_1}\mathrm{d}t'\,A(t')\frac{e^{-\frac{1}{2}iB^2(t-t')}}{(t-t')^{3/2}}$$
$$\cdot\left(x_{cl}(t')e^{c-\frac{b_1^2}{4a}}\left[\sqrt{\frac{\pi}{\rho}}\mathrm{erfc}\left(\frac{\alpha_1\sqrt{\rho}}{\sqrt{\beta^2+\rho}}\right)\right]+x_{cl}(t')e^{c-\frac{b_2^2}{4a}}\left[\sqrt{\frac{\pi}{\rho}}\mathrm{erf}\left(\frac{\alpha_2\sqrt{\rho}}{\sqrt{\beta^2+\rho}}\right)+\sqrt{\frac{\pi}{\rho}}\right]\right) \tag{B.64}$$

where coefficients are defined as

$$\begin{aligned}\alpha_1&=\sqrt{\frac{i}{2t}}(-x_{cl}(t')-iBt')\\ \alpha_2&=\sqrt{\frac{i}{2t}}(-x_{cl}(t')+iBt')\\ \beta&=\sqrt{\frac{i}{2t}}\\ \rho&=-\frac{i}{2(t-t')}.\end{aligned}$$

Simplifying further

$$\begin{aligned}\frac{B^2}{2}\sqrt{\frac{i}{2\pi}}\int_0^{t_1}\mathrm{d}t'\,A(t')\frac{e^{-\frac{1}{2}iB^2(t-t')}}{(t-t')^{3/2}}x_{cl}(t')\sqrt{\frac{\pi}{\rho}}&\\ \cdot\left(e^{c-\frac{b_1^2}{4a}}\left[\mathrm{erfc}\left(-\frac{\left(\frac{1}{2}+\frac{i}{2}\right)(x_{cl}(t')+iBt')}{\sqrt{t'}}\right)\right]&\\ +e^{c-\frac{b_2^2}{4a}}\left[\mathrm{erf}\left(-\frac{\left(\frac{1}{2}+\frac{i}{2}\right)(x_{cl}(t')-iBt')}{\sqrt{t'}}\right)+1\right]\right)&\end{aligned} \tag{B.65}$$

and substituting in the rest of the original values for the coefficients, the current contribution from Term II is

$$\boxed{\begin{aligned}\frac{iB^2}{2}\int_0^{t_1}\mathrm{d}t'\,A(t')\frac{x_{cl}(t')}{t-t'}&\left(e^{-Bx_{cl}(t')}\left[\mathrm{erfc}\left(-\frac{\left(\frac{1}{2}+\frac{i}{2}\right)(x_{cl}(t')+iBt')}{\sqrt{t'}}\right)\right]\right.\\ &\left.+e^{Bx_{cl}(t')}\left[\mathrm{erf}\left(-\frac{\left(\frac{1}{2}+\frac{i}{2}\right)(x_{cl}(t')-iBt')}{\sqrt{t'}}\right)+1\right]\right).\end{aligned}} \tag{B.66}$$

B.5 Term III

The first step in simplifying Term III

$$\psi_F^*(x,t)p_{cl}(t)iB\int_0^t\mathrm{d}t'\,\psi(0,t')K_F(x,t|0,t') \tag{B.67}$$

is to substitute in the known quantities K_F

$$\psi_F^*(x,t)p_{cl}(t)iB\left(\frac{B^{1/2}}{\sqrt{2\pi i}}e^{ixp_{cl}(t)-iS_{cl}(t)}\int_0^{t_1}\mathrm{d}t'\,A(t')\frac{e^{\frac{i}{2}\left(B^2t'+\frac{(x-x_{cl}(t)+x_{cl}(t'))^2}{t-t'}\right)}}{(t-t')^{1/2}}\right) \tag{B.68}$$

and ψ_F

$$\begin{aligned}
&p_{cl}(t)\frac{iB}{2}\sqrt{B}e^{-ixp_{cl}(t)+iS_{cl}(t)}e^{-\frac{1}{2}iB^2t}\\
&\quad\cdot\left(e^{B(x-x_{cl}(t))}\left[\mathrm{erfc}\left(\sqrt{\frac{i}{2t}}\,(x-x_{cl}(t)-iBt)\right)\right.\right.\\
&\quad\left.\left.+e^{-B(x-x_{cl}(t))}\left[\mathrm{erf}\left(\sqrt{\frac{i}{2t}}\,(x-x_{cl}(t)+iBt)\right)+1\right]\right)\\
&\quad\cdot\left(\frac{B^{1/2}}{\sqrt{2\pi i}}e^{ixp_{cl}(t)-iS_{cl}(t)}\int_0^{t_1}\mathrm{d}t'\,A(t')\frac{e^{\frac{i}{2}\left(B^2t'+\frac{(x-x_{cl}(t)+x_{cl}(t'))^2}{t-t'}\right)}}{(t-t')^{1/2}}\right)
\end{aligned} \tag{B.69}$$

and simplifying exponents and grouping common terms, Term III can be written as

$$\begin{aligned}
&p_{cl}(t)\frac{B^2}{2}\sqrt{\frac{i}{2\pi}}\int_0^{t_1}\mathrm{d}t'\,A(t')\frac{e^{-\frac{1}{2}iB^2(t-t')}}{(t-t')^{1/2}}e^{\frac{i}{2}\frac{(x-x_{cl}(t)+x_{cl}(t'))^2}{t-t'}}\\
&\quad\cdot\left(e^{B(x-x_{cl}(t))}\left[\mathrm{erfc}\left(\sqrt{\frac{i}{2t}}\,(x-x_{cl}(t)-iBt)\right)\right]\right.\\
&\quad\left.+e^{-B(x-x_{cl}(t))}\left[\mathrm{erf}\left(\sqrt{\frac{i}{2t}}\,(x-x_{cl}(t)+iBt)\right)+1\right]\right).
\end{aligned} \tag{B.70}$$

Inserting the substitution $y = x - x_{cl}(t)$, the expression becomes

$$\begin{aligned}
&p_{cl}(t)\frac{B^2}{2}\sqrt{\frac{i}{2\pi}}\int_0^{t_1}\mathrm{d}t'\,A(t')\frac{e^{-\frac{1}{2}iB^2(t-t')}}{(t-t')^{1/2}}\\
&\quad\underbrace{\cdot\,e^{\frac{i}{2}\frac{(y+x_{cl}(t'))^2}{t-t'}}\left(e^{By}\left[\mathrm{erfc}\left(\sqrt{\frac{i}{2t}}\,(y-iBt)\right)\right]+e^{-By}\left[\mathrm{erf}\left(\sqrt{\frac{i}{2t}}\,(y+iBt)\right)+1\right]\right)}_{\text{Part i}}.
\end{aligned} \tag{B.71}$$

The integration of Part i with respect to y was previously calculated in (B.56). Using this result, Term III becomes

$$\begin{aligned} p_{cl}(t)\frac{B^2}{2}\sqrt{\frac{i}{2\pi}}\int_0^{t_1}\mathrm{d}t'\,A(t')\frac{e^{-\frac{1}{2}iB^2(t-t')}}{(t-t')^{1/2}}\sqrt{2\pi i(t-t')} \\ \cdot\left(e^{-\frac{1}{2}iB^2(t-t')-Bx_{cl}(t')}\left[\mathrm{erfc}\left(-\frac{\left(\frac{1}{2}+\frac{i}{2}\right)\left(x_{cl}(t')+iBt'\right)}{\sqrt{t'}}\right)\right]\right. \\ \left.+e^{-\frac{1}{2}iB^2(t-t')+Bx_{cl}(t')}\left[\mathrm{erf}\left(-\frac{\left(\frac{1}{2}+\frac{i}{2}\right)\left(x_{cl}(t')-iBt'\right)}{\sqrt{t'}}\right)+1\right]\right). \end{aligned} \tag{B.72}$$

Simplifying further and the contribution from Term III is

$$\boxed{\begin{aligned} p_{cl}(t)\frac{iB^2}{2}\int_0^{t_1}\mathrm{d}t'\,A(t')e^{-iB^2(t-t')} \\ \cdot\left(e^{-Bx_{cl}(t')}\left[\mathrm{erfc}\left(-\frac{\left(\frac{1}{2}+\frac{i}{2}\right)\left(x_{cl}(t')+iBt'\right)}{\sqrt{t'}}\right)\right]\right. \\ \left.+e^{Bx_{cl}(t')}\left[\mathrm{erf}\left(-\frac{\left(\frac{1}{2}+\frac{i}{2}\right)\left(x_{cl}(t')-iBt'\right)}{\sqrt{t'}}\right)+1\right]\right). \end{aligned}} \tag{B.73}$$

B.6 Term IV

Parts of the current contribution for Term IV have already been calculated. Below is the starting expression

$$-\left[\frac{x-x_{cl}(t)}{t}+p_{cl}(t)\right]\psi_F(x,t)iB\int_0^t\mathrm{d}t'\,\psi^*(0,t')K_F^*(x,t|0,t'). \tag{B.74}$$

It separates nicely into Part i and Part ii

$$\begin{aligned} \underbrace{-\left[\frac{x-x_{cl}(t)}{t}\right]\psi_F(x,t)iB\int_0^t\mathrm{d}t'\,\psi^*(0,t')K_F^*(x,t|0,t')}_{\text{i}} \\ \underbrace{-p_{cl}(t)\psi_F(x,t)iB\int_0^t\mathrm{d}t'\,\psi^*(0,t')K_F^*(x,t|0,t')}_{\text{ii}}. \end{aligned} \tag{B.75}$$

The current contribution from Part i is zero. This was determined during the derivation of Term II, specifically equation (B.60), by performing the change of variables $y = x - x_{cl}(t)$ and integrating over y. Essentially Part i is an integral of an even

function multiplied by an odd function. It is also clear that Part ii is the complex conjugate expression of Term III. Therefore the total contribution from Term IV is simply

$$\boxed{\begin{aligned}-p_{cl}(t)\frac{iB^2}{2}\int_0^{t_1}\mathrm{d}t'\,A(t')e^{iB^2(t-t')}&\\ \cdot\left(e^{-Bx_{cl}(t')}\left[\mathrm{erfc}\left(-\frac{\left(\frac{1}{2}-\frac{i}{2}\right)\left(x_{cl}(t')-iBt'\right)}{\sqrt{t'}}\right)\right]&\\ +e^{Bx_{cl}(t')}\left[\mathrm{erf}\left(-\frac{\left(\frac{1}{2}-\frac{i}{2}\right)\left(x_{cl}(t')+iBt'\right)}{\sqrt{t'}}\right)+1\right]\right).&\end{aligned}} \tag{B.76}$$

B.7 Term V

To find the contribution from Term V, the first step is to individually simplify Part i and Part ii

$$B^2\underbrace{\left(\int_0^{t_1}\mathrm{d}t'\,\psi(0,t')\left[\frac{x-x_{cl}(t)+x_{cl}(t')}{t-t'}\right]K_F(x,t|0,t')\right)}_{\text{i}}\underbrace{\left(\int_0^{t_2}\mathrm{d}t''\,\psi^*(0,t'')K_F^*(x,t|0,t'')\right)}_{\text{ii}} \tag{B.77}$$

For Part i the following steps are performed:

$$\int_0^{t_1}\mathrm{d}t'\,\psi(0,t')\left[\frac{x-x_{cl}(t)+x_{cl}(t')}{t-t'}\right]K_F(x,t|0,t') \tag{B.78}$$

$$\begin{aligned}\int_0^{t_1}\mathrm{d}t'\,A(t')B^{1/2}e^{i\frac{B^2t'}{2}}e^{-iS_{cl}(t')}\left[\frac{x-x_{cl}(t)+x_{cl}(t')}{t-t'}\right]&\\ \cdot e^{ixp_{cl}(t)-iS_{cl}(t)+iS_{cl}(t')}K_0(x-x_{cl}(t),t|-x_{cl}(t'),t')&\end{aligned} \tag{B.79}$$

$$B^{1/2}e^{ixp_{cl}(t)}e^{-iS_{cl}(t)}\int_0^{t_1}\mathrm{d}t'\,A(t')\left[x-x_{cl}(t)+x_{cl}(t')\right]\frac{e^{\frac{i}{2}B^2t'}}{t-t'}\frac{e^{-\frac{(x-x_{cl}(t)+x_{cl}(t'))^2}{2i(t-t')}}}{\sqrt{2\pi i}\sqrt{t-t'}} \tag{B.80}$$

$$\frac{B^{1/2}}{\sqrt{2\pi i}}e^{ixp_{cl}(t)}e^{-iS_{cl}(t)}\int_0^{t_1}\mathrm{d}t'\,A(t')\left[x-x_{cl}(t)+x_{cl}(t')\right]\frac{e^{\frac{i}{2}\left[B^2t'+\frac{(x-x_{cl}(t)+x_{cl}(t'))^2}{t-t'}\right]}}{(t-t')^{3/2}} \tag{B.81}$$

and for Part ii:

$$\int_0^{t_2} \mathrm{d}t''\, \psi^*(0,t'') K_F^*(x,t|0,t'') \tag{B.82}$$

$$\int_0^{t_2} \mathrm{d}t''\, A^*(t'') B^{1/2} e^{-i\frac{B^2 t''}{2}} e^{iS_{cl}(t'')} e^{-ixp_{cl}(t)+iS_{cl}(t)-iS_{cl}(t'')} \frac{e^{-\frac{(x-x_{cl}(t)+x_{cl}(t''))^2}{2i(t''-t)}}}{\sqrt{2\pi i}\sqrt{(t''-t)}} \tag{B.83}$$

$$\frac{B^{1/2}}{\sqrt{2\pi i}} e^{-ixp_{cl}(t)+iS_{cl}(t)} \int_0^{t_2} \mathrm{d}t''\, A^*(t'') e^{-i\frac{B^2 t''}{2}} \frac{e^{-\frac{\left(x-x_{cl}(t)+x_{cl}(t'')\right)^2}{2i(t''-t)}}}{(t''-t)^{1/2}} \tag{B.84}$$

$$\frac{B^{1/2}}{\sqrt{2\pi i}} e^{-ixp_{cl}(t)+iS_{cl}(t)} \int_0^{t_2} \mathrm{d}t''\, A^*(t'') \frac{e^{\frac{i}{2}\left(-B^2 t''+\frac{\left(x-x_{cl}(t)+x_{cl}(t'')\right)^2}{t''-t}\right)}}{(t''-t)^{1/2}} \tag{B.85}$$

Combining these two terms (B.81) and (B.85), Term V now has the form

$$\begin{aligned} &\frac{B^3}{2\pi i} \int_0^{t_1} \mathrm{d}t'\, A(t') \left[x - x_{cl}(t) + x_{cl}(t')\right] \frac{e^{\frac{i}{2}\left[B^2 t' + \frac{(x-x_{cl}(t)+x_{cl}(t'))^2}{t-t'}\right]}}{(t-t')^{3/2}} \\ &\quad \cdot \int_0^{t_2} \mathrm{d}t''\, A^*(t'') \frac{e^{\frac{i}{2}\left(-B^2 t''+\frac{\left(x-x_{cl}(t)+x_{cl}(t'')\right)^2}{t''-t}\right)}}{(t''-t)^{1/2}}. \end{aligned} \tag{B.86}$$

Rearranging the two time integrals and grouping x terms, it can be written as

$$\begin{aligned} &\frac{B^3}{2\pi} \int_0^{t_1} \mathrm{d}t' \int_0^{t_2} \mathrm{d}t''\, A(t') A^*(t'') \frac{e^{\frac{i}{2}B^2(t'-t'')}}{(t-t')^{3/2}(t-t'')^{1/2}} \left[x - x_{cl}(t) + x_{cl}(t')\right] \\ &\qquad \cdot e^{\frac{i}{2}\left[\frac{\left(x-x_{cl}(t)+x_{cl}(t')\right)^2}{t-t'} + \frac{\left(x-x_{cl}(t)+x_{cl}(t'')\right)^2}{t''-t}\right]}. \end{aligned} \tag{B.87}$$

Focusing on the terms only containing x, the integral over all space is

$$\int \mathrm{d}x\, \left[x - x_{cl}(t) + x_{cl}(t')\right] e^{\frac{i}{2}\left[\frac{\left(x-x_{cl}(t)+x_{cl}(t')\right)^2}{t-t'} + \frac{\left(x-x_{cl}(t)+x_{cl}(t'')\right)^2}{t''-t}\right]}. \tag{B.88}$$

As done before, the change of variables $y = x - x_{cl}(t)$ is performed, and terms are grouped with equal power of y

$$\int \mathrm{d}y\, \left[y + x_{cl}(t')\right] e^{\frac{i}{2}\left[\frac{\left(y+x_{cl}(t')\right)^2}{t-t'} + \frac{\left(y+x_{cl}(t'')\right)^2}{t''-t}\right]} \tag{B.89}$$

$$\int \mathrm{d}y\, \left[y + x_{cl}(t')\right] e^{\frac{i}{2}\left\{\left[\frac{1}{t-t'} + \frac{1}{t''-t}\right]y^2 + \left[\frac{2x_{cl}(t')}{t-t'} + \frac{2x_{cl}(t'')}{t''-t}\right]y + \left[\frac{x_{cl}^2(t')}{t-t'} + \frac{x_{cl}^2(t'')}{t''-t}\right]\right\}}. \tag{B.90}$$

If the following coefficients are defined

$$\begin{aligned} a =& \frac{i}{2}\left[\frac{1}{t-t'}+\frac{1}{t''-t}\right] \\ b =& \frac{i}{2}\left[\frac{2x_{cl}(t')}{t-t'}+\frac{2x_{cl}(t'')}{t''-t}\right] \\ c =& \frac{i}{2}\left[\frac{x_{cl}^2(t')}{t-t'}+\frac{x_{cl}^2(t'')}{t''-t}\right] \end{aligned}$$

then the integrals are simple Gaussians

$$\int \mathrm{d}y\ [y+x_{cl}(t')]\, e^{\left[ay^2+by+c\right]} \tag{B.91}$$

$$\int \mathrm{d}y\, y e^{\left[ay^2+by+c\right]} + x_{cl}(t') \int \mathrm{d}y\, e^{\left[ay^2+by+c\right]} \tag{B.92}$$

and can be evaluated to

$$\frac{i\sqrt{\pi}b}{2a^{3/2}} e^{c-\frac{b^2}{4a}} + i x_{cl}(t') \sqrt{\frac{\pi}{a}} e^{c-\frac{b^2}{4a}} \tag{B.93}$$

$$\left(\frac{i\sqrt{\pi}b}{2a^{3/2}} + i x_{cl}(t') \sqrt{\frac{\pi}{a}}\right) e^{c-\frac{b^2}{4a}}. \tag{B.94}$$

Substituting the coefficients back into the above resulting expressions, the spatial integral is equal to

$$\left(\frac{\sqrt{2\pi i}\sqrt{t-t'}\sqrt{t-t''}}{(t'-t'')^{3/2}}\left[t x_{cl}(t') - t x_{cl}(t'') + t' x_{cl}(t'') - t'' x_{cl}(t')\right] + \frac{i\sqrt{2\pi i}\sqrt{t'-t}\sqrt{t-t''}}{\sqrt{t'-t''}} x_{cl}(t')\right) \cdot e^{-\frac{i}{2}\frac{\left[x_{cl}(t')-x_{cl}(t'')\right]^2}{t'-t''}} \tag{B.95}$$

and therefore Term V is equal to

$$\begin{aligned} \int_0^{t_1} \mathrm{d}t' \int_0^{t_2} \mathrm{d}t'' \Bigg(& \frac{B^3}{2\pi} A(t') A^*(t'') \frac{e^{\frac{i}{2}B^2(t'-t'')}}{(t-t')^{3/2}(t-t'')^{1/2}} \frac{\sqrt{2\pi i}\sqrt{t-t'}\sqrt{t-t''}}{(t'-t'')^{3/2}} \\ & \cdot \left[t x_{cl}(t') - t x_{cl}(t'') + t' x_{cl}(t'') - t'' x_{cl}(t')\right] \\ & - \frac{B^3}{2\pi} A(t') A^*(t'') \frac{e^{\frac{i}{2}B^2(t'-t'')}}{(t-t')^{3/2}(t-t'')^{1/2}} \frac{\sqrt{2\pi i}\sqrt{t-t'}\sqrt{t-t''}}{\sqrt{t'-t''}} x_{cl}(t') \Bigg) e^{-\frac{i}{2}\frac{\left[x_{cl}(t')-x_{cl}(t'')\right]^2}{t'-t''}}. \end{aligned} \tag{B.96}$$

Many simplification steps can be performed to find that the expression is equal to

$$\int_0^{t_1}\mathrm{d}t'\int_0^{t_2}\mathrm{d}t''\left(B^3\sqrt{\frac{i}{2\pi}}A(t')A^*(t'')\frac{e^{\frac{i}{2}B^2(t'-t'')}}{(t-t')(t'-t'')^{3/2}}\left[tx_{cl}(t')-tx_{cl}(t'')+t'x_{cl}(t'')-t''x_{cl}(t')\right]\right.$$
$$\left.-B^3\sqrt{\frac{i}{2\pi}}A(t')A^*(t'')\frac{e^{\frac{i}{2}B^2(t'-t'')}}{(t-t')(t'-t'')^{1/2}}x_{cl}(t')\right)e^{-\frac{i}{2}\frac{\left[x_{cl}(t')-x_{cl}(t'')\right]^2}{t'-t''}} \tag{B.97}$$

and equal to

$$B^3\sqrt{\frac{i}{2\pi}}\int_0^{t_1}\mathrm{d}t'\int_0^{t_2}\mathrm{d}t''\,A(t')A^*(t'')\frac{e^{\frac{i}{2}B^2(t'-t'')}}{(t-t')(t'-t'')^{1/2}}e^{-\frac{i}{2}\frac{\left[x_{cl}(t')-x_{cl}(t'')\right]^2}{t'-t''}}$$
$$\cdot\left(\frac{tx_{cl}(t')-tx_{cl}(t'')+t'x_{cl}(t'')-t''x_{cl}(t')-t'x_{cl}(t')+t''x_{cl}(t')}{t'-t''}\right). \tag{B.98}$$

The final expression for the current contribution from Term V

$$\boxed{B^3\sqrt{\frac{i}{2\pi}}\int_0^{t_1}\mathrm{d}t'\int_0^{t_2}\mathrm{d}t''\,A(t')A^*(t'')\frac{e^{\frac{i}{2}B^2(t'-t'')}}{(t'-t'')^{3/2}}e^{-\frac{i}{2}\frac{\left[x_{cl}(t')-x_{cl}(t'')\right]^2}{t'-t''}}\left(x_{cl}(t')-x_{cl}(t'')\right).} \tag{B.99}$$

B.8 Term VI

To solve for Term VI, the starting expression is again split into Part i and Part ii, and are simplified separately:

$$p_{cl}(t)B^2\underbrace{\left(\int_0^{t_1}\mathrm{d}t'\,\psi^*(0,t')K_F^*(x,t|0,t')\right)}_{\text{i}}\underbrace{\left(\int_0^{t_2}\mathrm{d}t''\,\psi(0,t'')K_F(x,t|0,t'')\right)}_{\text{ii}}. \tag{B.100}$$

For Part i:

$$\int_0^{t_1}\mathrm{d}t'\,\psi^*(0,t')K_F^*(x,t|0,t') \tag{B.101}$$

$$\int_0^{t_1}\mathrm{d}t'\,A^*(t')B^{1/2}e^{-i\frac{B^2t'}{2}}e^{iS_{cl}(t')}e^{-ixp_{cl}(t)+iS_{cl}(t)-iS_{cl}(t')}\frac{e^{-\frac{(x-x_{cl}(t)+x_{cl}(t'))^2}{2i(t'-t)}}}{\sqrt{2\pi i}\sqrt{(t'-t)}} \tag{B.102}$$

$$\frac{B^{1/2}}{\sqrt{2\pi i}}e^{-ixp_{cl}(t)+iS_{cl}(t)}\int_0^{t_1}\mathrm{d}t'\,A^*(t')e^{-i\frac{B^2t'}{2}}\frac{e^{-\frac{\left(x-x_{cl}(t)+x_{cl}(t')\right)^2}{2i(t'-t)}}}{(t'-t)^{1/2}} \tag{B.103}$$

$$\frac{B^{1/2}}{\sqrt{2\pi i}}e^{-ixp_{cl}(t)+iS_{cl}(t)}\int_0^{t_1}\mathrm{d}t'\,A^*(t')\frac{e^{\frac{i}{2}\left(-B^2t'+\frac{\left(x-x_{cl}(t)+x_{cl}(t')\right)^2}{t'-t}\right)}}{(t'-t)^{1/2}} \tag{B.104}$$

Since Part ii is the complex conjugate of Part i, except with the replacements $t' \to t''$ and $t_1 \to t_2$, the same simplifications steps are performed:

$$\int_0^{t_2} \mathrm{d}t''\, \psi(0,t'') K_F(x,t|0,t'') \tag{B.105}$$

$$\int_0^{t_2} \mathrm{d}t''\, A(t'') B^{1/2} e^{i\frac{B^2 t''}{2}} e^{-iS_{cl}(t'')} e^{ixp_{cl}(t) - iS_{cl}(t) + iS_{cl}(t'')} \frac{e^{-\frac{(x-x_{cl}(t)+x_{cl}(t''))^2}{2i(t-t'')}}}{\sqrt{2\pi i}\sqrt{(t-t'')}} \tag{B.106}$$

$$\frac{B^{1/2}}{\sqrt{2\pi i}} e^{ixp_{cl}(t) - iS_{cl}(t)} \int_0^{t_2} \mathrm{d}t''\, A(t'') e^{i\frac{B^2 t''}{2}} \frac{e^{-\frac{(x-x_{cl}(t)+x_{cl}(t''))^2}{2i(t-t'')}}}{(t-t'')^{1/2}} \tag{B.107}$$

$$\frac{B^{1/2}}{\sqrt{2\pi i}} e^{ixp_{cl}(t) - iS_{cl}(t)} \int_0^{t_2} \mathrm{d}t''\, A(t'') \frac{e^{\frac{i}{2}\left(B^2 t'' + \frac{(x-x_{cl}(t)+x_{cl}(t''))^2}{t-t''}\right)}}{(t-t'')^{1/2}} \tag{B.108}$$

Combine Part i and Part ii, Term VI becomes

$$\frac{B}{2\pi i} \int_0^{t_1} \mathrm{d}t' \int_0^{t_2} \mathrm{d}t''\, A^*(t') A(t'') \frac{e^{\frac{i}{2}B^2(t''-t')}}{(t'-t)^{1/2}(t-t'')^{1/2}} e^{\frac{i}{2}\left[\frac{(x-x_{cl}(t)+x_{cl}(t'))^2}{t'-t} + \frac{(x-x_{cl}(t)+x_{cl}(t''))^2}{t-t''}\right]} \tag{B.109}$$

Focusing on the terms involving x, the integral over all space is

$$\int \mathrm{d}x\, e^{\frac{i}{2}\left[\frac{(x-x_{cl}(t)+x_{cl}(t'))^2}{t'-t} + \frac{(x-x_{cl}(t)+x_{cl}(t''))^2}{t-t''}\right]}. \tag{B.110}$$

Performing a change of variables $y = x - x_{cl}(t)$ and grouping terms with equal power of y, it is clear that it is a Gaussian integral

$$\int \mathrm{d}y\, e^{\frac{i}{2}\left\{\left[\frac{1}{t-t''} + \frac{1}{t'-t}\right]y^2 + \left[\frac{2x_{cl}(t'')}{t-t''} + \frac{2x_{cl}(t')}{t'-t}\right]y + \left[\frac{x_{cl}^2(t'')}{t-t''} + \frac{x_{cl}^2(t')}{t'-t}\right]\right\}}. \tag{B.111}$$

Defining the coefficients

$$\begin{aligned} a =& \frac{i}{2}\left[\frac{1}{t-t''} + \frac{1}{t'-t}\right] \\ b =& \frac{i}{2}\left[\frac{2x_{cl}(t'')}{t-t''} + \frac{2x_{cl}(t')}{t'-t}\right] \\ c =& \frac{i}{2}\left[\frac{x_{cl}^2(t'')}{t-t''} + \frac{x_{cl}^2(t')}{t'-t}\right] \end{aligned}$$

allows for the following identity to be used

$$\int \mathrm{d}y\, e^{\left[ay^2+by+c\right]} = i\sqrt{\frac{\pi}{a}} e^{c-\frac{b^2}{4a}}. \tag{B.112}$$

Substituting the coefficients back into the equation and simplifying, the spatial integral is simply

$$\frac{i\sqrt{2\pi i}\sqrt{t-t'}\sqrt{t-t''}}{\sqrt{t''-t'}}e^{\frac{i}{2}\frac{[x_{cl}(t')-x_{cl}(t'')]}{t'-t''}}. \tag{B.113}$$

Term VI can now be written as

$$p_{cl}(t)B^2\left(\frac{B}{2\pi i}\int_0^{t_1}\mathrm{d}t'\int_0^{t_2}\mathrm{d}t''\,A^*(t')A(t'')\frac{e^{\frac{i}{2}B^2(t''-t')}}{(t'-t)^{1/2}(t-t'')^{1/2}}\frac{i\sqrt{2\pi i}\sqrt{t-t'}\sqrt{t-t''}}{\sqrt{t''-t'}}e^{\frac{i}{2}\frac{[x_{cl}(t')-x_{cl}(t'')]}{t'-t''}}\right) \tag{B.114}$$

and simplified into

$$\boxed{-p_{cl}(t)B^3\sqrt{\frac{i}{2\pi}}\int_0^{t_1}\mathrm{d}t'\int_0^{t_2}\mathrm{d}t''\,A^*(t')A(t'')\frac{e^{-\frac{i}{2}B^2(t'-t'')}}{\sqrt{t'-t''}}e^{\frac{i}{2}\frac{[x_{cl}(t')-x_{cl}(t'')]}{t'-t''}}.} \tag{B.115}$$

B.9 Final results

Combining each of the Terms, the total contribution to probability current is the real part of the following equation

$$\begin{aligned}
&p_{cl}(t)\\
&+\frac{iB^2}{2}\int_0^{t_1}\mathrm{d}t'\,A(t')\frac{x_{cl}(t')}{t-t'}\\
&\cdot\left(e^{-Bx_{cl}(t')}\left[\mathrm{erfc}\left(-\frac{\left(\frac{1}{2}+\frac{i}{2}\right)(x_{cl}(t')+iBt')}{\sqrt{t'}}\right)\right]+e^{Bx_{cl}(t')}\left[\mathrm{erf}\left(-\frac{\left(\frac{1}{2}+\frac{i}{2}\right)(x_{cl}(t')-iBt')}{\sqrt{t'}}\right)+1\right]\right)\\
&+p_{cl}(t)\frac{iB^2}{2}\int_0^{t_1}\mathrm{d}t'\,A(t')e^{-iB^2(t-t')}\\
&\cdot\left(e^{-Bx_{cl}(t')}\left[\mathrm{erfc}\left(-\frac{\left(\frac{1}{2}+\frac{i}{2}\right)(x_{cl}(t')+iBt')}{\sqrt{t'}}\right)\right]+e^{Bx_{cl}(t')}\left[\mathrm{erf}\left(-\frac{\left(\frac{1}{2}+\frac{i}{2}\right)(x_{cl}(t')-iBt')}{\sqrt{t'}}\right)+1\right]\right)\\
&-p_{cl}(t)\frac{iB^2}{2}\int_0^{t_1}\mathrm{d}t'\,A(t')e^{iB^2(t-t')}\\
&\cdot\left(e^{-Bx_{cl}(t')}\left[\mathrm{erfc}\left(-\frac{\left(\frac{1}{2}-\frac{i}{2}\right)(x_{cl}(t')-iBt')}{\sqrt{t'}}\right)\right]+e^{Bx_{cl}(t')}\left[\mathrm{erf}\left(-\frac{\left(\frac{1}{2}-\frac{i}{2}\right)(x_{cl}(t')+iBt')}{\sqrt{t'}}\right)+1\right]\right)\\
&+B^3\sqrt{\frac{i}{2\pi}}\int_0^{t_1}\mathrm{d}t'\int_0^{t_2}\mathrm{d}t''\,A(t')A^*(t'')\frac{e^{\frac{i}{2}B^2(t'-t'')}}{(t'-t'')^{3/2}}e^{-\frac{i}{2}\frac{[x_{cl}(t')-x_{cl}(t'')]^2}{t'-t''}}(x_{cl}(t')-x_{cl}(t''))\\
&-p_{cl}(t)B^3\sqrt{\frac{i}{2\pi}}\int_0^{t_1}\mathrm{d}t'\int_0^{t_2}\mathrm{d}t''\,A^*(t')A(t'')\frac{e^{-\frac{i}{2}B^2(t'-t'')}}{\sqrt{t'-t''}}e^{\frac{i}{2}\frac{[x_{cl}(t')-x_{cl}(t'')]}{t'-t''}}.
\end{aligned} \tag{B.116}$$

From the identity stated in (B.28), the result (B.116) can be simplified to

$$p_{cl}(t) + \frac{iB^2}{2}\int_0^{t_1} \mathrm{d}t'\, A(t')\frac{x_{cl}(t')}{t-t'}$$
$$\cdot\left(e^{-Bx_{cl}(t')}\left[\operatorname{erfc}\left(-\frac{\left(\frac{1}{2}+\frac{i}{2}\right)\left(x_{cl}(t')+iBt'\right)}{\sqrt{t'}}\right)\right] + e^{Bx_{cl}(t')}\left[\operatorname{erf}\left(-\frac{\left(\frac{1}{2}+\frac{i}{2}\right)\left(x_{cl}(t')-iBt'\right)}{\sqrt{t'}}\right)+1\right]\right)$$
$$+ B^3\sqrt{\frac{i}{2\pi}}\int_0^{t_1}\mathrm{d}t'\int_0^{t_2}\mathrm{d}t''\, A(t')A^*(t'')\frac{e^{\frac{i}{2}B^2(t'-t'')}}{(t'-t'')^{3/2}}e^{-\frac{i}{2}\frac{\left[x_{cl}(t')-x_{cl}(t'')\right]^2}{t'-t''}}\left(x_{cl}(t')-x_{cl}(t'')\right). \tag{B.117}$$

This is total time dependent current of the 1D Dirac-delta potential model for an arbitrary excitation field. Since most propagation simulations only use the nonlinear current, the linear part must be subtracted from this. For this task, an algebra program was used and the resulting nonlinear current expressions are presented in Chapter 2, Equations (2.35) to (2.37).

Appendix C

Derivation of 1D Dirac-Delta Resonances

This Appendix provides a more thorough derivation of the resonant state expressions of the 1D Dirac-delta potential system that were shown in Section 4.4.1.

C.1 Wavefunctions

The Hamiltonian for the 1D Dirac-delta potential model with external field F is

$$H = -\frac{1}{2}\nabla^2 - B\delta(x) - xF$$

where B is the strength of interaction with the delta function and also defines the ground state energy: $E_g = B^2/2$. The unnormalized wavefunctions are a linear combination of Airy functions

$$g(x, F(t)) = \begin{cases} Ai[\alpha(x+\beta)]Ci(\alpha\beta) & x < 0 \\ Ci[\alpha(x+\beta)]Ai(\alpha\beta) & x > 0 \end{cases} \tag{C.1}$$

where $\alpha = -(2F)^{1/3}$ and $\beta = E(F)/F$. These wavefunctions are continuous in value at $x = 0$, but discontinuous in derivative.

C.2 Eigenvalue equation

The delta function forces a particular boundary condition for the wavefunctions at its location, namely

$$\frac{d\psi(0^+)}{dx} - \frac{d\psi(0^-)}{dx} = -2B\psi(0).$$

Substituting the unnormalized wavefunction into the boundary condition results in the eigenvalue equation

$$\boxed{1 = \frac{2\pi B}{(2F)^{1/3}} Ai\left(-\frac{2E}{(2F)^{2/3}}\right) Ci\left(-\frac{2E}{(2F)^{2/3}}\right).} \tag{C.2}$$

By rearranging this quantity and from the definition of the unnormalized wavefunctions, it is apparent that

$$g(x=0, F) = Ai\left(-\frac{2E}{(2F)^{2/3}}\right) Ci\left(-\frac{2E}{(2F)^{2/3}}\right)$$

and therefore

$$g(x=0,F) = \frac{(2F)^{1/3}}{2\pi B} = -\frac{\alpha}{2\pi B}.$$

It is interesting that all resonances (the ground state, Right family or Left family) share a common property. The value of all unnormalized wavefunctions at the location of the delta function $g(x=0)$ are equal and only dependent on the field F and strength of the interaction B. However, the normalization factor is different for each resonant state. This property is extremely useful in simplifying the expressions presented below.

C.3 Normalizaton

The wavefunctions are normalized $\psi = g/N$ by calculating the normalization factor using the integral

$$\begin{aligned} N(F)^2 &= \int_{-\infty}^{\infty} g(x,F)^2 dx \\ &= \int_{-\infty}^{0} Ai^2(\alpha(x+\beta))Ci^2(\alpha\beta)dx + \int_{0}^{\infty} Ci^2(\alpha(x+\beta))Ai^2(\alpha\beta)dx \end{aligned}$$

The integration of x over the range $(-\infty,\infty)$ represents integration along the contour $\mathcal{C}$ shown in Figure 4.1. For this integral, the identity (VS 3.50) in Vallée [104] is used. If A is a linear combination of Airy functions (Ai and/or Bi), then

$$\int A[\alpha(x+\beta)]^2 dx = (x+\beta)A[\alpha(x+\beta)]^2 - \frac{1}{\alpha}A'[\alpha(x+\beta)]^2.$$

Given that wavefunctions and their derivatives decay ($A[x]\to 0$, $A'[x]\to 0$) for large $|x|$ along the contour $\mathcal{C}$, then

$$N(F)^2 = -\frac{1}{\alpha}\left[Ci^2(\alpha\beta)Ai'^2(\alpha\beta) - Ci'^2(\alpha\beta)Ai^2(\alpha\beta)\right].$$

This result is simplified further using the Wronskian relation

$$AiBi' - Ai'Bi = \frac{1}{\pi} \implies AiCi' - Ai'Ci = \frac{1}{\pi}$$

resulting in the normalization factor

$$\boxed{N(F) = \sqrt{\frac{Ci(\alpha\beta)Ai'(\alpha\beta) + Ai(\alpha\beta)Ci'(\alpha\beta)}{\alpha\pi}}.} \tag{C.3}$$

The normalized wavefunctions ψ are now explicitly

$$\boxed{\psi(x,F(t)) = \begin{cases} Ai[\alpha(x+\beta)]Ci(\alpha\beta)/N(F) & x<0 \\ Ci[\alpha(x+\beta)]Ai(\alpha\beta)/N(F) & x>0 \end{cases}} \tag{C.4}$$

C.4 Other useful relations

Many other useful relations can be found from the quantities presented in the previous section. The change in the normalization w.r.t. field $\partial_F N(F)$ may appear in future calculations (though it is not currently used) and is given here as reference

$$\partial_F N = -\frac{N}{6F} + \frac{Ai'(\alpha\beta)Ci'(\alpha\beta)\dot{E}(F)}{\pi N F} - \frac{2E(F)Ai'(\alpha\beta)Ci'(\alpha\beta)}{3\pi N F^2} - \frac{2^{1/3}E(F)\dot{E}(F)}{\pi N F^{5/3}} + \frac{2^{4/3}E(F)^2}{3\pi N F^{8/3}}. \tag{C.5}$$

This quantity is simplified further by using a relation for $\dot{E}(F) = \partial_F E(F)$, which is calculated by differentiating the eigenvalue equation (C.2) w.r.t F

$$\partial_F \left[\frac{\pi B}{(2F)^{1/3}} Ai\left(-\frac{2E}{(2F)^{2/3}}\right) Ci\left(-\frac{2E}{(2F)^{2/3}}\right)\right] = 0$$

and solving for $\dot{E}(F)$

$$\dot{E}(F) = -\frac{F^{2/3}Ai(\alpha\beta)Ci(\alpha\beta) - 2^{4/3}\overbrace{\left(Ci(\alpha\beta)Ai'(\alpha\beta) + Ci'(\alpha\beta)Ai(\alpha\beta)\right)}^{\pi\alpha N(F)^2} E(F)}{3\cdot 2^{1/3}\underbrace{\left(Ci(\alpha\beta)Ai'(\alpha\beta) + Ci'(\alpha\beta)Ai(\alpha\beta)\right)}_{\pi\alpha N(F)^2} F}$$

$$\dot{E}(F) = \frac{2E(F)}{3F} + \frac{Ai(\alpha\beta)Ci(\alpha\beta)}{3\pi\alpha^2 N(F)^2}$$

and with help from the eigenvalue equation $Ai(\alpha\beta)Ci(\alpha\beta) = -\frac{\alpha}{2\pi B}$

$$\boxed{\dot{E}(F) = \frac{2E(F)}{3F} - \frac{1}{6\pi^2\alpha B N(F)^2}.} \tag{C.6}$$

The expression (C.5) is now simplified to

$$\boxed{\partial_F N = -\frac{N}{6F} + \frac{\alpha}{12\pi^3 B N^3 F^2}\left(\frac{E}{\pi} + \alpha Ai'(\alpha\beta)Ci'(\alpha\beta)\right).} \tag{C.7}$$

C.5 Coupling matrix elements

In Section 4.4.1 expressions for the coupling matrix elements $\langle\partial_F\psi_n|\psi_k\rangle$ were given. Here the full details of the calculation are presented. Before proceeding, one more quantity is needed in order to compute it: the derivative of the wavefunctions w.r.t. the field F

$$\partial_F g(x) = \begin{cases} \zeta\gamma Ci'(\alpha\beta)Ai[\alpha(x+\beta)] + \zeta(\gamma - Fx)Ci(\alpha\beta)Ai'[\alpha(x+\beta)] & x < 0 \\ \zeta\gamma Ai'(\alpha\beta)Ci[\alpha(x+\beta)] + \zeta(\gamma - Fx)Ai(\alpha\beta)Ci'[\alpha(x+\beta)] & x > 0 \end{cases} \tag{C.8}$$

where

$$\zeta = \frac{2^{1/3}}{3F^{5/3}} = -\frac{\alpha}{3F^2}, \quad \gamma = 2E(F) - 3F\dot{E}(F) = \frac{3F}{6\pi^2\alpha B N^2}.$$

The wavefunctions for $x < 0$ labeled with subscript L are written as

$$\partial_F g_L(x) = -\frac{2^{1/3}}{3F^{5/3}}(3\dot{E}F-2E)Ci'(\alpha\beta)Ai[\alpha(x+\beta)]-\frac{2^{1/3}}{3F^{5/3}}(3\dot{E}F-2E+Fx)Ci(\alpha\beta)Ai'[\alpha(x+\beta)]$$

and wavefunctions for $x > 0$ labeled R are

$$\partial_F g_R(x) = -\frac{2^{1/3}}{3F^{5/3}}(3\dot{E}F-2E)Ai'(\alpha\beta)Ci[\alpha(x+\beta)]-\frac{2^{1/3}}{3F^{5/3}}(3\dot{E}F-2E+Fx)Ai(\alpha\beta)Ci'[\alpha(x+\beta)].$$

Using

$$\dot{E} = \frac{2E}{3F} - \frac{1}{6\pi^2\alpha B N^2}$$

the quantity $\partial_F g$ is simplified to

$$\partial_F g_L(x) = \Delta Ci'(\alpha\beta)Ai[\alpha(x+\beta)] + \Delta Ci(\alpha\beta)Ai'[\alpha(x+\beta)] - \frac{2x}{3\alpha^2}Ci(\alpha\beta)Ai'[\alpha(x+\beta)]$$

$$\partial_F g_R(x) = \Delta Ai'(\alpha\beta)Ci[\alpha(x+\beta)] + \Delta Ai(\alpha\beta)Ci'[\alpha(x+\beta)] - \frac{2x}{3\alpha^2}Ai(\alpha\beta)Ci'[\alpha(x+\beta)]$$

where $\Delta = 1/(3\pi^2\alpha^3 B N^2)$. Given the quantities $\partial_F g_L$ and $\partial_F g_R$, the sought coupling terms $\langle \partial_F \psi_n | \psi_k \rangle$ are simply

$$\langle \partial_F \psi_n | \psi_k \rangle = \frac{1}{N_n N_k} \langle \partial_F g_n | g_k \rangle .$$

To explicitly evaluate these quantities, the following integrals must be evaluated, where Airy function arguments $\{n, k\}$ signify $\{\alpha\beta_n, \alpha\beta_k\}$:

$$\begin{aligned}
\langle \partial_F g_n | g_k \rangle = {} & \Delta Ci'(n)Ci(k)\int_{-\infty}^{0} Ai[\alpha(x+\beta_n)]Ai[\alpha(x+\beta_k)]dx \\
& + \Delta Ai'(n)Ai(k)\int_{0}^{\infty} Ci[\alpha(x+\beta_n)]Ci[\alpha(x+\beta_k)]dx \\
& + \Delta Ci(n)Ci(k)\int_{-\infty}^{0} Ai'[\alpha(x+\beta_n)]Ai[\alpha(x+\beta_k)]dx \\
& + \Delta Ai(n)Ai(k)\int_{0}^{\infty} Ci'[\alpha(x+\beta_n)]Ci[\alpha(x+\beta_k)]dx \\
& - \frac{2}{3\alpha^2}Ci(n)Ci(k)\int_{-\infty}^{0} xAi'[\alpha(x+\beta_n)]Ai[\alpha(x+\beta_k)]dx \\
& - \frac{2}{3\alpha^2}Ai(n)Ai(k)\int_{0}^{\infty} xCi'[\alpha(x+\beta_n)]Ci[\alpha(x+\beta_k)]dx.
\end{aligned}$$

There are 3 types of Airy integrals to solve: $\int ABdx$, $\int A'Bdx$, $\int xA'Bdx$, where A and B are linear combinations of Airy functions. For the first integral, Vallée (3.53) is used:

$$\begin{aligned}&\int A[\alpha(x+\beta_n)]B[\alpha(x+\beta_k)]dx\\&\quad=\frac{1}{\alpha^2(\beta_n-\beta_k)}\Big[A'[\alpha(x+\beta_n)]B[\alpha(x+\beta_k)]-A[\alpha(x+\beta_n)]B'[\alpha(x+\beta_k)]\Big].\end{aligned}\tag{C.9}$$

To deal with the divergent behavior of the wavefunctions far from the origin, integration is performed along the contour $\mathcal{C}$ that decays the resonant state wavefunctions and their derivatives $\to 0$ as $x \to \pm\infty$. Using (C.9), the first two integrals can be evaluated resulting in

$$\begin{aligned}\langle\partial_F g_n|g_k\rangle=&\frac{\Delta}{\alpha^2(\beta_n-\beta_k)}\Big[Ai'(n)Ai(k)Ci(n)Ci'(k)-Ai(n)Ai'(k)Ci'(n)Ci(k)\Big]\\&+\Delta Ci(n)Ci(k)\int_{-\infty}^{0}Ai'[\alpha(x+\beta_n)]Ai[\alpha(x+\beta_k)]dx\\&+\Delta Ai(n)Ai(k)\int_{0}^{\infty}Ci'[\alpha(x+\beta_n)]Ci[\alpha(x+\beta_k)]dx\\&-\frac{2}{3\alpha^2}Ci(n)Ci(k)\int_{-\infty}^{0}xAi'[\alpha(x+\beta_n)]Ai[\alpha(x+\beta_k)]dx\\&-\frac{2}{3\alpha^2}Ai(n)Ai(k)\int_{0}^{\infty}xCi'[\alpha(x+\beta_n)]Ci[\alpha(x+\beta_k)]dx.\end{aligned}$$

The last four integrals can be written in a more compact form:

$$\begin{aligned}\langle\partial_F g_n|g_k\rangle=&\frac{\Delta}{\alpha^2(\beta_n-\beta_k)}\Big[Ai'(n)Ai(k)Ci(n)Ci'(k)-Ai(n)Ai'(k)Ci'(n)Ci(k)\Big]\\&+\Delta\int_{-\infty}^{\infty}A'Bdx\\&-\frac{2}{3\alpha^2}\int_{-\infty}^{\infty}xA'Bdx.\end{aligned}$$

The second and third integrals are not found in any published resource, so the solutions must be derived using some clever symmetry properties of resonant states. An integration technique has been developed for these types of integrals. This procedure is detailed in Appendix A. The results of the second integral can be written using

$$\boxed{\int_{-\infty}^{\infty}A'Bdx=-\frac{1}{\alpha^2(\beta_n-\beta_k)}(A'B')\Big|_{0^+}^{0^-}}\tag{C.10}$$

and results in

$$\begin{aligned}\langle \partial_F g_n | g_k \rangle = &\frac{\Delta}{\alpha^2(\beta_n - \beta_k)} \Big[Ai'(n)Ai(k)Ci(n)Ci'(k) - Ai(n)Ai'(k)Ci'(n)Ci(k) \Big] \\ &- \frac{\Delta}{\alpha^2(\beta_n - \beta_k)} \Big[Ai'(n)Ai'(k)Ci(n)Ci(k) - Ai(n)Ai(k)Ci'(n)Ci'(k) \Big] \\ &- \frac{2}{3\alpha^2} \int_{-\infty}^{\infty} xA'Bdx.\end{aligned}$$

The first two lines contain a lot of symmetry with respect to Airy function derivatives. This hints that the Wronskian relation $Ai(z)Ci'(z) - Ai'(z)Ci(z) = \frac{1}{\pi}$ should be used to simplify. These two lines are simplified using the following steps:

$$\begin{aligned}&\frac{\Delta}{\alpha^2(\beta_n - \beta_k)} \cdot \Big[Ai'(n)Ci(n) \big(\underbrace{Ai(k)Ci'(k) - Ai'(k)Ci(k)}_{1/\pi} \big) \\ &\qquad - Ai(n)Ci'(n) \big(\underbrace{Ai'(k)Ci(k) - Ai(k)Ci'(k)}_{-1/\pi} \big) \Big] \\ &= \frac{\Delta}{\alpha(\beta_n - \beta_k)} \underbrace{\frac{1}{\alpha\pi} \Big[Ai'(n)Ci(n) + Ai(n)Ci'(n) \Big]}_{N_n^2} \\ &= \frac{\Delta N_n^2}{\alpha(\beta_n - \beta_k)}\end{aligned}$$

The coupling term can now be simplified down to

$$\boxed{\langle \partial_F g_n | g_k \rangle = \frac{\Delta N_n^2}{\alpha(\beta_n - \beta_k)} - \frac{2}{3\alpha^2} \int_{-\infty}^{\infty} xA'Bdx.} \tag{C.11}$$

The solution to the last unknown integral found in Appendix A is

$$\int_{-\infty}^{\infty} xA'Bdx = -\frac{\alpha^2}{\beta_n - \beta_k} \left[\frac{\beta_k A'B - \beta_n AB'}{\alpha^5(\beta_n - \beta_k)} + \frac{6}{\alpha^7(\beta_n - \beta_k)^2} A'B' \right] \Bigg|_{0^+}^{0^-}.$$

Substituting this expression back into the coupling elements gives

$$\langle \partial_F g_n | g_k \rangle = \frac{\Delta N_n^2}{\alpha(\beta_n - \beta_k)} - \frac{2}{3\alpha^2} \left\{ \frac{\alpha^2}{\beta_n - \beta_k} \left[\frac{1}{\alpha^5(\beta_n - \beta_k)} \Big(\beta_k A'B - \beta_n AB' \Big) + \frac{6}{\alpha^7(\beta_n - \beta_k)^2} A'B' \right] \Bigg|_{0^+}^{0^-} \right\},$$

which simplifies a bit further into

$$\langle \partial_F g_n | g_k \rangle = \frac{\Delta N_n^2}{\alpha(\beta_n - \beta_k)} - \frac{2}{3\alpha^5(\beta_n - \beta_k)^2}\left[\left(\underbrace{\beta_k A'B - \beta_n AB'}_{Term\ 1}\right) + \frac{6}{\alpha^2(\beta_n - \beta_k)}\underbrace{A'B'}_{Term\ 2}\right]\Bigg|_{0^+}^{0^-}.$$

Terms 1 and 2 are simplified using the Wronskian relation

$$\begin{aligned}
\beta_k A'B - \beta_n AB'\Big|_{0^+}^{0^-} &= \Big[\beta_k Ci(n)Ai'(n)Ci(k)Ai(k) - \beta_n Ci(n)Ai(n)Ci(k)Ai'(k) \\
&\quad - \beta_k Ci'(n)Ai(n)Ci(k)Ai(k) - \beta_n Ci(n)Ai(n)Ci'(k)Ai(k)\Big] \\
&= \beta_k Ai(k)Ci(k)\Big[\underbrace{Ci(n)Ai'(n) - Ci'(n)Ai(n)}_{-1/\pi}\Big] \\
&\quad + \beta_n Ai(n)Ci(n)\Big[\underbrace{Ai(k)Ci'(k) - Ai'(k)Ci(k)}_{1/\pi}\Big] \\
&= \frac{1}{\pi}\Big(\beta_n Ci(n)Ai(n) - \beta_k Ci(k)Ai(k)\Big)
\end{aligned}$$

and also

$$\begin{aligned}
A'B'\Big|_{0^+}^{0^-} &= Ci(n)Ai'(n)Ci(k)Ai'(k) - Ai(n)Ci'(n)Ai(k)Ci'(k) \\
&= -\frac{1}{\pi}\Big(Ai'(n)Ci(n) + Ai(k)Ci'(k)\Big).
\end{aligned}$$

Given these expressions, the coupling term can be written in a much simpler form:

$$\boxed{\begin{aligned}
\langle \partial_F g_n | g_k \rangle = \frac{\Delta N_n^2}{\alpha(\beta_n - \beta_k)} &- \frac{2}{3\pi\alpha^5}\frac{1}{(\beta_n - \beta_k)^2}\Big[\beta_n Ci(n)Ai(n) - \beta_k Ci(k)Ai(k)\Big] \\
&- \frac{4}{\pi\alpha^7}\frac{1}{(\beta_n - \beta_k)^3}\Big[Ai'(n)Ci(n) + Ai(k)Ci'(k)\Big],
\end{aligned}} \tag{C.12}$$

but there is still one more remarkable simplification that can be made. The first line of (C.12) is equal to zero! To show this begin by substituting $Ai(n)Ci(n) = Ai(k)Ci(k) = -\alpha/(2\pi B)$ (from the eigenvalue equation). The first line is now

$$\frac{\Delta N_n^2}{\alpha(\beta_n - \beta_k)} - \frac{1}{3\pi^2\alpha^2 B(\beta_n - \beta_k)}.$$

Substituting into the equation $\Delta = 1/(3\pi^2\alpha^3 B N_n^2)$ results in

$$\frac{1}{3\pi^2\alpha^3 B N_n^2}\frac{N_n^2}{\alpha(\beta_n-\beta_k)} - \frac{1}{3\pi^2\alpha^2 B(\beta_n-\beta_k)}$$

$$\frac{1}{3\pi^2\alpha^2 B(\beta_n-\beta_k)} - \frac{1}{3\pi^2\alpha^2 B(\beta_n-\beta_k)} = 0$$

Now the coupling terms are equal to

$$\langle \partial_F g_n | g_k \rangle = -\frac{4}{\pi\alpha^7}\frac{1}{(\beta_n-\beta_k)^3}\Big[Ai'(n)Ci(n) + Ai(k)Ci'(k)\Big]$$

and simplifying a bit further by replacing $\beta = E/F$ they become

$$\langle \partial_F g_n | g_k \rangle = \frac{\alpha^2}{2\pi(E_n-E_k)^3}\Big[Ai'(\alpha\beta_n)Ci(\alpha\beta_n) + Ai(\alpha\beta_k)Ci'(\alpha\beta_k)\Big].$$

For the normalized Siegert states ψ, we divide by the two normalization factors

$$\langle \partial_F \psi_n | \psi_k \rangle = \frac{(2F)^{2/3}}{2\pi(E_n-E_k)^3}\frac{1}{N_n N_k} \cdot \left[Ai'\left(-\frac{2E_n}{(2F)^{2/3}}\right)Ci\left(-\frac{2E_n}{(2F)^{2/3}}\right) + Ai\left(-\frac{2E_k}{(2F)^{2/3}}\right)Ci'\left(-\frac{2E_k}{(2F)^{2/3}}\right)\right]. \tag{C.13}$$

This expression could serve as the final result for the coupling terms. It is compact and contains all of the primitive quantities (energy, field, wavefunctions). However, there is a beautiful simplification that can be done in order to remove any hint of the wavefunction's actual form. Beginning with

$$\langle \partial_F \psi_n | \psi_k \rangle = \frac{\alpha^2}{2\pi(E_n-E_k)^3}\frac{1}{N_n N_k}\left[Ai'(\alpha\beta_n)Ci(\alpha\beta_n) + Ai(\alpha\beta_k)Ci'(\alpha\beta_k)\right],$$

using the Wroskian relation $Ai'Ci = AiCi' - 1/\pi$

$$\langle \partial_F \psi_n | \psi_k \rangle = \frac{\alpha^2}{2\pi(E_n-E_k)^3}\frac{1}{N_n N_k}\left[-\frac{1}{\pi} + Ai(\alpha\beta_n)Ci'(\alpha\beta_n) + Ai(\alpha\beta_k)Ci'(\alpha\beta_k)\right],$$

and using a (rearranged) Wronskian relation for N^2

$$\alpha\pi N^2 = Ai'Ci + AiCi' = -\frac{1}{\pi} + 2AiCi'$$

it becomes possible to replace the Airy functions with normalization factors

$$\langle \partial_F \psi_n | \psi_k \rangle = -\frac{F}{2\left(E_n - E_k\right)^3} \frac{N_n^2 + N_k^2}{N_n N_k}.$$

The final form for the coupling elements is

$$\boxed{\langle \partial_F \psi_n | \psi_k \rangle = -\frac{F}{2\left(E_n - E_k\right)^3} \left(\frac{N_n}{N_k} + \frac{N_k}{N_n} \right).} \tag{C.14}$$

This is really a remarkable result that coupling term can be defined in terms of such fundamental quantities.

C.6 Dipole matrix elements

The next important quantities to calculate are the dipole matrix elements. The procedure will make use of known integral identities (3.51) and (3.54) from Vallée. The diagonal terms are defined as

$$\langle \psi_n | \hat{X} | \psi_n \rangle = \frac{1}{N_n^2} \int_{\mathcal{C}} z \; g[\alpha(x + \beta_n)]^2 \; dz$$

and the off-diagonal terms are defined as

$$\langle \psi_n | \hat{X} | \psi_k \rangle = \frac{1}{N_n N_k} \int_{\mathcal{C}} z \; g[\alpha(x + \beta_n)] g[\alpha(x + \beta_k)] \; dz.$$

Beginning with the diagonal terms, Vallée (3.51) is used to find that

$$\langle \psi_n | \hat{X} | \psi_n \rangle = \frac{g(0)}{3\alpha^2} \left[Ai'(n) Ci(n) - Ai(n) Ci'(n) \right] + \frac{2E}{3F} \underbrace{\frac{1}{\alpha} \left[(Ai'(n) Ci(n))^2 - (Ai(n) Ci'(n))^2 \right]}_{-N_n^2}.$$

Using $g(0) = -\alpha / 2\pi B$ and the Wronskian $Ai'Ci - AiCi' = -1/\pi$, the expression is greatly simplified to

$$\langle \psi_n | \hat{X} | \psi_n \rangle = \frac{1}{6\pi^2 \alpha B N_n^2} - \frac{2E}{3F}.$$

Comparing this expression to (C.6), it is clear that

$$\boxed{\langle \psi_n | \hat{X} | \psi_n \rangle = -\partial_F E.}$$

For the off-diagonal elements

$$\langle \psi_n | \hat{X} | \psi_k \rangle = \frac{1}{N_n N_k} \int_{\mathcal{C}} z \; g[\alpha(x + \beta_n)] g[\alpha(x + \beta_k)] \; dz,$$

Vallée (3.54) is used to find that

$$\langle\psi_n|\,\hat{X}\,|\psi_k\rangle = \frac{1}{N_nN_k}\frac{2}{\alpha^5(\beta_n-\beta_k)^3}\big[Ci(n)Ci(k)Ai'(n)Ai(k) - Ci(n)Ci(k)Ai(n)Ai'(k) \\ - Ai(n)Ai(k)Ci'(n)Ci(k) + Ai(n)Ai(k)Ci(n)Ci'(k)\big] \\ + \frac{1}{N_nN_k}\frac{2}{\alpha^4(\beta_n-\beta_k)^2}\big[Ci(n)Ci(k)Ai'(n)Ai'(k) - Ai(n)Ai(k)Ci'(n)Ci'(k)\big].$$

The first term is zero, which can be seen by using the Wronksian relation

$$Ci(k)Ai(k)[\underbrace{Ai'(n)Ci(n) - Ai(n)Ci'(n)}_{-1/\pi}] + Ci(n)Ai(n)[\underbrace{Ai(k)Ci'(k) - Ai'(k)Ci(k)}_{1/\pi}]$$

$$\frac{1}{\pi}[Ci(n)Ai(n) - Ci(k)Ai(k)] = \frac{1}{\pi}\left[\frac{-\alpha}{2\pi B} - \frac{-\alpha}{2\pi B}\right] = 0.$$

The resulting off-diagonal elements are

$$\langle\psi_n|\,\hat{X}\,|\psi_k\rangle = \frac{1}{N_nN_k}\frac{2}{\alpha^4(\beta_n-\beta_k)^2}\big[Ci(n)Ci(k)Ai'(n)Ai'(k) - Ai(n)Ai(k)Ci'(n)Ci'(k)\big]$$

or more simply

$$\langle\psi_n|\,\hat{X}\,|\psi_k\rangle = \frac{1}{N_nN_k}\frac{2}{\alpha^4(\beta_n-\beta_k)^2}\big[-\frac{1}{\pi}\big(Ai'(n)Ci(n) + Ai(k)Ci'(k)\big)\big].$$

Just as with the coupling elements, using the Wronskian relationship and an alternative form of the normalization factor

$$Ai'Ci = AiCi' - \frac{1}{\pi}, \quad \frac{\alpha\pi N^2}{2} = -\frac{1}{2\pi} + AiCi'$$

it is possible to simplify the expression greatly to

$$\langle\psi_n|\,\hat{X}\,|\psi_k\rangle = \frac{F}{2(E_n-E_k)^2}\left[\frac{N_n}{N_k} + \frac{N_k}{N_n}\right].$$

In summary, the dipole matrix elements are

$$\boxed{\langle\psi_n|\,\hat{X}\,|\psi_k\rangle = \begin{cases} -\partial_F E & n = k \\ \frac{F}{2(E_n-E_k)^2}\left[\frac{N_n}{N_k} + \frac{N_k}{N_n}\right] & n \neq k \end{cases}} \tag{C.15}$$

This final expression is used to verify the connection, Eq. (4.10), between the coupling matrix elements and the dipole matrix elements.

Appendix D

Derivation of 1D Square Well Resonances

This Appendix provides a more thorough derivation of the resonant state expressions of the square well potential system that were shown in Section 4.4.2.

D.1 Wavefunctions

The Hamiltonian for the 1D square well potential model with external field F is

$$H = -\frac{1}{2}\nabla^2 + V(x) - xF$$

where the potential is defined as

$$V(x) = \begin{cases} 0 & x < -d \\ V_0 & -d < x < d \\ 0 & x > d \end{cases}$$

The half-width of the well is d and the depth (a negative number) is V_0. Due to the piecewise nature of the potential, a different Hamiltonian is solved for each region: I, II, and III (shown in Figure D.1). The locations near the well boundaries are labeled as 0, 1, 2, 3. The unnormalized wavefunctions of the square well potential have the following form:

$$\psi(x,F) = \begin{cases} \kappa_0 Ai[\alpha(x+\beta)] & x < -d \\ \kappa_1 Ai[\alpha(x+\beta')] + \kappa_2 Bi[\alpha(x+\beta')] & -d < x < d \\ \kappa_3 Ci[\alpha(x+\beta)] & x > d \end{cases} \tag{D.1}$$

where $\alpha = -(2F)^{1/3}$, $\beta = E/F$ and $\beta' = (E - V_0)/F$. The κ's are coefficients that force continuity of value and derivative between regions I, II and III.

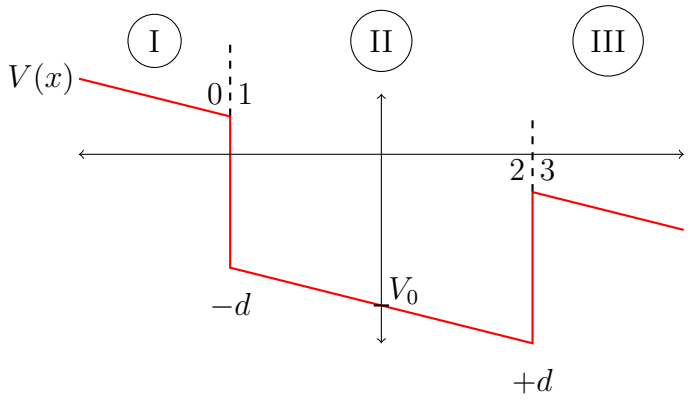

FIGURE D.1. The square well potential with external field for a half-width d and depth V_0. Given the piecewise nature of the well, there are three distinct regions I, II and III with boundary interfaces labeled 0, 1, 2, 3.

D.2 Continuity equations

To simplify the notation, the BC location numbers are used to designate the argument of the Airy functions. For example, an argument containing $x = +d$ and β' is designated as a subscript 2, therefore the wavefunction at that location becomes $\kappa_1 A_2 + \kappa_2 B_2$. In summary,

$$\begin{array}{lcl} \psi_I(x=-d) & \Longrightarrow & \kappa_0 A_0 \\ \psi_{II}(x=-d) & \Longrightarrow & \kappa_1 A_1 + \kappa_2 B_1 \\ \psi_{II}(x=+d) & \Longrightarrow & \kappa_1 A_2 + \kappa_2 B_2 \\ \psi_{III}(x=+d) & \Longrightarrow & \kappa_3 C_3 \end{array}$$

Using this new notation, the boundary conditions for continuous wavefunctions (both value and derivative) across well walls are

$$BC = \begin{cases} \kappa_0 A_0 = & \kappa_1 A_1 + \kappa_2 B_1 & \\ \kappa_0 A_0' = & \kappa_1 A_1' + \kappa_2 B_1' & \\ & \kappa_1 A_2 + \kappa_2 B_2 & = \kappa_3 C_3 \\ & \kappa_1 A_2' + \kappa_2 B_2' & = \kappa_3 C_3' \end{cases} \tag{D.2}$$

The κ's are found by solving the BC pairwise using simple substitutions. The first step is to take the first two BC's

$$\kappa_0 A_0 = \kappa_1 A_1 + \kappa_2 B_1, \quad \kappa_0 A_0' = \kappa_1 A_1' + \kappa_2 B_1'$$

and solve each for κ_2 and then equate them. The resulting steps give an expression for κ_1 in terms of κ_0:

$$\frac{\kappa_0 A_0 - \kappa_1 A_1}{B_1} = \frac{\kappa_0 A_0' - \kappa_1 A_1'}{B_1'}$$

$$\kappa_0[A_0B_1' - A_0'B_1] = \kappa_1[\underbrace{A_1B_1' - A_1'B_1}_{1/\pi}]$$

$$\boxed{\kappa_1 = \pi[A_0B_1' - A_0'B_1]\kappa_0}$$

Similarly, solving for κ_1 and equating expressions gives κ_2

$$\frac{\kappa_0A_0 - \kappa_2B_1}{A_1} = \frac{\kappa_0A_0' - \kappa_2B_1'}{A_1'}$$

$$\kappa_0[A_0A_1' - A_0'A_1] = \kappa_2[\underbrace{A_1'B_1 - A_1B_1'}_{-1/\pi}]$$

$$\boxed{\kappa_2 = -\pi[A_0A_1' - A_0'A_1]\kappa_0}$$

Proceed with the third and forth BC's and retrieve similar equations for κ_1 and κ_2 in terms of κ_3.

$$\kappa_1A_2 + \kappa_2B_2 = \kappa_3C_3, \quad \kappa_1A_2' + \kappa_2B_2' = \kappa_3C_3'$$

Solve for κ_2 and equate

$$\frac{\kappa_3C_3 - \kappa_1A_2}{B_2} = \frac{\kappa_3C_3' - \kappa_1A_2'}{B_2'}$$

$$\kappa_1[\underbrace{A_2'B_2 - A_2B_2'}_{-1/\pi}] = \kappa_3[B_2C_3' - B_2'C_3]$$

$$\boxed{\kappa_1 = -\pi[B_2C_3' - B_2'C_3]\kappa_3}$$

Now solve for κ_1 and equate

$$\frac{\kappa_3C_3 - \kappa_2B_2}{A_2} = \frac{\kappa_3C_3' - \kappa_2B_2'}{A_2'}$$

$$\kappa_2[\underbrace{A_2'B_2 - A_2B_2'}_{-1/\pi}] = \kappa_3[A_2'C_3 - A_2C_3']$$

$$\boxed{\kappa_2 = \pi[A_2C_3' - A_2'C_3]\kappa_3}$$

To summarize, the following constraints are imposed on the coefficients in order to have continuous wavefunctions across well boundaries

$$\begin{aligned} \kappa_1 &= +\pi[A_0B_1' - A_0'B_1]\kappa_0 & \kappa_2 &= -\pi[A_0A_1' - A_0'A_1]\kappa_0 \\ \kappa_1 &= -\pi[B_2C_3' - B_2'C_3]\kappa_3 & \kappa_2 &= +\pi[A_2C_3' - A_2'C_3]\kappa_3 \end{aligned} \tag{D.3}$$

From these constraints, it is clear that there is some freedom in how to choose the concrete values of the κ's. Due to the symmetric potential, the κ's should be chosen

to make the wavefunctions in region I and III have a similar form. A reasonable choice is

$$\kappa_0 = A_2C_3' - A_2'C_3 \tag{D.4}$$
$$\kappa_1 = \pi\left(A_0B_1' - A_0'B_1\right)\left(A_2C_3' - A_2'C_3\right) \qquad = \pi\left(A_0B_1' - A_0'B_1\right)\kappa_0 \tag{D.5}$$
$$\kappa_2 = -\pi\left(A_0A_1' - A_0'A_1\right)\left(A_2C_3' - A_2'C_3\right) \qquad = \pi\kappa_3\kappa_0 \tag{D.6}$$
$$\kappa_3 = -\left(A_0A_1' - A_0'A_1\right) \tag{D.7}$$

D.3 Eigenvalue equation

To find the eigenvalue equation for the square well, the equations for κ_1, κ_2 in (D.3) are equated

$$\kappa_1 = +\pi[A_0B_1' - A_0'B_1]\kappa_0 = -\pi[B_2C_3' - B_2'C_3]\kappa_3$$
$$\kappa_2 = -\pi[A_0A_1' - A_0'A_1]\kappa_0 = +\pi[A_2C_3' - A_2'C_3]\kappa_3$$

and then solved for κ_0/κ_3. Combining these expressions leads to the eigenvalue equation

$$\boxed{(A_0A_1' - A_0'A_1)(B_2C_3' - B_2'C_3) - (A_0B_1' - A_0'B_1)(A_2C_3' - A_2'C_3) = 0} \tag{D.8}$$

which determines for a given field F which eigenvalue energies E exists.

D.4 Normalization

To solve for the normalization factor Vallée (3.50) is used:

$$\int A[\alpha(x+\beta)]^2dx = (x+\beta)A[\alpha(x+\beta)]^2 - \frac{1}{\alpha}A'[\alpha(x+\beta)]^2$$

where A is a linear superposition of Airy functions (Ai, Bi) and the integration is performed along a contour $\mathcal{C}$ shown in Figure 4.1. Given that the wavefunctions are continuous in value and derivative at the well boundaries, Vallée (3.50) is reduced to

$$\int_a^b A[\alpha(x+\beta)]^2 = \beta_{a,b}A[\alpha(x+\beta)]^2\Big|_a^b \tag{D.9}$$

where $\beta_{a,b}$ is chosen to be inside or outside the well accordingly. Throughout the following derivations, continuity at the well boundaries greatly simplifies integral calculations for the square well. For instance, only terms multiplied by the scaled energy β are retained, since β is not continuous across well boundaries. All other terms that are products of wavefunctions or their derivatives are continuous and can

therefore be ignored. The normalization factor of the wavefunction is found from a sum of the integrals in each region

$$N^2 = \int_{-\infty}^{-d} \psi_{\mathrm{I}}^2 dx + \int_{-d}^{d} \psi_{\mathrm{II}}^2 dx + \int_{d}^{\infty} \psi_{\mathrm{III}}^2 dz.$$

The result of these integrals is simply

$$N^2 = \beta\psi(-d)^2 - \beta'\psi(-d)^2 + \beta'\psi(+d)^2 - \beta\psi(+d)^2$$

$$\boxed{N^2 = \frac{V_0}{F}\left(\psi(-d)^2 - \psi(d)^2\right)}$$

Using the wavefunctions in region I and III, this expression can be written as

$$N^2 = \frac{V_0}{F}\left(\kappa_0^2 Ai(-d)^2 - \kappa_3^2 Ci(d)^2\right)$$

$$N = \sqrt{\frac{V_0}{F}\left(\kappa_0^2 Ai(-d)^2 - \kappa_3^2 Ci(d)^2\right)} \tag{D.10}$$

One interesting property to note is that wavefunction values at the well boundaries are a function of the well depth and external field, since for a normalized wavefunction

$$1 = \frac{V_0}{F}\left(\psi(-d)^2 - \psi(d)^2\right).$$

This property is similar to the property of 1D Dirac-delta potential, where the wavefunction's value at the location of the delta potential is $\psi(x=0) = -\alpha/2\pi BN$, a function of field value and potential depth B.

D.5 Relevant Airy integrals

Using the integrals in Vallée and from Appendix A, all quantities necessary for time evolution of the square well resonant states can be calculated. In this section, many of the most common integral results are listed. Similar to Vallée the quantities A, B are defined to be a linear combination of Airy functions with shifted arguments:

$$A[\alpha(x+\beta_1)] \quad \text{and} \quad B[\alpha(x+\beta_2)] \tag{D.11}$$

The prime symbol $'$ represents a derivative on the *whole* argument of the Airy function. A' corresponds to the derivative Airy functions: e.g. $Ai'(z)$ or $Bi'(z)$. This is done to keep track of α's when taking derivatives. For example, $\partial_x A[\alpha(x+\beta)] = \alpha A'[\alpha(x+\beta)]$. From Appendix A, it was shown that

$$\int_{-\infty}^{\infty} A'B dx = -\frac{\alpha^2}{2}(\beta_1 - \beta_2)\int_{-\infty}^{\infty} xAB dx. \tag{D.12}$$

For the square well, this results in

$$\int_{-\infty}^{\infty} xABdx = -\frac{V_0}{F^2(\beta_1-\beta_2)^2}\left[AB(d)-AB(-d)\right], \tag{D.13}$$

and therefore,

$$\int_{-\infty}^{\infty} A'Bdx = -\frac{\alpha^2 V_0}{2F^2(\beta_1-\beta_2)}\left[AB(d)-AB(-d)\right]. \tag{D.14}$$

Also in Appendix A, it was found that

$$\int_{-\infty}^{\infty} xA'Bdx = -\frac{\alpha^2(\beta_1-\beta_2)}{4}\int_{-\infty}^{\infty} x^2ABdx. \tag{D.15}$$

For the square well, this results in

$$\begin{aligned}\int_{-\infty}^{\infty} x^2ABdx =& -\frac{2V_0d}{F^2(\beta_1-\beta_2)^2}[AB(d)+AB(-d)]\\ &-\frac{4V_0}{F^2\alpha^2(\beta_1-\beta_2)^3}[A'B(-d)-A'B(d)-AB'(-d)+AB'(d)]\\ &+\frac{6V_0}{F^3(\beta_1-\beta_2)^4}[AB(d)-AB(-d)],\end{aligned} \tag{D.16}$$

and therefore

$$\begin{aligned}\int_{-\infty}^{\infty} xA'Bdx =& -\frac{V_0d}{F\alpha(\beta_1-\beta_2)}[AB(d)+AB(-d)]\\ &+\frac{V_0}{F^2(\beta_1-\beta_2)^2}[A'B(-d)-A'B(d)-AB'(-d)+AB'(d)]\\ &+\frac{3V_0}{F^2\alpha(\beta_1-\beta_2)^3}[AB(d)-AB(-d)].\end{aligned} \tag{D.17}$$

Two more integrals are necessary for calculating the coupling terms and observables. Due to the piece-wise nature of the well, some integrals must be calculated over a finite range, not just over $(-\infty,\infty)$. For definite integrals over a finite range (a,b) the above integrals are modified to

$$\int_a^b A'Bdx = -\frac{\alpha^2}{2}(\beta_1-\beta_2)\int_a^b xABdx + \underbrace{\left(\frac{1}{2\alpha}AB+\frac{1}{2}xA'B-\frac{1}{2}xAB'\right)\Bigg|_a^b}_{new} \tag{D.18}$$

The additional terms labeled "new" will vanish when $a \to -\infty$ and $b \to \infty$, since the integral is performed along the contour $\mathcal{C}$ which decays the wavefunction's value and derivative to zero. Including the additional terms, the integral's result is

$$\begin{aligned}\int_a^b xABdx = &-\left(\frac{a}{\alpha^2(\beta_1-\beta_2)}+\frac{2}{\alpha^5(\beta_1-\beta_2)^3}\right)(A'B(a)-AB'(a))\\ &+\left(\frac{b}{\alpha^2(\beta_1-\beta_2)}+\frac{2}{\alpha^5(\beta_1-\beta_2)^3}\right)(A'B(b)-AB'(b))\\ &+\frac{1}{\alpha^3(\beta_1-\beta_2)^2}[(\beta_1'+\beta_2'+2a)AB(a)-(\beta_1'+\beta_2'+2b)AB(b)]\\ &+\frac{2}{\alpha^4(\beta_1-\beta_2)^2}[A'B'(b)-A'B'(a)].\end{aligned} \tag{D.19}$$

D.6 Coupling matrix elements

The coupling elements $\langle \partial_F \psi_i | \psi_j \rangle$ are one of the two primary quantities needed in order to simulate the dynamics of a square well system in the presence of an external light field. Alternatively the dipole matrix elements can be used and are shown in the next section. The coupling elements are found by integrating a wavefunction and its derivative w.r.t. the field.

$$\int_{-\infty}^{\infty}(\partial_F\psi_i)\psi_j dx = \frac{1}{N_iN_j}\int_{-\infty}^{\infty}(\partial_F g_i)g_j dx. \tag{D.20}$$

The first step in solving this integral is to calculate $\partial_F g$. Since g is a linear combination of Airy functions A, each region ($x < -d$, $-d < x < d$, and $x > d$) will have the same form

$$\partial_F g = \partial_F(\kappa A[\alpha(x+\beta)]) = (\partial_F\kappa)A + \kappa(\partial_F A) \tag{D.21}$$

where

$$\partial_F A[\alpha(x+\beta)] = \frac{\alpha}{3F}[3E' + x - 2\beta]A'[\alpha(x+\beta)]. \tag{D.22}$$

Therefore

$$\partial_F g = (\partial_F\kappa)A + \kappa\frac{\alpha}{3F}[3E' + x - 2\beta]A'[\alpha(x+\beta)]. \tag{D.23}$$

With the expressions for $\partial_F g$, the coupling elements can now be written in terms of integrals. The following expressions are quite large and many coefficients must be kept track of. Separate coefficients for the two wavefunctions g_i and g_j are needed and therefore κ is used for g_i and γ for g_j. A shorthand notation for Airy functions is also used where subscripts indicate which β is within the argument. For example, $A_i = Ai[\alpha(x+\beta_i)]$ and $A_j = Ai[\alpha(x+\beta_j)]$. (Be careful not to confuse these Airy subscripts A_i, C_j with the well boundary subscripts A_1, C_3 that were used earlier when

deriving the eigenvalue equation. Here the subscripts i, j are for specifying β values.) To calculated the coupling elements the following integrals must be evaluated:

$$\begin{aligned}\int_{-\infty}^{\infty}(\partial_F g_i)g_j dx = &\int_{-\infty}^{-d}(\partial_F\kappa_0)\gamma_0 A_i A_j + \kappa_0\gamma_0(\partial_F A_i)A_j dx \\ &+ \int_{-d}^{d}[(\partial_F\kappa_1)A_i + (\partial_F\kappa_2)B_i][\gamma_1 A_j + \gamma_2 B_j]dx \\ &+ \int_{-d}^{d}[\kappa_1(\partial_F A_i) + \kappa_2(\partial_F A_j)][\gamma_1 A_j + \gamma_2 B_j]dx \\ &+ \int_{d}^{\infty}(\partial_F\kappa_3)\gamma_3 C_i C_j + \kappa_3\gamma_3(\partial_F C_i)C_j dx.\end{aligned} \tag{D.24}$$

Each of the integrals can be solved, but care must be taken w.r.t. continuity, since not all of these terms are continuous across well boundaries. This is due to the derivatives of the coefficients κ and γ. It is apparent that the second term in the first line, the third line, and the second term in the last line represent continuous wavefunctions (since they don't contain $\partial_F\kappa$ or $\partial_F\gamma$). These should be collected, then using (D.22) for the derivatives applied to Airy functions, the expression can be changed to

$$\begin{aligned}\int_{-\infty}^{\infty}(\partial_F g_i)g_j dx = &\int_{-\infty}^{-d}(\partial_F\kappa_0)\gamma_0 A_i A_j dx \\ &+ \int_{-d}^{d}[(\partial_F\kappa_1)A_i + (\partial_F\kappa_2)B_i][\gamma_1 A_j + \gamma_2 B_j]dx \\ &+ \int_{d}^{\infty}(\partial_F\kappa_3)\gamma_3 C_i C_j dx \\ &+ \frac{\alpha}{3F}\int_{-\infty}^{\infty}(3E_i' + x - 2\beta_i)g_i' g_j dx \\ &+ \frac{2\alpha V_0}{3F^2}\int_{-d}^{d} g_i' g_j dx.\end{aligned} \tag{D.25}$$

The last two lines contain integrals that were solved in the previous section, namely $\int_{-\infty}^{\infty} A'B dx$, $\int_{-\infty}^{\infty} xA'B dx$ and $\int_{-d}^{d} A'B dx$. The very last line of (D.25) seems out of place, but it results from the fact that β is not continuous across well boundaries. Explicitly, this integral is a result of three integrals in each region

$$\int_{-\infty}^{\infty}\beta_i g_i' g_j dx = \int_{-\infty}^{-d}\beta_i g_i' g_j dx + \int_{-d}^{d}\beta_i' g_i' g_j dx + \int_{d}^{\infty}\beta_i g_i' g_j dx. \tag{D.26}$$

where $\beta' = \beta - \frac{V_0}{F}$ in the center region II. Given this, it is easy to verify that

$$\int_{-\infty}^{\infty}\beta A'B dx = \beta\int_{-\infty}^{\infty} A'B dx - \frac{V_0}{F}\int_{-d}^{d} A'B dx. \tag{D.27}$$

The coefficients are also functions of the field, and therefore taking the derivative w.r.t. F leads to the following equations

$$\partial_F \kappa_0 = \frac{\alpha^2 V_0}{3F^3}(3E'F - Fd + 2V_0 - 4E)A_2 C_3 + \frac{2\alpha V_0}{3F^2} A_2' C_3' \tag{D.28}$$

$$\partial_F \kappa_1 = \pi \left\{ \left[-\frac{\alpha^2 V_0}{3F^3}(3E'F + Fd + 2V_0 - 4E)A_0 B_1 - \frac{2\alpha V_0}{3F^2} A_0' B_1' \right] k_0 + (A_0 B_1' - A_0' B_1)(\partial_F k_0) \right\} \tag{D.29}$$

$$\partial_F \kappa_2 = \pi[(\partial_F \kappa_3)\kappa_0 + \kappa_3(\partial_F \kappa_0)] \tag{D.30}$$

$$\partial_F \kappa_3 = \frac{\alpha^2 V_0}{3F^3}(3E'F + Fd + 2V_0 - 4E)A_0 A_1 + \frac{2\alpha V_0}{3F^2} A_0' A_1' \tag{D.31}$$

Now that all the pieces are known, the coupling elements can be calculated. Unfortunately the resulting expressions are quite large and up until the writing of this dissertation, a nice simplification of them has yet to be achieved. Instead these equations were numerically check and found to really be the resulting coupling matrix elements. It is surprising how difficult simplification is given that the dipole matrix elements (shown in the next section) have relatively simple expressions.

D.7 Dipole matrix elements

For the diagonal dipole matrix elements, Vallée (3.51) is used

$$\int x A[\alpha(x+\beta)]^2 dx = -\frac{1}{3}\left(x\beta + 2\beta^2\right) A[\alpha(x+\beta)]^2 + \frac{2\beta}{3\alpha} A'[\alpha(x+\beta)]^2$$

where terms that do not contain the factors x or β are ignored due to continuity of the wavefunctions. Evaluating this expression for the square well results in

$$\begin{aligned} \langle\psi|x|\psi\rangle = &\frac{V_0}{3F}\left[(d-4\beta)\psi(-d)^2 + (d+4\beta)\psi(d)^2\right] \\ &+ \frac{2V_0^2}{3F^2}\left[\psi(-d)^2 - \psi(d)^2\right] \\ &+ \frac{2V_0}{3F\alpha}\left[\psi'(-d)^2 - \psi'(d)^2\right]. \end{aligned} \tag{D.32}$$

This expression can be simplified using the expression for normalization

$$\frac{V_0}{F}\left[\psi(-d)^2 - \psi(d)^2\right] = 1$$

and therefore the diagonal elements are

$$\langle\psi|x|\psi\rangle = \frac{1}{3F}\left\{2V_0 - 4E + V_0 d\left[\psi(-d)^2 + \psi(d)^2\right] + 2V_0\left[\frac{1}{\alpha}\left(\psi'(-d)^2 - \psi'(d)^2\right)\right]\right\}. \tag{D.33}$$

The integral for the off-diagonal elements were shown previously

$$\int_{-\infty}^{\infty} xABdx = -\frac{V_0}{F^2(\beta_1 - \beta_2)^2} \left[AB(d) - AB(-d)\right]. \tag{D.34}$$

and can be rewritten as

$$\langle\psi_1|x|\psi_2\rangle = -\frac{V_0}{F^2(\beta_1 - \beta_2)^2} \frac{g_1(d)g_2(d) - g_1(-d)g_2(-d)}{N_1 N_2} \tag{D.35}$$

or in the nicer form

$$\langle\psi_n|\, x\, |\psi_k\rangle_S = \frac{V_0}{(E_n - E_k)^2} \left[\psi_n(-d)\psi_k(-d) - \psi_n(d)\psi_k(d)\right]. \tag{D.36}$$

When comparing these relatively simple expressions for dipole moment to the complex coupling elements of the previous section, hints that there must exist many identities that help reduce the very complex coupling elements, but at the date of this writing they remain unknown.

References

[1] Tenio Popmintchev, Ming-Chang Chen, Paul Arpin, Margaret M. Murnane, and Henry C. Kapteyn. The attosecond nonlinear optics of bright coherent x-ray generation. *Nat Photon*, 4(12):822–832, 2010.

[2] Ferenc Krausz and Misha Ivanov. Attosecond physics. *Rev. Mod. Phys.*, 81:163–234, Feb 2009.

[3] A. Couairon and A. Mysyrowicz. Femtosecond filamentation in transparent media. *Physics Reports*, 441(24):47 – 189, 2007.

[4] L Berg, S Skupin, R Nuter, J Kasparian, and J-P Wolf. Ultrashort filaments of light in weakly ionized, optically transparent media. *Reports on Progress in Physics*, 70(10):1633, 2007.

[5] M. Kolesik and J. V. Moloney. Nonlinear optical pulse propagation simulation: From maxwell's to unidirectional equations. *Phys. Rev. E*, 70:036604, Sep 2004.

[6] V. Loriot, E. Hertz, O. Faucher, and B. Lavorel. Measurement of high order kerr refractive index of major air components. *Opt. Express*, 17(16):13429–13434, Aug 2009.

[7] V Loriot, E Hertz, O Faucher, and B Lavorel. Measurement of high order kerr refractive index of major air components (vol 17, pg 13429, 2009). *Opt. Express*, 18(3):3011–3012, February 2010.

[8] Arkady Major, Fumiyo Yoshino, Irkalis Nikolakakos, J. Stewart Aitchison, and Peter W. E. Smith. Dispersion of the nonlinear refractive index in sapphire. *Opt. Lett.*, 29(6):602–604, Mar 2004.

[9] M Th Hassan, Tran Trung Luu, Antoine Moulet, O Raskazovskaya, P Zhokhov, Manish Garg, Nicholas Karpowicz, AM Zheltikov, V Pervak, Ferenc Krausz, et al. Optical attosecond pulses and tracking the nonlinear response of bound electrons. *Nature*, 530(7588):66–70, 2016.

[10] Eli Yablonovitch and N. Bloembergen. Avalanche ionization and the limiting diameter of filaments induced by light pulses in transparent media. *Phys. Rev. Lett.*, 29:907–910, Oct 1972.

[11] A. Couairon, E. Brambilla, T. Corti, D. Majus, O. de J. Ramírez-Góngora, and M. Kolesik. Practitioner's guide to laser pulse propagation models and simulation. *Eur. Phys. J. Special Topics*, 199(1):5–76, 2011.

[12] LV Keldysh et al. Ionization in the field of a strong electromagnetic wave. *Sov. Phys. JETP*, 20(5):1307–1314, 1965.

[13] K. Mishima, M. Hayashi, J. Yi, S. H. Lin, H. L. Selzle, and E. W. Schlag. Generalization of keldysh's theory. *Phys. Rev. A*, 66:033401, Sep 2002.

[14] AM Perelomov, VS Popov, and MV Terentev. Ionization of atoms in an alternating electric field. *Sov. Phys. JETP*, 23(5):924–934, 1966.

[15] AM Perelomov, VS Popov, and MV Terentev. Ionization of atoms in an alternating electric field: Ii. *Sov. Phys. JETP*, 24(1):207–217, 1967.

[16] M Kolesik and J V Moloney. Modeling and simulation techniques in extreme nonlinear optics of gaseous and condensed media. *Reports on Progress in Physics*, 77(1):016401, 2014.

[17] Muhammad Nurhuda, Akira Suda, and Katsumi Midorikawa. Ionization-induced high-order nonlinear susceptibility. *Phys. Rev. A*, 66:041802, Oct 2002.

[18] M. Nurhuda, A. Suda, and K. Midorikawa. Generalization of the Kerr effect for high intensity, ultrashort laser pulses. *New J. Phys.*, 10(5):053006, 2008.

[19] Maria Richter, Serguei Patchkovskii, Felipe Morales, Olga Smirnova, and Misha Ivanov. The role of the kramershenneberger atom in the higher-order kerr effect. *New Journal of Physics*, 15(8):083012, 2013.

[20] P. Béjot, E. Cormier, E. Hertz, B. Lavorel, J. Kasparian, J.-P. Wolf, and O. Faucher. High-field quantum calculation reveals time-dependent negative kerr contribution. *Phys. Rev. Lett.*, 110:043902, Jan 2013.

[21] Rolf Wiehle, Bernd Witzel, Hanspeter Helm, and Eric Cormier. Dynamics of strong-field above-threshold ionization of argon: Comparison between experiment and theory. *Phys. Rev. A*, 67:063405, Jun 2003.

[22] E. A. Volkova, A. M. Popov, and O. V. Tikhonova. Nonlinear polarization response of an atomic gas medium in the field of a high-intensity femtosecond laser pulse. *JETP Lett.*, 94(7):519–524, 2011.

[23] E A Volkova, Alexander M Popov, and O V Tikhonova. Polarisation response of a gas medium in the field of a high-intensity ultrashort laser pulse: high order kerr nonlinearities or plasma electron component? *Quantum Electronics*, 42(8):680, 2012.

[24] A M Popov, O V Tikhonova, and E A Volkova. Polarization response of an atomic system in a strong mid-ir field. *Laser Physics Letters*, 10(8):085303, 2013.

[25] M Petrarca, Y Petit, S Henin, R Delagrange, P Béjot, and J Kasparian. Higher order kerr improve quantitative modeling of laser filamentation. *Optics Letters*, 37(20):4347–4349, 2012.

[26] P. Bejot, E. Hertz, B. Lavorel, J. Kasparian, J. P. Wolf, and O. Faucher. From higher-order Kerr nonlinearities to quantitative modeling of third and fifth harmonic generation in argon. *Opt. Lett.*, 36(6):828–830, 2011.

[27] Pierre Béjot and Jérôme Kasparian. Conical emission from laser filaments and higher-order kerr effect in air. *Optics letters*, 36(24):4812–4814, 2011.

[28] Carsten Brée, Ayhan Demircan, and Günter Steinmeyer. Saturation of the all-optical kerr effect. *Physical review letters*, 106(18):183902, 2011.

[29] Christian Köhler, Roland Guichard, Emmanuel Lorin, Szczepan Chelkowski, André D. Bandrauk, Luc Bergé, and Stefan Skupin. Saturation of the nonlinear refractive index in atomic gases. *Phys. Rev. A*, 87:043811, Apr 2013.

[30] M Kolesik, EM Wright, and JV Moloney. Femtosecond filamentation in air and higher-order nonlinearities. *Optics Lett.*, 35(15):2550–2552, August 2010.

[31] P. Polynkin, M. Kolesik, E. M. Wright, and J. V. Moloney. Experimental tests of the new paradigm for laser filamentation in gases. *Phys. Rev. Lett.*, 106(15):153902, 2011.

[32] Olga Kosareva, Jean-Francois Daigle, Nikolay Panov, Tiejun Wang, Sima Hosseini, Shuai Yuan, Gilles Roy, Vladimir Makarov, and See Leang Chin. Arrest of self-focusing collapse in femtosecond air filaments: higher order kerr or plasma defocusing? *Optics letters*, 36(7):1035–1037, 2011.

[33] JK Wahlstrand, Y-H Cheng, Y-H Chen, and HM Milchberg. Optical nonlinearity in ar and n 2 near the ionization threshold. *Physical review letters*, 107(10):103901, 2011.

[34] E. Lorin, S. Chelkowski, and A. Bandrauk. The WASP model: a micro–macro system of wave-Schrödinger-plasma equations for filamentation. *Commun. Comput. Phys.*, 9(2):406–440, 2011.

[35] Emmanuel Lorin, Szczepan Chelkowski, E Zaoui, and André Bandrauk. Maxwell–schrödinger–plasma (masp) model for laser–molecule interactions: Towards an understanding of filamentation with intense ultrashort pulses. *Physica D: Nonlinear Phenomena*, 241(12):1059–1071, 2012.

[36] K. Schuh, J. Hader, J. V. Moloney, and S. W. Koch. Influence of many-body interactions during the ionization of gases by short intense optical pulses. *Phys. Rev. E*, 89:033103, Mar 2014.

[37] A V Bogatskaya, E A Volkova, V Yu Kharin, and A M Popov. Polarization response in extreme nonlinear optics: when can the semiclassical approach be used? *Laser Physics Letters*, 13(4):045301, 2016.

[38] M.A. Naimark. *Linear differential operators*. Dover Publications, 2012.

[39] P. eba. Regularized potentials in nonrelativistic quantum mechanics. *Czechoslovak Journal of Physics B*, 36(4):455–461, 1986.

[40] M.G. Krein. On the resolvents of an hermitian operator with defect-index (m,m). *Dokl. Akad. SSSR*, 52:657–660, 1946.

[41] R M Cavalcanti, P Giacconi, and R Soldati. Decay in a uniform field: an exactly solvable model. *Journal of Physics A: Mathematical and General*, 36(48):12065, 2003.

[42] H. L. Cycon, R.G. Froese, W. Kirsch, and B. Simon. *Schrödinger Operators*. Springer-Verlag, 1987.

[43] S. Albeverio and P. Kurasov. *Singular perturbations of diferential operators*. Cambridge University Press, 2000.

[44] S. Geltman. Ionisation dynamics of a model atom in an electrostatic field. *J. Phys. B: Atom. Mol. Phys.*, 11(19):3323–3337, 1978.

[45] G. P. Arrighini and M. Gavarini. Ionization of a model atom by strong and superstrong electric fields. *Lett. Nuovo Cimento*, 33(12):353–358, 1982.

[46] W. Elberfeld and M. Kleber. Tunneling from an ultrathin quantum well in a strong electrostatic field: A comparison of different methods. *Z. Phys. B: Cond. Matt.*, 73(1):23–32, 1988.

[47] Gerald V. Dunne and Christopher S. Gauthier. Simple soluble molecular ionization model. *Phys. Rev. A*, 69(5):053409, May 2004.

[48] Gabriel Alvarez and Bala Sundaram. Perturbation theory for the stark effect in a double quantum well. *J. Phys. A: Math. and Gen.*, 37(41):9735–9748, 2004.

[49] Haydar Uncu, Hakan Erkol, Ersan Demiralp, and Haluk Beker. Solutions of the schrdinger equation for dirac delta decorated linear potential. *Central European Journal of Physics*, 3(2):303–323, 2005.

[50] Vctor M. Villalba and Luis A. Gonzlez-Daz. Particle resonance in the dirac equation in the presence ofadeltainteraction and a perturbative hyperbolic potential. *The European Physical Journal C*, 61(3):519–525, 2009.

[51] A. Teleki, E. M. Wright, and M. Kolesik. Microscopic model for the higher-order nonlinearity in optical filaments. *Phys. Rev. A*, 82:065801, Dec 2010.

[52] Q Su, B P Irving, C W Johnson, and J H Eberly. Stabilization of a one-dimensional short-range model atom in intense laser fields. *Journal of Physics B: Atomic, Molecular and Optical Physics*, 29(23):5755, 1996.

[53] S Geltman. Short-pulse model-atom studies of ionization in intense laser fields. *Journal of Physics B: Atomic, Molecular and Optical Physics*, 27(8):1497, 1994.

[54] TP Grozdanov, PS Krstic, and MH Mittleman. Distortion of a model atom in intense, high-frequency laser field of linear polarization. *Physics Letters A*, 149(2):144–150, 1990.

[55] Jan Mostowski and Joseph H Eberly. Approximate atomic ionization rates in the stabilization regime of the kramers–henneberger picture. *JOSA B*, 8(6):1212–1217, 1991.

[56] A Sanpera, Q Su, and L Roso-Franco. Ionization suppression in a very-short-range potential. *Physical Review A*, 47(3):2312, 1993.

[57] Theodoros Mercouris and Cleanthes A Nicolaides. The continuous spectrum in the solution of the time-dependent schrödinger equation for laser-atom interactions. *Journal of Physics B: Atomic, Molecular and Optical Physics*, 33(11):2095, 2000.

[58] J Matulewski, A Raczyński, and J Zaremba. Drift of the scattered wave packet in strong-field atomic stabilization. *Physical Review A*, 61(4):043402, 2000.

[59] Xiaoxin Zhou, Baiwen Li, and C. D. Lin. Linear-least-squares-fitting procedure for the solution of a time-dependent wave function of a model atom in a strong laser field in the kramers-henneberger frame. *Phys. Rev. A*, 64:043403, Sep 2001.

[60] ZX Zhao, BD Esry, and CD Lin. Boundary-free scaling calculation of the time-dependent schrödinger equation for laser-atom interactions. *Physical Review A*, 65(2):023402, 2002.

[61] VD Rodriguez and RO Barrachina. Gauge independent theory applied to a model of atomic ionization by an intense laser pulse. *The European Physical Journal D*, 64(2-3):593–599, 2011.

[62] T Dziubak and J Matulewski. Stabilization of one-dimensional soft-core and singular model atoms. *The European Physical Journal D*, 59(2):321–327, 2010.

[63] Kendall E Atkinson. The numerical solution of an abel integral equation by a product trapezoidal method. *SIAM Journal on Numerical Analysis*, 11(1):97–101, 1974.

[64] P.B. Visscher. A fast explicit algorithm for the time-dependent schrödinger equation. *Computers in Physics*, 5, 1991.

[65] Jane Lee, David R. Carlson, and R. Jason Jones. Optimizing intracavity high harmonic generation for xuv fs frequency combs. *Opt. Express*, 19(23):23315–23326, Nov 2011.

[66] P. B. Corkum. Plasma perspective on strong field multiphoton ionization. *Phys. Rev. Lett*, 71:1994–1997, 1993.

[67] M. Lewenstein, P. Balcou, M. Yu. Ivanov, A. L'Huillier, and P. B. Corkum. Theory of high harmonics generation by low-frequency laser fields. *Phys. Rev. A*, 49:2117–2132, 1994.

[68] K. J. Schafer, Baorui Yang, L. F. DiMauro, and K. C. Kulander. Above threshold ionization beyond the high harmonic cutoff. *Phys. Rev. Lett.*, 70(11):1599–1602, March 1993.

[69] A Bideau-Mehu, Y Guern, R Abjean, and A Johannin-Gilles. Measurement of refractive indices of neon, argon, krypton and xenon in the 253.7–140.4 nm wavelength range. dispersion relations and estimated oscillator strengths of the resonance lines. *Journal of Quantitative Spectroscopy and Radiative Transfer*, 25(5):395–402, 1981.

[70] F. Schapper, M. Holler, T. Auguste, A. Zaïr, M. Weger, P. Salières, L. Gallmann, and U. Keller. Spatial fingerprint of quantum path interferences in high order harmonic generation. *Opt. Express*, 18(3):2987–2994, Feb 2010.

[71] S.m. Teichmann, D.r. Austin, P. Bates, S. Cousin, A. Grn, M. Clerici, A. Lotti, D. Faccio, P. Di Trapani, A. Couairon, and J. Biegert. Trajectory interferences in a semi-infinite gas cell. *Laser Physics Letters*, 9(3):207211, 2012.

[72] A. L'Huillier, K. J. Schafer, and K. C. Kulander. Higher-order harmonic generation in xenon at 1064 nm: The role of phase matching. *Phys. Rev. Lett.*, 66:2200–2203, Apr 1991.

[73] P. Salires, A. L'Huillier, and M. Lewenstein. Coherence control of high-order harmonics. *Phys. Rev. Lett.*, 74(19):3776–3779, 1995.

[74] E. Constant, D. Garzella, P. Breger, E. Mvel, Ch. Dorrer, C. Le Blanc, F. Salin, and P. Agostini. Optimizing high harmonic generation in absorbing gases: Model and experiment. *Phys. Rev. Lett.*, 82(8):1668–1671, February 1999.

[75] R. J. Jones, K. D. Moll, M. J. Thorpe, and J. Ye. Phase-coherent frequency combs in the vacuum ultraviolet via high-harmonic generation inside a femtosecond enhancement cavity. *Physical Review Letters*, 94(19):193201, 2005.

[76] C. Gohle, T. Udem, M. Herrmann, J. Rauschenberger, R. Holzwarth, H. A. Schuessler, F. Krausz, and T. W. Hansch. A frequency comb in the extreme ultraviolet. *Nature*, 436(7048):234–237, 2005.

[77] D. R. Carlson, Jane Lee, John Mongelli, E. M. Wright, and R. J. Jones. Intracavity ionization and pulse formation in femtosecond enhancement cavities. *Optics Letters*, 36(15):2991–2993, Aug 2011.

[78] P Béjot, Jérôme Kasparian, Stefano Henin, V Loriot, T Vieillard, E Hertz, O Faucher, B Lavorel, and J-P Wolf. Higher-order kerr terms allow ionization-free filamentation in gases. *Physical Review Letters*, 104(10):103903, 2010.

[79] J. M. Brown, A. Lotti, A. Teleki, and M. Kolesik. Exactly solvable model for nonlinear light-matter interaction in an arbitrary time-dependent field. *Phys. Rev. A*, 84:063424, Dec 2011.

[80] G. Gamow. Zur Quantentheorie des Atomkernes. *Zeitschrift fur Physik*, 51:204–212, March 1928.

[81] A. J. F. Siegert. On the derivation of the dispersion formula for nuclear reactions. *Phys. Rev.*, 56:750–752, Oct 1939.

[82] W. P. Reinhardt. Complex coordinates in the theory of atomic and molecular structure and dynamics. *Annual Review of Physical Chemistry*, 33(1):223–255, 1982.

[83] M. Kolesik, J. M. Brown, A. Teleki, P. Jakobsen, J. V. Moloney, and E. M. Wright. Metastable electronic states and nonlinear response for high-intensity optical pulses. *Optica*, 1(5):323–331, Nov 2014.

[84] L. Hamonou, T. Morishita, and O. I. Tolstikhin. Molecular siegert states in an electric field. *Phys. Rev. A*, 86:013412, Jul 2012.

[85] M. Glück, A. R. Kolovsky, and H. J. Korsch. Wannier-stark resonances in optical and semiconductor superlattices. *Physics Reports*, 366(3):103 – 182, 2002.

[86] Sara Cruz y Cruz and Oscar Rosa-Ortiz. Leaky modes of waveguides as a classical optics analogy of quantum resonances. *Advances in Mathematical Physics*, 2015(281472), 2015.

[87] C. M. Bender. Making sense of non-hermitian hamiltonians. *Reports on Progress in Physics*, 70(6):947, 2007.

[88] N. Moiseyev. Quantum theory of resonances: calculating energies, widths and cross-sections by complex scaling. *Physics Reports*, 302(56):212 – 293, 1998.

[89] D. C. Brody. Biorthogonal quantum mechanics. *Journal of Physics A: Mathematical and Theoretical*, 47(3):035305, 2014.

[90] A. Bohm. Resonances/decaying states and the mathematics of quantum physics. *Reports on Mathematical Physics*, 67(3):279 – 303, 2011.

[91] T. Berggren. On the use of resonant states in eigenfunction expansions of scattering and reaction amplitudes. *Nuclear Physics A*, 109(2):265 – 287, 1968.

[92] R. de la Madrid, G. Garcia-Calderon, and J. G. Muga. Resonance expansions in quantum mechanics. *Czechoslovak Journal of Physics*, 55(9):1141–1150, 2005.

[93] J Julve and F J de Urres. Inner products of resonance solutions in 1d quantum barriers. *Journal of Physics A: Mathematical and Theoretical*, 43(17):175301, 2010.

[94] W. J. Romo. Inner product for resonant states and shell-model applications. *Nuclear Physics A*, 116(3):617 – 636, 1968.

[95] P. Lindl. Completeness relations and resonant state expansions. *Phys. Rev. C*, 47(5):1903 – 1920, 1993.

[96] O. Civitarese and M. Gadella. Physical and mathematical aspects of Gamow states. *Physics Reports*, 396(2):41 – 113, 2004.

[97] T. Berggren. Expectation value of an operator in a resonant state. *Physics Letters B*, 373(13):1 – 4, 1996.

[98] N. Hatano, T. Kawamoto, and J. Feinberg. Probabilistic interpretation of resonant states. *Pramana*, 73(3):553–564, 2009.

[99] A. H. Larsen, U. De Giovannini, D. L. Whitenack, A. Wasserman, and A. Rubio. Stark ionization of atoms and molecules within density functional resonance theory. *The Journal of Physical Chemistry Letters*, 4(16):2734–2738, 2013.

[100] Y. Okajima, O. I. Tolstikhin, and T. Morishita. Adiabatic theory of high-order harmonic generation: One-dimensional zero-range-potential model. *Phys. Rev. A*, 85:063406, Jun 2012.

[101] Ya. B. Zel'dovich. On the theory of unstable states. *J. Exptl. Theoret. Phys. (U.S.S.R.)*, 39:776–780, Sept 1960.

[102] R. M. More and E. Gerjuoy. Properties of resonance wave functions. *Phys. Rev. A*, 7:1288–1303, Apr 1973.

[103] N. Moiseyev. *Non-Hermitian quantum mechanics*. Cambridge University Press, 2011.

[104] O. Valle and M. Soares. *Airy Functions And Applications To Physics*. Imperial College Press, 57 Shelton St, Covent Garden, London, England WC2H 9HE, 2004.

[105] D. Bohm. *Quantum Theory*. Dover Books on Physics Series. Dover Publications, 1951.

[106] A. Mondragn and E. Hernndez. Accidental degeneracy and berry phase of resonant states. In A. Bohm, H.-D. Doebner, and P. Kielanowski, editors, *Irreversibility and Causality Semigroups and Rigged Hilbert Spaces*, volume 504-504 of *Lecture Notes in Physics*, pages 257–281. Springer Berlin Heidelberg, 1998.

[107] S. Panda and B. K. Panda. Analytic methods for field induced tunneling in quantum wells with arbitrary potential profiles. *Pramana*, 56(6):809–822, 2001.

[108] A. Emmanouilidou and N. Moiseyev. Stark and field-born resonances of an open square well in a static external electric field. *The Journal of Chemical Physics*, 122(19), 2005.

[109] Oleg I Tolstikhin, Toru Morishita, and Shinichi Watanabe. Adiabatic theory of ionization of atoms by intense laser pulses: One-dimensional zero-range-potential model. *Physical Review A*, 81(3):033415, 2010.

[110] Oleg I. Tolstikhin, Valentin N. Ostrovsky, and Hiroki Nakamura. Siegert pseudostates as a universal tool: Resonances, S matrix, green function. *Phys. Rev. Lett.*, 79:2026–2029, Sep 1997.

[111] Gastón García-Calderón, Alejandro Máttar, and Jorge Villavicencio. Hermitian and non-hermitian formulations of the time evolution of quantum decay. *Physica Scripta*, 2012(T151):014076, 2012.

[112] Anand Bahl, Aba Teleki, Per Kristen Jakobsen, Ewan M. Wright, and Miroslav Kolesik. Reflectionless beam propagation on a piecewise linear complex domain. *J. Lightwave Technol.*, 32(22):3670–3676, Nov 2014.

[113] Frank WJ Olver. *NIST handbook of mathematical functions*. Cambridge University Press, 2010.

[114] Fredrik Johansson et al. *mpmath: a Python library for arbitrary-precision floating-point arithmetic (version 0.19)*, June 2014. `http://mpmath.org/`.

[115] L Hamonou, T Morishita, O. I. Tolstikhin, and S. Watanabe. Siegert-state method for ionization of molecules in strong field. *Journal of Physics: Conference Series*, 388(3):032030, 2012.

[116] J. Andreasen and M. Kolesik. Nonlinear propagation of light in structured media: Generalized unidirectional pulse propagation equations. *Phys. Rev. E*, 86:036706, 2012.

[117] Yang Xiang, Yueping Niu, and Shangqing Gong. Above-threshold ionization by few-cycle nonlinear chirped pulses. *Physical Review A*, 80(2):023423, 2009.

[118] Vinod Prasad, Brijender Dahiya, and Koichi Yamashita. Ionization of the h atom in ultrashort chirped laser pulses. *Physica Scripta*, 82(5):055302, 2010.

[119] Han-Sung Chan, Zhi-Ming Hsieh, Wei-Hong Liang, AH Kung, Chao-Kuei Lee, Chien-Jen Lai, Ru-Pin Pan, and Lung-Han Peng. Synthesis and measurement of ultrafast waveforms from five discrete optical harmonics. *Science*, 331(6021):1165–1168, 2011.

[120] P Béjot, G Karras, F Billard, J Doussot, E Hertz, B Lavorel, and O Faucher. Subcycle engineering of laser filamentation in gas by harmonic seeding. *Physical Review A*, 92(5):053417, 2015.

[121] J Doussot, P Béjot, G Karras, F Billard, and O Faucher. Phase control of two-color filamentation. *Journal of Physics B: Atomic, Molecular and Optical Physics*, 48(18):184005, 2015.

[122] P Béjot, G Karras, F Billard, E Hertz, B Lavorel, E Cormier, and O Faucher. Harmonic generation and nonlinear propagation: when secondary radiations have primary consequences. *Physical Review Letters*, 112(20):203902, 2014.

[123] Trenton R Ensley, Dmitry A Fishman, Scott Webster, Lazaro A Padilha, David J Hagan, and Eric W Van Stryland. Energy and spectral enhancement of femtosecond supercontinuum in a noble gas using a weak seed. *Optics express*, 19(2):757–763, 2011.

[124] Trenton Ryan Ensley. *White Light Continuum for Broadband Nonlinear Spectroscopy*. PhD thesis, University of Central Florida Orlando, Florida USA, 2015.

[125] RR Freeman, PH Bucksbaum, H Milchberg, S Darack, D Schumacher, and ME Geusic. Above-threshold ionization with subpicosecond laser pulses. *Physical review letters*, 59(10):1092, 1987.

[126] J. M. Brown, E. M. Wright, J. V. Moloney, and M. Kolesik. On the relative roles of higher-order nonlinearity and ionization in ultrafast light-matter interactions. *Opt. Lett.*, 37(10):1604–1606, May 2012.

[127] A Bahl, JM Brown, EM Wright, and M Kolesik. Assessment of the metastable electronic state approach as a microscopically self-consistent description for the nonlinear response of atoms. *Optics letters*, 40(21):4987–4990, 2015.

[128] XM Tong and CD Lin. Empirical formula for static field ionization rates of atoms and molecules by lasers in the barrier-suppression regime. *Journal of Physics B: Atomic, Molecular and Optical Physics*, 38(15):2593, 2005.

[129] JK Wahlstrand, Y-H Cheng, and HM Milchberg. High field optical nonlinearity and the kramers-kronig relations. *Physical review letters*, 109(11):113904, 2012.

[130] Edson R. Peck and Donald J. Fisher. Dispersion of argon. *J. Opt. Soc. Am.*, 54(11):1362–1364, Nov 1964.

[131] Xinhua Xie, Stefan Roither, Markus Schöffler, Erik Lötstedt, Daniil Kartashov, Li Zhang, Gerhard G Paulus, Atsushi Iwasaki, Andrius Baltuška, Kaoru Yamanouchi, et al. Electronic predetermination of ethylene fragmentation dynamics. *Physical Review X*, 4(2):021005, 2014.

[132] Willy Thomas. Über die zahl der dispersionselektronen, die einem stationären zustande zugeordnet sind.(vorläufige mitteilung). *Naturwissenschaften*, 13(28):627–627, 1925.

[133] Fritz Reiche and Willy Thomas. Über die zahl der dispersionselektronen, die einem stationären zustand zugeordnet sind. *Zeitschrift für Physik*, 34(1):510–525, 1925.

[134] Werner Kuhn. Über die gesamtstärke der von einem zustande ausgehenden absorptionslinien. *Zeitschrift für Physik*, 33(1):408–412, 1925.

[135] Sanwu Wang. Generalization of the thomas-reiche-kuhn and the bethe sum rules. *Phys. Rev. A*, 60:262–266, Jul 1999.

[136] A. Bahl, J. M. Brown, E. M. Wright, and M. Kolesik. Assessment of the metastable electronic state approach as a microscopically self-consistent description for the nonlinear response of atoms. *Opt. Lett.*, 40(21):4987–4990, Nov 2015.

[137] J. K. Wahlstrand, Y.-H. Cheng, and H. M. Milchberg. Absolute measurement of the transient optical nonlinearity in N_2, O_2, N_2O, and Ar. *Phys. Rev. A*, 85(4):043820, 2012.

[138] Y-H Chen, S Varma, TM Antonsen, and HM Milchberg. Direct measurement of the electron density of extended femtosecond laser pulse-induced filaments. *Physical review letters*, 105(21):215005, 2010.